

University of Alberta

**PERFORMANCE OF HYBRID FIBER-REINFORCED
POLYMER NANOCOMPOSITE PIPES**

by

Mohammad Towhidul Bashar

A thesis submitted to the Faculty of Graduate Studies and Research
in partial fulfillment of the requirements for the degree of

Doctor of Philosophy

Department of Mechanical Engineering

©Mohammad Towhidul Bashar

Fall 2013

Edmonton, Alberta

Permission is hereby granted to the University of Alberta Libraries to reproduce single copies of this thesis and to lend or sell such copies for private, scholarly or scientific research purposes only. Where the thesis is converted to, or otherwise made available in digital form, the University of Alberta will advise potential users of the thesis of these terms.

The author reserves all other publication and other rights in association with the copyright in the thesis and, except as herein before provided, neither the thesis nor any substantial portion thereof may be printed or otherwise reproduced in any material form whatsoever without the author's prior written permission.

Dedication

“This thesis is dedicated to my late wife Jannatul Ferdous, you who have made the ultimate sacrifice. You encouraged and supported me in every step of this PhD degree. It is the fond memory of your love, patience and understanding that would always inspire me.”

Abstract

Due to their attractive properties, pipes and vessels made from fiber-reinforced polymer composites are increasingly being used for the storage and transmission of pressurized fluids. Yet, the inherent anisotropy and inhomogeneity of fiber-reinforced composites in conjunction with complex loading conditions may result in a variety of failure mechanisms that restrict their application. In composite pipes, structural failure such as burst and collapse is characterized by a fast loss of the contained fluid, whereas functional failure occurs due to transverse matrix micro-cracking that generates interconnected pathways through the pipe thickness allowing for the fluid to escape.

Recently, polymer nanocomposites have evolved as a new class of high-performance multifunctional materials that often outperform conventionally filled and unfilled polymers in terms of their properties. In the present study, the effect of nano-reinforcements on matrix micro-cracking in filament-wound composites was investigated. It was hypothesized that transverse matrix cracking in polymer composites can be mitigated by reinforcing the matrix with an appropriate nano-particulate phase.

This research work involved the synthesis, characterization and property evaluation of bulk epoxy nanocomposites and hybrid fiber-reinforced epoxy nanocomposites modified with organophilic nanoclay and acrylic triblock-copolymer. The epoxy-clay nanocomposites exhibited superior tensile stiffness with a reduction in ductility. Block-copolymer addition enhanced toughness and ductility of bulk epoxy. The present study further demonstrated that optimal mechanical property enhancements in an epoxy can be

achieved through the formation of a ternary nanocomposite incorporating nanoclay and acrylic triblock-copolymer.

The presence of nanoparticles in the matrix of fiber-reinforced composites imparted an insignificant effect on delamination fracture toughness, while decreasing fiber volume fraction significantly improved fracture toughness. In block-copolymer modified composite pipes, enhanced matrix ductility caused a build-up of strain energy during applied loading until a sudden release of this energy resulted in the initiation and subsequent propagation of matrix cracks. In response an improvement in leakage failure strain was observed, however the process did not suppress matrix micro-cracking in composite pipes, and failure strength remained unaffected. Strength was even reduced in composite pipes modified with nanoclay, which is thought to stem from nanoclay aggregates that may have acted as stress concentration points expediting micro-crack initiation.

Acknowledgements

I would like to extend my sincere gratitude to my supervisors, Dr. Pierre Mertiny and Dr. Uttandaraman Sundararaj for their invaluable guidance and inspiration during the course of this research project. Their thoughtful ideas and encouragement provided constant motivation throughout this degree program.

I am also very grateful for the continued research funding provided by Dr. Pierre Mertiny from his research grant and his constant support throughout this study.

The author would also like to convey his thanks to Dr. Zihui Xia and the members of the Advanced Composite Materials Engineering group for their support, technical expertise and suggestions during the time of this research work. The author acknowledges the helpful instructions of Dr. Anastasia Elias in regards to the DMA analysis. The author also acknowledges the generous contribution of Dr. Robert Barsotti from Arkema in providing the M52 and M52N block-copolymers. The author wants to thank Bernie Faulkner for helping with the test setup and lab assistance. I also thank Randy Mandryk, Diane Caired, George Braybrooke and Joyce Chau in providing analytical and experimental resources. All assistance rendered by the faculty, technical and staff members of the Department of Mechanical Engineering are also greatly acknowledged.

Finally, I would like to thank the Department of Mechanical Engineering at University of Alberta for giving me the opportunity to conduct this research project.

Table of Contents

Chapter 1. Introduction	1
1.1 BACKGROUND	1
1.2 FILAMENT-WOUND COMPOSITE PIPE	2
1.2.1 Stress Analysis and Elastic Properties of Composite Pipe	4
1.2.2 Failure Mechanisms in Filament-wound Composite Pipe	5
1.2.3 Functional Failure in Filament-wound Composite Pipe	7
1.2.4 Matrix Cracking in Fiber-reinforced Composite Laminates	9
1.2.5 Puck's Failure Theory for Filament-wound Composite Pipe	12
1.3 TOUGHENING OF THERMOSET EPOXY	14
1.3.1 Toughening Mechanisms in Epoxy	16
1.3.1.1 <i>Shear Yielding and Cavitation</i>	18
1.3.1.2 <i>Crazing/Normal Yielding</i>	19
1.3.1.3 <i>Crack-tip Blunting</i>	20
1.3.1.4 <i>Rubber Stretching and Tearing</i>	21
1.3.1.5 <i>Crack Pinning</i>	22
1.3.1.6 <i>Crack Deflection/Crack Bifurcation</i>	22
1.4 POLYMER NANOCOMPOSITES	24
1.4.1 Epoxy-clay Nanocomposites	25
1.4.1.1 <i>Structure of Layered Silicate Clay</i>	25
1.4.1.2 <i>Morphology of Epoxy-clay Nanocomposites</i>	27
1.4.1.3 <i>Exfoliation Behavior of Epoxy-clay Nanocomposites</i>	28
1.4.1.4 <i>Physical and Mechanical Properties of Epoxy-clay Nanocomposites</i>	31
1.5 NANOSTRUCTURED BLOCK-COPOLYMERS	32
1.5.1 Synthesis of Block-copolymers	33
1.5.2 Phase Behavior of Block-copolymers	34
1.5.3 Application of Self-assembled Nanostructured Block-copolymers	37
1.6 OBJECTIVE AND SCOPE OF THE PRESENT RESEARCH	39
1.6.1 Organization of the Dissertation	40

REFERENCES	42
Chapter 2. Materials and Experimental Procedure	58
2.1 MATERIAL SYSTEM	58
2.2 PREPARATION OF NANOCOMPOSITES	64
2.2.1 Epoxy-clay Nanocomposites	64
2.2.1.1 <i>Mechanical Dispersion</i>	64
2.2.1.2 <i>Ultrasonic Dispersion</i>	66
2.2.2 Block-copolymer/Epoxy Blends	67
2.2.3 Epoxy Hybrid Nanocomposites	69
2.2.4 Machining of the Specimens	69
2.2.5 Fabrication of Fiber-reinforced Epoxy Nanocomposites	70
2.2.6 Nanocomposite Pipe Fabrication	72
REFERENCES	73
Chapter 3. Characterization and Testing Methods of Nanocomposites	76
3.1 X-RAY DIFFRACTION	76
3.2 TRANSMISSION OPTICAL MICROSCOPY	78
3.3 TRANSMISSION ELECTRON MICROSCOPY	78
3.4 SCANNING ELECTRON MICROSCOPY	79
3.5 DIFFERENTIAL SCANNING CALORIMETRY	81
3.6 FOURIER TRANSFORM INFRARED SPECTROSCOPY	83
3.7 DYNAMIC MECHANICAL THERMAL ANALYSIS	84
3.8 TENSILE TEST	87
3.9 MODE-I FRACTURE TOUGHNESS TEST	89
3.10 MODE-I INTERLAMINAR FRACTURE TOUGHNESS TEST	93
3.11 FIBER VOLUME FRACTION MEASUREMENT	97
3.12 MECHANICAL TESTING OF NANOCOMPOSITE TUBES	97
3.13 DETECTION OF PIPE FAILURES	99

REFERENCES	100
Chapter 4. Morphology, Mechanical and Fracture Properties of Epoxy-clay Nanocomposites	103
4.1 INTRODUCTION	103
4.2 RESULTS AND DISCUSSION	106
4.2.1 Morphology of the Epoxy-clay Nanocomposites	106
4.2.2 Tensile Property of the Epoxy-clay Nanocomposites	115
4.2.3 Fracture Property of the Epoxy-clay Nanocomposites	119
4.2.4 Fractographic Study of the Epoxy-clay Nanocomposites	121
4.2.5 Thermal Property of the Epoxy-clay Nanocomposites	125
4.3 CONCLUSIONS	126
REFERENCES	128
Chapter 5. Study of Morphology and Mechanical Property of Acrylic Triblock-copolymer Modified Epoxy	132
5.1 INTRODUCTION	132
5.2 RESULTS AND DISCUSSION	134
5.2.1 Miscibility of Block-copolymer/Epoxy Blends	134
5.2.2 Microstructure of Cured Block-copolymer/Epoxy Blends	136
5.2.3 Tensile Properties of Block-copolymer/Epoxy Blends	140
5.2.4 Fracture Properties of Block-copolymer/Epoxy Blends	143
5.3 CONCLUSIONS	148
REFERENCES	149
Chapter 6. Microstructure and Mechanical Properties of Epoxy Hybrid Nanocomposites	154
6.1 INTRODUCTION	154
6.2 RESULTS AND DISCUSSION	156
6.2.1 X-ray Diffraction Analysis of Hybrid Nanocomposites	156

6.2.2	Microstructure Study of Hybrid Nanocomposites	157
6.2.3	Tensile Properties of Hybrid Nanocomposites	160
6.2.4	Fracture Properties of Hybrid Nanocomposites	164
6.2.5	Fracture Surface Study of Hybrid Nanocomposites	167
6.3	CONCLUSIONS	169
	REFERENCES	171

Chapter 7. Interlaminar Fracture Behavior of Nanoparticle **175**

Modified Epoxy/Basalt Fiber-reinforced Laminates

7.1	INTRODUCTION	175
7.2	RESULTS AND DISCUSSION	177
7.2.1	Mode-I Interlaminar Fracture Toughness of the Fiber Composites	177
7.2.2	Comparison of Bulk Polymer and Fiber Composite Fracture Energy	183
7.2.3	Fracture Surface Analysis	187
7.3	CONCLUSIONS	190
	REFERENCES	190

Chapter 8. Study of Matrix Micro-cracking in Nanoclay and **194**

Acrylic Triblock-copolymer Modified Epoxy/Basalt Fiber-reinforced Pressure-retaining Structures

8.1	INTRODUCTION	194
8.2	RESULTS AND DISCUSSION	196
8.2.1	TOM Microscopy Study of Bulk Epoxy Nanocomposites	196
8.2.2	Fracture Properties of Bulk Epoxy Nanocomposites	198
8.2.3	Mechanical Properties of Hybrid Nanocomposite Tubes	200
8.2.3.1	<i>Qualitative Analysis of Functional and Structural Failure</i>	201
8.2.3.2	<i>Biaxial Stress-strain Response</i>	203
8.2.3.3	<i>Fracture Analysis of Hybrid Nanocomposite Tubes</i>	206
8.3	CONCLUSIONS	210
	REFERENCES	210

Chapter 9. Conclusions	214
9.1 SUMMARY OF RESEARCH FINDINGS AND CONTRIBUTIONS	214
9.2 TOPICS OF FUTURE STUDY	215
9.2.1 Permeability Based Leakage Modeling to Detect Functional Failure in Composite Pipe	216
9.2.2 Micromechanical Modeling of Damage in Nanoparticle Filled Composite Pipe	217
9.2.3 Final Considerations	219
REFERENCES	220
Appendix A	223
EXPERIMENTALLY GENERATED GRAPHS	223
Appendix B	234
EXPERIMENTAL DATA	234

List of Tables

Table 2-1	Physical characteristics of the epoxy resin system [8].	62
Table 2-2	Physical properties of the neat epoxy resin in cured state [8].	62
Table 2-3	Physical properties of the layered silicate nanoclay [10-12].	63
Table 2-4	Physical and chemical properties of the Nanostrength® M52N [13].	63
Table 2-5	Property of the basalt fiber reinforcements [14].	63
Table 4-1	Clay, organic modifier, <i>d</i> -spacing and corresponding nanocomposite morphology.	115
Table 4-2	Property of epoxy nanocomposites containing various concentrations of I.30E.	116
Table 5-1	Property of modified epoxy blends constraining various types and concentrations of block-copolymers.	141
Table 6-1	Compositions of different single-component epoxy systems and hybrid nanocomposites.	157
Table 6-2	Mechanical properties of modified epoxy containing various types and compositions of nanofiller.	162
Table 7-1	Fracture energy of bulk epoxy and its nanocomposites and corresponding fiber-reinforced composites.	180
Table 8-1	Fiber volume fraction and nominal wall thickness for fiber-reinforced nanocomposite tubes.	201
Table 8-2	Experimental failure stresses of hybrid fiber-reinforced nanocomposite tubes.	205

List of Figures

Figure 1.1	Pictures of the exterior of a pipe taken during weepage test (an ultraviolet die penetrant was used).	8
Figure 1.2	$\sigma_1, \sigma_2, \sigma_3, \tau_{23}, \tau_{31}$ and τ_{21} are stresses acting on a unidirectional composite element related to the natural axes. The stresses σ_n, τ_{nt} and τ_{n1} , which are decisive for interfiber failure are defined by the (x_l, x_n, x_t) coordinate system. Reprinted with permission from [49]. Copyright 1998 Elsevier Limited.	14
Figure 1.3	Toughening mechanisms in rubber modified polymers. Reprinted with permission from [51]. Copyright 1988 Elsevier Limited.	17
Figure 1.4	A SEM micrographs of acrylic based block-copolymer (M52) modified epoxy fracture surface illustrating features from particle cavitation and matrix shear deformation process.	19
Figure 1.5	(a) A schematic of crack-pinning mechanism (Adapted from [51]. Copyright 1988 Elsevier Limited.), and (b) a SEM micrograph of epoxy-clay (I.28E) nanocomposite fracture surface showing features from crack-pinning mechanism.	23
Figure 1.6	SEM micrographs of epoxy-clay (I.30E) nanocomposite fracture surface showing: (a) crack deflection/bifurcation mechanism, and (b) crack deflection and matrix deformation.	24
Figure 1.7	Idealized structure of 2:1 layered silicates (MMT). Reprinted with permission from [110, 128]. Copyright 1999 Springer-Verlag Berlin Heidelberg.	27
Figure 1.8	A schematic illustration of three basic nanoclay structures in a polymer matrix.	28
Figure 1.9	Phase diagram of a linear diblock-copolymer melt predicted from self-consistent mean-field theory. Four ordered morphologies are shown: lamellar (lam), gyroid (gyr), hexagonal (hex) and body-centered cubic (bcc), and a disordered (dis) phase. Reprinted with	35

permission from [136, 143]. Copyright 2004 John Wiley and Sons.

Figure 1.10	Different nanostructured block-copolymer morphologies formed inside an epoxy resin.	37
Figure 2.1	Formation of an epoxy prepolymer.	59
Figure 2.2	A schematic representation of the epoxy curing reaction.	60
Figure 2.3	Representative chemical structures of the alkylammonium ions and acrylic block-copolymers used in this study.	61
Figure 2.4	Picture of powdered nano-fillers: (a) I.30E and (b) M52N.	62
Figure 2.5	Mold used for epoxy casting.	65
Figure 2.6	Process flow diagram of nanocomposite fabrication by mechanical mixing method.	65
Figure 2.7	Liquid epoxy resin EPON 826 with and without nano-fillers.	67
Figure 2.8	Processing steps for nanocomposite fabricated by ultrasonic mixing method.	68
Figure 2.9	A schematic of the processing steps for fiber-reinforced epoxy nanocomposites.	71
Figure 2.10	Tubular specimen geometry and fiber direction.	73
Figure 2.11	Tubular basalt fiber-reinforced epoxy/M52N composite specimens.	73
Figure 3.1	X-ray diffraction trace of I.30E organoclay.	77
Figure 3.2	TOM image of modified epoxy containing 1 wt% M52N block-copolymer.	78
Figure 3.3	TEM microscopy images of (a) 1 wt% nanoclay and (b) 3 wt% block-copolymer modified epoxy.	79
Figure 3.4	SEM microscopy images of (a) 3 wt% nanoclay and (b) 3 wt% block-copolymer modified epoxy.	80
Figure 3.5	Schematic of a DSC instrument.	82
Figure 3.6	DSC trace of cured neat epoxy sample (EPON 826/EPIKURE 9551).	82
Figure 3.7	FTIR spectrum of cured neat epoxy (EPON 826/EPIKURE 9551).	84
Figure 3.8	(a) A schematic of the DMA 8000 instrument and mode of testing [7] and (b) epoxy specimens used for DMTA analysis.	85
Figure 3.9	DMTA analysis showing storage modulus and $\tan\delta$ curves of	86

	modified epoxy containing 5 wt% M52 block-copolymer.	
Figure 3.10	Geometry of the tensile test specimen (dimensions in millimeters).	88
Figure 3.11	(a) Tensile testing setup and (b) failed specimens after tensile testing.	88
Figure 3.12	Typical stress-strain response of the neat epoxy sample (EPON 826/EPIKURE 9551).	89
Figure 3.13	A schematic of the single edge notch bend specimen (dimensions in millimeters).	91
Figure 3.14	Pre-cracking arrangements for (a) blunt crack and (b) sharp crack.	92
Figure 3.15	Pre-crack configurations: (a) blunt crack and (b) sharp crack.	92
Figure 3.16	Mode-I fracture toughness testing of bulk epoxy nanocomposite.	92
Figure 3.17	A schematic of the double-cantilever beam specimen.	94
Figure 3.18	Mode-I interlaminar fracture toughness testing of fiber-reinforced nanocomposite laminates.	95
Figure 3.19	Load-displacement curves of the DCB test specimen (neat epoxy).	95
Figure 3.20	Data reduction procedures employed: (a) modified beam theory, (b) compliance calibration and (c) modified compliance calibration.	96
Figure 3.21	Resistance curves obtained from different data reduction methods.	96
Figure 3.22	(a) Multi-axial testing instrument and (b) structurally failed tubular test specimens.	98
Figure 3.23	Global biaxial stress-strain response of filament-wound pipe made with an epoxy polymer containing 3 wt% of M52N block-copolymer.	99
Figure 3.24	Fluid volume versus intensifier pressure for pipe tested under biaxial loading.	100
Figure 4.1	Typical X-ray diffraction peaks of the organoclay and unmodified clay.	107
Figure 4.2	XRD analysis results showing interlamellar spacing of nanoclay at various stages of I.30E-epoxy nanocomposite processing: (a) organoclay, (b) organoclay in epoxy resin before curing agent addition and (c) after cure.	108
Figure 4.3	X-ray scattering traces of nanocomposites containing 1 wt% nanoclay in epoxy.	109

Figure 4.4	X-ray diffraction patterns of nanocomposites: (a), (b) and (c) prepared by ultrasonic dispersion and (d) and (e) by mechanical dispersion of I.30E clay.	110
Figure 4.5	Transparency of: (a) neat epoxy and nanocomposites containing 1 wt%, 2 wt% and 3wt% I.30E clay and (b) nanocomposites containing 1 wt% of respective nanoclays, both prepared by ultrasonic dispersion method.	111
Figure 4.6	TEM micrographs of nanocomposites made by ultrasonic dispersion of epoxy containing (a) 1 wt% I.30E (high magnification) and 2 wt% I.30E clay at (b) high magnification and at (c) low magnification.	112
Figure 4.7	TEM micrographs of nanocomposites prepared by mechanical mixing of epoxy containing: 1 wt% I.30E at (a) high and (b) low magnifications and (c) 2 wt% I.30E clay.	113
Figure 4.8	TEM images of nanocomposites comprising 1 wt% I.28E in epoxy at: (a) high magnification and (b) low magnification.	114
Figure 4.9	TEM images of nanocomposites comprising 1 wt% PGW in epoxy at: (a) high magnification and (b) low magnification.	114
Figure 4.10	Influence of I.30E clay concentration on tensile modulus of nanocomposites.	117
Figure 4.11	Tensile strength of nanocomposites as a function of I.30E clay content.	117
Figure 4.12	Relation between tensile elongation and I.30E clay loading of nanocomposites.	118
Figure 4.13	Tensile properties of different nanoclay filled epoxy (ultrasonic mixing).	118
Figure 4.14	Influence of I.30E clay concentration on fracture toughness of nanocomposites.	120
Figure 4.15	The variation of fracture energy of nanocomposites with I.30E clay loading.	120
Figure 4.16	Fracture energy of the different nanoclay reinforced nanocomposites.	121
Figure 4.17	SEM micrograph of a neat epoxy fracture surface.	121

Figure 4.18	Fracture surface micrographs (SEM) of nanocomposites made by ultrasonic dispersion of epoxy containing (a) 1 wt%, (b) 1 wt% (high magnification), (c) 2 wt% and (d) 3 wt% I.30E clay.	123
Figure 4.19	Fracture surface micrographs (SEM) of nanocomposites made by mechanical dispersion of epoxy containing (a) 1 wt%, (b) 1 wt% (high magnification), (c) 2 wt% and (d) 3 wt% I.30E clay.	124
Figure 4.20	Fracture surface micrographs (SEM) of nanocomposites comprised of 1 wt% I.28E clay in epoxy at: (a) low magnification and (b) high magnification.	125
Figure 4.21	Fracture surface micrographs (SEM) of nanocomposites comprised of 1 wt% PGW clay in epoxy at: (a) low magnification and (b) high magnification.	125
Figure 4.22	Glass transition temperature of nanocomposites as a function of I.30E clay content.	127
Figure 5.1	FTIR spectra of cured (a) neat epoxy and (b) 5 wt% M52 and (c) 5 wt% M52N modified epoxy blends.	136
Figure 5.2	Transparency of (a) neat epoxy and (b) 3 wt% M52, (c) 3 wt% M52N, (d) 5 wt% M52N and (e) 5 wt% M52 modified epoxy blends.	137
Figure 5.3	TEM micrographs of 3 wt% M52 block-copolymer modified epoxy blends at (a) low and (b) high magnifications.	138
Figure 5.4	TEM micrographs: (a) 3 wt% M52N (without osmic acid straining) and (b) 5 wt% M52N (with osmic acid staining) block-copolymer modified epoxy blends.	138
Figure 5.5	DSC thermograms of cured (a) neat epoxy and (b) 5 wt% M52 and (c) 5 wt% M52N block-copolymer modified epoxy.	139
Figure 5.6	DMTA plot showing storage modulus and $\tan \delta$ curves of neat and 5 wt% block-copolymer modified epoxy.	140
Figure 5.7	Tensile modulus of modified epoxy as a function of block-copolymer content.	142
Figure 5.8	Influence of block-copolymer concentration on tensile strength of modified epoxy.	142

Figure 5.9	Effect of block-copolymer content on modulus of modified epoxy.	143
Figure 5.10	Fracture toughness of modified epoxy plotted against corresponding block-copolymer concentration.	144
Figure 5.11	Strain energy release rate of modified epoxy plotted against corresponding block-copolymer concentration.	145
Figure 5.12	Fracture surface micrographs (SEM) of modified epoxy comprised of 3 wt% M52 block-copolymer at (a) low (1000x) and (b) high (10000x) magnifications.	147
Figure 5.13	Fracture surface micrographs (SEM) of modified epoxy comprised of 3 wt% M52N block-copolymer: (a) low magnification of 20000x and high magnification of (b) 50000x and (c) 100000x.	147
Figure 6.1	X-ray diffraction patterns of (a) organoclay and cured nanocomposites: (b) 1 wt% and (c) 2 wt% I.30E nanoclay filled epoxy, (d) 3B&1C and (e) 1B&3C hybrid compounds.	158
Figure 6.2	TEM images of (a) sample 1C a nanoclay filled epoxy and (b) sample 3B a block-copolymer dispersed epoxy.	159
Figure 6.3	TEM images of 3B&1C a hybrid nanocomposite: pictures are taken at high magnification for specimens (a) without and (b) with osmic acid staining and (d) at low magnification.	160
Figure 6.4	Tensile stress-strain response of modified epoxy with respect to nanofiller contents.	161
Figure 6.5	Tensile modulus of composites in reference to different nanofiller compositions.	162
Figure 6.6	Tensile strength of composites as a function of different nanofiller compositions in epoxy.	163
Figure 6.7	Dependence of composite tensile elongation on various nanofiller compositions in modified epoxy.	164
Figure 6.8	Crack initiation and crack growth behavior of SENB specimens made with: (a) neat epoxy, (b) sample 3C a nanoclay filled epoxy and 1B&3C a hybrid nanocomposite and (c) sample 3B a block-copolymer modified epoxy and 3B&1C a hybrid nanocomposite.	165

Figure 6.9	Fracture toughness of epoxy composites as a function of different nanofiller compositions.	167
Figure 6.10	SEM images of SENB fracture surfaces of sample 3C a nanoclay filled epoxy nanocomposite at (a) low magnification and (b) high magnification.	168
Figure 6.11	SEM images of SENB fracture surfaces of sample 3B a block-copolymer modified epoxy at (a) low magnification and (c) high magnification.	169
Figure 6.12	SEM images of SENB fracture surfaces of 1B&1C a hybrid nanocomposite at (a)-(b) high magnification.	170
Figure 7.1	Load-displacement curves of the DCB test specimens made with: (a) neat epoxy and modified epoxy containing (b) 3 wt% I.30E and (c) 5 wt% M52N respectively.	178
Figure 7.2	Variations in strain energy release rate with delamination length of different fiber composites.	179
Figure 7.3	Dependence of delamination energy on fiber volume fraction of different fiber composites.	182
Figure 7.4	SEM pictures of the cross-section of laminate made with neat epoxy taken at: (a) low and (b) high magnifications.	182
Figure 7.5	Crack initiation energy (NL) of the fiber composites with corresponding fracture energy of the bulk polymers as a function of I.30E content.	184
Figure 7.6	Crack initiation energy (NL) of the fiber composites with corresponding fracture energy of the bulk polymers as a function of M52N content.	185
Figure 7.7	Comparison between steady-state delamination energy of fiber composites and strain energy of bulk polymers.	186
Figure 7.8	Fiber bridging that took place during delamination in a laminate made of neat resin and basalt fiber.	187
Figure 7.9	SEM image of a DCB fracture surface of a laminate made with neat epoxy.	188

Figure 7.10	SEM images of DCB fracture surface of 3 wt% I.30E modified epoxy laminate taken at (a) low and (b) high magnifications.	189
Figure 7.11	SEM images of the DCB fracture surface of 3 wt% M52N modified epoxy laminate taken at (a) low and (b)-(d) high magnifications.	189
Figure 8.1	TOM images of cured block-copolymer/epoxy blend: sharp pre-cracked fracture surface examined under (a) bright field, (b) cross-polarized light and (c) blunt pre-cracked surface under cross-polarized light.	197
Figure 8.2	Critical stress intensity factors of nanocomposites relative to I.30E nanoclay concentration.	199
Figure 8.3	Critical stress intensity factors of nanocomposites relative to M52N block-copolymer concentration.	200
Figure 8.4	Photographs of specimen failure mode: (a) functional failure (epoxy/glass fiber tube) and (b) structural failure (epoxy/basalt fiber tube).	202
Figure 8.5	Hoop stress-strain response for [2H:1A] loading of $[\pm 60_3]_T$ wound tubes containing 3 wt% filler-matrix content.	204
Figure 8.6	Axial stress-strain response for [2H:1A] loading of $[\pm 60_3]_T$ wound tubes containing 3 wt% filler-matrix content.	205
Figure 8.7	Maximum hoop strain corresponding to functional failure of hybrid nanocomposite tubes as a function of nanofiller loading.	207
Figure 8.8	Hoop failure stress of hybrid nanocomposite tubes as a function of M52N block-copolymer loading.	207
Figure 8.9	Hoop failure stress of hybrid nanocomposite tubes as a function of I.30E nanoclay loading.	209
Figure 9.1	Unit-cell model for filament-wound composite pipe.	217
Figure 9.2	(a) Axial stress-strain response and (b) bi-axial straining of the filament-wound pipe.	219

Nomenclature

Δ	is the delamination correction factor determined as the x-axis intercept of the $C^{1/3}$ versus a_I plot
Φ	is the energy calibration factor
δ	is the phase lag
δ_I	is the load-point displacement
δ_{tc}	is the crack-opening displacement
ε	is the engineering strain
ε_0	is the strain amplitude
$\varepsilon_1, \varepsilon_2$	are the normal strains in the local coordinate system
$\bar{\varepsilon}$	is the true tensile strain
ε_c	is the critical strain for craze formation
ε_f	is the matrix failure strain
$\varepsilon_x, \varepsilon_y$	are the normal strains in the global coordinate system
$\{\varepsilon^0\}$	are the midplane strains of the laminate
γ	is the tear energy of rubber
γ_{12}	is the shear strain in the local coordinate system
γ_m	is the fracture energy of the matrix
γ_{xy}	is the shear strain in the global coordinate system
$\{\kappa\}$	are the midplane curvatures of the laminate
λ	is the wavelength (0.17889 nm) of X-ray beam (Co/K-alpha1 radiation)
λ_I	is the extension ratio when rubber particle tear
μ_s	is a pressure coefficient
$\bar{\nu}$	is the wavenumber, which is reciprocal of the wavelength of radiation
θ	is the filament winding angle
θ_0	is the angle of incidence
ρ	is the crack-tip radius
ρ_f, ρ_m, ρ_p	are the density of the fiber, matrix and nanoparticles, respectively
σ	is the engineering stress

σ_0	is the stress amplitude
$\sigma_1, \sigma_2, \sigma_3$	are the normal stresses in the local coordinate system
$\bar{\sigma}$	is the true tensile stress
$\sigma_{ }, \sigma_{\perp}$	are normal stresses parallel and perpendicular to the fibers, respectively
$\sigma_{ ff}, \sigma_{ mf}$	are longitudinal strengths related to fiber and matrix failure, respectively
$\sigma_{\perp mf}, \sigma_{\perp Af}$	are transverse strengths corresponding to matrix and interface failure, respectively
$\sigma_{ mF}$	is a fictitious strength value attainable if the fibers were elongated up to the breaking point of the matrix
$\sigma_{\perp F}$	is the normal strength perpendicular to the fibers
σ_A	is the axial stress applied to the pipe
σ_H	is the hoop stress applied to the pipe
σ_c	is the critical stress attained at a distance c ahead of the crack-tip
σ_m	is the hydrostatic stress
σ_{ys}	is the yield stress
σ_n	normal stress (Mohr's stress) acting on the fracture plane
σ_x, σ_y	are the normal stresses in the global coordinate system
τ_0	is the intrinsic shear strength of the material
τ_{12}	is the shear stress in the local coordinate system
$\tau_{\#}$	are shear stresses parallel and perpendicular to the fibers
$\tau_{\#mf}, \tau_{\#Af}$	are shear strengths referring to the types of failure in the composite
$\tau_{\#F}$	is the shear strength
τ_{nt}, τ_{nl}	shear stresses (Mohr's stresses) acting on the fracture plane
τ_{oct}	is the critical octahedral shear stress
τ_{xy}	is the shear stress in the global coordinate system
ν, ν_{12}	are the Poisson's ratios
ν_0	is the frequency of radiation
ω	is the angular frequency
A_1	is taken as the slope of a plot between a_1/h_0 and cube root of compliance $C^{1/3}$

a	is the overall crack length of the SENB specimen
a_o	is the initial delamination length of the DCB specimen
a_l	is the delamination length of the DCB specimen
B	is the thickness of the SENB specimen
b	is the width of the DCB specimen
C	is the compliance defined as the ratio of the load-point displacement to the applied load, δ_l/P_l
c	is the velocity of light (2.998×10^8 m/s)
D	is the internal pipe diameter
d_{001}	is the spacing between imaginary atomic planes (interlamellar spacing of nanoclay)
$2d$	is the interparticle spacing
E	is the Young's modulus
E_0	is the energy of a photon
E_1, E_2	are the Young's moduli of the lamina
E_l	is the loss modulus
E_s	is the storage modulus
F	is the axial force applied to the pipe
$f(x)$	is a shape factor
G_{I2}	is the shear modulus
G_{IC}	is the strain energy release rate
ΔG_{IC}	is the increase in fracture energy
G_Q	is the conditional strain energy release rate
H	is the Planck's constant (6.626×10^{-34} J.s)
h_0	is the thickness of the DCB sample
h'	is the laminate thickness
K_I	is the stress intensity factor
K_{IC}	is the fracture toughness
K_{ICs}	is the measured stress intensity factor at the onset of crack growth
m_f, m_m, m_p	are the mass of the fiber, matrix and nanoparticles, respectively
N_x, N_y, N_{xy}	are the resultant in-plane forces acting in a laminate

n	is an integer
n_l	is the slope of a least square plot of $\log(\delta_l/P_l)$ versus $\log(a_l)$
P, P_l	is the applied load
$p_{\perp\perp}^{(-)}, p_{\perp\parallel}^{(-)}$	are the slopes of the (σ_n, τ_{nl}) and $(\sigma_n, \tau_{n\parallel})$ fracture envelopes, respectively at $\sigma_n=0$
p_i	is the internal pressure in the pipe
p_o	is the atmospheric pressure
$Q_{11}, Q_{12}, Q_{22}, Q_{66}$	are the reduced stiffness coefficients
$R_{\perp}^{(+A)}, R_{\perp\perp}^A, R_{\perp\parallel}^A$	are fracture resistances
r	is the particle radius
r_y	is the radius of the plastic zone
S	is the support span distance during fracture testing of the SENB specimen
T	is the line energy of the crack front
t	is the time
t_0	is the wall thickness of the pipe
t_g	is the glass transition temperature
U	is the energy estimated by integrating the area under the load versus load-point displacement curve of the mode-I fracture test
V_f	is the fiber volume fraction
V_p	is the volume fraction of the rubber particle
W	is the width of the SENB specimen
X, Y	are time and temperature dependent parameters

Abbreviations

ACME	advanced composite materials engineering
ASTM	American standard test method
BDMA	benzyl dimethylamine
BTFA	boron trifluoride monoethylamine
CC	compliance calibration method
CDS	characteristic damage state
CTBN	carboxyl-terminated butadiene-acrylonitrile
DCB	double-cantilever beam
DMTA	dynamic mechanical thermal analysis
DSC	differential scanning calorimetry
FTIR	Fourier transform infrared spectroscopy
MBT	modified beam theory
MCC	modified compliance calibration method
MDA	methylene dianiline
NMA	nadic methyl anhydride
ODA	octadecyl ammonium
ODT	order-disorder transition
ODTMA	octadecyl trimethyl ammonium
OOT	order-order transition
SCMF	self-consistent mean-field
SEM	scanning electron microscopy
SENB	single edge notch bend
TEM	transmission electron microscopy
TGAP	triglycidyl <i>p</i> -amino phenol
TGDDM	tetraglycidyl diamino diphenylmethane
TOM	transmission optical microscopy
WAXD	wide angle X-ray diffraction
XRD	X-ray diffraction

Chapter 1

Introduction

1.1 BACKGROUND

Excellent load bearing capacity and exceptional resilience against extreme climatic conditions have made filament-wound composite structures especially attractive in challenging conditions, such as applications in arctic and cryogenic environment, oil and gas exploration (e.g. off-shore risers and on-shore down-hole tubulars) and aerospace (e.g. fuselages and propellant tanks) [1]. Lately, filament-wound composites are being used in automotive drive shafts, utility poles and process/high-pressure piping under varied service conditions. Similar to other fiber-reinforced polymeric composites, the primary advantages of adopting filament-wound composite piping are corrosion resistance and a high strength-to-weight ratio. In recent times, with the advent of computer-controlled winding machines, it has become possible to fabricate composite pipes having almost any conceivable winding angle, pattern and lay-up configuration designed to perform in specific application. As in most composite materials, fibers are the structural back-bone of a composite piping providing strength and stiffness. The polymer matrix, on the other hand, provides structural integrity, corrosion resistance, easy processability and cost effectiveness of the composite part, and during service, transfers load between the fibers. High-pressure tubulars are intended to sustain diverse loading conditions throughout their service life, which may be from internal pressure and/or axial loading. However, failure mechanism in composite tubulars, involving damage initiation and progression, accumulation and interaction under varied loading (e.g. uniaxial, multiaxial, monotonic or fatigue loading) and environmental conditions, are extremely complex (e.g. localized or global failure of the material). Inhomogeneity and anisotropy in the composite structure and diversity in available material systems further engender any particular damage mechanism and failure criterion to accurately and reliably describe the composite behavior. A state-of-the-art filament-winding facility was setup at the Mechanical Engineering Department of the University of Alberta with the intention to investigate and

understand the material behavior and failure mechanisms of fiber-reinforced polymeric tubulars. As part of a comprehensive study on the performance of high-pressure composite tubulars, discrete failure modes are being investigated under a variety of loading, processing and geometric conditions at the Advanced Composite Materials Engineering (ACME) lab [1]. Specifically, the aim of these investigations was to study deformation and fracture behavior [1-8], determine functional and structural failure strengths, and develop failure envelopes for composite pipes. To date, the studies carried out by Ellyin et al. [1-2], Mertiny et al. [3-5, 9] and Martens and Ellyin [6, 10] all have recognized two distinct failure events that commonly appear in a pressurized tubular. One is functional failure, also known as leakage/weepage failure that results as a consequence of cracking in the matrix phase, even though the structural integrity and load bearing capacity of the pipe may be unaffected. The other kind of failure is structural or burst failure that happens when the structure is unable to carry the applied loading or collapses completely.

To this extent, the present new research initiative was implemented to focus on synthesis, characterization, manufacturing and application of filament-wound hybrid basalt/epoxy/nanoparticle reinforced composite pipes. In the present study a strong emphasis is given on the mitigation of leakage, and hence transverse matrix cracking in filament-wound composite pipes in the framework of nanotechnology. It is understood that up until now there has only been a limited amount of studies that are devoted to reinforcing filament-wound structures with nanoparticles [11].

1.2 FILAMENT-WOUND COMPOSITE PIPE

The performance of filament-wound composite structure is dependent on the properties of constituent materials (i.e. fiber, matrix and fiber-matrix interface) as well as on the manufacturing and design parameters (e.g. fiber lay-up, laminate stacking sequence, mandrel diameter, winding tension, winding time, fiber wet-out, etc.). This has been revealed by the investigations conducted by Cohen [12] and Cohen et al. [13]. Previously, Spencer and Hull [14] investigated the effect of winding angle ($\pm 35^\circ$, $\pm 45^\circ$, $\pm 65^\circ$ and $\pm 75^\circ$) on the deformation and failure of composite pipes. In the case of weepage failure, they observed the pipe that was wound with a $\pm 55^\circ$ winding angle sustained maximum axial and hoop stresses under pressure vessel type loading. Soden et al. [15] documented that an increasing winding angle

relative to the tube axis provided greater circumferential tensile strength, while lower winding angles developed higher axial strength in the pipe. Mertiny et al. [4] studied the effect of different multi-angle lay-up configurations ($[\pm 60^\circ_3]_T$, $[\pm 45^\circ, \pm 60^\circ_2]_T$ and $[\pm 30^\circ, \pm 60^\circ_2]_T$) under varied biaxial stress ratios, and concluded that multi-angle filament wound tubes performed better in preventing damage. The use of a multidirectional laminate is typical for a composite structure that is subject to combined and complex loading situations. Rousseau et al. [16] studied the degree of interweaving (winding pattern) in filament-wound pipes, and observed an increase in damage growth occurring at crossover undulating regions for condition of closed-ended internal pressure loading. From experimental observation, Mertiny and Ellyin [3] stated that the winding bandwidth and fiber volume fraction of finished parts are influenced by the imposed winding tension during the fabrication process. In another study, Mertiny and Ellyin [5] reported increasing winding tension to lead to higher consolidation of the fiber material, hence producing tubulars with higher fiber volume fraction, which also resulted in greater failure stresses for fiber dominated loading conditions. The loading scenario, such as the type of loading (e.g. tension, compression, bending, torsion, internal pressure, etc.), loading ratio, loading rate, cyclic or monotonic loading and environmental effect [17] (e.g. temperature, aqueous or acidic condition, etc.) all have relevant contributions to the failure characteristics of a composite pipe. The typical loading conditions for pressure pipes are combinations of biaxial stress ratios caused by internal pressure and axial stress under monotonic or fatigue loading. Three main loading ratios have frequently been stated in many publications; these are pure axial tension or compression, pure internal pressure, and the closed end condition or pressure vessel type loading [18-19]. It has been documented that for a tube with a particular lay-up configuration the leakage and ultimate failure strength varied significantly depending on the applied circumferential to axial loading ratio [15]. Studies conducted by Ellyin et al. [2] and Carroll et al. [20] demonstrated that biaxial failure stress-strain behavior of filament-wound glass-fiber/epoxy tubular are dependent on loading rate, i.e. failure stresses increased with higher loading rate. Similarly, Mertiny and Gold [9] and others have observed the effect of time-dependent behavior on stress-strain response and damage mechanism of composite pipes [20-21]. In the case of functional failure, a loading rate dependency is to be expected as weepage is the outcome of a matrix-dominated failure event. Ellyin and Martens [10] and Kujawski et al. [22] studied

functional failure behavior of multidirectional glass-fiber/epoxy pipes under fatigue loading, and noted early damage initiation for cyclic loading. In a dynamic loading scheme, damage by matrix cracking, fiber debonding and delamination are major causes of concern for fatigue life reduction in composite tubulars.

In the present study, a $[\pm 60^{\circ}_3]_T$ angle-ply lay-up was chosen purposefully for the design loading condition (where circumferential to axial load ratio is 2:1). It has been documented in the published literature that this winding angle produces a high discrepancy between leakage and ultimate failure strengths under a loading ratio of 2:1 [23], hence indicating a strong susceptibility of this combination of lay-up geometry and loading to leakage failure.

It is natural to expect an axial oriented winding angle to sustain a larger axial load. Alternatively, a hoop winding would provide maximum strength in the circumferential direction. The highest stress that a tubular structure will endure before fiber failure (i.e. rupture of the pipe) can be estimated using the netting analysis technique, which assumes applied stresses to be carried by forces in the fibers and a negligible contribution from resin phase. Applying netting analysis approximation for the selected loading condition, $\tan^2\theta = 2$, where θ is the fiber angle with respect to the cylindrical axis, an optimum winding angle of approximately $\pm 55^{\circ}$ is found. It can be surmised that the selected lay-up configuration of $[\pm 60^{\circ}_3]_T$ provides a stronger performance for hoop dominated loading ratios, while it contributes rather poorly for axial loading conditions.

1.2.1 Stress Analysis and Elastic Properties of Composite Pipe

The composite structure of a filament-wound pipe can be envisaged as an angle-ply laminate. As the cylindrical shell of a composite pipe is usually relatively thin compared to other dimensions only in-plane stresses (plane stress condition) are considered. In this context, classical laminate theory has widely been applied, which considers each lamina to be composed of a linear elastic orthotropic homogenous material. The fundamental unit in a laminate is the single unidirectional lamina. The stress-strain relationship of an angle-ply lamina in a local coordinate frame can be written as.

$$\begin{Bmatrix} \sigma_1 \\ \sigma_2 \\ \tau_{12} \end{Bmatrix} = \begin{Bmatrix} Q_{11} & Q_{12} & 0 \\ Q_{12} & Q_{22} & 0 \\ 0 & 0 & Q_{66} \end{Bmatrix} \begin{Bmatrix} \varepsilon_1 \\ \varepsilon_2 \\ \gamma_{12} \end{Bmatrix} \quad (1.1)$$

The reduced stiffness coefficients are $Q_{11} = \frac{E_1}{1-\nu_{12}\nu_{21}}$, $Q_{12} = \frac{\nu_{12}E_2}{1-\nu_{12}\nu_{21}}$, $Q_{22} = \frac{E_2}{1-\nu_{12}\nu_{21}}$ and $Q_{66} = G_{12}$, where E_1 and E_2 are the Young's moduli in parallel and transverse to the fiber directions, $\nu_{12} = \frac{\nu_{21}E_2}{E_1}$ is the Poisson's ratio, and G_{12} is the shear modulus.

It is assumed that in a laminate the laminae are perfectly bonded to each other, which implies no slip occurs at the interfaces between different laminae. If the strain varies linearly through the laminate thickness, then the laminate strains in a global coordinate system are:

$$\begin{Bmatrix} \varepsilon_x \\ \varepsilon_y \\ \gamma_{xy} \end{Bmatrix} = \begin{Bmatrix} \varepsilon_x^0 \\ \varepsilon_y^0 \\ \gamma_{xy}^0 \end{Bmatrix} + z \begin{Bmatrix} \kappa_x \\ \kappa_y \\ \kappa_{xy} \end{Bmatrix} \quad (1.2)$$

where $\{\varepsilon^0\}$ and $\{\kappa\}$ are midplane strains and curvatures. Then stresses in each lamina can be integrated over the whole laminate thickness to give the resultant in-plane forces.

$$\begin{Bmatrix} N_x \\ N_y \\ N_{xy} \end{Bmatrix} = \int_{-h/2}^{h/2} \begin{Bmatrix} \sigma_x \\ \sigma_y \\ \tau_{xy} \end{Bmatrix} dz \quad (1.3)$$

where h' is the laminate thickness. As expressed above the stress analysis and elastic properties of the composite pipe can be predicted from the constitutive properties of the laminae by laminate theory. But, the laminate theory does not adequately address the complexity of the composite structure (e.g. the effect of material inhomogeneity, lay-up sequences, etc.). As well, it does not give answers to damage micromechanics and mechanisms of the fracture process. Classical laminate theory, while being restrictive in theoretical and computational premise for the accurate analysis and prediction of pre-existing, progressive or degradative damage, can still be regarded as a useful tool for failure analysis of composite pipes.

1.2.2 Failure Mechanisms in Filament-wound Composite Pipe

In recent years, significant research has been conducted to find accurate and reliable design methodologies and analytical predictions for the behavior of filament-wound composite pipes. A review of the existing literatures revealed that failure behavior of $\pm 60^\circ$ and $\pm 55^\circ$ helically wound pipes [18-19, 23] have been the subject of many studies that has provided substantial understating of failure mechanism in these lay-up geometries. A large amount of

literature is available on stress-strain behavior, failure micromechanics, damage description and failure modes of composite pipes [5-6]. Experimentally determined failure envelopes (biaxial failure envelopes) have been developed for various combinations of biaxial loading ratio for filament-wound pipes with given lay-up configurations [10, 15, 23]. In an actual setup, these failure envelopes can be adopted to provide an acceptable design basis and guideline for safe operational specifications, under the condition that the material and fabrication system remain the same for comparable loading scenarios.

In accordance to the physical observations made during testing of $\pm 60^\circ$ filament-wound pipes, Meijer and Ellyin [7] characterized failure events into five general categories based on the first failure mode detected for various combinations of hoop and axial loading. These are tensile axial failure under axial dominated load ratios (0:1 and 1:1), weepage under closed end pressure vessel type loading (2:1), local leakage in constrained end condition manifested by fine jets of fluid spraying from local sites (4:1, 4.5:1 and 5:1), burst failure under hoop dominated stress ratios (7:1, 1:0, 7:-1 and 2:-1) and compressive axial failure (0:-1). The load ratio shown in brackets corresponds to applied biaxial hoop to axial stresses. Spencer and Hull [14] observed the following phenomena to occur during failure of composite pipes: nonlinearity in elastic response, whitening, audible cracking, weepage, bending, bucking and fiber failure followed by prominent structural damage to the composite pipe. Damage mechanisms in filament-wound structures are not mutually exclusive, besides not restricted to any particular failure event. For instance, a study by Mertiny and Ellyin [5] on filament-wound glass fiber-reinforced $[\pm 60^\circ_3]_T$ pipes confirmed that in the case of pure hoop loading (1:0) and pure axial loading (1:15) functional failure coincided with structural failure. They also documented that the functional failure occurred at 0.3% transverse strain (i.e. strain transverse to the fiber direction) regardless of the considered stress ratios [5]. Similar findings were reported by Aps et al. [24]. Even though substantial progress has been made in understating the material and failure behavior of composite pipes, limited knowledge is still prevalent in areas like weepage failure concerning transverse matrix cracking [25]. Therefore, in order to produce reliable and safe composite tubulars it is of great importance that the uncertainty regarding matrix cracking should be addressed adequately.

1.2.3 Functional Failure in Filament-wound Composite Pipe

Micro-damage associated with the evolution of leakage in composite pipes wound at $\pm 55^\circ$ and $\pm 65^\circ$ fiber angles was studied by Jones and Hull [26]. They witnessed first visual evidence of matrix damage in the form of thin white streaks parallel to the fibers as the pipe was subject to applied loading. On further pressurization more streaks became evident with increasing number and length, along with small opaque areas in the matrix. These striations evolved in all the laminae that made up the tube shell, and propagated rapidly in the through-thickness direction forming a continuous interconnected network through which fluid can permeate. They correlated the appearance of these fine striations to transverse cracking perpendicular to the lamina plane and opaque patches as cracking parallel to the lamina plane (i.e. interlaminar cracking).

Normally functional failure is recognized through manifestation of the weepage phenomenon by appearance of fluid droplets on the wall of a pipe after sufficient matrix damage has developed [26]. Figure 1.1 presents photographs of a composite pipe that has suffered leakage failure. The images show white streaks parallel to the fiber direction and droplets of a fluorescent fluid under ultraviolet light. The cracking may have initiated from debonding at the fiber-matrix interface or within the matrix itself in a region at or near the fiber surface where the strain concentration is significantly high [26]. Strain magnification takes place in the resin between densely packed fibers, because fibers and polymers have elastic constants that are very different from each other. Bai et al. [18] studied the mechanical behavior of glass-fiber/epoxy filament-wound tubes, and observed transverse crack nucleation arising from pre-existing defects (e.g. porosity, voids and debonded fibers) [16]. Generally, transverse cracks propagate through the resin around the fibers which has frequently been associated with interlaminar cracking. Transverse cracking results from tensile stress acting transverse to the fiber, whereas interlaminar cracking develops in response to shear stresses. It is therefore perceived that in a composite pipe the through-thickness leakage path consists of both intralaminar cracks (transverse matrix cracking) in the laminae and interlaminar cracks (delamination) between the laminae. Slow weepage of contained fluid is an indication that sufficient matrix cracking has developed to result in fluid loss towards the outer surface of the tube wall. Transverse cracking unavoidably results in changes in thermoelastic properties (e.g. stiffness reduction), redistribution of internal stresses and stress-strain

nonlinearity in the composite structure, which are indications of damage initiation and accumulation in the laminate [27]. Weepage considerably reduces the operating pressure of the filament-wound pipes. Consequently, without any additional containment medium (e.g. liner), functional failure restricts their application in any high-pressure system.

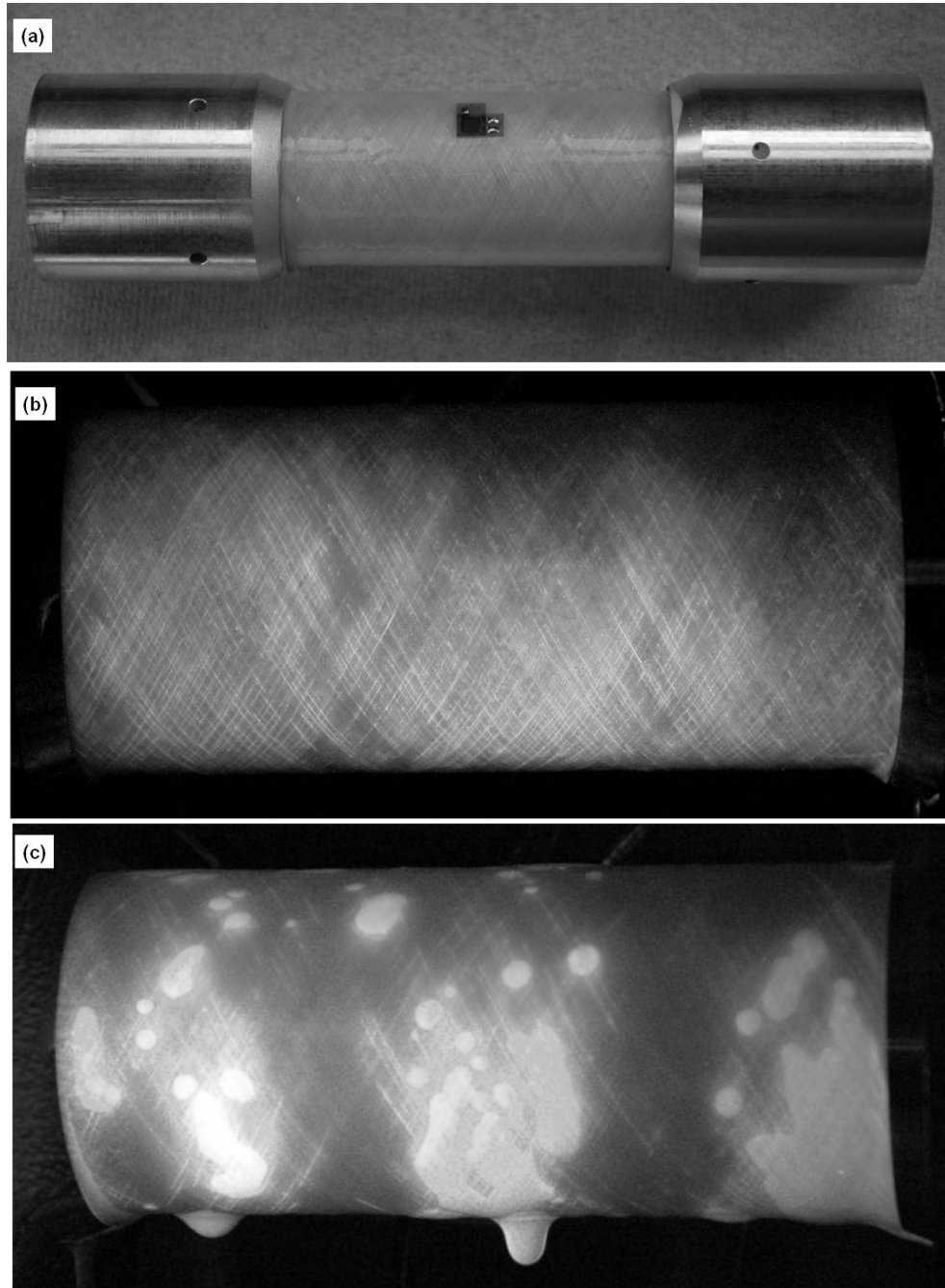


Figure 1.1 Pictures of the exterior of a pipe taken during weepage test (an ultraviolet die penetrant was used).

1.2.4 Matrix Cracking in Fiber-reinforced Composite Laminates

In many composite systems matrix cracking is usually the initial damage mode that subsequently evolves into more severe forms of structural failure. In laminated fiber-polymer composites a multiplicity of damage modes is manifested by matrix cracking, fiber breaking and fiber-matrix interfacial debonding. Matrix cracking may arise in the form of intralaminar cracks, that is, transverse matrix cracking in off-axis plies, and interlaminar cracking in between adjacent plies of a laminate. The overall matrix cracking phenomena can be considered a three step process consisting of crack initiation, growth and localization superseded by final structural failure that frequently involves the concurrence of different failure modes [28]. Damage growth in a composite is usually associated with stress-strain nonlinearities in the material response resulting from redistribution of the stress field after matrix cracking. As stated earlier, transverse matrix microcracking significantly affects the overall mechanical performance regarding strength, stiffness and service life of the laminated structures. Apparently, the complexity in matrix cracking behavior and corresponding degradation of material properties emphasize the need for a predictive model to precisely portend the material response.

The traditional laminate theory in conjunction with the approximate ply discount method for first ply and consecutive ply failures can predict stiffness reduction, but this has limited accuracy (underestimating/overestimating) in determining the stiffness of a cracked laminate [27]. A great number of research activities has been carried out to understand the transverse matrix cracking phenomena (pertaining to initiation and damage growth) and its effect on mechanical properties (e.g. stiffness and Poisson's ratio change) of the laminate from both experimental and theoretical grounds [28-43]. Many of these studies were primarily devoted to finding a threshold stress or strain at the onset of cracking and crack spacing measurements [29]. Hahn and Tsai [30] were one of the first to associate stiffness reduction in a symmetric cross-ply laminate to that of transverse cracks in 90° plies. Garrett and Bailey [29] studied transverse cracking in cross-ply laminates, and observed matrix cracking to occur at a much lower strain than the ultimate resin failure strain. They also perceived the fact that spacing between transverse cracks decreased with increasing stress and decreasing thickness of the transverse ply.

Various analytical models (i.e. shear-lag [28, 31], continuum damage mechanics [32], self-consistent approximation [33-34] and variational approach [35]) have been developed mainly to evaluate the influence of transverse matrix cracking on effective material properties of the cracked laminates. Aveston and Kelly [36] developed a multiple fracture theory that describes the theoretical stress-strain behavior of a composite after matrix cracking. Reifsnider [37] analyzed transverse matrix cracks in laminates, and made the important finding of the formation of distinct cracking pattern after sufficient loading to the composite. Reifsnider termed this uniform periodic saturation pattern in crack spacing at particular off-axis plies as characteristic damage state (CDS). Highsmith and Reifsnider [31] were among the first researchers to conduct analytical studies based on shear-lag analysis to predict stiffness reduction as a result of matrix cracking in composite laminates. They implemented a shear-lag analysis to model the stress transfer between the cracked lamina and the neighboring laminae, where a thin layer of matrix rich region is assumed to transfer load between adjacent plies. In developing this analytical model, they neglected the mutual interactions between cracks, and assumed that normal stresses in the loading direction are constant across the ply thickness. Hence, they have observed good correlation between experimental and analytical data. Lee and Daniel [28] used shear-lag analysis to adopt a progressive transverse cracking model for cross-ply laminates under uniaxial tensile loading. Their proposed method gave closed form solutions for stiffness, crack density and stress distribution in the cracked laminate as a function of applied loading and properties of the laminae. McCartney [38] modeled stress transfer between adjacent plies in a 0° - 90° - 0° cross-ply laminate containing transverse cracks, and estimated the effect of matrix cracking on laminate stiffness, Poisson's ratio and thermal expansion coefficient. By employing a self-consistent method Dvorak et al. [33] evaluated thermoelastic properties (e.g. stiffness and thermal expansion coefficients) of a damaged lamina that contains a specified density of transverse cracks. Based on fracture mechanics principles Dvorak and Laws [34] further investigated the mechanics of transverse matrix cracking in a single ply of a composite laminate under in-plane loading. They presumed transverse cracking to initiate from localized regions of debonded fibers acting as crack nucleation

sites, and studied the onset of unstable cracking by considering the influence of adjacent plies on the cracked ply.

Hashin [35, 39] used variational methods to evaluate stiffness reductions and stresses in cross-ply laminates in the presence of intralaminar cracks based on the principle of minimum complementary potential energy. Applying the variational approach he predicted the stiffness reduction in a $[0^\circ/90^\circ_3]_S$ glass/epoxy laminate, which was in good agreement with experimental results. Talreja [32] presented a continuum mechanics model to characterize the mechanical response of a damaged laminate by a set of internal vector field variables that represent the damage state. A constitutive equation for isothermal small-deformation behavior of the composite was derived by taking into account the condition of the damaged laminate. Continuum damage modeling does not only require the elastic constants of the constituents of the undamaged composite but also damage-related material constants, which have to be determined experimentally. The stiffness changes associated with transverse cracking determined by continuum damage modeling showed good agreement with the experimental results [27, 40]. On the hypothesis of Talreja's [32] continuum damage mechanics theory a lamina-based damage model was presented by Li et al. [41] that can describe the mechanical response of the damaged laminate. In this model the damage variables are associated with each specific cracked lamina allowing effective material properties to be related directly to individual laminae. This lamina-based damage representation can subsequently be resolved into a more detailed ply-by-ply laminate analysis for determining general material properties of the composite by taking into account lay-up configurations and position of the cracked ply. Their complete damage model combines vector field representation of damage with a damage growth law in the form of crack multiplication.

Recently, Roberts et al. [42] formulated a shear-lag based model to relate crack density as a function of applied stress, and used the procedure developed by Gudmundson and Zang [43] to determine the thermoelastic properties of cracked laminates by deriving an expression for compliance, strains and thermal strains (related to crack density). Finally, combining these two functions yielded an expression for a nonlinear stress-strain relationship. They have found excellent agreement between the predicted stress-strain

behavior and experimental results obtained from biaxial testing (internal pressure and axial load) done with fiber-reinforced composite pipe.

1.2.5 Puck's Failure Theory for Filament-wound Composite Pipe

A number of failure theories exist as documented by the World Wide Failure Exercise [25, 44] that increases the debate and uncertainty regarding their proper use in modeling and designing composite materials. Based on sound physical background both micro-mechanical and phenomenological models are widely used in the design practice.

According to Puck's laminate failure theory, the types of failure that occur in composites fall into three general categories, i.e. cohesive failures of the fiber and matrix, and adhesive failure of the fiber-matrix interface [45]. Fiber failure is followed by ultimate failure of the structure, and in many instances preceded by matrix or interfacial failure. Puck inferred that theoretically interfiber failure (i.e. matrix and interfacial failure) should be evaluated separately from fiber failure with different failure criteria. Based on simplified micromechanical assumptions Puck and Schneider [45] established a failure criterion that gives a better approximation and reasonable basis for failure analysis of filament-wound composite tubes, i.e.:

For fiber failure

$$\frac{\sigma_{\parallel}}{\sigma_{\parallel ff}} = 1 \quad (1.4)$$

For matrix failure

$$\left(\frac{\sigma_{\parallel}}{\sigma_{\parallel mf}}\right)^2 + \left(\frac{\sigma_{\perp}}{\sigma_{\perp mf}}\right)^2 - \frac{1}{3}\left(\frac{\sigma_{\parallel}\sigma_{\perp}}{\sigma_{\parallel mf}\sigma_{\perp mf}}\right) + \left(\frac{\tau_{\#}}{\tau_{\# mf}}\right)^2 = 1 \quad (1.5)$$

For interface failure

$$\frac{\sigma_{\perp}}{\sigma_{\perp Af}} + \left(\frac{\tau_{\#}}{\tau_{\# Af}}\right)^2 = 1 \quad (1.6)$$

where σ_{\parallel} and σ_{\perp} are normal stresses parallel and perpendicular to the fibers, respectively, and $\tau_{\#}$ are shear stresses parallel and perpendicular to the fibers. $\sigma_{\parallel ff}$ and $\sigma_{\parallel mf}$ are longitudinal strengths related to fiber and matrix failure, respectively, and $\sigma_{\perp mf}$ and $\sigma_{\perp Af}$ are transverse strengths related correspondingly to matrix and interface failure. $\tau_{\# mf}$ and $\tau_{\# Af}$ are shear strengths with subscripts referring to the types of failure in the composite. Since in

equations (1.5) and (1.6) the criteria for resin and interface failures were hypothetical in nature, Puck in subsequent publications [46-47] modified the interfiber failure theory into a semi-empirical equation as expressed in the following.

$$\left(\frac{\sigma_{\parallel}}{\sigma_{\parallel mF}}\right)^2 + \left(\frac{\sigma_{\perp}}{\sigma_{\perp F}}\right)^2 + \left(\frac{\tau_{\#}}{\tau_{\#F}}\right)^2 \leq 1 \quad (1.7)$$

where, $\sigma_{\perp F}$ is the normal strength perpendicular to the fibers, and $\tau_{\#F}$ is the shear strength. $\sigma_{\parallel mF}$ is a fictitious strength value attainable if the fibers were elongated up to the breaking point of the matrix. Since, leakage failure (i.e. transverse cracking) in composite pipe is associated with matrix and interfacial failure, then for transverse cracks to grow both transverse tensile stress σ_{\perp} and shear stress $\tau_{\#}$ need to be considered. Previously, validity of the above failure criteria has been proven in the literature [14, 47] under combined torsional and axial tensile loading for hoop wound tubes. As $\sigma_{\parallel} = 0$, equation (1.7) becomes.

$$\left(\frac{\sigma_{\perp}}{\sigma_{\perp F}}\right)^2 + \left(\frac{\tau_{\#}}{\tau_{\#F}}\right)^2 \leq 1 \quad (1.8)$$

Composites made of epoxy and glass fibers are intrinsically very brittle, and a failure theory based on a brittle fracture criterion would be more appropriate to describe their fracture behavior. Then a fracture hypothesis employing Coulomb-Mohr brittle fracture theory would be more applicable than a failure criterion based on von Mises yield theory for ductile metals. Puck adopted a Coulomb-Mohr brittle failure hypothesis to transform his failure theory into a physically based phenomenological fracture criterion. Puck's theory for interfiber fracture is formulated based on Mohr's stresses (normal stress σ_n and shear stresses τ_{nt} and τ_{nl} as shown in Figure 1.2) acting on the fracture plane. Based on Puck's theory the fracture condition for interfiber failure can be expressed as [48-50]:

$$\left(\frac{\tau_{nt}}{R_{\perp\perp}^A}\right)^2 + \left(\frac{\tau_{n1}}{R_{\perp\parallel}^A}\right)^2 + C_2 \left(\frac{\sigma_n}{R_{\perp}^{(+A)}}\right)^2 + C_1 \left(\frac{\sigma_n}{R_{\perp}^{(+A)}}\right) = 1 \text{ for } \sigma_n \geq 0 \quad (1.9)$$

$$\frac{\tau_{nt}^2}{(R_{\perp\perp}^A)^2 - 2p_{\perp\perp}^{(-)} R_{\perp\perp}^A \sigma_n} + \frac{\tau_{n1}^2}{(R_{\perp\parallel}^A)^2 - 2p_{\perp\parallel}^{(-)} R_{\perp\parallel}^A \sigma_n} = 1 \text{ for } \sigma_n < 0 \quad (1.10)$$

where $R_{\perp}^{(+A)}$, $R_{\perp\perp}^A$ and $R_{\perp\parallel}^A$ are fracture resistances, and $p_{\perp\perp}^{(-)}$ and $p_{\perp\parallel}^{(-)}$ are the slopes of the (σ_n, τ_{nt}) and (σ_n, τ_{n1}) fracture envelopes, respectively at $\sigma_n = 0$.

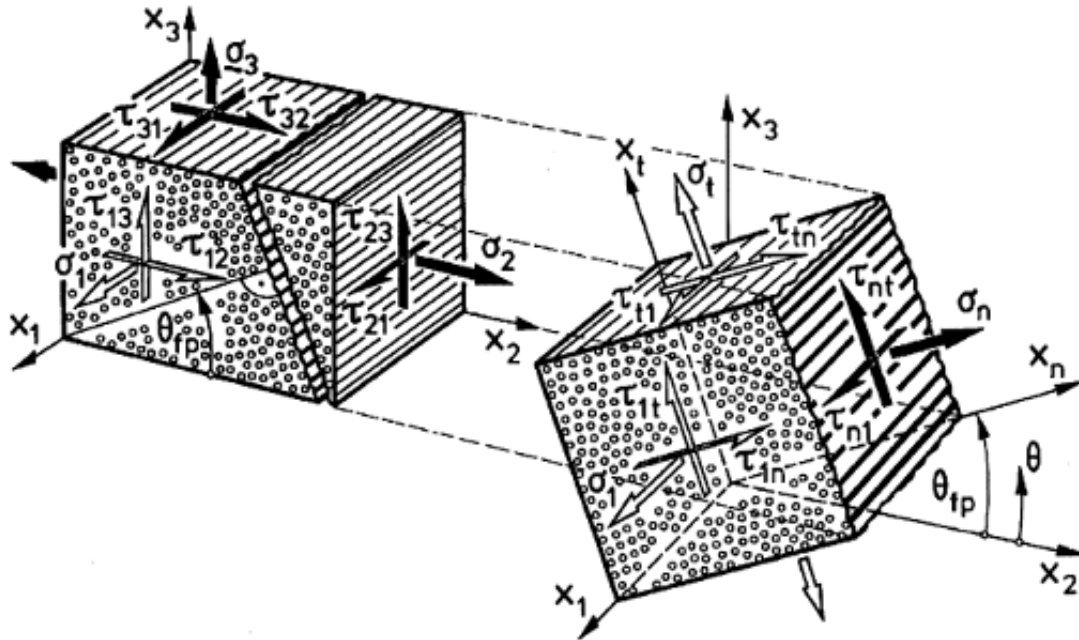


Figure 1.2 σ_1 , σ_2 , σ_3 , τ_{23} , τ_{31} and τ_{21} are stresses acting on a unidirectional composite element related to the natural axes. The stresses σ_n , τ_{nt} and τ_{n1} , which are decisive for interfiber failure are defined by the (x_1, x_n, x_t) coordinate system. Reprinted with permission from [49].

Copyright 1998 Elsevier Limited.

1.3 TOUGHENING OF THERMOSET EPOXY

In regard to conventional and novel applications, thermosetting epoxy is one of the mainstream and versatile polymers available for structural parts, adhesives, thin film coatings and matrix material for fiber-reinforced polymer composites. At present, epoxy has been extensively used in aerospace, marine and automotive applications. The application of epoxy has marked advantages over many engineering polymers, i.e. better stiffness, creep resistance, chemical inertness and elevated temperature applicability. However, the impressive physical and mechanical properties of epoxy bring about certain drawbacks, such as high brittleness and notch sensitivity. As a consequence of this inherent brittleness the structural strength of the finished part made from epoxy degrades easily subsequent to matrix damaged. Toughening of epoxy has therefore gained a great deal of attention, and substantial activities and efforts have been focused towards this direction. In general, common epoxies have mode-I fracture energy values in the range of 80-300 J/m², either in bulk or adhesive or delamination fracturing in fiber composites

[51]. The significance of toughness in the sense of material failure is that it is a physical parameter (i.e. plane-strain critical stress intensity factor (K_{Ic}), strain energy release rate (G_{Ic}), Izod impact strength and area under the tensile stress-strain curve) that estimates the failure energy or failure stress of a material.

In an elastomer technology handbook, Sue et al. [52] mentioned many different approaches by which an epoxy can be toughened, that is, (1) chemical modification/functionalization of the epoxy backbone; (2) increasing the epoxide monomer molecular weight; (3) decreasing the cross-link density of cured epoxy; and (4) adding a second dispersed phase. The process of incorporating a toughener phase (typically less than 20 wt%) may involve organic modifiers, liquid rubbers [53-59], thermoplastic spheres [60], core-shell particles [61-63] and nanostructured block-copolymers [64]. Furthermore, the addition of inorganic particles, notably silica [65-66], glass beads [67], alumina [65] and nanoclay [68-69] has become a commonly recognized practice. In this respect, butadiene-acrylonitrile elastomers (e.g. carboxyl-terminated butadiene-acrylonitrile (CTBN)) are used extensively to toughen epoxy [70]. In modified epoxies, impressive improvements in fracture energies as high as 2-4 kJ/m² for elastomers and 0.5-1 kJ/m² for particle filled systems have been achieved [51]. Bagheri et al. [70] presented a critical review exploring the aspect of different material behaviors/parameters that leverage rubber-toughening of epoxy. It has been shown that material properties, such as matrix cross-link density [56, 71-72], type of rubber particle [73], particle morphology [74-76] and size [55, 58, 61, 77], degree of dispersion [61] and interfacial property [52] play important roles in the toughness enhancement of modified epoxy.

Even though, the incorporation of rubber dispersants to an epoxy resin can significantly improve the fracture energy of the modified epoxy, the process also affects the glass transition temperature, thermal expansion coefficient, yield strength and stiffness [78]. The extent of changes in epoxy properties is dependent on modifier composition and volume fraction. It has been affirmed in previous publications that the toughness of rubber modified epoxy increases with increasing rubber content until it reaches a plateau, while for rubber concentrations exceeding 15-20 wt% toughness decreases [59, 79-80]. This is because a phase inversion is expected when elastomer becomes the dominant

phase. Bascom et al. [80-81] reported a significant increase in bulk epoxy fracture energy by a factor of 30 after addition of elastomers, but did not observe any enhancement by a similar magnitude when modified epoxy was used as an adhesive. Likewise, Hunston [82] did not observe comparable increases in fracture energies of bulk resin and fiber composites. In adhesives the constraining effect of bondline thickness on the development of the plastic zone, and in fiber composites fibers restricting matrix deformation, are thought responsible for suppression of toughening effects. The general consensus conveyed in the published literature is that increasing resin toughness over a limiting value (roughly a strain energy value of 700 J/m^2) cannot effectively be translated into interlaminar fracture toughness considering that fiber volume fraction to remain constant [82-85].

In engineering and specialty polymers, certain types of particulate fillers play a unique role for improving physical and mechanical properties of the substrate polymer. The presence of inorganic particles [65-67] in a thermoset epoxy may enhance matrix toughness, stiffness and strength [86]. Furthermore, toughening of epoxy by particulate reinforcements brings about changes in the coefficient of thermal expansion, thermal conductivity, glass transition temperature and ductility. Recently, the concept of hybrid composite by infusion of two or more rubbery and rigid particulate reinforcements with a polymer matrix has been shown as an effective method of creating novel multifunctional material [62-63, 65-69]. A brief review on hybrid composites revealed that significant improvements in fracture energy is attainable while at the same time maintaining stiffness, strength and ductility of the unmodified epoxy by the formation of a ternary composite system [63]. These studies pointed out the fact that the development of superior material properties mainly stems from a cooperative influence of both rubbery and rigid particles in thermosetting epoxy.

1.3.1 Toughening Mechanisms in Epoxy

In light of the foregoing discussion it can be ascertained that it is very important to understand the basic fundamentals of different operative toughening mechanisms in epoxy, and the circumstances under which they operate. There have been reports of several possible toughening mechanisms that can explain the principle behind toughness

enhancements in modified polymers (see Figure 1.3) [51-52]. The plausible toughening theories are [51]: (1) Shear banding near rubber particles; (2) rupture of rubber particles after cavitation; (3) stretching, (4) debonding and (5) tearing of rubber particles; (6) transparticle fracture; (7) debonding of hard particles; (8) crack deflection by hard particles; (9) voided/cavitated rubber particles; (10) crazing; (11) plastic zone at craze tip; (12) diffuse shear yielding; (13) shear band/craze interaction; and (14) crack pinning by hard particles. Typically, most of these toughening phenomena have in common that they associate dissipation of fracture energy primarily to a deformation process. It has been explained by Kinloch et al. [53] that in unmodified and rubber modified epoxies three types of crack growth behaviours commonly occur, i.e. brittle stable crack growth, brittle unstable crack growth in slip-stick fashion, and ductile stable crack growth. Moreover, crack growth in polymers is effected by stain rate and temperature in response to their viscoelastic nature [67, 87]. The crack growth behaviour of the different nanocomposite systems studied in this research is the subject matter of Section 6.2.4.

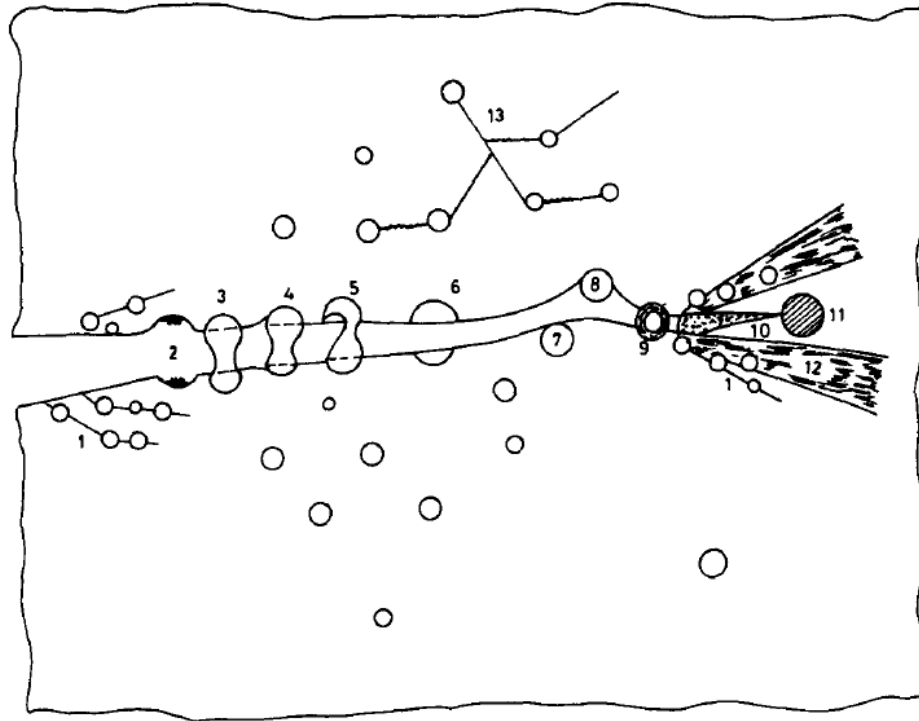


Figure 1.3 Toughening mechanisms in rubber modified polymers. Reprinted with permission from [51]. Copyright 1988 Elsevier Limited.

1.3.1.1 Shear Yielding and Cavitation

In general, yield flow behaviour in polymer is manifested by shear yielding or crazing. Shear yielding is one of the most recognised toughening mechanisms in polymers. Polymer yields by sliding of molecules that are conducive to each other when experiencing a critical shear stress for yielding. A modified von Mises criterion based on the octahedral shear stress and taking into consideration the pressure dependency of polymer can appropriately describe the shear yielding behaviour as expressed below.

$$\tau_{oct} = \tau_o - \mu_s \sigma_m \quad (1.11)$$

$$\tau_{oct} = \frac{1}{3} \sqrt{(\sigma_1 - \sigma_2)^2 + (\sigma_2 - \sigma_3)^2 + (\sigma_3 - \sigma_1)^2} \quad (1.12)$$

where τ_{oct} is the critical octahedral shear stress, τ_o is the intrinsic shear strength of the material, μ_s is a pressure coefficient, σ_m is the hydrostatic stress, and σ_1 , σ_2 , and σ_3 are the principal stresses. Originally, the von Mises criterion was developed for metals, which assumes that yielding will take place when resultant shear stress in any material plane exceeds the critical octahedral shear stress. Bascom et al. [80, 88] documented substantial enhancement in fracture energy associated with a large plastic zone resulting from the cavitation of the CTBN rubber in modified epoxy. The cavitated rubber particles act as initiation sites for plastic shear yielding, or it can be interpreted that cavitation simply promotes large scale plastic shear yielding [79]. Kinloch et al. [53, 67] and Pearson and Yee [55-57, 59] undertook a series of studies on rubber toughened epoxies that put forward further experimental evidence and explanation in support of the aforementioned toughening mechanism. In rubber toughened epoxies Pearson and Yee [55] observed the following sequential toughening events to take place. First, rubber particle cavitation occurs (either by internal cavitation or debonding at the interface), which is followed by shear banding. It was speculated that a large hydrostatic tensile stress component at the crack-tip results in cavitated particles by relieving the plane-strain constraint through reduction of the bulk modulus. At that point, the concentrated deviatoric stress component is sufficient enough to cause shear yielding. There are notable distinctions in the characteristics of different shear yielding processes found in polymers; the term yielded zone is used to define the crack-tip plastic zone, and diffused shear involves shear straining over a large volume, while localised shear is more concentrated to certain areas

in the specimen. Figure 1.4 shows features from the cavitation/debonding and succeeding shear deformation on the fracture surface of a block-copolymer (M52) modified epoxy.

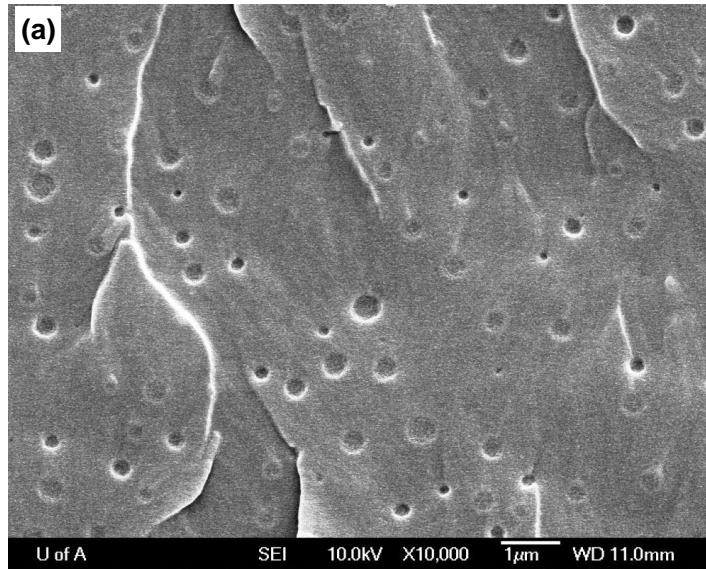


Figure 1.4 A SEM micrograph of acrylic based block-copolymer (M52) modified epoxy fracture surface illustrating features from particle cavitation and matrix shear deformation process.

1.3.1.2 Crazing/Normal Yielding

Sultan and McGarry [58] were among the first researchers to study the effect of rubber dispersion on toughness of epoxy. They observed micro-cavitation to develop in the epoxy samples that contained CTBN rubber having $\sim 1.2 \mu\text{m}$ particle size. They have attributed such yielding phenomenon to craze formation and matrix stretching. Crazing represents an important yielding mechanism in thermoplastics, but before Bucknall [89] it was not recognized in thermosets. The physical interpretation of craze initiation in polymer has developed through the work of Maxwell et al. [90] and Bucknall et al. [89, 91]. In glassy thermoplastics crazing is a form of tensile yielding accompanied with molecular rearrangement leading to cavitation (micro-voids) when experiencing critical straining of the material. Crazing is a highly localised deformation process that appears as a stress-whitening zone on the stressed polymer. However, many researchers [56-57, 59] have expressed their scepticism about the occurrence of craze in thermosetting epoxy,

and did not find convincing evidence for craze formation in cured epoxies where the chain length between cross-links is very small. To satisfy the condition for craze formation Oxborough and Bowden [92] developed a critical strain based criterion of the following form:

$$E\varepsilon_c = (\sigma_1 - \nu\sigma_2 - \nu\sigma_3) = \frac{X}{(\sigma_1 + \sigma_2 + \sigma_3)} + Y \quad (1.13)$$

where ε_c is the critical strain for craze formation, E is the Young's modulus, σ_1 , σ_2 and σ_3 are principal stresses, ν is the Poisson's ratio, and X and Y are time and temperature dependent parameters.

1.3.1.3 Crack-tip Blunting

The yield behaviour of polymer involving localized plastic shear deformation can be explained in the context of an associated crack-tip blunting process. In principle the localized shear yielding relieves the effective stress intensity by crack-tip blunting, thereby requiring higher applied stress for crack initiation. The yielding behaviour of material at the crack-tip, in turn, will bear significance on the subsequent mode of crack growth, and hence on the toughness value [93]. The relevant parameter of crack-opening displacement can define the extent of crack-tip blunting according to the following expression:

$$\delta_{tc} = \frac{K_{Ics}^2}{E\sigma_{ys}} \quad (1.14)$$

where K_{Ics} is the measured stress intensity factor at the onset of crack growth, and σ_{ys} is the tensile yield stress. It can be inferred from the above equation that crack-tip blunting would increase with decreasing yield stress of the material. A quantitative model developed for certain epoxy systems by Kinloch and Williams [87] correlates fracture toughness with the degree of crack-tip blunting at the onset of crack propagation, which is expressed as:

$$\frac{K_{Ics}}{K_I} = \frac{(1 + \rho/2c)^{3/2}}{(1 + \rho/c)} \quad (1.15)$$

$$K_I = \sigma_c \sqrt{2\pi c} \quad (1.16)$$

where ρ is the crack-tip radius, σ_c is the critical stress attained at a distance c ahead of the crack-tip, and K_I is the stress intensity for propagating a sharp crack. This equation

provides a quantitative approximation of crack-tip blunting through a relationship between toughness (K_{Ics}/K_I) and crack-tip radius.

1.3.1.4 Rubber Stretching and Tearing

Based on studies of rubber modified epoxy Kunz-Douglass et al. [54] explored the idea of particle bridging, which was proposed by Merz et al. [94]. They hypothesized that rubber stretching and tearing are the primary crack resistance mechanisms in rubber modified epoxy. These researchers neither observed shear deformation nor any craze formation in the matrix around the particles. Ultimately, they have developed an analytical model for predicting the fracture energy of rubber modified epoxy in terms of the stored elastic energy in the stretched rubber that is being dissipated irreversibly at the time of particle failure. The model attributes the increase in fracture energy to the volume fraction and tearing energy of the rubber according to the following expression:

$$\Delta G_{IC} = 4\gamma V_p \left[1 - \frac{6}{\lambda_1^2 + \lambda_1 + 4} \right] \quad (1.17)$$

where ΔG_{IC} is the increase in fracture energy, λ_1 is the extension ratio when rubber particles tear, γ is the tear energy of rubber, and V_p is the volume fraction of rubber. The toughness enhancement observed by Kunz-Douglass et al. [54] using this model was significantly lower than what was experimentally observed in other publications [56-57, 59]. Therefore, doubts have been raised about the applicability of this model, which estimates fracture energy based on the elastic energy stored during rubber stretching. Furthermore, in order for the particle bridging to occur the rubber-polymer interface must be strong enough to overcome the cohesive strength of the particle. Also, the particle size should be larger than the crack-tip radius, and that rubber should be able to span between the exposed crack surfaces.

In particulate (e.g. alumina, glass bead and silica) filled epoxies, crack deflection, crack pinning and crack-tip blunting are few of the possible crack resistance phenomena commonly observed. Among these the latter two are known for significant contributions to toughness in filled epoxies [51, 95]. The presence of a second particulate phase that has elastic properties very different from that of the polymer will cause the stress field at the wake of the crack-tip to be altered [52].

1.3.1.5 Crack Pinning

It is known that in a brittle matrix when a crack front is obstructed and pinned down by a rigid well-bonded particle, the crack front becomes bowed out between the particles resulting in secondary cracks to form. Consequently, more energy would be required to propagate this new non-linear crack front, which depends on particle size and interparticle spacing. Lange has put forward an expression for increasing fracture energy as a result of crack pinning [96-97], i.e.:

$$\Delta G_{IC} = \frac{T}{2d} \quad (1.18)$$

where T is the line energy of the crack front, and $2d$ is the interparticle spacing. The ratio of the particle size (diameter = $2r$) to particle spacing is related to the particle volume fraction:

$$\frac{2r}{3d} = \frac{V_p}{(1 - V_p)} \quad (1.19)$$

For a penny-shaped crack, Lange's line energy is a function of the particle size, hence:

$$T = \frac{2r}{3} \gamma_m \quad (1.20)$$

Finally,

$$\Delta G_{IC} = \frac{r\gamma_m}{3d} \quad (1.21)$$

where γ_m is the fracture energy of the matrix. The above equation shows that the increase in fracture energy is linearly dependent on the ratio of r and d . Figure 1.5 shows the micrographic evidence of the crack pinning mechanism in an epoxy-clay (I.28E) nanocomposite.

1.3.1.6 Crack Deflection/Crack Bifurcation

The presence of second phase particles in the path of a propagating crack may results in repeated perturbation of the crack front from its original propagation path. As a result additional facture surface is created by deflection and/or bifurcation of the primary crack into multiple secondary cracks which are not necessarily coplanar [98]. The increase in fracture energy as a consequence of the distorted crack path can be estimated from the following equation.

$$\Delta G_{IC} = \frac{3\gamma_m V_p}{2} \quad (1.22)$$

Figure 1.6 shows severely textured surface morphology resulted from a crack deflection mechanism when the path of a propagating crack encountered uniformly distributed nanoparticles. It has been reported in literatures that the occurrence of crack deflection mechanism only brings about modest toughness improvement [51, 98]. The rigid particles may also introduce local stress concentration as the particles have elastic properties (i.e. Young's modulus) significantly different from those of the matrix. The presence of these stress concentrator particles ahead of the crack-tip aid in initiating localized matrix shear deformation that result in blunting of the crack-tip.

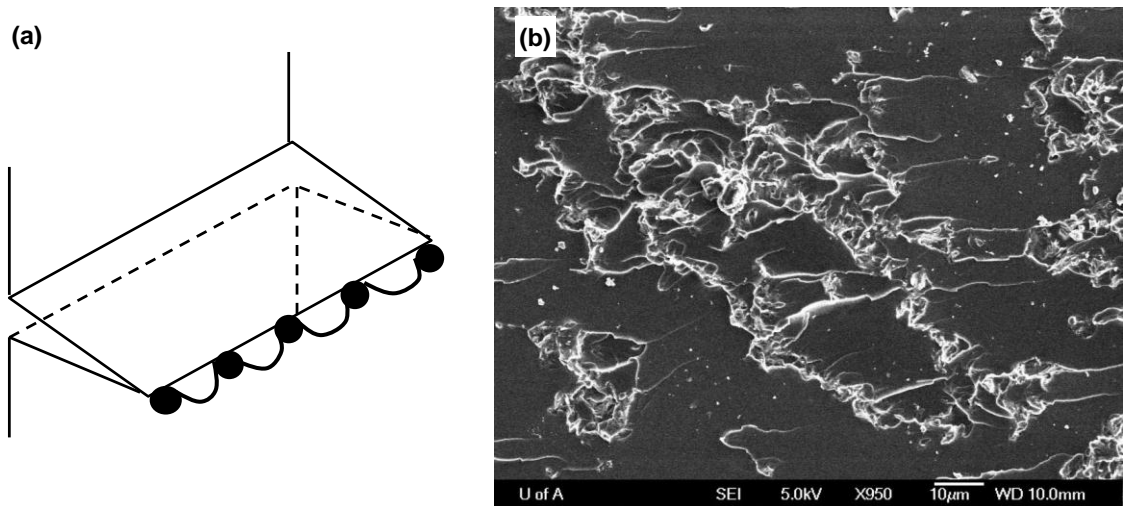


Figure 1.5 (a) Schematic of crack-pinning mechanism (Adapted from [51]. Copyright 1988 Elsevier Limited.), and (b) a SEM micrograph of epoxy-clay (I.28E) nanocomposite fracture surface showing features from crack-pinning mechanism.

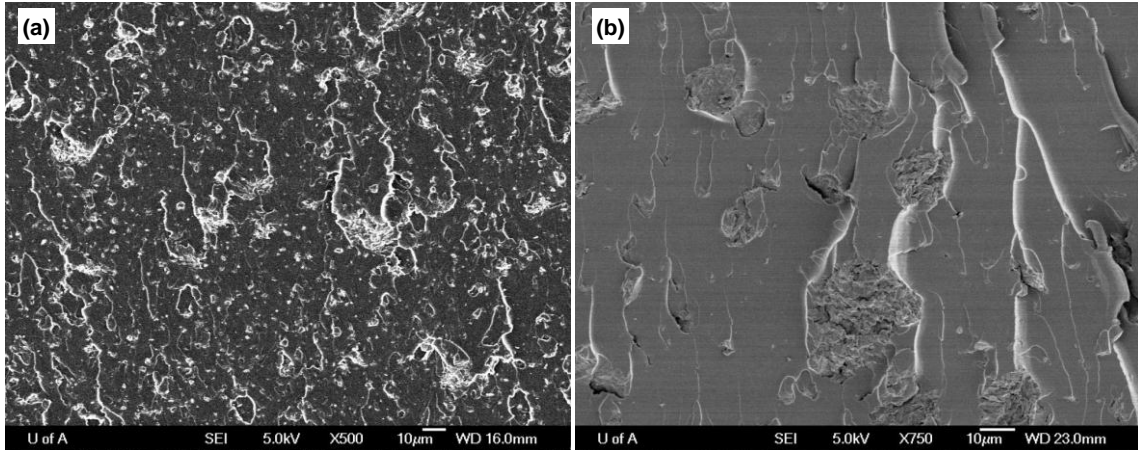


Figure 1.6 SEM micrographs of epoxy-clay (I.30E) nanocomposite fracture surface showing: (a) crack deflection/bifurcation mechanism, and (b) crack deflection and matrix deformation.

1.4 POLYMER NANOCOMPOSITES

In recent years there have been tremendous efforts and interest in developing multifunctionality and diversity in polymer properties that has fostered innovative research approaches towards synthesizing advanced nanostructured materials. Polymer nanocomposites are a combination of a polymeric phase (e.g. thermoplastic, thermoset or elastomer) with one or more reinforcing filler material having at least one dimension in the nanometer scale (0.1-100 nm) [99]. Polymer nanocomposites exhibit novel material properties with significantly enhanced mechanical, thermal, electrical and physicochemical properties. The unique characteristics of nanoparticles, i.e. having nanoscale dimensions, large surface area per unit volume (high aspect ratio) and molecular perfections by their nature, can yield a high-performance material when incorporated into a polymer matrix. Properties of nanocomposites are also influenced by the nature of the constituents (matrix and filler), their morphology, interfacial characteristics, degree of mixing and synthesis methods. Lately, polymer nanocomposites are finding applications in gas barrier films, scratch resistant coatings, flame retardant products and even in structural and commodity plastics (e.g. automotive parts) [100]. According to their geometric dimensions nano-reinforcements can be classified into three distinct categories: isodimensional nanoparticles (e.g. nanosilica, carbon black, and

polyhedral oligomeric silsesquioxane), fibrous materials (e.g. carbon nanofibers and carbon nanotubes) and layered materials (when the nanofillers have one dimension in the nanometer range such as graphite and layered silicate (clay)) [101-102]. Polymer-clay nanocomposite was first developed by researchers at the Toyota research center from polyamide 6 and organoclay [103-104]. This procedure has later been adopted for other polymer systems, namely epoxy, unsaturated polyester, poly(ϵ -caprolactone), silicon rubber, polystyrene, polyimide, polypropylene, poly(ethylene terephthalate) polyurethane and others [105].

1.4.1 Epoxy-clay Nanocomposites

Polymer-clay nanocomposites are inorganic/organic hybrids. Nanoscale dispersion of the layered silicate into a polymer resin, thus generating polymer-clay nanocomposite, may result in exceptional enhancements in material properties relative to the micro and fiber composites [101, 106]. Normally, polymer-clay nanocomposites contain very small amounts of nano-dispersants, about 2-3 vol%. Consequently the finished products are light-weight (owing to their comparable property enhancement) compared to traditionally filled composites. Polymer nanocomposites can be processed employing conventional processing techniques, for instance extrusion, injection molding and resin casting (e.g. wet lay-up, resin transfer molding, resin film infusion, etc.).

1.4.1.1 Structure of Layered Silicate Clay

In nanocomposite research, layered silicate clays are sometimes referred to as nanoclay or organoclay, which are actually inorganic particles derived from synthetic or natural source. Silicate clay (e.g. montmorillonite, hectorite and saponite) shown in Figure 1.7 falls into the general class of phyllosilicates that has a 2:1 layered type structure consisting of either hydrous magnesium or aluminum silicates. Their crystal structure is made of an edge-shared aluminum or magnesium octahedral layer fused between two silicon tetrahedral sheets. Montmorillonite ($M_{0.5-1.2}(Al_{3.5-2.8}Mg_{0.5-1.2})Si_8O_{20}(OH)_4$), hectorite ($M_{0.5-1.2}(Mg_{5.5-4.8}Li_{0.5-1.2})Si_8O_{20}(OH)_4$) and saponite ($M_{0.5-1.2}(Mg_6)(Si_{7.5-6.8}Al_{0.5-1.2})O_{20}(OH)_4$) are the most widely used smectite type clays, among which montmorillonite (MMT) is the most accounted for layered silicate known for processing

of nanocomposites [101]. Typically, in a layered silicate each layer thickness is ~ 1 nm, having lateral dimension about 30 nm to ~ 1 μm , aspect ratio of 10~1000, and an approximate surface area of 750 m^2/g . Layered silicate constitutes a moderate surface charge due to isomorphous substitution of Si^{4+} for Al^{3+} in the tetrahedral lattice or substitution of Al^{3+} in the octahedral by Mg^{2+} or Fe^{2+} . As a result, the layered silicate becomes negatively charged that is counterbalanced by charge compensating counter-ion (Li^+ , Na^+ , K^+ , Ca^{2+}) attached to the surface. Normally, the surface charge of a clay is quantified by a parameter known as cation exchange capacity (CEC is expressed in $\text{meq}/100\text{g}$) of the layered silicate [107-108]. Naturally, individual clay nanolayers arrange themselves into repeat structures (i.e. tactoids) giving rise to usual van der Waals gaps (also known as gallery or interlayer region) between two clay platelets. The intrinsic hydrophilicity of layered silicates requires that they must be made organophilic for application with the polymer, and to improve wetting properties of the clay. Lan et al. [109] showed that long chain alkylammonium (also alkylphosphonium and alkylsulfonium) surface modifiers can render organophilic characteristic to layered silicate, and reduce the surface energy of the silicate layers thus improving their compatibility towards epoxy [110]. In order for the intragallery adsorption of polymer to happen the polarity of the clay surface modifier should match that of the polymer [105]. Quaternary ammonium salts, tertiary amine, phenylene methylamine, imidazole, etc. are commonly used as organic surface modifiers for epoxy-clay nanocomposite preparation. In a study Brown et al. [111] observed that the hydroxyl-substituted quaternary ammonium surface modifiers rendered catalytic functionality as well enhanced miscibility of clay towards both components of the epoxy/diamine reactive mixture. They have also mentioned about three specific types of interactions present between quaternary ammonium ions and the polymer matrix as per surfactant used: strong specific interactions (H-bonding), dipolar (aromatic) and van der Waals (alkyl). Pinnavaia and Wang [112] showed that the acidic form of ion-exchanged (e.g. acidic onium ions) montmorillonite clay can catalyze homopolymerization of diglycidyl ether of bisphenol A (DGEBA) in the clay galleries at sufficiently high temperature. The influence (e.g. amount, size, functionally, polarity and acidity) of silicate interlayer surfactants on

preparation of epoxy-clay nanocomposites has been studied by many researchers, notably Kornmann et al. [113], Zilg et al. [114] and Xidas and Triantafyllidis [115].

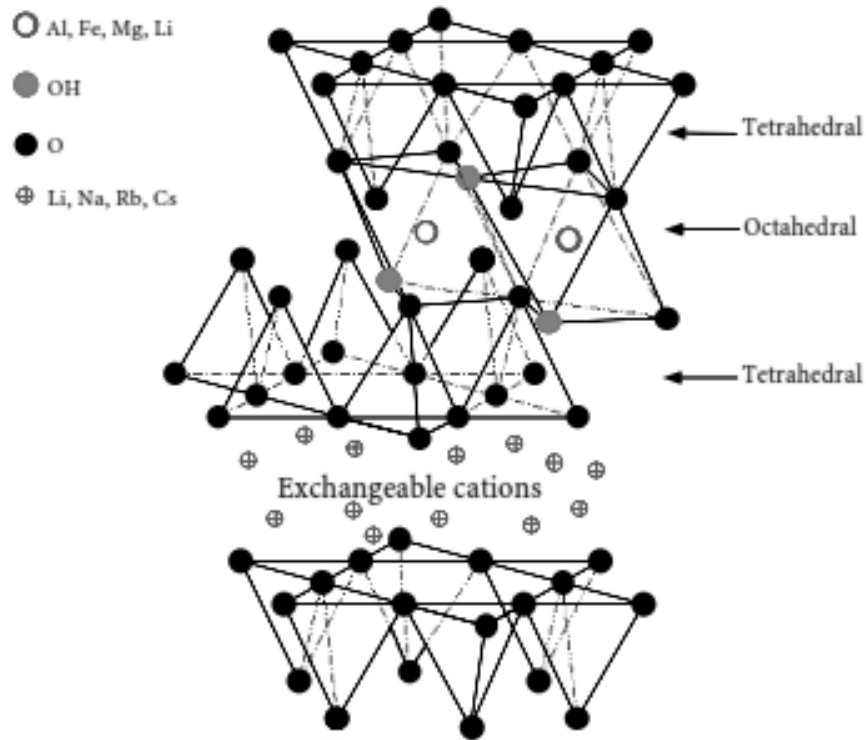


Figure 1.7 Idealized structure of 2:1 layered silicates (MMT). Reprinted with permission from [110, 128]. Copyright 1999 Springer-Verlag Berlin Heidelberg.

1.4.1.2 Morphology of Epoxy-clay Nanocomposites

Based on the combination of the different constituents chosen (e.g. layered silicate, organic cation and polymer) and the adopted processing conditions, organoclay can be transformed to give rise to micro or nanostructured morphologies inside a polymer matrix. A mixture of polymer and inorganic silicate does not necessarily produce a nanocomposite, rather the immiscibility or partial miscibility between constituents in most cases develop conventional microcomposites (i.e. phase-separated structure) having clay microaggregates evenly or unevenly distributed in the matrix. In the phase-separated morphology polymers are unable to penetrate between the silicate layers. Inefficient chemical or physical interaction between the polymer and the dispersant typically ushers

inferior material properties in such microcomposites. If in a compatible polymer and clay system the monomers or oligomers are able to migrate into the clay galleries, two more fundamental clay morphologies can be distinguished, i.e. intercalated and exfoliated nanocomposites. If the clay is still able to maintain a well-ordered multilayer structure even after the presence of diffusing polymers/prepolymers into the interlayers an intercalated nanocomposite evolves. In an intercalated architecture, polymers are able to swell and increase the interlayer distance, but are unable to completely dislodge the clay platelets. As a result, intercalated nanocomposites are expected to have less than the optimal property enhancement. A nanocomposite can be regarded as an exfoliated or delaminated structure when individual silicate platelets are homogenously and uniformly dispersed in the polymer matrix, typically rendering a monolithic structure [100-101, 105-108]. This molecularly dispersed clay configuration generally brings about the highest degree of property enhancement that is possible in the epoxy-clay nanocomposites. Figure 1.8 shows the three main types of epoxy-clay nanocomposite morphologies.

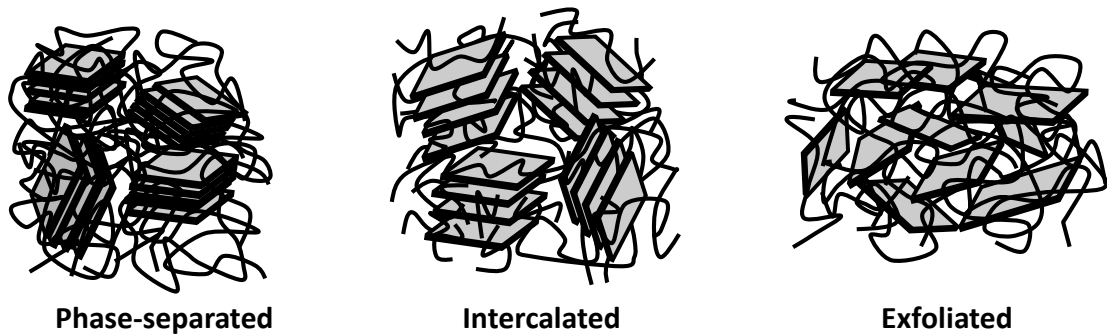


Figure 1.8 A schematic illustration of three basic nanoclay structures in a polymer matrix.

1.4.1.3 Exfoliation Behavior of Epoxy-clay Nanocomposites

For the successful processing of epoxy-clay nanocomposites it is a prerequisite that enough epoxy monomers or oligomers are pre-intercalated into the clay galleries in order to participate in the intragallery polymerization that must also be comparable or higher

than the extragallery polymerization rate. The steps for processing exfoliated or intercalated epoxy-clay nanocomposites sequentially involve: ion-exchange to make layered silicate organophilic; dispersion of organoclay in epoxy resin; swelling of the clay galleries by epoxy precursor; mixing and curing that facilitate epoxy and curing agent migration into the clay interlayers; and finally, curing reaction causing increased distance or complete separation of platelets. Based on a study of epoxy-clay nanocomposites Park and Jana [116] proposed a mechanism of clay layer exfoliation, i.e. the elastic force developed in the clay galleries from cross-linking epoxy molecules is responsible for clay exfoliation, while the viscous force and sum of the attractive forces due to electrostatic attraction and van der Waals force act opposing exfoliation. At critical entropy when the elastic force exceeds the attractive and viscous forces, exfoliation takes place [116]. The extent of clay layer separation depends on chain length of the organic cations, acidity of the organic cation and the curing condition [117]. It has been substantiated by Pinnavaia et al. [117] that as the carbon numbers of the alkyl chain of the alkylammonium exchanged clay ($\text{CH}_3(\text{CH}_2)_{n-1}\text{NH}_3^+$ -MMT, where $n = 4, 8, 10, 12, 16$ or 18) increase, so does the proportional increase of the basal spacing of the clay. The above statement was found justified by Lan et al. [109] as they observed that organic cations having a carbon number greater than eight produced exfoliated clay, whereas short chain alkylammonium ions imposed restriction on epoxy monomer permeation, and hence resulted in intercalated nanocomposites. Upon diffusion of epoxy molecules inside the clay galleries, a vertical reorientation of the organic surfactants takes shape from their initial (bilayer, monolayer or inclined paraffin-like) configuration accommodating epoxy molecules in between the exchanged cations. The process is dependent on the alkyl chain length, and together with the clay layer charge density control the amount of epoxy solvation into the clay galleries [109, 118]. Chen and Curliss [118] inferred that lower charge density clay having less pendant group attached to its surface promotes more epoxy penetration into the gallery than higher charge density clay [119]. Inorganic cations (Na^+ and NH_4^+) only generated microcomposites, as they are hydrophobic in character that results clay not being wetted by epoxy monomers. Exfoliation behavior of clay has been reported to be influenced by the acidity of the organic cations. Lan et al. [109] observed that the primary ($\text{CH}_3(\text{CH}_2)_{17}\text{NH}_3^+$) and secondary alkylammonium ions

$(\text{CH}_3(\text{CH}_2)_{17}\text{N}(\text{CH}_3)\text{H}_2^+)$ performed better than the tertiary $(\text{CH}_3(\text{CH}_2)_{17}\text{N}(\text{CH}_3)_2\text{H}^+)$ and quaternary $(\text{CH}_3(\text{CH}_2)_{17}\text{N}(\text{CH}_3)_3^+)$ ammonium ions regarding exfoliation of the layered silicate when cured with *m*-phenylene diamine. Additionally, it was noted that all these surfactants have same C_{18} chain length and initial swelling of the clay interlayer by epoxy prepolymer. According to the authors of this study alkylammonium ions can catalyze an epoxy-amine curing reaction that depends on the acidity of the cation, thereby causing catalytic polymerization inside the clay gallery to be higher than outside the interlayer, facilitating further separation of the clay layers [107].

The choice of epoxy resin and curing agent plays an important role in influencing the exfoliation of silicate layers. Becker et al. [120-121] investigated the influence of different high-functionality epoxy resins, bifunctional diglycidyl ether of bisphenol-A, trifunctional triglycidyl *p*-amino phenol (TGAP) and tetrafunctional tetraglycidyl diamino diphenylmethane (TGDDM) on exfoliation of octadecyl ammonium ion-modified montmorillonite. It was found from their study that bifunctional epoxy (DGEBA) provided better exfoliation than high-functionality resins. Messersmith and Giannelis [122] studies different curing agents, nadic methyl anhydride (NMA), benzyldimethylamine (BDMA), boron trifluoride monoethylamine (BTFA) and methylenedianiline (MDA) in preparation of epoxy-clay nanocomposites. The composites prepared by the addition of NMA, BDMA or BTFA, respectively in the DGEBA/organoclay mixture resulted in delamination of the organoclay, unlike the MDA, which produced an opaque composite. It was thought that the bifunctional amine molecules may have caused bridging of the silicate layers thus preventing further separation of the clay galleries [122]. Park and Jana [116] inferred that layer separation of clay occurs before gelation of the reactive resin mixture; hence, this imposes a time constraint on the exfoliation process [123]. Furthermore, the degree of exfoliation and intercalation is dependent on mixing and curing conditions, such as mixing time, curing time and temperature [117]. It was stated by Lan et al. [109] that a low curing temperature and slow diffusion of polymer in the clay galleries will adversely affect exfoliation [124]. On the contrary, too high curing temperature is also not preferred because that would favor faster extragallery polymerization resulting in intercalated nanocomposites. Also the dispersion technique, e.g. mechanical or ultrasonic mixing has

a pronounced influence on epoxy solvation into the clay gallery and successive delamination into nanolayers. The effect of mixing efficiency on exfoliation behavior of epoxy-clay nanocomposites has been investigated by Hernandez et al. [125] Liu et al. [126] and Yasmin et al. [127].

Synthesis approaches for the preparation of epoxy-clay nanocomposites includes several established fabrication methodologies: exfoliation-adsorption, in-situ intercalative polymerization and melt intercalation [101, 128]. In the exfoliated-adsorption method a suitable solvent (in which the polymer is soluble) is used to disperse the layered silicate into single layers, whereby adsorbing the polymer or prepolymer onto the silicate nanolayers. When the solvent is extracted, the clay nano-sheets reassemble into clay tactoids fusing in between the polymer. The in-situ intercalative polymerization requires layered silicate to be swollen/pre-intercalated within the liquid monomer (that acts as solubilizing agent) enabling polymerization to initiate subsequently in the gallery spaces either by addition of heat or an initiator. Alternatively, in the melt intercalation method organoclay is directly mixed statically or under shear with the molten polymer. This is a preferred method for processing thermoplastic-clay nanocomposites employing such techniques as extrusion or injection molding. However, exfoliation-adsorption and in-situ intercalative polymerization processes are frequently adopted for the fabrication of epoxy-clay nanocomposites.

1.4.1.4 Physical and Mechanical Properties of Epoxy-clay Nanocomposites

Polymer-clay nanocomposites have significantly improved physical and mechanical properties, which can be advantageous for specific engineering applications and in specialty products. The versatility in nanocomposite properties comes in many different forms and parameters, such as mechanical properties (stiffness, strength, and fracture and impact resistance), dimensional stability, barrier properties (for gas and liquid), flame retardance, chemical resistance, optical properties and thermal stability [129]. In a study of mechanical properties of clay-reinforced nanocomposite Lan and Pinnavaia [130] documented an almost tenfold increase in modulus and strength of a rubbery epoxy for a 15 wt% addition of organoclay. In an exfoliated nanocomposite the impressive increase

in stiffness is attributed to a mechanism of shear deformation and stress transfer to the high stiffness and high aspect ratio individual silicate platelets [117, 130]. Kornmann et al. [124] reported simultaneous improvements in fracture toughness and Young's modulus of epoxy-clay nanocomposites, while maintaining the tensile strength constant. Studies on raising the fracture toughness of epoxy-clay nanocomposites have shown mixed results. A uniformly dispersed phase-separated or intercalated nanoclay is generally known to enhance toughness as observed by Kornmann [113] and Zerda and Lesser [131], while insignificant toughness improvements are reported for perfectly exfoliated layered silicate [132].

An increase in glass transition temperature was reported in the literature, and limited segmental mobility at the polymer-clay interphase is thought to be the main reason [122, 129]. Conversely, a reduction in the glass transition temperature was also documented for epoxy-clay nanocomposites [129]. Layered silicate nanocomposite can improve dimensional stability as shown by a reduction of the thermal expansion coefficients [133]. Enhanced barrier and solvent absorption resistance are due to the presence of homogeneously dispersed high aspect ratio clay lamellae, which make the migration path for the diffusing molecules more torturous and thus impermeable [106, 134]. As already mentioned, silicate layers reduce permeability; the thermal stability is thereby increased by affecting the diffusion of the volatile decompositions during thermal degradation [135]. Clay nanocomposites may also provide extraordinary self-extinguishing and increased flame retardance [111]. In epoxy-clay nanocomposites the exceptional barrier property, chemical resistant, flammability resistance and decreased solvent uptake mechanisms primarily stem from the diffusion inhibition/perturbation caused by the clay platelets.

1.5 NANOSTRUCTURED BLOCK-COPOLYMERS

Block-copolymers are composed of two or more chemically dissimilar homopolymers bonded together by covalent linkage to form macromolecular networks that have the ability to spontaneously self-assemble to arrange into nanostructures [136]. A diverse array of nanostructured materials is possible by utilizing the ability of block-copolymers to generate periodic ordered structures. The knowledge of block-copolymer synthesis and

the underlying principle of self-organizing characteristics has gone through steady development for years, but only recently are nanotechnological applications emerging. The development of nanoscale structures and their repeatability, control over domain sizes and directional properties of block-copolymers has promising new applications in high-value-added specialty products. The great control over morphology and domain dimensions of block-copolymer nanostructures is associated with molecular parameters (molecular weight and molecular architecture) and the composition of the copolymers. In a recent review Lodge [137] emphasized future directions of block-copolymer research referring to the following unique aspects of their behavior: absolute control over domain dimensions; control over morphology; control over domain functionality; quantitative prediction of equilibrium structures; and the advantage of being a polymeric material.

1.5.1 Synthesis of Block-copolymers

The most common synthesis processes for block-copolymers are anionic polymerization and controlled radical polymerization techniques [136]. But, there are other possible routes through which block-copolymers can be prepared. A chain-growth polymerization allowing for the sequential addition of monomers through active polymerization centers and avoiding unwanted chain transfer and termination reactions is the general process of controlled/living polymerization for block-copolymer synthesis. Industrial production of common thermoplastic elastomer polystyrene-*b*-polybutadiene-*b*-polystyrene and amphiphilic block-copolymer polyoxyethylene-*b*-polyoxypropylene-*b*-polyoxyethylene involves anionic polymerization. Recently, living polymerization of polyolefins (e.g. polyethylene and polypropylene) by metal-catalyzed synthesis method has made possible processing of new olefin based block-copolymers. A short review on synthetic approaches for block-copolymers was presented by Hillmyer [138]. The advent of synthetic chemistry made achievable the synthesis of almost any imaginable block-copolymer architectures by reasonably manipulating chemical composition of the constituents. For instance, a block-copolymer made of two dissimilar monomers A and B can have variety of structural configurations, i.e. diblock (AB), linear triblock (ABA), multiblock (AB)_n, stars with diblock arm (AB)_n, hetero-arm star, H-shaped copolymer, etc. [136]. If a third block C is present more complex and diverse range of architectures

(e.g. ABC, ACB, CAB, etc.) are possible. Moreover, a block-copolymer made of more than two copolymer segments would have significant variations in its constituents, composition, architecture, sequence and functionality. Then, the alternative to an ABC triblock-copolymer would be to blend different (e.g. AB and AC) diblock-copolymers. In this regard the extensive and elaborate research activities that have been carried out so far developed various exquisitely structured block-copolymers, but still there are areas that have immense potential for future development.

1.5.2 Phase Behavior of Block-copolymers

The block-copolymer phase behavior in the molten state has been the subject of many theoretical and experimental investigations that involve finding the three-dimensional periodic ordered morphologies, which develop by a self-assembling microphase separation process. In block-copolymer melts, microphase separation is driven by an interplay between thermodynamic incompatibilities (unfavorable mixing enthalpy and small mixing entropy) and chemical bond constraints of different chemically dissimilar block segments [139- 140]. In block-copolymers the formation of these uniformly-spaced ordered structures are responsible for their specific properties.

A linear AB diblock is the simplest block-copolymer structure that has been well studied to establish an equilibrium phase behavior [139, 141-143]. The morphology diagram of a linear AB type diblock-copolymer is presented in Figure 1.9 [136, 143], where f is the volume fraction of one block, $N=N_A+N_B$ is the overall degree of polymerization (where N_A and N_B are numbers of A and B monomers, respectively), and χ is the temperature dependent Flory-Huggins interaction parameter representing interaction between different block segments. The product of χN is used to evaluate the extent of microphase separation, and when this value passes a critical value an order-disorder transition (ODT) takes place, and block-copolymers microphase separate leading to spatially-distributed repeated structures. For a symmetric diblock-copolymer ($f_a = 0.5$) a lamellar phase (lam) is observed, while asymmetry in the composition gives rise to alternating phase structures that include hexagonally packed cylinders (hex), body-centered cubic spheres (bcc) and bicontinuous cubic gyroid (gyr). It has been shown that for a symmetric diblock-copolymer order-disorder transition occurs at $\chi N \approx 10.5$, and order-order transition

(OOT) from (bcc) to (hex) to (lam) with increasing χN takes place. Unlike composition, the architecture of (AB-type) block-copolymers has little influence on the phase behavior as an identical set of ordered morphologies (i.e. lamellar, cylindrical, spherical and gyroid) were observed for homologous triblock (ABA) and diblock (AB) melts [144]. However, it can be speculated that the phase behavior of multi-component block-copolymers (e.g. ABC triblock-copolymer) would be rather complex with the interplay of more than one interaction parameters [145].

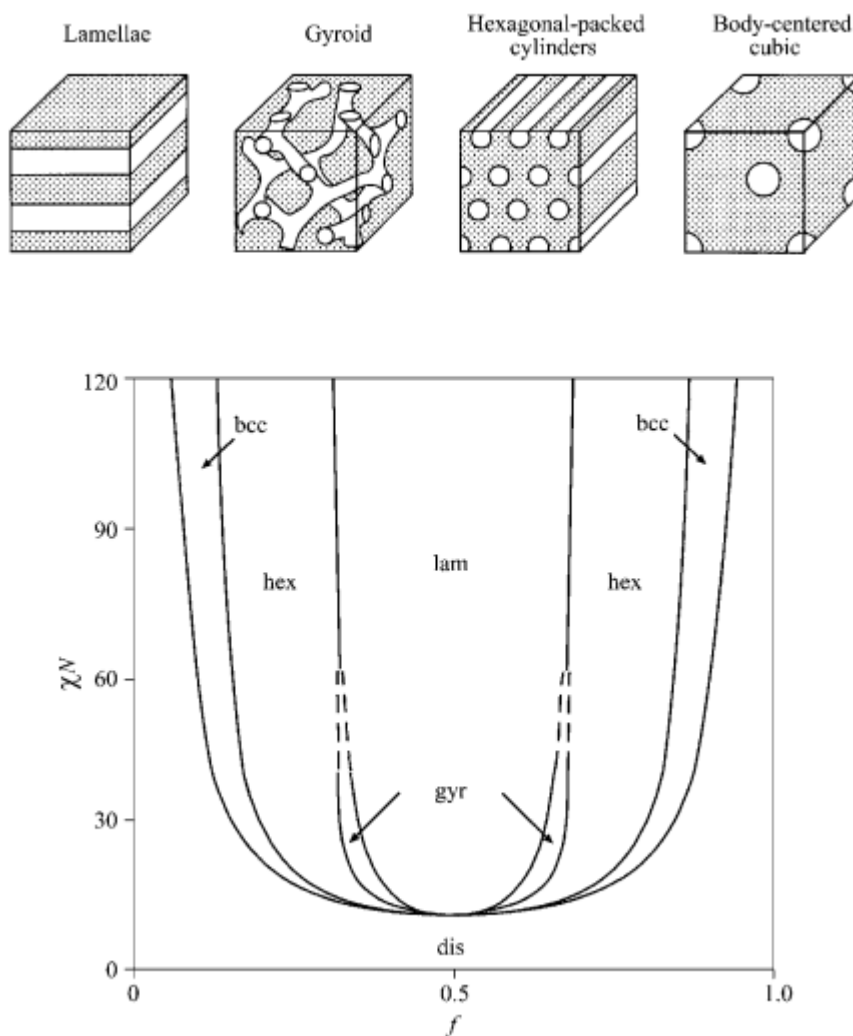


Figure 1.9 Phase diagram of a linear diblock-copolymer melt predicted from self-consistent mean-field theory. Four ordered morphologies are shown: lamellar (lam), gyroid (gyr), hexagonal (hex) and body-centered cubic (bcc), and a disordered (dis) phase. Reprinted with permission from [136, 143]. Copyright 2004 John Wiley and Sons.

Meier [146] developed the basic understanding of microdomain formation in block-copolymers in terms of molecular and thermodynamic concepts as interplay between interfacial tension and chain stretching. Later, the implementation of self-consistent mean-field (SCMF) theory provided the basic theoretical premise for block-copolymer phase diagram on the basis of computing the free energy of possible microdomain structures. Helfand and coworkers [141, 147] used the SCMF scheme to describe the phase behavior in the strong-segregation limit ($\chi N \gg 10$), while Leibler's [142] approach focuses on the stability of the disordered phase in the weak-segregation limit ($\chi N \sim 10$). Recently, a more accurate theoretical prediction of the block-copolymer phase diagram employing a novel technique for solving self-consistent field equations has been adapted by Matsen et al. [143, 148] that adequately correlates to experimental observations.

Traditionally, amphiphilic block-copolymers have been used as compatibilizers or surfactants due to their ability to reduce interfacial tension between immiscible polymer phases similar to small amphiphiles (e.g. soap and detergent) in water [136, 149]. The amphiphilic characteristic that allows selective partitioning of one block over another in a selective solvent or in another homopolymer has significant importance in the self-assembling property of block-copolymers. Similar to the structures commonly observed in surfactant systems, the blend of a block-copolymer with a homopolymer that is compatible with one of the segments has been found to generate the following morphologies: spherical and worm-like micelles, vesicles, and lamellar, cylindrical, cubic spherical and bicontinuous phases [149]. The formation of spherical micelles by aggregation of the immiscible block has been observed in selective solvent/homopolymer in the case of the miscible block being the dominant phase. As the concentration of the immiscible block is increased relative to the miscible block, the local packing changes resulting in the insoluble block being assembled into cylindrical micelles or vesicles. The configurations and ordering into these microstructures depend on the concentration and volume ratio between insoluble and soluble blocks, and are also influenced by such parameters as temperature, molecular weight, monomer interactions (e.g. block/block, block/solvent and block/homopolymer interactions), chain flexibility and copolymer architectures. Recently, the formation of nanoscale morphologies in reactive blends of thermosetting epoxy and block-copolymers has been brought into light by numerous

researchers [150-151]. Traditionally, epoxy has been toughened with rubber dispersants by formation of micron size inclusions in the epoxy precursor. Improvement in toughness by rubber modifiers has particular drawbacks of degrading the important thermo-mechanical properties of the cured epoxy. The process also has the tendency to expel rubber from the epoxy matrix during network formation. An alternative to this approach would be to use a block-copolymer having one of its segments soluble in the epoxy resin [150-151]. The ability of block-copolymers to generate distinct nanostructure phases in a moderate-to-high concentration of epoxy precursor has the potential to yield commercially viable products having novel material properties. Figure 1.10 shows schematics of a few block-copolymer nanostructures observed in a selective solvent/homopolymer, such as epoxy.

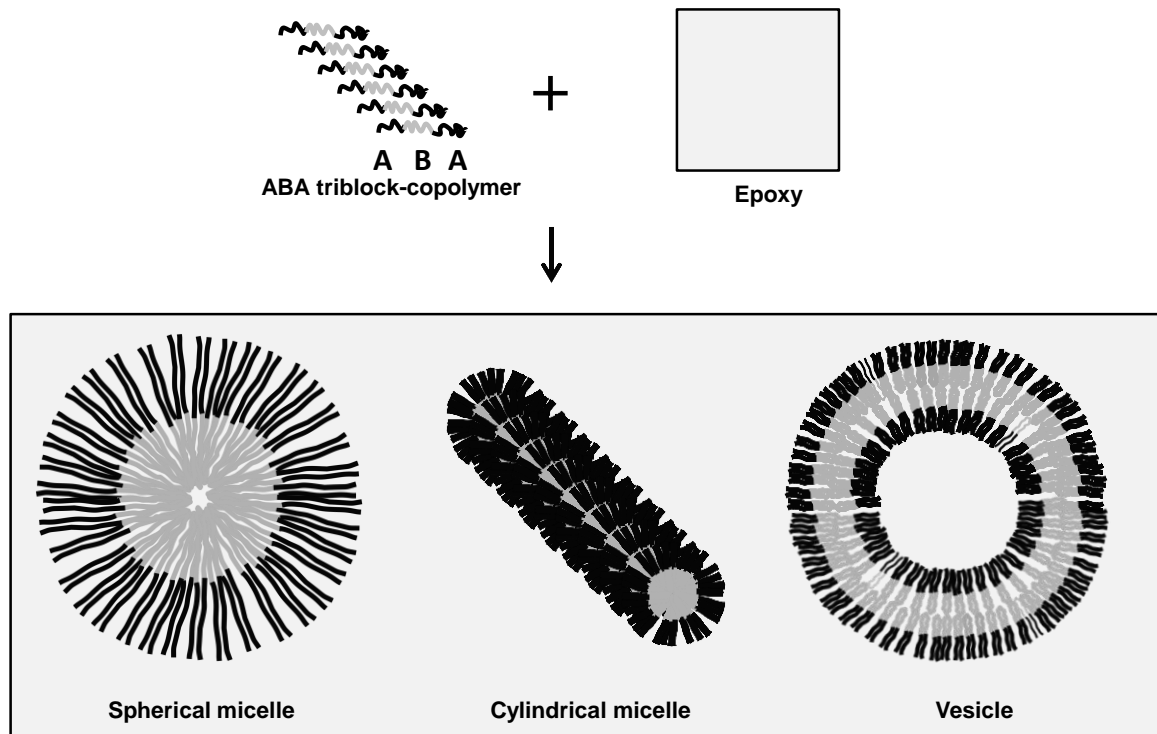


Figure 2.10 Different nanostructured block-copolymer morphologies formed inside an epoxy resin.

1.5.3 Application of Self-assembled Nanostructured Block-copolymers

High-value-added specialty polymers (e.g. nanocomposites) that utilize the self-directing nature of block-copolymers to form nanostructures can achieve extraordinary

improvements in toughness, ductility, creep resistance and permeability properties. A class of industrially important block-copolymers that has been in use commercially for almost forty years is known as thermoplastic elastomers. Thermoplastic elastomers consist of a thermoplastic segment that is covalently linked to an elastomeric segment, and possesses properties, such as rubber elasticity and processability of a thermoplastic [152]. Hillmyer et al. [151] were the first to develop a method for the synthesis of nanostructure domains in blends of reactive epoxy resin and a diblock-copolymer (e.g. polyethyleneoxide-*b*-polyethylene or polyethyleneoxide-*b*-poly(ethylene-*alt*-propylene)). The block-copolymers retained their ordered nanostructures even after thermoset cross-linking reaction. Recent work on modified epoxy having well-defined block-copolymer nanostructures has been shown to accomplish marked improvements in toughness and ductility [153-155].

It has been predicted that block-copolymer nanostructures also have potential applications in biomedical science, chemical separation, catalysis and electronics. The self-ordering nano-structuring mechanism of block-copolymers has exciting and far-reaching application in synthesis and processing of various organic and inorganic nanoporous materials (by templating approach) [156-157]. The specific porosity and surface property of these mesoporous materials can find special applications in separation catalysis, nanoporous membrane technology and nanomaterial templating. Chen et al. [158] showed that polymerization between dicyclopentadiene and a diblock-copolymer (made of a chemically etchable polylactide block and non-degradable polystyrene block) and subsequent removal of the minority phase can develop nanoscopic porosity in the matrix. Influence of external fields on block-copolymer microstructure was explored by Keller et al. [159], who investigated the degree of alignment in extruded triblock-copolymers. It is now well understood that orientation of the microstructures to a certain extent is possible when block-copolymers are subjected to flow [159-160] or in the presence of an electrical field [161]. The resulting morphologies that evolve from domain alignment can find promising new applications particularly in lithography, patterning and thin films. The development of nanostructures in solution and control over the integrity of these domain structures has practical applications in the biomedical and pharmaceutical fields for drug delivery, tissue engineering and medical imaging. In-situ hydrogel

formation by assembly of block-copolymers in aqueous solution, block-copolymer micelles as solubilizing agent and physicochemical response of these microphases to stimuli have potential application in controlled release of therapeutic drugs [162-163].

However, formidable challenges still exist with regards to block-copolymer nanostructuration. For example, Lodge [137] pointed out several key issues that need to be overcome: having block-copolymer nanostructures free of defects; developing microdomains with specific orientations; preparing irregular three-dimensional nanostructures; expediting the kinetics of the self-assembly process; and separating processing and thermodynamic constraints.

1.6 OBJECTIVE AND SCOPE OF THE PRESENT RESEARCH

Pressure piping and vessels made from fiber-reinforced polymer composites possessing novel material properties have overcome many of the deficiencies of metallic structures as storage and transmission medium for a variety of fluids. Fiber composites have significantly higher strength in the fiber direction, and consequently a relatively small transverse tensile loading perpendicular to the fiber can initiate matrix micro-cracking. Transverse matrix cracking may develop by cohesive failure of the matrix or adhesive failure of the fiber-matrix interface. It was generally observed for fiber composites that transverse cracks initiate from zones of higher fiber packing, and propagate rapidly in the through thickness direction. Leakage failure in response to transverse cracking limits the suitability of fiber-reinforced composite pipes in certain high-pressure applications, and can severely reduce the useful service life in a process or field operation. Failure events in filament-wound composite structures (i.e. functional and structural failures) are dependent on properties of the constituent materials, specimen fabrication procedures and imposed loading conditions. It has been mentioned earlier in this chapter that by judiciously working with the many design and manufacturing parameters one may find means (e.g. using a liner) for hindering or circumventing leakage failure in pressure-bearing composite structures. But, a preferable alternative would be to modify or reinforce the existing material system with a suitable modifier (e.g. nano or micro particles). In this regard, the modified resin system (with nanoparticles) may allow full utilization of the ultimate strength of the composite by effectively resisting transverse

cracking. To date, any development in nanotechnology concerning filament-wound pressure retaining structures is very limited [164], and the most recent studies were narrowly focused on reducing gas permeability and micro-cracking in cryogenic environments [165-167].

The primary objective of the present research was to enhance the mechanical properties of fiber-reinforced polymer piping by incorporating nanoparticles into the material system. It was anticipated that the process would prevent matrix damage and enhance composite strength and strain at leakage failure. The undertaken research initiative involved an extensive experimental study based on a phenomenological approach to understand the complex deformation and failure mechanism of composite pipes under specific biaxial loading conditions. Furthermore, this investigation was intended to study the damage events, leakage prediction and fracture analysis of polymer composite pressure pipes by applying the principle of emerging nanotechnology. In this scheme, synthesis, characterization and material property evaluation of the bulk epoxy nanocomposites and hybrid fiber-reinforced composite pipes were performed.

1.6.1 Organization of the Dissertation

This section outlines the presentation of the thesis. In Chapter 2 novel ideas regarding synthesis, formulation and development of cutting-edge polymer nanocomposite systems are explored. A description on preparation of polymer nanocomposite materials and manufacturing of fiber-reinforced polymer pressure pipes is also provided. In Chapter 3 designing of appropriate experimental procedures, characterization criteria, data acquisition, data validation and data analysis methods for evaluation of the behavior of composite samples are presented. In this chapter analysis and testing methodologies for the determination of morphological, chemical, physical, thermal, mechanical and fracture properties of polymer composites are also explained. In Chapter 4 a study on the influence of alkylammonium ion surface modifiers and different nanoclay dispersion methods (i.e. ultrasonic mixing and mechanical blending) on the development of various nanocomposite morphologies is presented. The manner in which nanoclay microstructures affected the mechanical properties, deformation and fracture process of the nanocomposite was discussed. In Chapter 5 the study of the effect of acrylic triblock-

copolymer concentration, composition, and generated nanostructures on the thermo-mechanical properties of the modified epoxy is reported. Miscibility and nanostructure development in block-copolymer/epoxy blends were herein studied. In Chapters 4 and 5 causal relationships between the modifiers (nanoclay and block-copolymer) morphology and resulting property enhancement in the modified epoxy are presented. The research findings summarized in Chapter 6 convey the idea of a synergistic improvement of important thermo-mechanical properties by commixing two or more nano-reinforcements with a polymeric substrate. A hybrid nanocomposite prepared by combining an acrylic triblock-copolymer with organophilic nanoclay in a thermosetting epoxy was able to take advantage of the favorable properties of different nanoparticles. It has been documented in the past that transverse cracking in composite pipes has frequently been associated with interlaminar cracking [26], hereby motivating an experimental study aimed at understanding the interlaminar fracture behavior of filament-wound composites. In Chapter 7 the effect of nano-reinforcements on delamination mechanism of filament-wound basalt fiber-reinforced laminates is described. A qualitative correlation was sought regarding the translation of bulk epoxy fracture energy in delamination energy of fiber composites. In composite laminates interlaminar fracture is influenced by matrix toughness as well as other crack resistance phenomena (e.g. fiber pull-out, fiber bridging and fiber breakage) commonly associated with the fibers. In Chapter 8 the study of fracture behavior of nanoclay and acrylic triblock-copolymer modified epoxy/basalt fiber-reinforced pipes is presented. This investigation was embarked upon based on the hypothesis that nanoparticles would enhance matrix toughness; in response to that transverse matrix micro-cracking would be suppressed. The consequence of nanoparticle addition on the extent of transverse matrix cracking was ascertained in terms of leakage failure stresses and strains of the modified systems. In Chapter 9 a few recommendations are made on future work with the filament-wound composite pipes.

REFERENCES

1. ELLYIN, F., 2002. On the design and analysis of fiber reinforced polymeric composite pipes and vessels, *American Society of Mechanical Engineers, Pressure Vessels and Piping Division (Publication) PVP 2002*, pp. 153-162.
2. ELLYIN, F., CARROLL, M., KUJAWSKI, D. and CHIU, A.S., 1997. Behavior of multidirectional filament wound fibre glass/epoxy tubulars under biaxial loading. *Composites Part A: Applied Science and Manufacturing*, **28**(9-10), pp. 781-790.
3. MERTINY, P. and ELLYIN, F., 2001. Selection of optimal processing parameters in filament winding, *33rd International SAMPE Technical Conference -Advancing Affordable Materials Technology-*, November 5, 2001 - November 8, 2001 2001, Soc. for the Advancement of Material and Process Engineering, pp. 1084-1095.
4. MERTINY, P., ELLYIN, F. and HOTHAN, A., 2004. An experimental investigation on the effect of multi-angle filament winding on the strength of tubular composite structures. *Composites Science and Technology*, **64**(1), pp. 1-9.
5. MERTINY, P. and ELLYIN, F., 2002. Influence of the filament winding tension on physical and mechanical properties of reinforced composites. *Composites Part A: Applied Science and Manufacturing*, **33**(12), pp. 1615-1622.
6. MARTENS, M. and ELLYIN, F., 2000. Biaxial monotonic behavior of a multidirectional glass fiber epoxy pipe. *Composites Part A: Applied Science and Manufacturing*, **31**(9), pp. 1001-1014.
7. MEIJER, G. and ELLYIN, F., 2008. A failure envelope for 60 filament wound glass fibre reinforced epoxy tubulars. *Composites Part A: Applied Science and Manufacturing*, **39**(3), pp. 555-564.
8. WOŁODKO, J., MERTINY, P., MEIJER, G., MARTENS, M. and ELLYIN, F., 2001. Development of a facility for filament winding GFRP tubulars, *46th International SAMPE Symposium and Exhibition 2001 a Materials and Processes Odyssey, May 6, 2001 - May 10, 2001*, Soc. for the Advancement of Material and Process Engineering, pp. 1271-1282.
9. MERTINY, P. and GOLD, A., 2007. Quantification of leakage damage in high-pressure fibre-reinforced polymer composite tubular vessels. *Polymer Testing*, **26**(2), pp. 172-179.

10. ELLYIN, F. and MARTENS, M., 2001. Biaxial fatigue behaviour of a multidirectional filament-wound glass-fiber/epoxy pipe. *Composites Science and Technology*, **61**(4), pp. 491-502.
11. BASHAR, M.T., SUNDARARAJ, U. and MERTINY, P., 2011. Study of Matrix Micro-cracking in Nanoclay and Acrylic Tri-block-copolymer Modified Epoxy/basalt Fiber-reinforced Pressure-retaining Structures. *Express polymer letters*, **5**, pp. 882-896.
12. COHEN, D., 1997. Influence of filament winding parameters on composite vessel quality and strength. *Composites Part A: Applied Science and Manufacturing*, **28**(12), pp. 1035-1047.
13. COHEN, D., MANTELL, S.C. and ZHAO, L., 2001. The effect of fiber volume fraction on filament wound composite pressure vessel strength. *Composites Part B:Engineering*, **32**(5), pp. 413-429.
14. SPENCER, B. and HULL, D., 1978. Effect of winding angle on the failure of filament wound pipe. *Composites*, **9**(4), pp. 263-271.
15. SODEN, P.D., KITCHING, R., TSE, P.C., TSAVALAS, Y. and HINTON, M.J., 1993. Influence of winding angle on the strength and deformation of filament-wound composite tubes subjected to uniaxial and biaxial loads. *Composites Science and Technology*, **46**(4), pp. 363-378.
16. ROUSSEAU, J., PERREUX, D. and VERDIÈRE, N., 1999. The influence of winding patterns on the damage behaviour of filament-wound pipes. *Composites Science and Technology*, **59**(9), pp. 1439-1449.
17. MERTINY, P., 2012. Leakage failure in fibre-reinforced polymer composite tubular vessels at elevated temperature. *Polymer Testing*, **31**(1), pp. 25-30.
18. BAI, J., SEELEUTHNER, P. and BOMPARD, P., 1997. Mechanical behaviour of $\pm 55^\circ$ filament-wound glass-fibre/epoxy-resin tubes: I. Microstructural analyses, mechanical behaviour and damage mechanisms of composite tubes under pure tensile loading, pure internal pressure, and combined loading. *Composites Science and Technology*, **57**(2), pp. 141-153.
19. HULL, D., LEGG, M.J. and SPENCER, B., 1978. Failure of glass/polyester filament wound pipe. *Composites*, **9**(1), pp. 17-24.

20. CARROLL, M., ELLYIN, F., KUJAWSKI, D. and CHIU, A.S., 1995. The rate-dependent behaviour of $\pm 55^\circ$ filament-wound glass-fibre/epoxy tubes under biaxial loading. *Composites Science and Technology*, **55**(4), pp. 391-403.
21. Macek, R.W. and Hackett, R.M., 1992. Viscoelastic analysis of filament-wound composite material systems. *Journal of Reinforced Plastics and Composites*, **11**, pp.567-581.
22. KUJAWSKI, D., ELLYIN, F. and CULEN, M.S., 1998. The fatigue behaviour of filament-wound fiberglass/epoxy tubes under cyclic pressure. *Journal of Reinforced Plastics and Composites*, **17**(3), pp. 268-281.
23. SODEN, P.D., KITCHING, R. and TSE, P.C., 1989. Experimental failure stresses for $\pm 55^\circ$ filament wound glass fibre reinforced plastic tubes under biaxial loads. *Composites*, **20**(2), pp. 125-135.
24. ASP, L.E., BERGLUND, L.A. and TALREJA, R., 1996. Prediction of matrix-initiated transverse failure in polymer composites. *Composites Science and Technology*, **56**(9), pp. 1089-1097.
25. HINTON, M.J., KADDOUR, A.S. and SODEN, P.D., 2002. A comparison of the predictive capabilities of current failure theories for composite laminates, judged against experimental evidence. *Composites Science and Technology*, **62**(12-13), pp. 1725-1797.
26. JONES, M.L.C. and HULL, D., 1979. Microscopy of failure mechanisms in filament-wound pipe. *Journal of Materials Science*, **14**(1), pp. 165-174.
27. TALREJA, R., 1985. Transverse cracking and stiffness reduction in composite laminates. *Journal of Composite Materials*, **19**(4), pp. 355-375.
28. LEE, J.W. and DANIEL, I.M., 1990. Progressive transverse cracking of crossply composite laminates. *Journal of Composite Materials*, **24**(11), pp. 1225-1243.
29. GARRETT, K.W. and BAILEY, J.E., 1977. Multiple transverse fracture in 90° cross-ply laminates of a glass fibre-reinforced polyester. *Journal of Materials Science*, **12**(1), pp. 157-168.
30. HAHN, H.T. and TSAI, S.W., 1974. On the behaviour of composite laminates after initial failures. *Journal of Composite Materials*, **8**, pp. 288-305.
31. HIGHSMITH, A.L. and REIFSNIDER, K.L., 1982. Stiffness-reduction mechanisms in composite laminates. *Damage in Composite Materials*, **775**, pp. 103-117.

32. TALREJA, R., 1985. CONTINUUM MECHANICS CHARACTERIZATION OF DAMAGE IN COMPOSITE MATERIALS. Proceedings of the Royal Society of London, Series A: Mathematical and Physical Sciences, 399(1817), pp. 195-216.
33. DVORAK, G.J., LAWS, N. and HEJAZI, M., 1985. Analysis of progressive matrix cracking in composite laminates-I. Thermoelastic properties of a ply with cracks. *Journal of Composite Materials*, **19**(3), pp. 216-234.
34. DVORAK, G.J. and LAWS, N., 1987. Analysis of progressive matrix cracking in composite laminates-II. First ply failure. *Journal of Composite Materials*, **21**(4), pp. 309-329.
35. HASHIN, Z., 1986. Analysis of stiffness reduction of cracked cross-ply laminates. *Engineering Fracture Mechanics*, **25**(5-6), pp. 771-778.
36. AVESTON, J. and KELLY, A., 1973. Theory of multiple fracture of fibrous composites. *Journal of Materials Science*, **8**(3), pp. 352-362.
37. REIFSNIDER, K.L. 1977. SOME FUNDAMENTAL ASPECTS OF THE FATIGUE AND FRACTURE RESPONSE OF COMPOSITE MATERIALS. *Proceedings 14th Annual Meeting, Society of Engineering Science*, Bethlehem, PA 1977, pp. 343-383.
38. MCCARTNEY, L.N., 1992. Theory of stress transfer in a 0° - 90° - 0° cross-ply laminate containing a parallel array of transverse cracks. *Journal of the Mechanics and Physics of Solids*, **40**(1), pp. 27-68.
39. HASHIN, Z., 1985. Analysis of cracked laminates: a variational approach. *Mechanics of Materials*, **4**(2), pp. 121-136.
40. TALREJA, R., YALVAC, S., YATS, L. and WETTERS, D., 1992. Transverse cracking and stiffness reduction in cross ply laminates of different matrix toughness. *Journal of Composite Materials*, **26**(11), pp. 1644-1663.
41. LI, S., REID, S.R. and SODEN, P.D., 1998. A continuum damage model for transverse matrix cracking in laminated fibre-reinforced composites. *Philosophical Transactions of the Royal Society London, Series A (Mathematical, Physical and Engineering Sciences)*, **356**(1746), pp. 2379-412.

42. ROBERTS, S.J., EVANS, J.T., GIBSON, A.G. and FROST, S.R., 2003. The effect of matrix microcracks on the stress-strain relationship in fiber composite tubes. *Journal of Composite Materials*, **37**(17), pp. 1509-1523.
43. GUDMUNDSON, P. and ZANG, W., 1993. An analytic model for thermoelastic properties of composite laminates containing transverse matrix cracks. *International Journal of Solids and Structures*, **30**(23), pp. 3211-3231.
44. SODEN, P.D., HINTON, M.J. and KADDOUR, A.S., 1998. A comparison of the predictive capabilities of current failure theories for composite laminates. *Composites Science and Technology*, **58**(7), pp. 1225-1254.
45. PUCK, A. and SCHNEIDER, W., 1969. On failure mechanisms and failure criteria of filament-wound glass-fibre/resin composites. *Plastics and Polymers*, **37**(127), pp. 33-44.
46. PUCK, A., 1969. Calculating the strength of glass fiber/plastic laminates under combined load. *Kunststoffe, German Plastics*, **59**, pp. 18-19.
47. KNAPPE, W. and SCHNEIDER, W., 1973. ROLE OF FAILURE CRITERIA IN THE FRACTURE ANALYSIS OF FIBER/MATRIX COMPOSITES. , pp. 543-556.
48. PUCK, A. and SCHURMANN, H., 2002. Failure analysis of FRP laminates by means of physically based phenomenological models. *Composites Science and Technology*, **62**(12-13), pp. 1633-62.
49. PUCK, A. and SCHURMANN, H., 1998. Failure analysis of FRP laminates by means of physically based phenomenological models. *Composites Science and Technology*, **58**(7), pp. 1045-67.
50. Lutz G. The Puck theory of failure in laminates in the context of the new guideline VDI2014 Part 3. In: Proceedings of Conference on Damage in Composite Materials, Stuttgart, 2006.
51. GARG, A.C. and MAI, Y.-W., 1988. Failure mechanisms in toughened epoxy resins-A review. *Composites Science and Technology*, **31**(3), pp. 179-223.
52. SUE, H.-J., GARCIA-MEITIN, E.I. and PICKELMAN, D.M., 1993. Toughening concept of rubber-modified high performance epoxies. In: CHEREMISINOFF, N.P. and CHEREMISINOFF, P.N., ed, *Elastomer Technology Handbook*. Boca Raton: CRC Press, pp. 661.

53. KINLOCH, A.J., SHAW, S.J., TOD, D.A. and HUNSTON, D.L., 1983. Deformation and fracture behaviour of a rubber-toughened epoxy: 1. Microstructure and fracture studies. *Polymer*, **24**(10), pp. 1341-1354.
54. KUNZDOUGLASS, S., BEAUMONT, P. and ASHBY, M., 1980. A Model for the Toughness of Epoxy-Rubber Particulate Composites. *Journal of Materials Science*, **15**(5), pp. 1109-1123.
55. PEARSON, R.A. and YEE, A.F., 1991. Influence of particle size and particle size distribution on toughening mechanisms in rubber-modified epoxies. *Journal of Materials Science*, **26**(14), pp. 3828-3844.
56. PEARSON, R.A. and YEE, A.F., 1989. Toughening mechanisms in elastomer-modified epoxies - Part 3 The effect of cross-link density. *Journal of Materials Science*, **24**(7), pp. 2571-2580.
57. PEARSON, R.A. and YEE, A.F., 1986. Toughening mechanisms in elastomer-modified epoxies - Part 2 Microscopy studies. *Journal of Materials Science*, **21**(7), pp. 2475-2488.
58. SULTAN, J. and MCGARRY, F., 1973. Effect of Rubber Particle-Size on Deformation Mechanisms in Glassy Epoxy. *Polymer Engineering and Science*, **13**(1), pp. 29-34.
59. YEE, A.F. and PEARSON, R.A., 1986. Toughening mechanisms in elastomer-modified epoxies - Part 1 Mechanical studies. *Journal of Materials Science*, **21**(7), pp. 2462-2474.
60. KINLOCH, A.J., YUEN, M.L. and JENKINS, S.D., 1994. Thermoplastic-toughened epoxy polymers. *Journal of Materials Science*, **29**(14), pp. 3781-3790.
61. BÉCU-LONGUET, L., BONNET, A., PICHOT, C., SAUTEREAU, H. and MAAZOUZ, A., 1999. Epoxy networks toughened by core-shell particles: influence of the particle structure and size on the rheological and mechanical properties. *Journal of Applied Polymer Science*, **72**(6), pp. 849-858.
62. GAM, K.T., MIYAMOTO, M., NISHIMURA, R. and SUE, H.-J., 2003. Fracture behavior of core-shell rubber-modified clay-epoxy nanocomposites. *Polymer Engineering and Science*, **43**(10), pp. 1635-1645.

63. MAROUF, B.T., PEARSON, R.A. and BAGHERI, R., 2009. Anomalous fracture behavior in an epoxy-based hybrid composite. *Materials Science and Engineering A*, **515**(1-2), pp. 49-58.
64. THOMPSON, Z.J., HILLMYER, M.A., LIU, J., SUE, H.-J., DETTLOFF, M. and BATES, F.S., 2009. Block copolymer toughened epoxy: Role of cross-link density. *Macromolecules*, **42**(7), pp. 2333-2335.
65. MOLONEY, A.C., KAUSCH, H.H. and STIEGER, H.R., 1983. The fracture of particulate-filled epoxide resins - Part 1. *Journal of Materials Science*, **18**(1), pp. 208-216.
66. HSIEH, T.H., KINLOCH, A.J., MASANIA, K., SOHN LEE, J., TAYLOR, A.C. and SPRENGER, S., 2010. The toughness of epoxy polymers and fibre composites modified with rubber microparticles and silica nanoparticles. *Journal of Materials Science*, **45**(5), pp. 1193-1210.
67. KINLOCH, A.J., MAXWELL, D.L. and YOUNG, R.J., 1985. The fracture of hybrid-particulate composites. *Journal of Materials Science*, **20**(11), pp. 4169-4184.
68. FRÖHLICH, J., THOMANN, R. and MÜLHAUPT, R., 2003. Toughened epoxy hybrid nanocomposites containing both an organophilic layered silicate filler and a compatibilized liquid rubber. *Macromolecules*, **36**(19), pp. 7205-7211.
69. FRÖHLICH, J., THOMANN, R., GRYSCHUK, O., KARGER-KOCSIS, J. and MÜLHAUPT, R., 2004. High-performance epoxy hybrid nanocomposites containing organophilic layered silicates and compatibilized liquid rubber. *Journal of Applied Polymer Science*, **92**(5), pp. 3088-3096.
70. BAGHERI, R., MAROUF, B.T. and PEARSON, R.A., 2009. Rubber-toughened epoxies: A critical review. *Polymer Reviews*, **49**(3), pp. 201-225.
71. LEVITA, G., DE PETRIS, S., MARCHETTI, A. and LAZZERI, A., 1991. Crosslink density and fracture toughness of epoxy resins. *Journal of Materials Science*, **26**(9), pp. 2348-2352.
72. KANG, B.U., JHO, J.Y., KIM, J., LEE, S.-S., PARK, M., LIM, S. and CHOE, C.R., 2001. Effect of molecular weight between crosslinks on the fracture behavior of rubber-toughened epoxy adhesives. *Journal of Applied Polymer Science*, **79**(1), pp. 38-48.

73. BORGGREVE, R.J.M., GAYMANS, R.J. and SCHUIJER, J., 1989. Impact behaviour of nylon-rubber blends. 5. Influence of the mechanical properties of the elastomer. *Polymer*, **30**(1), pp. 71-77.
74. QIAN, J.Y., PEARSOR, R.A., DIMONIE, V.L., SHAFFER, O.L. and EL-AASSER, M.S., 1997. The role of dispersed phase morphology on toughening of epoxies. *Polymer*, **38**(1), pp. 21-30.
75. BAGHERI, R. and PEARSON, R.A., 1996. Role of blend morphology in rubber-toughened polymers. *Journal of Materials Science*, **31**(15), pp. 3945-3954.
76. DAY, R.J., LOVELL, P.A. and PIERRE, D., 1997. Toughening of epoxy resins using particles prepared by emulsion polymerization: Effects of particle surface functionality, size and morphology on impact fracture properties. *Polymer International*, **44**(3), pp. 288-299.
77. KIM, D.S., CHO, K., KIM, J.K. and PARK, C.E., 1996. Effects of particle size and rubber content on fracture toughness in rubber-modified epoxies. *Polymer Engineering and Science*, **36**(6), pp. 755-768.
78. GUILD, F.J. and YOUNG, R.J., 1989. A predictive model for particulate filled composite materials - Part 2 Soft particles. *Journal of Materials Science*, **24**(7), pp. 2454-2460.
79. BAGHERI, R. and PEARSON, R.A., 1996. Role of particle cavitation in rubber-toughened epoxies: 1. Microvoid toughening. *Polymer*, **37**(20), pp. 4529-4538.
80. BASCOM, W., COTTINGTON, R., JONES, R. and PEYSER, P., 1975. Fracture of Epoxy-Modified and Elastomer-Modified Epoxy Polymers in Bulk and as Adhesives. *Journal of Applied Polymer Science*, **19**(9), pp. 2545-2562.
81. HUNSTON, D.L. and BASCOM, W.D., 1984. FAILURE BEHAVIOR OF RUBBER-TOUGHENED EPOXIES IN BULK, ADHESIVE, AND COMPOSITE GEOMETRIES. *Rubber-Modified Thermoset Resins. Based on a symposium held at the 186th Meeting of the American Chemical Society*. 1984, ACS, pp. 83-99.
82. HUNSTON, D.L., 1984. Composite interlaminar fracture: effect of matrix fracture energy. *Composites technology review*, **6**(4), pp. 176-180.

83. HUNSTON, D.L., MOULTON, R.J., JOHNSTON, N.J. and BASCOM, W.D., 1987. MATRIX RESIN EFFECTS IN COMPOSITE DELAMINATION: MODE I FRACTURE ASPECTS. *ASTM Special Technical Publication* 1987, pp. 74-94.
84. BRADLEY, W.L., 1989. Understanding the translation of neat resin toughness into delamination toughness in composites. *Mechanical and corrosion properties. Series A, Key engineering materials*, **37**, pp. 161-198.
85. JORDAN, W., BRADLEY, W. and MOULTON, R., 1989. Relating resin mechanical-properties to composite delamination fracture-toughness. *Journal of Composite Materials*, **23**(9), pp. 923-943.
86. GUILD, F.J. and YOUNG, R.J., 1989. A predictive model for particulate-filled composite materials - Part 1 Hard particles. *Journal of Materials Science*, **24**(1), pp. 298-306.
87. KINLOCH, A.J. and WILLIAMS, J.G., 1980. Crack blunting mechanisms in polymers. *Journal of Materials Science*, **15**(4), pp. 987-96.
88. BASCOM, W.D., TING, R.Y., MOULTON, R.J., RIEW, C.K. and SIEBERT, A.R., 1981. The fracture of an epoxy polymer containing elastomeric modifiers. *Journal of Materials Science*, **16**(10), pp. 2657-64.
89. C.B. BUCKNALL, 1977. *Toughened Plastics*. London: Applied Science Publishers LTD.
90. MAXWELL, B. and RAHM, L.F., 1949. Rheological properties of polystyrene below 80C. *Industrial and Engineering Chemistry*, **41**, pp. 1988-1993.
91. BUCKNALL, C.B. and SMITH, R.R., 1965. Stress-whitening in high-impact polystyrenes. *Polymer*, **6**(8), pp. 437-446.
92. OXBOROUGH, R.J. and BOWDEN, P.B., 1973. A general critical-strain criterion for crazing in amorphous glassy polymers. *Philosophical Magazine*, **28**(3), pp. 547-59.
93. KINLOCH, A.J., SHAW, S.J., TOD, D.A. and HUNSTON, D.L., 1983. Deformation and fracture behaviour of a rubber-toughened epoxy: 2. Failure Criteria. *Polymer*, **24**(10), pp. 1355-1363.
94. MERZ, E.H., CLAVER, G.C. and BAER, M., 1956. Studies on heterogeneous polymeric systems. *Journal of Polymer Science*, **22**(101), pp. 325-341.

95. SPANOUDAKIS, J. and YOUNG, R.J., 1984. Crack propagation in a glass particle-filled epoxy resin. Part 1. Effect of particle volume fraction and size. *Journal of Materials Science*, **19**(2), pp. 473-486.
96. LANGE, F.F., 1970. The interaction of a crack front with a second-phase dispersion. *Philosophical Magazine*, **22**(179), pp. 983-92.
97. LANGE, E.F. and RADFORD, K.C., 1971. Fracture energy of an epoxy composite system. *Journal of Materials Science*, **6**(9), pp. 1197-203.
98. LEE, J. and YEE, A.F., 2000. Role of inherent matrix toughness on fracture of glass bead filled epoxies. *Polymer*, **41**, pp. 8375-8385.
99. KOO, J.H., 2006. *Polymer nanocomposites processing, characterization, and applications*. New York: McGraw-Hill.
100. OKAMOTO, M., 2006. Recent advances in polymer/layered silicate nanocomposites: An overview from science to technology. *Materials Science and Technology*, **22**(7), pp. 756-779.
101. HUSSAIN, F., HOJJATI, M., OKAMOTO, M. and GORGA, R.E., 2006. Review article: Polymer-matrix nanocomposites, processing, manufacturing, and application: An overview. *Journal of Composite Materials*, **40**(17), pp. 1511-1575.
102. THOSTENSON, E.T., LI, C. and CHOU, T., 2005. Nanocomposites in context. *Composites Science and Technology*, **65**(3-4), pp. 491-516.
103. KOJIMA, Y., USUKI, A., KAWASUMI, M., OKADA, A., FUKUSHIMA, Y., KURAUCHI, T. and KAMIGAITO, O., 1993. Mechanical properties of nylon 6-clay hybrid. *Journal of Materials Research*, **8**(5), pp. 1185-1189.
104. OKADA, A. and USUKI, A., 1995. The chemistry of polymer-clay hybrids. *Materials Science and Engineering C*, **3**(2), pp. 109-115.
105. LEBARON, P.C., WANG, Z. and PINNAVAIA, T.J., 1999. Polymer-layered silicate nanocomposites: An overview. *Applied Clay Science*, **15**(1-2), pp. 11-29.
106. GIANNELIS, E.P., 1996. Polymer layered silicate nanocomposites. *Advanced Materials*, **8**(1), pp. 29-35.
107. KE, Y.C., 2005. *Polymer-layered silicate and silica nanocomposites*. Amsterdam: Elsevier.

108. UTRACKI, L.A., 2004. *Clay containing polymer nanocomposites*. Shawbury, UK: Rapra Technology Ltd.
109. LAN, T., KAVIRATNA, P.D. and PINNAVAIA, T.J., 1995. Mechanism of clay tactoid exfoliation in epoxy-clay nanocomposites. *Chemistry of Materials*, **7**(11), pp. 2144-2150.
110. GIANNELIS, E.P., KRISHNAMOORTI, R. and MANIAS, E., 1999. Polymer-silicate nanocomposites: Model systems for confined polymers and polymer brushes. pp. 107-147.
111. BROWN, J.M., CURLISS, D. and VAIA, R.A., 2000. Thermoset-layered silicate nanocomposites. Quaternary ammonium montmorillonite with primary diamine cured epoxies. *Chemistry of Materials*, **12**(11), pp. 3376-3384.
112. WANG, M.S. and PINNAVAIA, T.J., 1994. Clay-polymer nanocomposites formed from acidic derivatives of montmorillonite and an epoxy resin. *Chemistry of Materials*, **6**(4), pp. 468-474.
113. KORNMANN, X., THOMANN, R., MÜLHAUPT, R., FINTER, J. and BERGLUND, L., 2002. Synthesis of amine-cured, epoxy-layered silicate nanocomposites: The influence of the silicate surface modification on the properties. *Journal of Applied Polymer Science*, **86**(10), pp. 2643-2652.
114. ZILG, C., MÜLHAUPT, R. and FINTER, J., 1999. Morphology and toughness/stiffness balance of nanocomposites based upon anhydride-cured epoxy resins and layered silicates. *Macromolecular Chemistry and Physics*, **200**(3), pp. 661-670.
115. XIDAS, P.I. and TRIANTAFYLLIDIS, K.S., 2010. Effect of the type of alkylammonium ion clay modifier on the structure and thermal/mechanical properties of glassy and rubbery epoxy-clay nanocomposites. *European Polymer Journal*, **46**(3), pp. 404-417.
116. PARK, J.H. and JANA, S.C., 2003. Mechanism of exfoliation of nanoclay particles in epoxy-clay nanocomposites. *Macromolecules*, **36**(8), pp. 2758-2768.
117. PINNAVAIA, T.J., LAN, T., WANG, Z., SHI, H. and KAVIRATNA, P.D., 1996. CLAY-REINFORCED EPOXY NANOCOMPOSITES: SYNTHESIS, PROPERTIES, AND MECHANISM OF FORMATION. *ACS Symposium Series 622*, 1996, pp. 250-261.

118. CHEN, C. and CURLISS, D., 2003. Preparation, Characterization, and Nanostructural Evolution of Epoxy Nanocomposites. *Journal of Applied Polymer Science*, **90**(8), pp. 2276-2287.
119. KORNMANN, X., LINDBERG, H. and BERGLUND, L.A., 2001. Synthesis of epoxy-clay nanocomposites: Influence of the nature of the clay on structure. *Polymer*, **42**(4), pp. 1303-1310.
120. BECKER, O., CHENG, Y.-B., VARLEY, R.J. and SIMON, G.P., 2003. Layered silicate nanocomposites based on various high-functionality epoxy resins: The influence of cure temperature on morphology, mechanical properties, and free volume. *Macromolecules*, **36**(5), pp. 1616-1625.
121. BECKER, O., VARLEY, R. and SIMON, G., 2002. Morphology, thermal relaxations and mechanical properties of layered silicate nanocomposites based upon high-functionality epoxy resins. *Polymer*, **43**(16), pp. 4365-4373.
122. MESSERSMITH, P.B. and GIANNELIS, E.P., 1994. Synthesis and characterization of layered silicate-epoxy nanocomposites. *Chemistry of Materials*, **6**(10), pp. 1719-1725.
123. KE, Y., LU, J., YI, X., ZHAO, J. and QI, Z., 2000. Effects of promoter and curing process on exfoliation behavior of epoxy/clay nanocomposites. *Journal of Applied Polymer Science*, **78**(4), pp. 808-815.
124. KORNMANN, X., BERGLUND, L.A., THOMANN, R., MULHAUPT, R. and FINTER, J., 2002. High performance epoxy-layered silicate nanocomposites. *Polymer Engineering and Science*, **42**(9), pp. 1815-1826.
125. HERNANDEZ, M., SIXOU, B., DUCHET, J. and SAUTEREAU, H., 2007. The effect of dispersion state on PMMA-epoxy-clay ternary blends: In situ study and final morphologies. *Polymer*, **48**(14), pp. 4075-4086.
126. LIU, W., HOA, S.V. and PUGH, M., 2005. Organoclay-modified high performance epoxy nanocomposites. *Composites Science and Technology*, **65**(2), pp. 307-316.
127. YASMIN, A., ABOT, J.L. and DANIEL, I.M., 2003. Processing of clay/epoxy nanocomposites by shear mixing. *Scripta Materialia*, **49**(1 SPEC.), pp. 81-86.

128. ALEXANDRE, M. and DUBOIS, P., 2000. Polymer-layered silicate nanocomposites: Preparation, properties and uses of a new class of materials. *Materials Science and Engineering R: Reports*, 28(1), pp. 1-63.
129. BECKER, O. and SIMON, G.P., 2005. Epoxy layered silicate nanocomposites. *Advances in Polymer Science*, 179, pp. 29-82.
130. LAN, T. and PINNAVAIA, T.J., 1994. Clay-reinforced epoxy nanocomposites. *Chemistry of Materials*, 6(12), pp. 2216-2219
131. ZERDA, A.S. and LESSER, A.J., 2001. Intercalated clay nanocomposites: Morphology, mechanics, and fracture behavior. *Journal of Polymer Science, Part B: Polymer Physics*, 39(11), pp. 1137-1146.
132. MIYAGAWA, H. and DRZAL, L.T., 2004. The effect of chemical modification on the fracture toughness of montmorillonite clay/epoxy nanocomposites. *Journal of Adhesion Science and Technology*, 18(13), pp. 1571-1588.
133. MASSAM, J. and PINNAVAIA, T.J., 1998. CLAY NANOLAYER REINFORCEMENT OF A GLASSY EPOXY POLYMER. *Materials Research Society Symposium Proceedings* 1998, 520, pp. 223-232.
134. BECKER, O., VARLEY, R.J. and SIMON, G.P., 2004. Thermal stability and water uptake of high performance epoxy layered silicate nanocomposites. *European Polymer Journal*, 40(1), pp. 187-195.
135. GILMAN, J.W., 1999. Flammability and thermal stability studies of polymer layered-silicate (clay) nanocomposites. *Applied Clay Science*, 15(1-2), pp. 31-49.
136. HAMLEY, I.W., 2004. *Developments in block copolymer science and technology*. West Sussex: John Wiley & Sons, Ltd.
137. LODGE, T.P., 2003. Block copolymers: Past successes and future challenges. *Macromolecular Chemistry and Physics*, 204(2), pp. 265-273.
138. HILLMYER, M., 1999. Block copolymer synthesis. *Current Opinion in Solid State and Materials Science*, 4(6), pp. 559-564.
139. BATES, F.S. and FREDRICKSON, G.H., 1999. Block copolymers-designer soft materials. *Physics Today*, 52(2), pp. 32-38.

140. SMART, T., LOMAS, H., MASSIGNANI, M., FLORES-MERINO, M.V., PEREZ, L.R. and BATTAGLIA, G., 2008. Block copolymer nanostructures. *Nano Today*, **3**(3-4), pp. 38-46.
141. HELFAND, E., 1975. Block copolymer theory. III. Statistical mechanics of the microdomain structure. *Macromolecules*, **8**(4), pp. 552-556.
142. LEIBLER, L., 1980. Theory of microphase separation in block copolymers. *Macromolecules*, **13**(6), pp. 1602-1617.
143. MATSEN, M.W. and BATES, F.S., 1996. Unifying weak- and strong-segregation block copolymer theories. *Macromolecules*, **29**(4), pp. 1091-1098.
144. MATSEN, M.W. and THOMPSON, R.B., 1999. Equilibrium behaviour of symmetric ABA triblock copolymer melts. *Journal of Chemical Physics*, **111**(15), pp. 7139-7146.
145. ZHENG, W. and WANG, Z., 1995. Morphology of ABC triblock copolymers. *Macromolecules*, **28**(21), pp. 7215-7215.
146. MEIER, D.J., 1996. Theory of block copolymers. I. Domain formation in A-B block copolymers. *Journal of Polymer Science, Part B: Polymer Physics*, **34**(11), pp. 1821-1838.
147. HELFAND, E. and WASSERMAN, Z.R., 1976. Block copolymer theory. 4. Narrow interphase approximation. *Macromolecules*, **9**(6), pp. 879-888.
148. MATSEN, M.W. and SCHICK, M., 1994. Stable and unstable phase of a diblock copolymer melt. *Physical Review Letters*, **72**(16), pp. 2660-2660.
149. RUZETTE, A.-V. and LEIBLER, L., 2005. Block copolymers in tomorrow's plastics. *Nature Materials*, **4**(1), pp. 19-31.
150. LIPIC, P.M., BATES, F.S. and HILLMYER, M.A., 1998. Nanostructured thermosets from self-assembled amphiphilic block copolymer/epoxy resin mixtures. *Journal of the American Chemical Society*, **120**(35), pp. 8963-8970.
151. HILLMYER, M.A., LIPIC, P.M., HAJDUK, D.A., ALMDAL, K. and BATES, F.S., 1997. Self-assembly and polymerization of epoxy resin-amphiphilic block copolymer nanocomposites. *Journal of the American Chemical Society*, **119**(11), pp. 2749-2750.

152. SPONTAK, R.J. and PATEL, N.P., 2000. Thermoplastic elastomers: Fundamentals and applications. *Current Opinion in Colloid and Interface Science*, **5**(5-6), pp. 334-341.
153. HYDRO, R.M. and PEARSON, R.A., 2007. Epoxies toughened with triblock copolymers. *Journal of Polymer Science, Part B: Polymer Physics*, **45**(12), pp. 1470-1481.
154. GERARD, P., BOUPAT, N.P., FINE, T., GERVAT, L. and PASCAULT, J.-P., 2007. Toughness properties of lightly crosslinked epoxies using block copolymers. *Macromolecular Symposia*, **256**, pp. 55-64.
155. WU, J., THIO, Y.S. and BATES, F.S., 2005. Structure and properties of PBO-PEO diblock copolymer modified epoxy. *Journal of Polymer Science, Part B: Polymer Physics*, **43**(15), pp. 1950-1965.
156. YANG, P., ZHAO, D., MARGOLESE, D.I., CHMELKA, B.F. and STUCKY, G.D., 1999. Block copolymer templating syntheses of mesoporous metal oxides with large ordering lengths and semicrystalline framework. *Chemistry of Materials*, **11**(10), pp. 2813-2826.
157. BRONSTEIN, L., KRÄMER, E., BERTON, B., BURGER, C., FÖRSTER, S. and ANTONIETTI, M., 1999. Successive use of amphiphilic block copolymers as nanoreactors and templates: Preparation of porous silica with metal nanoparticles. *Chemistry of Materials*, **11**(6), pp. 1402-1405.
158. CHEN, L., PHILLIP, W.A., CUSSLER, E.L. and HILLMYER, M.A., 2007. Robust nanoporous membranes templated by a doubly reactive block copolymer. *Journal of the American Chemical Society*, **129**(45), pp. 13786-13787.
159. KELLER, A., PEDEMONTE, E. and WILLMOUTH, F.M., 1970. Macro-lattice from segregated amorphous phases of a three block copolymer. *Nature*, **225**(5232), pp. 538-539.
160. HAMLEY, I.W., 2001. Structure and flow behaviour of block copolymers. *Journal of Physics Condensed Matter*, **13**(33), pp. R643-R671.
161. AMUNDSON, K., HELFAND, E., QUAN, X., HUDSON, S.D. and SMITH, S.D., 1994. Alignment of lamellar block copolymer microstructure in an electric field. 2. Mechanisms of alignment. *Macromolecules*®, **27**(22), pp. 6559-6570.

162. JEONG, B., BAE, Y.H., LEE, D.S. and KIM, S.W., 1997. Biodegradable block copolymers as injectable drug-delivery systems. *Nature*, **388**(6645), pp. 860-862.
163. JEONG, B., KIM, S.W. and BAE, Y.H., 2002. Thermosensitive sol-gel reversible hydrogels. *Advanced Drug Delivery Reviews*, **54**(1), pp. 37-51.
164. YOKOZEKI, T., IWAHORI, Y. and ISHIWATA, S., 2007. Matrix cracking behaviors in carbon fiber/epoxy laminates filled with cup-stacked carbon nanotubes (CSCNTs). *Composites Part A: Applied Science and Manufacturing*, **38**(3), pp. 917-924.
165. MILLER, S.G. and MEADOR, M.A., 2007. POLYMER- LAYERED SILICATE NANOCOMPOSITES FOR CRYOTANK APPLICATIONS, *Collection of Technical Papers - AIAA/ASME/ASCE/AHS/ASC Structures, Structural Dynamics and Materials Conference 2007*, pp. 7530-7538.
166. KIM, M., HONG, J., KANG, S. and KIM, C., 2008. Enhancement of the crack growth resistance of a carbon/epoxy composite by adding multi-walled carbon nanotubes at a cryogenic temperature. *Composites Part A: Applied Science and Manufacturing*, **39**(4), pp. 647-654.
167. TIMMERMAN, J.F., HAYES, B.S. and SEFERIS, J.C., 2002. Nanoclay reinforcement effects on the cryogenic microcracking of carbon fiber/epoxy composites. *Composites Science and Technology*, **62**(9), pp. 1249-1258.

Chapter 2

Materials and Experimental Procedure

SYNOPSIS: The experimental work involved the selection of appropriate constituents and material systems; development of nanocomposite synthesis techniques; setup of procedural standards and characterization criteria. After establishing proper experimental procedures through trial and error, a series of nanocomposite specimens and prototype pipe structures were fabricated. Epoxy-clay nanocomposites were synthesized by two separate nanoclay dispersion schemes, that is, in-situ intercalative polymerization and exfoliation-adsorption processes. Block-copolymer/epoxy blends were prepared through self-assembling pattern generation by dissolution of block-copolymer in the epoxy polymer. Hybrid nanocomposite samples were produced by following a special sample preparation technique that is specific to the intended material system. A state-of-the-art numerically controlled filament winding facility was used for manufacturing fiber-reinforced pipes having a specific lay-up configuration and fiber orientation.

2.1 MATERIAL SYSTEM

Epoxy can be referred to as the molecules that contain more than one epoxide group (also known as oxirane or epoxy group). The three-membered ring of an epoxy group is composed of an oxygen atom bonded with two carbon atoms [1-2]. The diepoxy resin diglycidyl ether of bisphenol-A (DGEBA) is undoubtedly the most commonly used epoxy polymer, which is derived from a step-growth polymerization (condensation polymerization) reaction between bisphenol-A and epichlorohydrin in the presence of a strong alkali [3]. The formation of a low molar mass epoxy resin is shown in Figure 2.1. The properties of the resulting epoxy compound depend on n , which is the number of repeating units and varies between 0 from 25 [4]. Another feature that characterizes the epoxy is the epoxide equivalent weight representing the weight of epoxy resin in grams that contains 1 mole of epoxide.

On reaction between the epoxide group and a reactive molecule known as hardener or curing agent a cross-linking reaction (curing reaction/polymerization reaction) takes place. The polymerization reaction can further be aided with the application of heat or irradiation. Among the commonly used curing agents are polyamine, polyamides, polyureas, polyisocyanates, dicyanamide, polymercaptans, polyphenols and acid anhydrides [2, 4]. The polyaddition reaction between the terminal epoxide group of the epoxy prepolymer and active hydrogen of a diamine curing agent is illustrated in Figure 2.2. Through the formation of a three-dimensional network by cross-linking favorable mechanical, thermal and chemical properties evolve in the final epoxy product. Usually, commercial grade epoxy resins are supplied in two parts: part A (e.g. epoxy prepolymer DGEBA) and part B (a curing agent) are mixed together to produce the desired end product through an exothermic reaction. The choice of a suitable resin system depends on such factors as the manufacturing steps and application and properties of the final product.

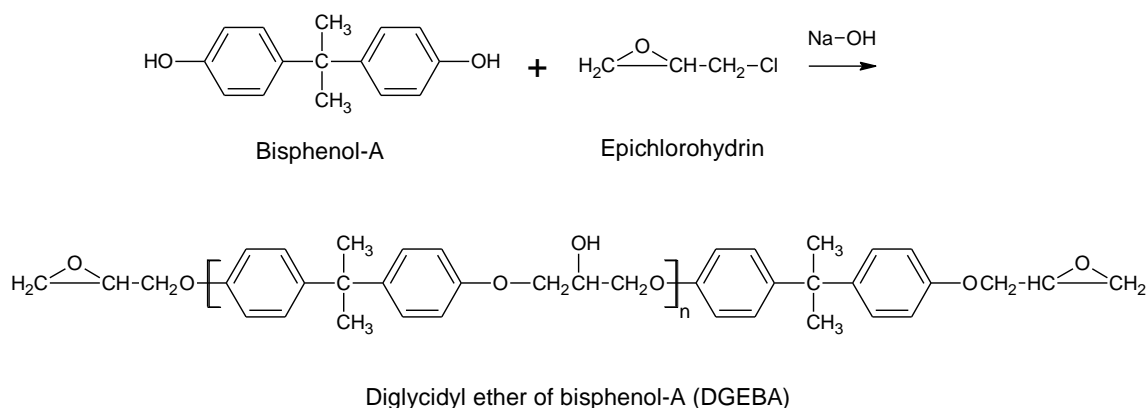
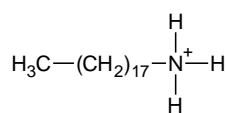


Figure 2.1 Formation of an epoxy prepolymer.

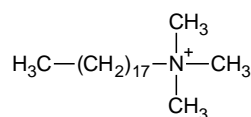
The two-part epoxy resin EPON™ 826 (epoxide equivalent weight 178-186 g/eq) and curing agent EPIKURE™ 9551 were used as received from Momentive (Columbus, Ohio, USA). EPON™ 826 is a liquid diglycidyl ether of bisphenol-A epoxy resin, and EPIKURE™ 9551 is a non-MDA (methylene dianiline) proprietary polyamine curing agent (see physical properties of epoxy resin in Tables 2-1 and 2-2). The recommended mixing ratio for this epoxy system by weight is 36 g of curing agent per 100 g of resin.

poly(methylmethacrylate-*b*-butylacrylate-*b*-methylmethacrylate) block-copolymer is comprised of an elastomeric middle block poly(*n*-butylacrylate) (PBuA) and two epoxy compatible side blocks of poly(methylmethacrylate) (PMMA). The M52N block-copolymer has similar structure as the M52 block-copolymer, but the side blocks are made of random copolymers of methylmethacrylate (MMA) and *N,N*-dimethylacrylamide (DMA). Incorporation of DMA units is intended to increase the block-copolymer miscibility with epoxy, and to provide greater stability of the nanostructures during the cross-linking reaction [5, 6]. The specific chemical formulae of the M52 and M52N are proprietary in nature and are withheld by the manufacturer. Figure 2.3 shows representative chemical structures of the clay surface modifiers and block-copolymers employed in this study. Figure 2.4 shows photographs of the as-delivered nano-filler materials.

The fiber composites were made with the basalt fiber KV12 (see properties in Table 2-5) having a liner density of 1200 tex, which was supplied by Kamenny Vek (Dubna, Moscow Region, Russia). A comparative study of basalt, E-glass and S-glass fiber reinforcements on the performance of filament-wound tubular structures can be found in reference [7].



Octadecyl ammonium



Octadecyl trimethyl ammonium

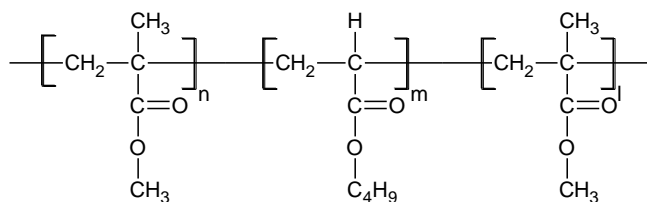
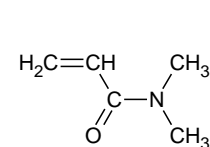
Poly(methylmethacrylate-*b*-butylacrylate-*b*-methylmethacrylate)*N,N*-dimethylacrylamide

Figure 2.3 Representative chemical structures of the alkylammonium ions and acrylic block-copolymers used in this study.

Table 2-1 Physical characteristics of the epoxy resin system [8].

Property	EPON 826	EPIKURE 9551
Viscosity at 25°C (cP)	6500-9500	30-70
Density at 25°C (g/cm ³)	1.16	0.96
Epoxide equivalent weight (g/eq)	178-186	
Amine hydrogen equivalent weight (g/eq)		57-67
Mix ratio of resin/curing agent by weight	100	36
Mix viscosity resin/curing agent at 25°C (cP)	1100	
Pot life (resin/curing agent) at 25°C, (h)	2.5	
Gel time (resin/curing agent) at 25°C, (h)	6.4	

Table 2-2 Physical properties of the neat epoxy resin in cured state [8].

Property	Value
Tensile strength at 25°C (MPa)	68.9
Tensile modulus at 25°C (GPa)	2.76
Tensile elongation at 25°C (%)	10.6
Fracture toughness (MPam ^{0.5})	1.27
Glass transition temperature (°C)	110
Coefficient of thermal expansion (µm/m°C)	56
Water up-take (%)	1.8

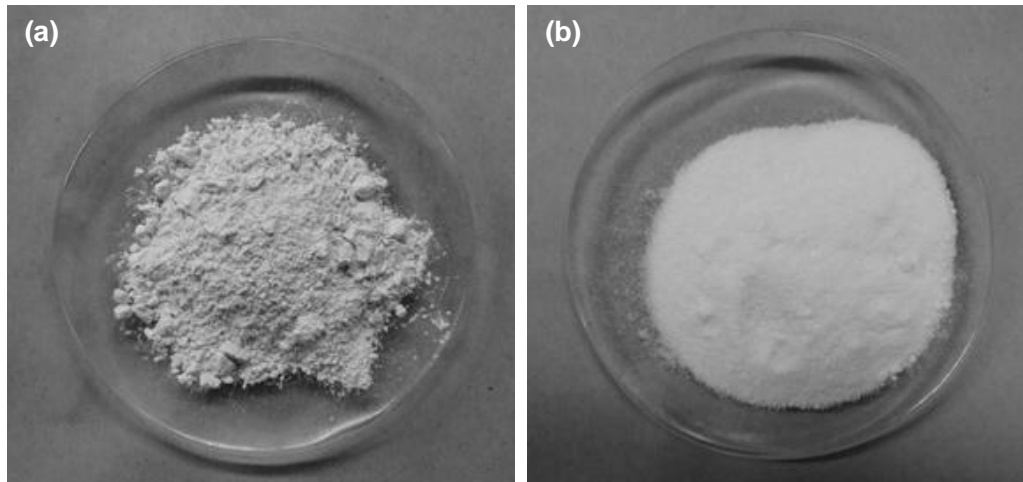
**Figure 2.4** Picture of powdered nano-fillers: (a) I.30E and (b) M52N.

Table 2-3 Physical properties of the layered silicate nanoclay [10-12].

Property	I.30E	I.28E	PGW
Appearance	White powder	White powder	White powder
Mean dry particle size (μm)	8-10	8-10	16-22 [9]
Specific gravity	1.71	1.9	2.6
Moisture content (%)	3 max	3 max	12 max
Aspect ratio			200-400
Surface area (m^2/g)		750	
CEC (meq/100g)			145
Organic content (wt%)	25-30 [9]	25-30 [9]	--

Table 2-4 Physical and chemical properties of the Nanostrength® M52N [13].

Property	Description
Appearance	White/yellow powder
Melting point	Approximately 160°C
Solubility in solvent	Aromatic solvents, aldehydes, ketones, acetic esters, chlorinated solvents
Solubility in water	Insoluble
Thermal decomposition	>280°C

Table 2-5 Property of the basalt fiber reinforcements [14].

Property	Description
Monofilament diameter (μm)	10-22
Linear density (tex)	1200
Type of sizing	Silane
Sizing content (wt%)	≥ 0.4
Resin compatibility	Epoxy and phenolic
Moisture content (wt%)	<0.1
Tensile strength of epoxy impregnated strand (MPa)	2800-3000 (ASTM D2343)
Tensile modulus of epoxy impregnated strand (GPa)	85-90

2.2 PREPARATION OF NANOCOMPOSITES

Preparation and processing of epoxy nanocomposites from resin, curing agent and nanofillers involved such major steps as mixing, dispersion, degassing and curing. In the following, optimum processing condition are described as found from several trials by manipulating processing (i.e. mixing time and temperature, extent of dispersion, method of dispersion, etc.) and material parameters.

2.2.1 Epoxy-clay Nanocomposites

Nanocomposites were synthesized by two separate nanoclay dispersion schemes. In-situ intercalative polymerization was performed using a mechanical agitator; this is hereafter termed as mechanical dispersion. An exfoliation-adsorption process was carried out using an ultrasonic probe with the aid of the solvent acetone, which is hereafter designated as ultrasonic dispersion.

2.2.1.1 Mechanical Dispersion

Prior to dispersion into the epoxy precursor, nanoclay I.30E was dried in an oven at an elevated temperature of 120°C for a period of 24 hours to remove any adsorbed water. Afterwards, the nanoclay was allowed to cool down to room temperature. Then, a measured amount of nanoclay (depending on the filler matrix loading) was gently added to 150 g of preheated EPON 826 resin at 60°C in a 250 ml glass beaker. The mixture was mechanically mixed for 30 minutes with an impeller type shear mixer (built in-house) running at 900 revolutions per minute. Pre-heating melted crystalline solids that may have been present as a result of storing epoxy resin at room temperature and also reduced resin viscosity. The low molecular weight of the epoxy prepolymer allowed direct addition of the nanoclay in the epoxy resin. Then, a stoichiometric amount of the curing agent was added to the epoxy-clay solution, followed by mechanical mixing at 60°C for five minutes using the same mechanical stirrer mentioned above. Any entrapped air and volatiles formed during mixing with the curing agent were evacuated by a vacuum pump operated at 80 kPa for 20 minutes. Vacuum was applied by placing the steel mold inside a specially designed vacuum chamber. The final mixture was cured in an open mold made of mild steel having internal dimensions of 21 cm by 11.5 cm by 2.5 cm (see Figure 2.5). The steel mold was coated with a layer of release

agent Frekote® 770-NC (Henkel, Rocky Hill, Connecticut, USA) and subsequently heated to 60°C before the resin mixture is poured into the mold cavity. Curing of the nanocomposite was performed in an oven at 120°C for two hours. Afterwards, it was allowed to cool down to room temperature. Composite samples having 1 wt%, 2 wt% and 3 wt% of I.30E clay were produced using this method. Figure 2.6 shows a process flow diagram for the mechanical dispersion method.



Figure 2.5 Mold used for epoxy casting.

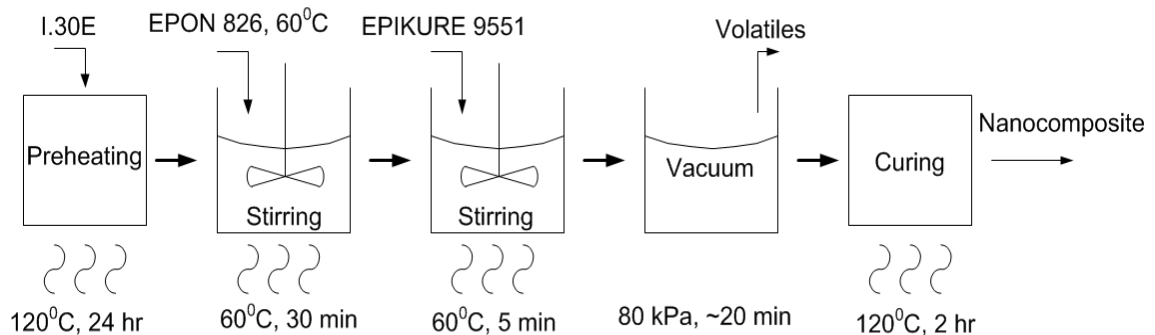


Figure 2.6 Process flow diagram of nanocomposite fabrication by mechanical mixing method.

Neat epoxy samples were prepared through a procedure where preheated epoxy resin was directly mixed with the curing agent and subsequently cured as per in the same manner as mentioned above. Note that with increasing filler loading, the reactive mixture becomes more

viscous. The highly viscous nature of the mixture significantly limits the ability to remove entrapped gases with vacuum. Hence, clay loading of nanocomposites prepared for this study did not exceed 3 wt% to maintain the integrity and uniformity of the samples. It was also confirmed from manufacturer technical data [11] that the dispersion of organoclay is expected to increase the mixture viscosity.

2.2.1.2 Ultrasonic Dispersion

At the beginning of the ultrasonic dispersion process, a specified amount of the dried nanoclay was added to 125 ml acetone in a 250 ml beaker. The mixture was then held at room temperature for six hours. During this time, pre-swelling of the clay occurred by diffusion of solvent into the clay interlayers. 150 g preheated EPON 826 at 60°C was then incorporated with the nanoclay solution in a 600 ml beaker, and immediately after the epoxy addition ultrasonic mixing was initiated. Roughly a 300 ml mixture of nanoclay, acetone and EPON 826 was subjected to sonication in a glass beaker. To obtain the desired level of resin viscosity for efficient ultrasonic mixing, the system temperature was slowly raised to 80°C. Sonication was performed by a Branson model S-75 Sonifier (Branson Ultrasonics Corporation, Danbury, Connecticut, USA) at 80°C for eight hours. The ultrasonic probe was operated at 75 W power output with 20 kHz output frequency. A step horn sonotrode with a 12.7 mm tip diameter was used to transmit ultrasonic energy. To prevent the generation of excessive heating during ultrasonic mixing of the polymer and nanoclay fillers, the temperature was maintained by momentarily stopping the ultrasonic probe. Ultrasonic dispersion was aided by the polar solvent acetone, which reduced the viscosity of the mixture to facilitate penetration of the epoxy precursor into the interlamellar region of the stacked clay sheets [15-16]. Afterward, the solution was mechanically blended for two hours. Acetone was removed from the solution by vacuum extraction performed at 80 kPa. Figure 2.7 shows an epoxy-nanoclay solution after acetone was stripped off and neat DGEBA epoxy resin.

The amount of resin as designated above was for preparing dog-bone specimens. To fabricate thicker specimens, as in the case of the fracture toughness testing, a greater amount of constituents was added in the starting solution. Finally, the epoxy-clay blend was mixed with EPIKURE 9551 curing agent. Subsequent exposure to vacuum the curing was accomplished

in a manner similar to that described above for mechanical dispersion. Nanocomposites containing 1, 2 and 3 wt% I.30E, 1 wt% I.28E and 1 wt% PGW clay were produced according to this procedure. Figure 2.8 shows a flow chart for the ultrasonic dispersion process.

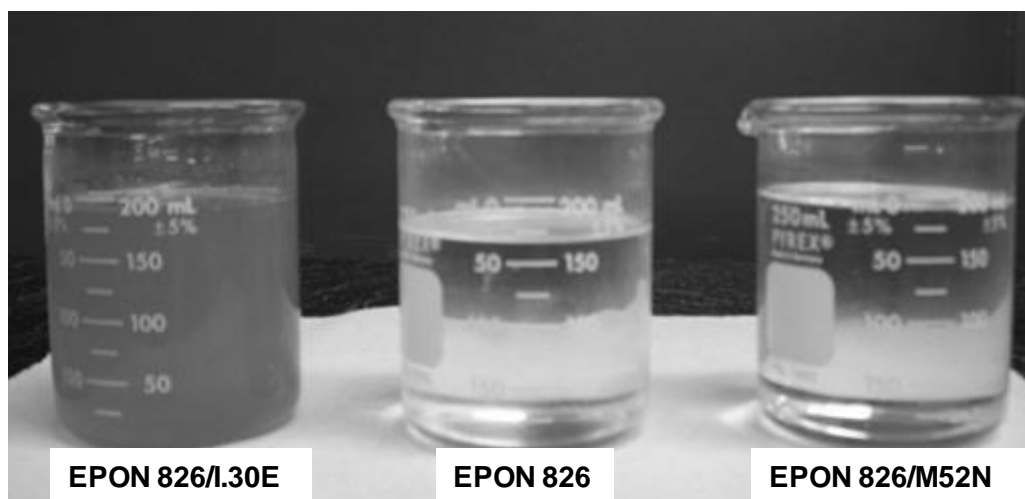


Figure 2.7 Liquid epoxy resin EPON 826 with and without nano-fillers.

2.2.2 Block-copolymer/Epoxy Blends

One of the advantages of M52 and M52N block-copolymers is their excellent solubility in epoxy precursor. Powdered block-copolymer was easily dissolved in the epoxy resin by melt mixing with the application of heat. To manufacture acrylic block-copolymer modified epoxy compounds, initially block-copolymer (i.e. M52 or M52N) powder was manually mixed with the EPON 826 epoxy resin at room temperature. The temperature of the mixture was raised to 80°C, which allowed the block-copolymer to dissolve into the epoxy resin with the application of prolonged heating. Heating was continued until complete miscibility of block-copolymer was achieved leading to a transparent and homogenous solution as shown in Figure 2.7. Caution was taken regarding the completion of block-copolymer dissolution in epoxy. The probable matching refractive indexes of the epoxy and swollen block-copolymer powder may give such misimpression of uniform homogenization of the mixture by casual visual observation. Therefore, each solution was carefully inspected under bright light to detect any remnant undissolved powder. Dissolution time varied upon block-copolymer concentration. After complete

dissolution was confirmed through good optical transparency, a stoichiometric amount of the EPIKURE 9551 curing agent was introduced to the solution at 60°C, and mixed for five minutes by a mechanical stirrer. Mechanical mixing was followed by a degassing cycle in a vacuum chamber at 80 kPa for 20 minutes to remove all the volatiles from the blend. Similar procedures were followed for cured epoxy blends containing 1, 3 and 5 wt% of respective M52 and M52N additives.

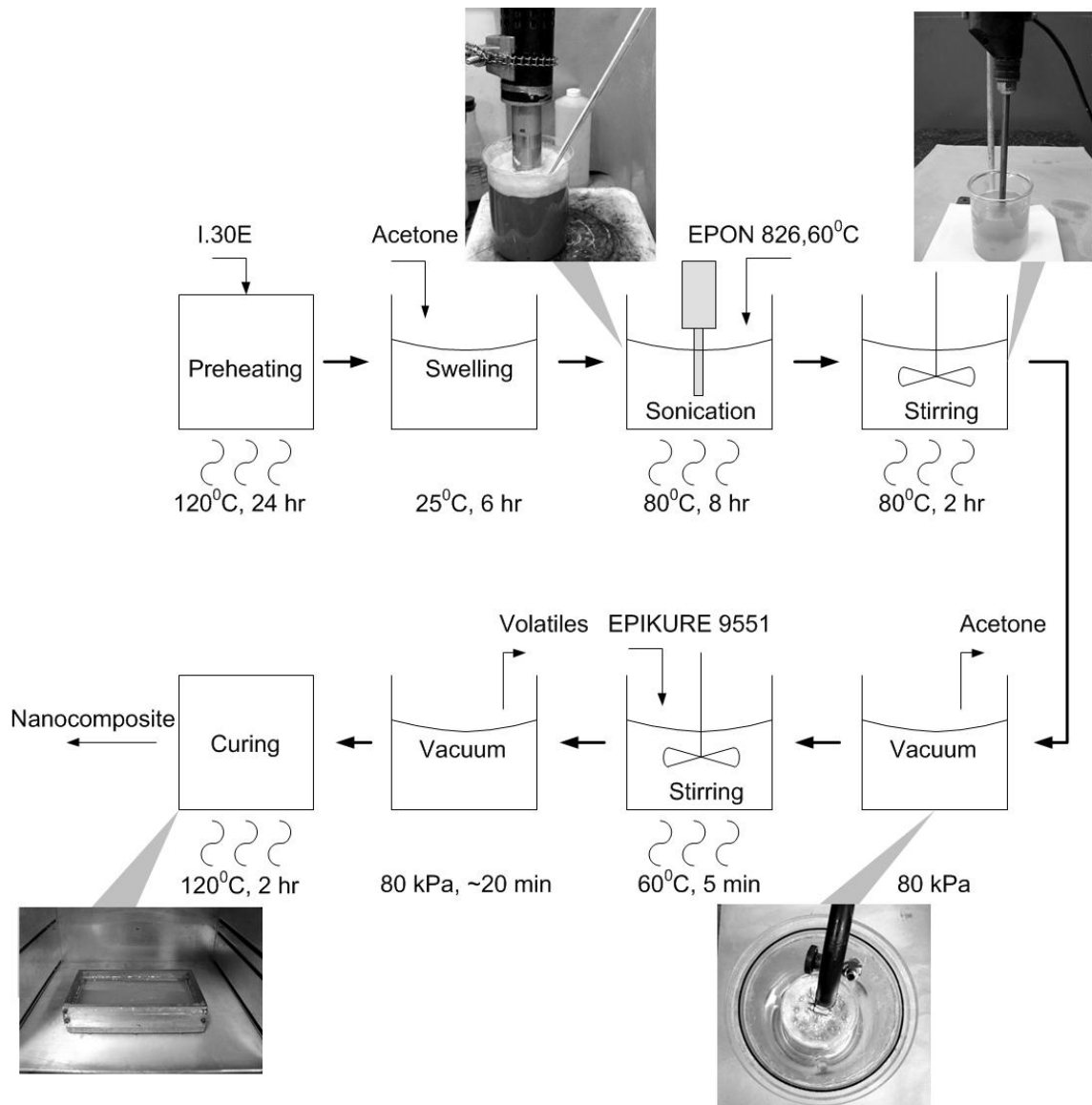


Figure 2.8 Processing steps for nanocomposite fabricated by ultrasonic mixing method.

2.2.3 Epoxy Hybrid Nanocomposites

To fabricate epoxy hybrid nanocomposites, an acetone-clay solution was mixed with an initially prepared blend of EPON 826-M52N block-copolymer. The preparation of acetone-clay solution and EPON 826-M52N blend are identical to those described in the previous Sections 2.2.1.2 and 2.2.2, respectively. The remaining steps were the same as for epoxy-clay nanocomposite processing done by the ultrasonic method. In hybrid nanocomposite processing, instead of adding EPON 826, the EPON 826-M52N blend was incorporated into the acetone-clay solution. The following hybrid nanocomposite formulations were produced: 1B&1C = 1 wt% M52N and 1 wt% I.30E; 1B&3C = 1 wt% M52N and 3 wt% I.30E; and 3B&1C = 3 wt% M52N and 1 wt% I.30E.

2.2.4 Machining of the Specimens

Standard test specimens were machined from the cured epoxy nanocomposites, conforming to the specific requirements of the intended test methods. Test specimens for tensile, fracture, and dynamic mechanical thermal analysis (DMTA) were machined from the cast neat epoxy and nanocomposite samples. The standard geometries were chosen by conforming with the ASTM standards, and the specific illustrations can be found in the testing section in Chapter 3. The machining of the tensile specimen begins with a cured epoxy plate about ~6 mm thick. First, the top and bottom surfaces of this epoxy sheet were machined down to the specified thickness with a digitally controlled milling machine. The final profiling to the dumbbell shape was done by a water jet cutter. A vacuum assisted clamping jig was used to clamp the specimen tight to the machine while milling is done on the opposite surface. After machining, the gauge-section of the tensile samples were polished successively with 400 and 600 grit emery cloths to provide a notch-free even surface finish. Considering the notch sensitivity of epoxy, polishing was done to avoid premature and unexpected fracture of specimen that may initiate from flaws and scratches. The cast epoxy plates for DMTA and fracture toughness testing specimen were machined by following a similar procedure as done before for tensile test samples. The final DMTA samples were cut using a hand saw from the flattened sheet to the exact dimension. In single edge notch bend (SENB) specimens used for fracture toughness testing a notch was created by the aforementioned milling machine using a 60°

diamond cutter. The deviations/variations from the exact design specifications were minimum and within ± 0.01 mm, which is within the recommended tolerance of the standards.

2.2.5 Fabrication of Fiber-reinforced Epoxy Nanocomposites

Basalt fiber-reinforced uniaxial laminate plates were manufactured by filament winding using a numerically controlled WMS 4-axis filament winding machine (McClellan Anderson, Schofield, WI, USA). This machine has the capacity to produce composite pipes as large as 4 m in length and 0.66 m in diameter [17]. To fabricate the laminated plates, continuous basalt fiber strands from three creels were hoop wound onto a rotating flat mandrel having dimensions of 150 mm by 200 mm. The surface of the mandrel was coated with release agent Frekote® 770-NC. While en-route to the mandrel, fiber strands were thoroughly impregnated with epoxy-nanoparticle formulation contained in a drum-type resin bath maintained at 30°C. A computer controlled fiber tensioning system was used to apply steady fiber tension during the winding process. Higher fiber tow tension consolidated fiber lay-ups and displaced excess resin. Increased winding tension is recommended to make parts having appropriate fiber volume fraction and low void content [18-19]. The winding tension was therefore manipulated depending on the fiber packing required. The fiber volume fraction was adjusted by changing the applied load from the tensioning system as well as selectively employing vacuum bagging (see subsequent paragraph) to those samples that were required to have increased fiber volume fraction. A 50 μm thin ethylene tetrafluoroethylene film insert was placed at the mid-plane of the laminate stack as a crack initiator. Laminates were made of 8 plies, four on top and the rest below the thin film insert. Each ply was approximately ~ 0.625 mm thick with the quasi unidirectional lay-up having a fiber configuration of $[\pm 89.5^\circ_4]_T$. A detailed description of the filament winding machine and the processing steps can be found in reference [20]. Figure 2.9 illustrates the filament winding manufacturing process used to fabricate laminate plates.

After completion of the winding process the mandrel with resin-wet fibers was covered with a layer of polyamide cloth peel fly, a polypropylene bleeder cloth, a release film and finally a vacuum bag to bleed out the excess resin, entrapped air and other volatiles. Curing was performed at 120°C for two hours with the application of continuous vacuum

of 80 kPa. After curing, the laminates were machined by a water jet cutter according to the specified dimensions, 120 mm long and 20 mm wide including an initial delamination length of 50 mm. Resin laden top and bottom surfaces were manually sanded down to give the average thickness of about ~5 mm using 400 grit emery cloth. Afterwards, piano hinges were attached on each side of the specimens using a 3M Scotch-Weld DP460 Off-White adhesive (3M, St. Paul, Minnesota, USA). After attaching the hinges, specimens were left overnight for the adhesive to cure. Laminates made with neat epoxy, 1 and 3 wt% I.30E clay and 1, 3 and 5 wt% M52N block-copolymer modified epoxy were processed by following the procedures mentioned in the preceding sections.

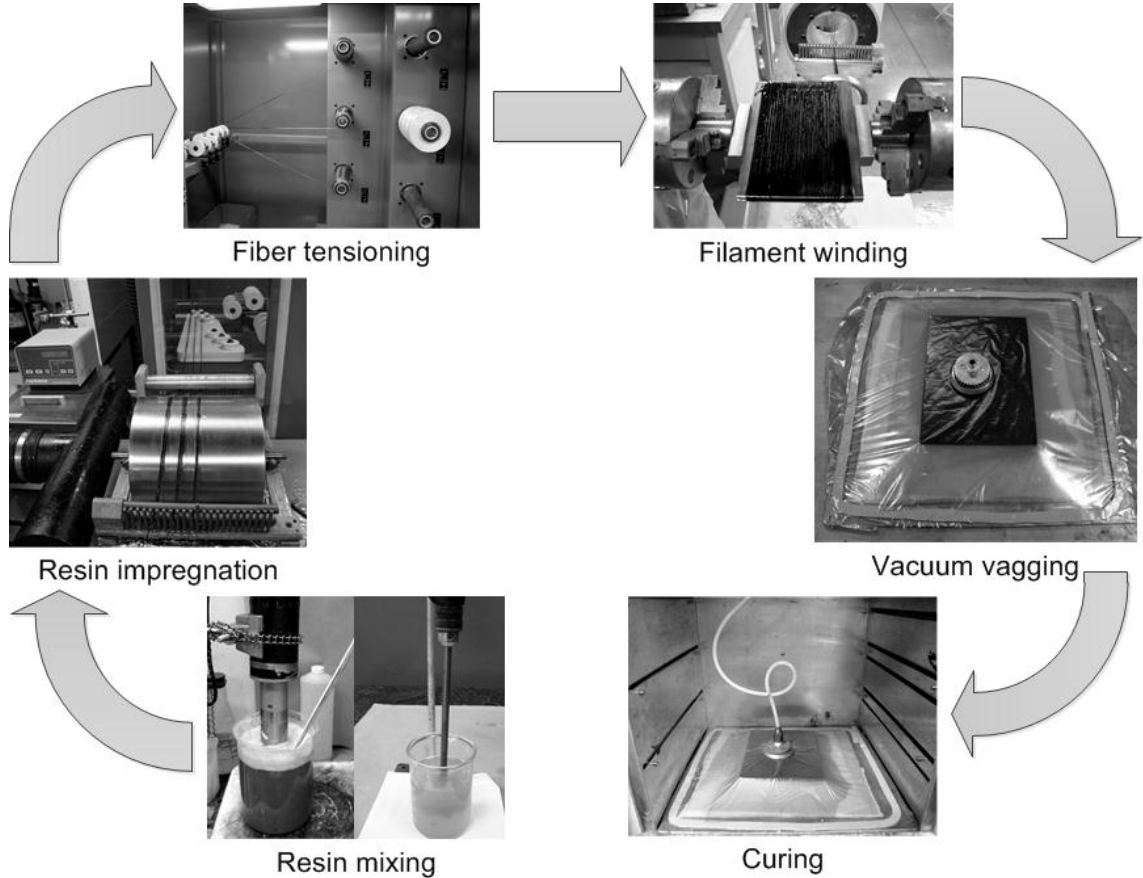


Figure 2.9 A schematic of the processing steps for fiber-reinforced epoxy nanocomposites.

2.2.6 Nanocomposite Pipe Fabrication

Filament-wound basalt fiber-reinforced epoxy nanocomposite tubes were fabricated, having various concentrations of either M52N or I.30E nanoparticles. Fiber-reinforced nanocomposite pipes were manufactured by pulling five continuous basalt fiber strands from their creels using the WMS 4-axis filament winding machine. The fiber rovings were impregnated with polymer resin by passing them through the drum-type resin bath before reaching the mandrel. Six layers of resin-wet fiber material were helical [$\pm 0^\circ$] wound successively onto a chrome-plated steel mandrel having a diameter and length of 38.1 mm and 762 mm, respectively. The mandrel surface was coated with a layer of release agent Frekote® 770-NC before initiation of the winding process. Throughout the manufacturing process a numerically controlled tensioning system steadily applied 26.7 N tension to each fiber strand. Curing of the specimens occurred at 80°C for one hour and 120°C for 2.5 hours, followed by cooling down to room temperature. Curing was performed in a digitally controlled industrial oven (Wisconsin Oven). The mandrels located in the oven were connected with a drive system to allow constant rotation during curing, which promoted part roundness and even resin accumulation on the surface. Upon completion of the curing cycle the filament-wound tubular specimens were extracted from the mandrel. 190 mm long finished pieces were cut from the extracted part using a tile saw, and tube extremities were reinforced with aluminum end connections. The pipe ends were attached with aluminum end connections to protect the pipe extremities from damage due to gripping by the testing machine. The bonding surfaces of the aluminum end-tabs were roughened by sand blasting and subsequently cleaned with acetone. Aluminum end-caps were then adhesively bonded to the pipe specimen by using Scotch-Weld DP460 Off-White adhesive from 3M. A specimen schematic is shown in Figure 2.10, where dimensions are in mm. For mechanical testing, a rubber bladder liner was inserted inside each tubular specimen. The rubber bladder was designed to enable the assessment of functional as well as structural failure in the same experiment. Composite pipes were also fitted with two strain gauge rosettes aligned at the middle of the gauge section, assigned parallel and perpendicular to the tube axis. All specimens had a [$\pm 60^\circ$]₃T interwoven angle-ply fiber architecture, an inside diameter of 38.1 mm and a gage length of 90 mm. Figure 2.11 shows a test specimen with attached aluminum end connections.

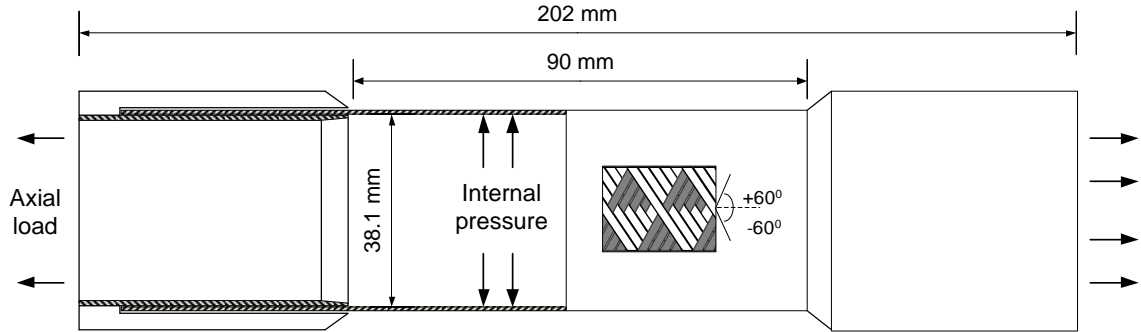


Figure 2.10 Tubular specimen geometry and fiber direction.



Figure 2.11 Tubular basalt fiber-reinforced epoxy/M52N composite specimens.

REFERENCES

1. Lee, H. and Neville, K., 1982. *HandBook of Epoxy Resins*. New York: McGraw Hill.
2. May, C.A. and Tanaka, Y., 1987. *Epoxy Resins Chemistry and Technology*. New York: Marcel Dekker.
3. Young, R.J. and Lovell, P.A., 2011. *Introduction to polymers*. Boca Raton: CRC press.
4. Salamone, J.C., 1996. *Polymeric Materials Encyclopedia*. New York: CRC press.

5. GERARD, P., BOUPAT, N.P., FINE, T., GERVAT, L. and PASCAULT, J.-P., 2007. Toughness properties of lightly crosslinked epoxies using block copolymers. *Macromolecular Symposia*, **256**, pp. 55-64.
6. MAIEZ-TRIBUT, S., PASCAULT, J.P., SOULÉ, E.R., BORRAJO, J. and WILLIAMS, R.J.J., 2007. Nanostructured epoxies based on the self-assembly of block copolymers: A new miscible block that can be tailored to different epoxy formulations. *Macromolecules*, **40**(4), pp. 1268-1273.
7. MERTINY, P., JUSS, K. and EL GHAREEB, M.M., 2009. Evaluation of glass and basalt fiber reinforcements for polymer composite pressure piping. *Journal of Pressure Vessel Technology, Transactions of the ASME*, **131**(6), pp. 0614071-0614076.
8. Starting formulation 8023, Resin system for filament winding and RTM, Momentive.
9. Xidas P. I., Triantafyllidis K. S.: Effect of the type of alkylammonium ion clay modifier on the structure and thermal/mechanical properties of glassy and rubbery epoxy-clay nanocomposites. *European Polymer Journal*, 46, 404-417 (2010).
10. Technical data, Lit. T-12, Nanocomposites using Nanomer® I.28E nanoclay, Nanocor.
11. Technical data, Lit. T-11, Epoxy nanocomposites using Nanomer® I.30E nanoclay, Nanocor.
12. Technical data, Lit. G-105, Polymer grade montmorillonites, Nanocor.
13. Material safety data sheet, NANOSTRENGTH® M52N NP, Arkema.
14. Product technical information, KV12, Kamenny Vek.
15. BALAKRISHNAN, S., START, P.R., RAGHAVAN, D. and HUDSON, S.D., 2005. The influence of clay and elastomer concentration on the morphology and fracture energy of preformed acrylic rubber dispersed clay filled epoxy nanocomposites. *Polymer*, **46**(25), pp. 11255-11262.
16. BROWN, J.M., CURLISS, D. and VAIA, R.A., 2000. Thermoset-layered silicate nanocomposites. Quaternary ammonium montmorillonite with primary diamine cured epoxies. *Chemistry of Materials*, **12**(11), pp. 3376-3384.
17. MEIJER, G. and ELLYIN, F., 2008. A Failure envelope for $\pm 60^\circ$ filament wound glass fibre reinforced epoxy tubulars. *Composites Part A*, **39**, pp. 555-564.

18. COHEN, D., MANTELL, S.C. and ZHAO, L., 2001. The effect of fiber volume fraction on filament wound composite pressure vessel strength. *Composites Part B:Engineering*, **32**(5), pp. 413-429.
19. MERTINY, P. and ELLYIN, F., 2001. SELECTION OF OPTIMAL PROCESSING PARAMETERS IN FILAMENT WINDING. *33rd International SAMPE Technical Conference 2001*, pp. 1084-1095.
20. WOLODKO, J., MERTINY, P., MEIJER, G., MARTENS, M. and ELLYIN, F., 2001. Development of a facility for filament winding GFRP tubulars, *46th International SAMPE Symposium and Exhibition 2001 a Materials and Processes Odyssey, May 6, 2001 - May 10, 2001*, Soc. for the Advancement of Material and Process Engineering, pp. 1271-1282.

Chapter 3

Characterization and Testing Methods of Nanocomposites

SYNOPSIS: Different characterization and testing methods were employed to provide insight into the material behavior of the nanocomposites. Design of experimental procedures, suitable testing regimes and data reduction schemes were developed allowing for the determination of material properties from a minimum number of tests. An array of advanced characterization and testing equipment were employed to perform the experimental study. Data acquisition, data analysis and data validation were done accordingly. Microstructure, morphology, chemical, physical, thermal and mechanical properties of the nanoparticles, polymers and nanocomposites were measured according to established design methodologies and standard test methods. Morphology and nanostructure of the nanoparticles and nanocomposites were examined by X-ray diffraction and various microscopic techniques. Chemical and physical analyses of the epoxy nanocomposites were done with Fourier transform infrared spectroscopy and differential scanning calorimetry. Final properties of the developed nanocomposites were evaluated with standard tensile testing, dynamic mechanical thermal analysis, mode-I fracture toughness testing and mode-I interlaminar testing. A multiaxial testing machine specially built for the assessment of fluid leakage and burst failures allowed determination of failure strengths of the pressurized composite tubulars.

3.1 X-RAY DIFFRACTION

Wide angle X-ray diffraction (WAXD) or simply X-ray diffraction (XRD) is a method of characterizing materials by knowing their atomic arrangement and crystal structure. Crystals are atomic structures that are ordered in a periodic manner. Using X-ray scattering principle, spacings of different imaginary atomic planes (d -spacing) of a crystal structure can be determined by Bragg's law as the distance between the diffracting planes. In this technique an incident beam of X-rays strikes a specimen placed on the

goniometer, which is simultaneously rotated allowing the angle of incidence to be varied. The incident X-rays are primarily scattered by the electrons of the sample's atom. A diffraction pattern is developed through constructive interference of the scattered X-rays. The detected interference pattern is then converted to provide useful information regarding structure of the material, i.e. scattering intensity as a function of diffraction angle (2θ). A wide-angle X-ray diffraction study of the epoxy-clay and hybrid nanocomposites was performed by Rigaku Geigerflex 2173 (Rigaku Corporation, Tokyo, Japan) diffractometer with a vertical goniometer. The diffractometer is fitted with a Co-tube as an X-ray source and a graphite monochromator to filter K-beta wavelength. Tests were run at 40 kV and 30 mA, and the samples were scanned between $2\theta = 1$ to 30° by changing the angle of incidence at a rate of $0.008\ 2\theta\text{sec}^{-1}$. XRD traces were analyzed to measure the basal spacing between the silicate layers. Figure 3.1 shows an XRD spectrum of organically modified I.30E nanoclay. In this figure a prominent peak can be seen that provided information about the interlamellar spacing of nanoclay, d_{001} according to Bragg's law [1].

$$d_{00n} = n\lambda / (2\text{Sin}\theta_0) \quad (3.1)$$

where n is an integer, $\lambda = 0.17889$ nm is wavelength of X-ray beam (Co/K-alpha1 radiation) and θ_0 is the angle of incidence.

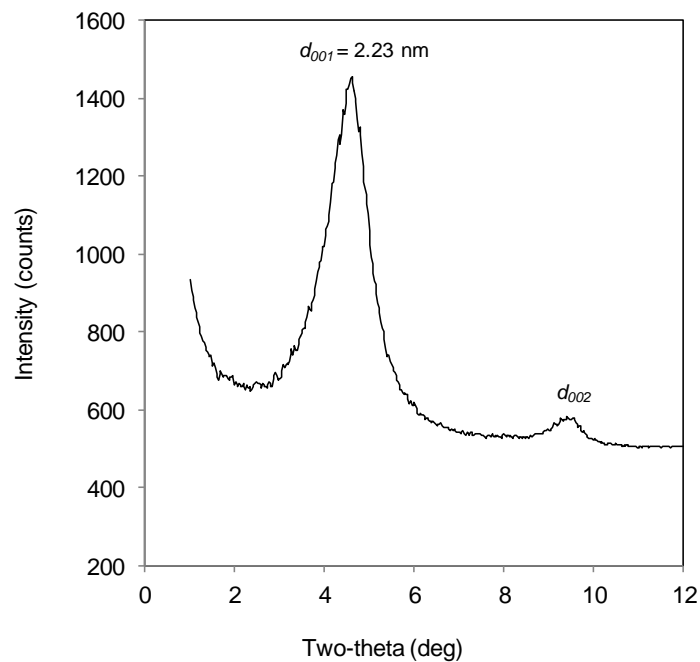


Figure 3.1 X-ray diffraction trace of I.30E organoclay.

3.2 TRANSMISSION OPTICAL MICROSCOPY

Transmission optical microscopy (TOM) is a light-optical microscopy method in which visible light penetrates an optically transparent thin sample and passes through a lens to produce a magnified image of the specimen.

Thin sections (5~10 μm) of the epoxy nanocomposite fracture surface were investigated by transmission optical microscopy. To prepare the thin sections, nanocomposite blocks were first placed in a Reichert-Jung Ultracut E (C. Reichert Optische Werke AG, Vienna, Austria) microtome and sectioned with a diamond cutter. These sections represent an area near the starter crack taken normal to the fracture surface and parallel to the crack propagation direction. The subsurface birefringent zone was explored under bright field and between cross polarizers using a Leica DMRXA (Leica Microsystems, Wetzlar, Germany) microscope directly connected to a Nikon DXM 1200 (Nikon Corp., Tokyo, Japan) digital camera. Figure 3.2 shows a thin layer of an epoxy sample viewed under transmission optical microscopy.

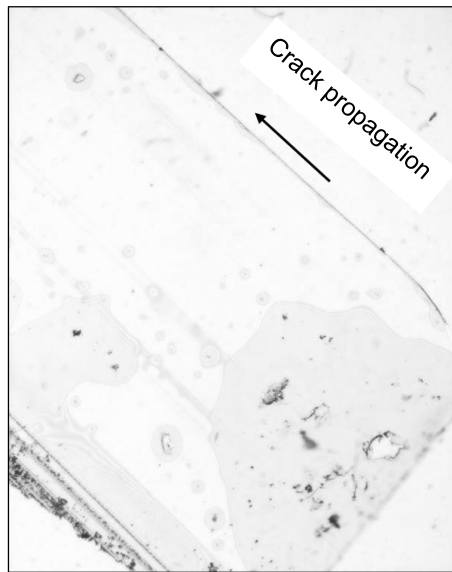


Figure 3.2 TOM image of modified epoxy containing 1 wt% M52N block-copolymer.

3.3 TRANSMISSION ELECTRON MICROSCOPY

In transmission electron microscopy (TEM) a beam of high-energy electrons is transmitted through an ultrathin ($<0.5 \mu\text{m}$) specimen. The transmitted electrons are

focused with a sequence of electromagnetic lenses, and images are recorded with an appropriate imaging device at a very high resolution. TEM is based on the same concept as transmission optical microscope [2].

In the present study, TEM offered direct visualization of the nanocomposite morphology. Information regarding size and structure of nanoparticles, particle distribution and degree of dispersion in a matrix material can be obtained from TEM. Microstructure of the cured epoxy nanocomposites was examined in a Morgagni 268 (FEI, Hillsboro, Oregon, USA) transmission electron microscope with an acceleration voltage of 80 kV. This device has a magnification of up to 200,000x. 40~60 nm thin sections were prepared by a Reichert-Jung Ultracut E microtome equipped with a diamond knife. Ultrathin sections were then laid onto 300 mesh copper grids and placed inside the TEM for scanning. Some of the composite samples containing M52N block-copolymer were allowed to stain overnight in 4% osmic acid (OsO_4). Figure 3.3 exhibits intercalated clay structures and block-copolymer vesicles in epoxy matrices.

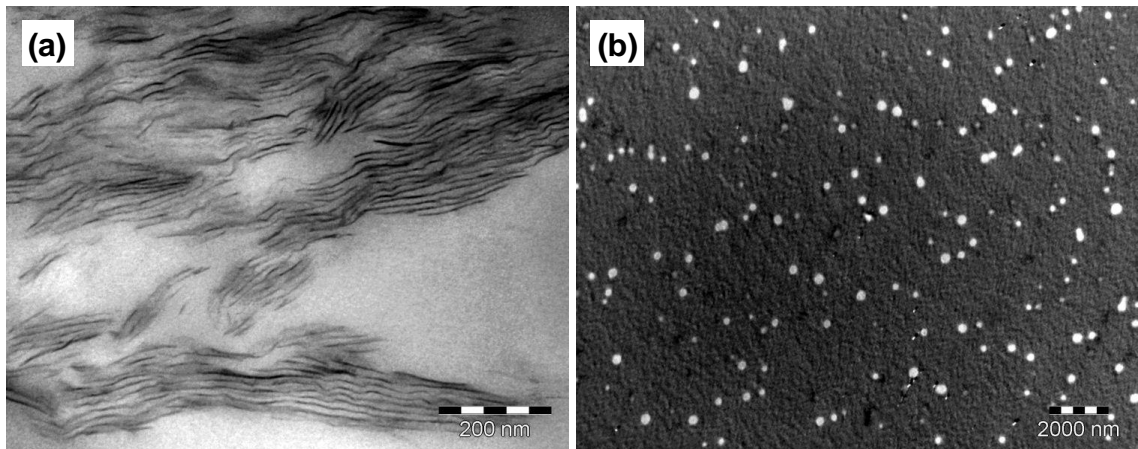


Figure 3.3 TEM microscopy images of (a) 1 wt% nanoclay and (b) 3 wt% block-copolymer modified epoxy.

3.4 SCANNING ELECTRON MICROSCOPY

Scanning electron microscopy (SEM) is a microscopy method that uses a beam of accelerated electrons to scan a sample surface [2]. The interaction of the incident electron beam with the specimen resulted in ejection of secondary electrons, backscattered electrons, transmitted electrons, X-rays, visible light and heat. Commonly secondary and back-scattered

electrons and X-rays are collected by special detectors and converted to generate images revealing the sample surface morphology, chemical composition and crystal structure. To be effectively examined by SEM the material must be electrically conductive or the sample surface should be coated with a layer of conductive substance like carbon, gold or chromium. Some of the advantages of SEM compared to conventional optical microscopy are higher image resolution, larger depth of field and clarity. The principle and fundamentals of electron microscopy can be explored in more detail in reference [2].

Fracture surfaces of neat epoxy and the corresponding nanocomposites were probed by a JEOL 6301F field emission scanning electron microscope (JEOL Ltd., Tokyo, Japan). Scanning electron microscopy was performed on fracture surfaces of single edge notch bend (SENB) specimens at an acceleration voltage of 5 kV and 10kV respectively for the clay and M52N filled epoxy samples. Depending on the size of the nano-inclusions and the type of constituents to be examined a conductive coating was applied on the sample surfaces. Fracture surfaces of epoxy-clay nanocomposites and M52 modified epoxy was coated with gold, while chrome was applied on the fracture surface of M52N toughened epoxy. The fracture surface of the laminate plates was carbon coated before being inspected by SEM. The JEOL 6301F SEM can generate high magnification images of up to 250,000x, thus allowing inspection of the nano-level surface features to a resolution of about ~3 nm. Figure 3.4 shows SEM micrographs of the modified epoxy fracture surfaces. Sub-micron size intercalated clay and cavities formed by pulled out block-copolymer vesicles are visible on the modified epoxy fracture surfaces of Figure 3.4.

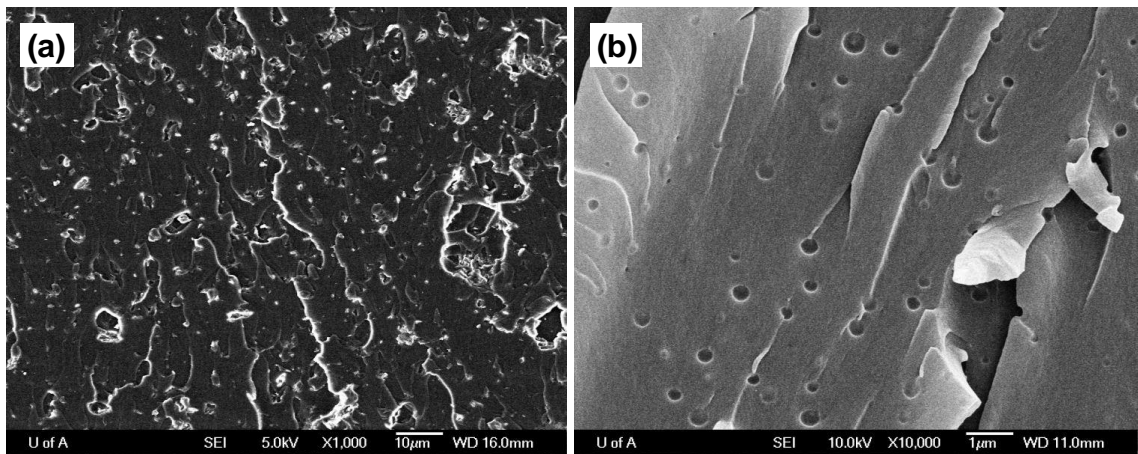


Figure 3.4 SEM microscopy images of (a) 3 wt% nanoclay and (b) 3 wt% block-copolymer modified epoxy.

3.5 DIFFERENTIAL SCANNING CALORIMETRY

Thermal analysis of the epoxy nanocomposites was performed by differential scanning calorimetry (DSC). In this method changes in the temperature of a material are measured in response to heat flow. The analysis provides information regarding thermal transitions occurring in a material associated with changes in the physical and chemical processes (melting, crystallization, polymerization reaction, glass transition temperature, etc.) [3]. Any endothermic or exothermic enthalpy changes or variations in heat capacity of a substance can be quantitatively and qualitatively determined by differential scanning calorimetry.

In a typical DSC experiment, the specimen and a reference material are heated or cooled separately at the same temperature in identical conditions and at a specified rate under controlled (e.g. nitrogen) environment. Alternatively, the materials can be heated simultaneously using a single heater at a predefined rate and continuously monitoring their temperature differences. Figure 3.5 illustrates the major parts of a DSC instrument. The differential heat input or differential temperature measurement data of a sample relative to the reference sample reveals thermal events that have taken place in the material. The variations in the rate of energy change correspond to the change of state/phase transition of the material. In an amorphous material a significant change in the specific heat capacity is representative of the glass transition temperature of the sample. In the recorded DSC data a sudden step change in the baseline value represents the glass transition of the material. At this transition, the supplied thermal energy causes the polymer to transform from a glassy to a rubbery state due to enhanced molecular motion. The glass transition can be explained by the free volume (i.e. the empty spaces between polymer molecules) concept. As the temperature increases, the free volume also increases in a polymer and entails molecules more mobility to change their conformation [3].

Differential scanning calorimetry was performed on a model Q100 DSC (TA Instruments, New Castle, Delaware, USA) to measure the glass transition temperature (t_g) of cured epoxy samples. Sample weights varied between measurements from 3.9 to 12.6 mg. Measurements were carried out at a heating rate of 4°C/min between the temperature range from 25°C to 200°C under nitrogen environment. The machine was first equilibrated at 25°C, after which the measurement process was composed of three cycles:

ramping up to 200°C and holding at an isothermal condition for 5 min; ramping down to 0°C followed by an isothermal process for 5 min; and finally, ramping up to 200°C, which signifies the end of the measurement process. Data presented in this study were derived from the third cycle. The glass transition temperature was estimated as the midpoint of the heat flow transition in the thermogram. Figure 3.6 shows a DSC thermogram revealing the glass transition temperature of neat epoxy approximately 117°C.

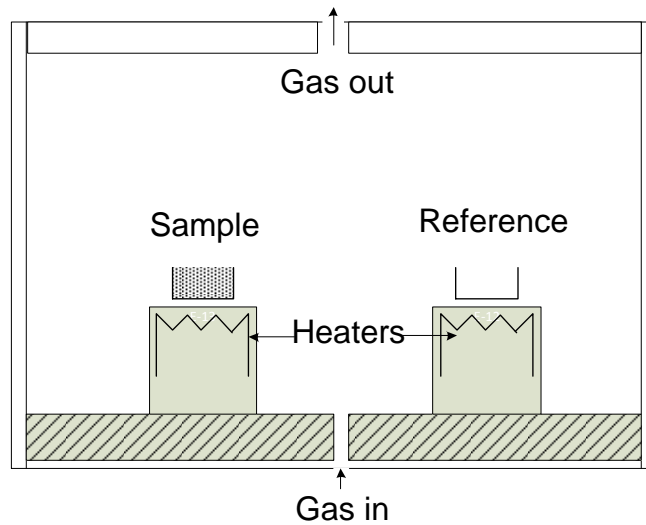


Figure 3.5 Schematic of a DSC instrument.

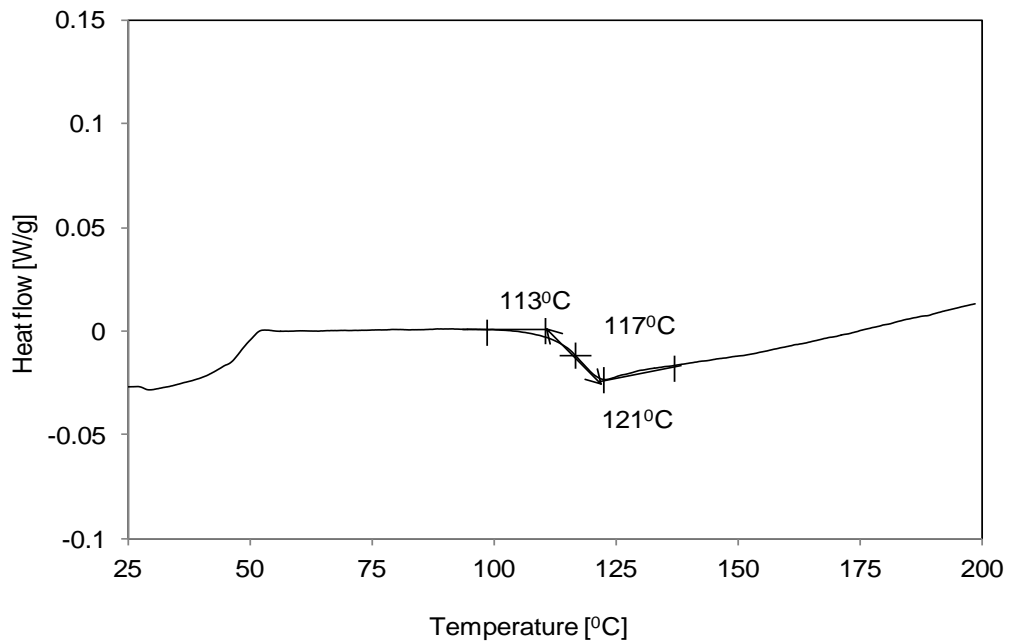


Figure 3.6 DSC trace of cured neat epoxy sample (EPON 826/EPIKURE 9551).

3.6 FOURIER TRANSFORM INFRARED SPECTROSCOPY

Fourier transform infrared (FTIR) spectroscopy is a method that involves the absorption/emission of infrared radiation of the electromagnetic spectrum by a material (i.e. solid, liquid or gas). IR spectroscopy can identify the chemical structure in a compound and provides information pertaining to its compositions, chemical bonds, functional groups and degree of branching. Molecules are composed of atoms that are constantly vibrating. The absorption of infrared radiation occurs when the frequency of vibrating atoms in a molecule equals the frequency of infrared radiation. The absorption of specific IR radiation by a molecule can therefore be associated with its molecular structure. A particular molecule can have many different vibrational modes (e.g. symmetric or asymmetric stretching and in plane or out of plane bending), but absorption only takes place for vibrations that cause an oscillating dipole moment [3]. In principle, the Fourier transform method generates absorbance or transmittance spectra from the recorded scans done on the sample with an infrared light for the specified wavelength range. The frequency of electromagnetic radiation is directly related to energy. The energy of a photon can be expressed by Planck's equation [3].

$$E_0 = h\nu_0 = hc\bar{\nu} \quad (3.2)$$

where h is the Planck's constant (6.626×10^{-34} J.s), c is the velocity of light (2.998×10^8 m/s), ν_0 is the frequency of radiation and $\bar{\nu}$ is the wavenumber, which is reciprocal of the wavelength of radiation.

FTIR was performed at a Nicolet Magna 750 FTIR spectrometer (Nicolet Instrument Corporation, Madison, Wisconsin, USA) connected to a Nic-Plan microscope. Infrared spectra of neat epoxy and epoxy blends containing certain weight fraction of block-copolymer were acquired. Cured epoxy specimens were placed onto a KBr plate and run at a resolution of 4 cm^{-1} . About 32 scans were performed for each sample. The specimen surfaces were initially smoothed before placing on the KBr plate. Figure 3.7 shows the IR spectrum of neat epoxy after curing. In the FTIR spectrum the infrared radiation is expressed by the wavenumber between 650 cm^{-1} and 4000 cm^{-1} . The following characteristic absorption bands are identified from infrared spectrum [4-5]. The O-H stretching vibration band is specified in the region of $3200\text{-}3600 \text{ cm}^{-1}$, which is centered at 3411 cm^{-1} . Stretching vibration bands of methyl and methylene (C-H) groups occur at

2963, 2928 and 2870 cm^{-1} . The C=O stretching absorption peak is found at 1709 cm^{-1} . Absorption bands at 1607, 1581 and 1508 cm^{-1} are suggestive of aromatic (C=C) stretching vibration. The absorption band at 1104 cm^{-1} can be assigned to C-N stretching. Stretching vibration bands of aromatic and aliphatic ethers (C-O-C) are specified at 1245 and 1035 cm^{-1} , respectively. Out of plane bending of a *p*-substituted phenyl ring is represented by 827 cm^{-1} band. Spectral data further reveals the disappearance of the characteristic absorption peaks 3056 (stretching) and 915 cm^{-1} (bending) bands [5] associated with the epoxy group as a result of the epoxy curing reaction.

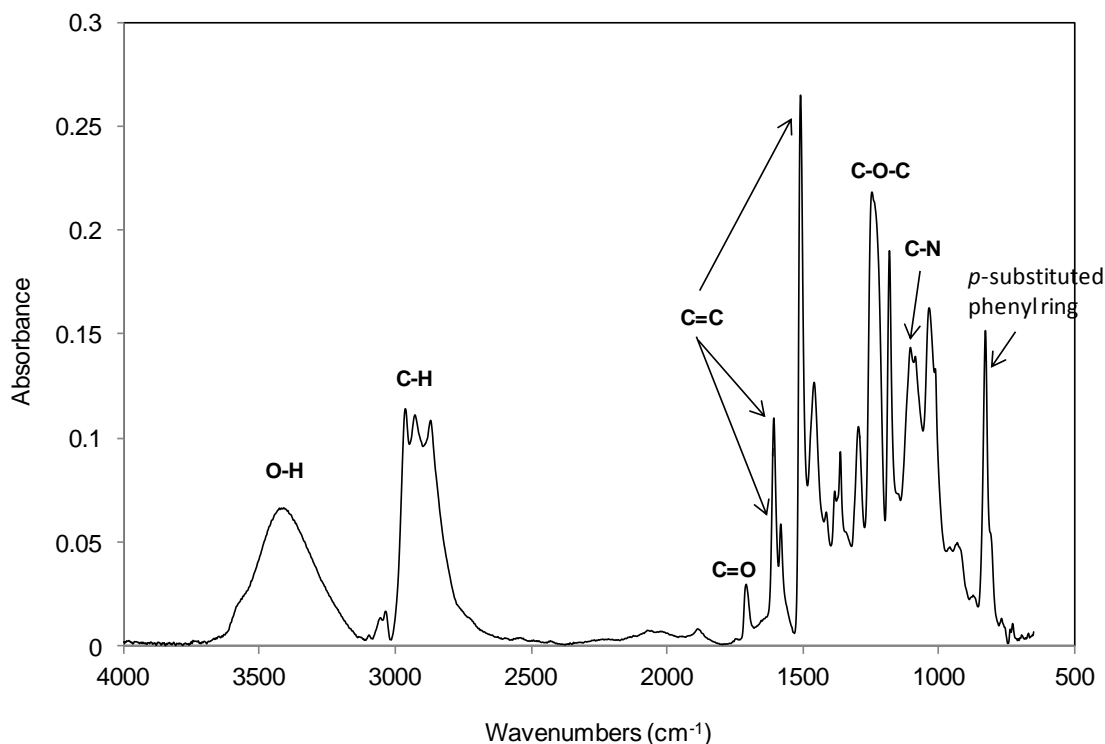


Figure 3.7 FTIR spectrum of cured neat epoxy (EPON 826/EPIKURE 9551).

3.7 DYNAMIC MECHANICAL THERMAL ANALYSIS

The viscoelastic properties of a polymer can be characterized by dynamic mechanical analysis. If a viscoelastic material is subjected to variable loading by an oscillating sinusoidal force (stress σ), it is known that the resultant displacement response (strain ε) will be out of phase (i.e. phase lag) to the stress [3, 6]. The conditions can be expressed as follows [3].

$$\sigma = \sigma_0 \sin(\omega t + \delta) \quad (3.3)$$

$$\varepsilon = \varepsilon_0 \sin \omega t$$

where ω is the angular frequency, t is the time and δ is the phase lag. The out of phase and in phase components of stress can be used to determine the complex modulus of a material, that is, the storage modulus, $E_s = (\sigma_0/\varepsilon_0)\cos\delta$, and the loss modulus, $E_l = (\sigma_0/\varepsilon_0)\sin\delta$, which represent the elastic and viscous energy portions, respectively. The $\tan\delta$ provides information on the damping behavior of the material. A schematic diagram of a dynamic mechanical thermal analysis (DMTA) system, loading mode and specimen geometry are shown in Figure 3.8.

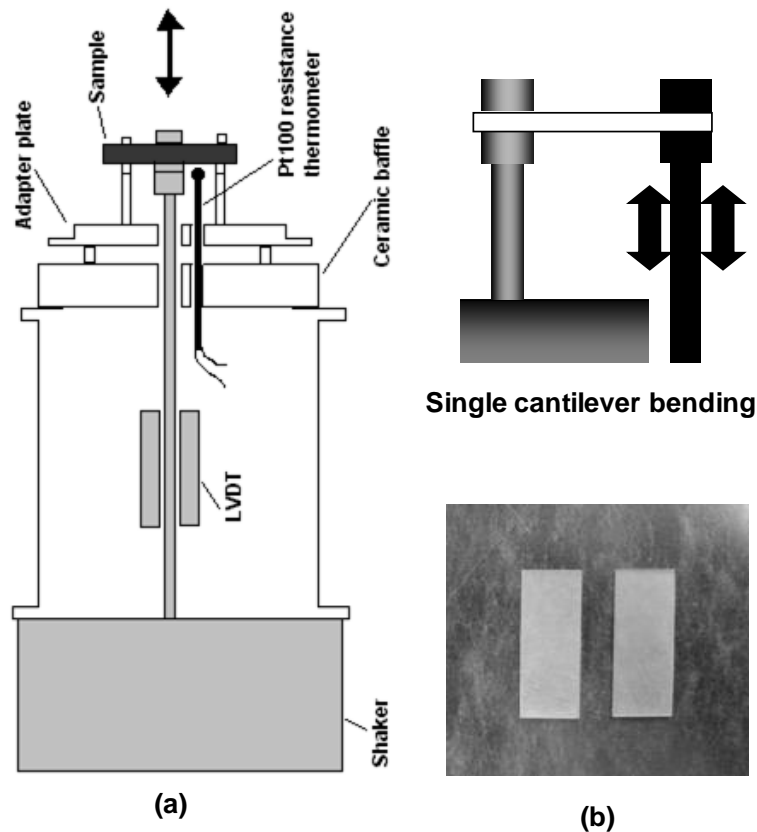


Figure 3.8 (a) A schematic of the DMA 8000 instrument and mode of testing [7] and (b) epoxy specimens used for DMTA analysis.

Dynamic mechanical thermal analysis of fully cured epoxy samples was performed on a DMA 8000 dynamic mechanical analyzer (PerkinElmer, Waltham, Massachusetts, USA). The present study involved two separate testing procedures to measure the stiffness and

damping behavior of the neat and filled epoxy. In one method the specimen stiffness as a function of modulus and geometry was measured at a constant frequency in an isothermal condition. In another approach the specimen temperature was varied while maintaining a constant frequency. The DMTA experiments were performed under single cantilever bending mode of the DMA 8000 analyzer having a working stiffness range of 2×10^2 to 1×10^8 N/m. Measurements were done at a heating rate of $5^\circ \text{C}/\text{min}$ over a temperature range of 25°C to 150°C . During the tests an oscillatory displacement with an amplitude of 0.05 mm was applied at a fixed frequency of 1 Hz. A specimen dimension of 20 by 8 by 1 mm was chosen according to standard ASTM D 4065-06 [8]. The dynamic storage modulus and glass transition temperature were determined. The glass transition was taken as the peak position representing a prominent change in the $\tan \delta$ curve. At this temperature the polymer chains acquired sufficient mobility to move past each other. Figure 3.9 shows a typical DMTA curve. From this plot the glass transition temperature and storage modulus (at room temperature) were estimated as 122°C and 2.41 GPa, respectively.

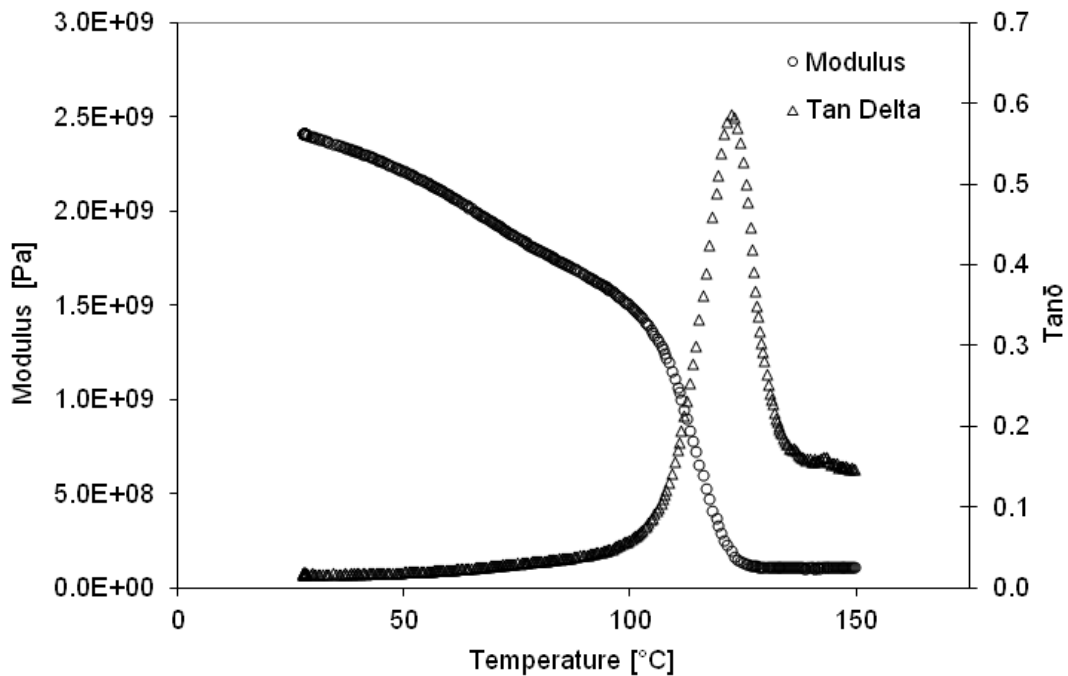


Figure 3.9 DMTA analysis showing storage modulus and $\tan \delta$ curves of modified epoxy containing 5 wt% M52 block-copolymer.

3.8 TENSILE TEST

Uniaxial tensile testing was conducted using dog-bone specimens by conforming to the procedure mentioned in the standard ASTM D 638-03 [9]. A representative schematic of the tensile test specimen is shown in Figure 3.10. Tensile testing was performed on a MTS 810 (MTS Systems Corporation, Eden Prairie, Minnesota, USA) universal testing machine, having MTS 647 axial hydraulic wedge grips and a Teststar™ IIs controller. The MTS machine has a maximum dynamic and static force capacity of 100 and 120 kN, respectively [10]. Samples were tested either under load or under displacement control mode. Under load control conditions a constant loading rate of 4.5 N/s was applied, and the load cell was adjusted for a maximum load of 4.5 kN before sample failure. For the given samples this loading rate is equivalent to an initial displacement rate of $\sim 5 \times 10^{-3}$ mm/s, but increases as testing progresses. This loading rate was chosen in accordance with testing done on the same epoxy system by previous researchers [11-12]. Some samples were tested also at stroke control condition at 8.33×10^{-3} mm/s, which corresponds to an initial loading rate of ~ 11 N/s that decreases with time. During mounting in the hydraulic gripping system, vertical alignment of the specimen was carefully adjusted. A MTS 634.12E-24 axial extensometer was attached to the specimen by MTS Quick-Attach springs. Model 634.12E-24 has a gauge length of 25 mm and maximum strain range of -10% to 50%. To protect the specimen from extensometer knife edge penetration, small pieces of cloth were bonded at the point of contact to the specimen using M-Bond strain gauge adhesive. The force, displacement and auxiliary strain signals were acquired. In this study true tensile stress and tensile strain at break were determined from Equation (3.4).

$$\bar{\sigma} = \sigma(1 + \varepsilon) \quad (3.4)$$

$$\bar{\varepsilon} = \ln(1 + \varepsilon)$$

where σ and ε are the engineering stress and strain, respectively. The modulus was estimated from the slope of the linear section of the stress-strain curve. Figure 3.11 shows the MTS 810 testing machine and few of the tested specimens. Slight differences in tensile test results were observed between two different loading conditions. For neat epoxy the average modulus, tensile strength and strain at break were estimated to be 2.82 GPa, 82.2 MPa and 8.53 % and 2.88 GPa, 73.3 MPa and 8.5 % respectively from the load

and displacement control tests. Material yielding was observed in the displacement control test. This behavior is reflective of the viscoelastic nature of the polymer due to the strain rate dependency as shown in the true stress-strain curves of Figure 3.12. A previous study done with the same EPON 826/ EPIKURE 9551 epoxy system demonstrated its nonlinear viscoelastic behavior that is dependent on the loading rate [13]. Any discretion regarding the viscoelastic nature of the present epoxy system was not made, as it was not the intension of this study. Though, the differences in resin property between the two test methods were obvious, but can be regarded negligible, for example variation in modulus was about 2%. To be consistent in the use of tensile test results, the load control test data were used throughout this thesis and stroke control results were limited in use only to the study of epoxy hybrid nanocomposites.

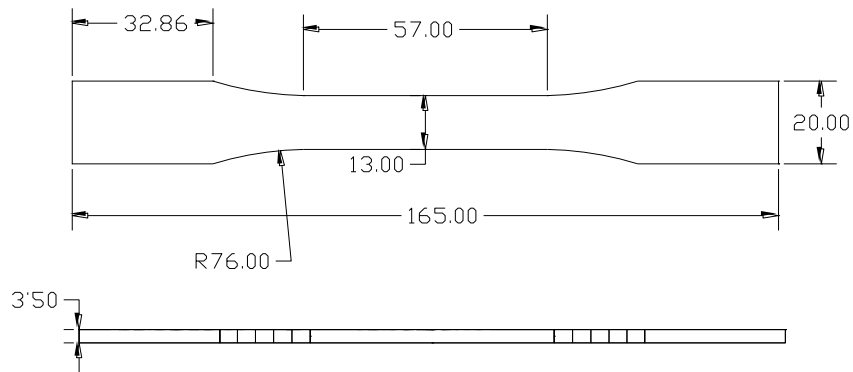


Figure 3.10 Geometry of the tensile test specimen (dimensions in millimeters).

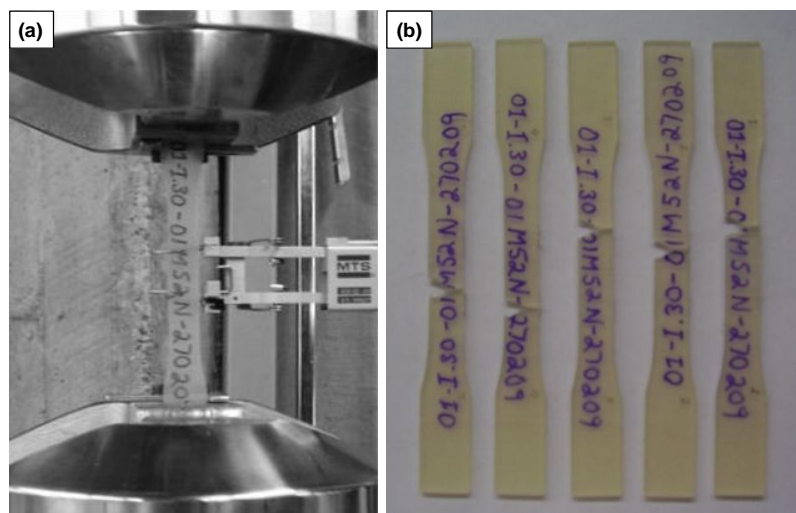


Figure 3.11 (a) Tensile testing setup and (b) failed specimens after tensile testing.

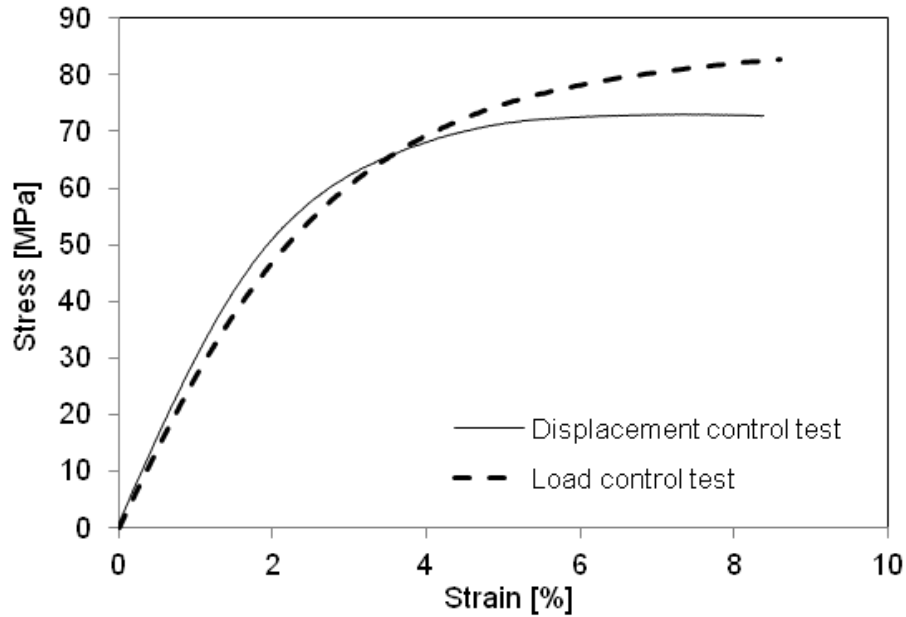


Figure 3.12 Typical stress-strain response of the neat epoxy sample (EPON 826/EPIKURE 9551).

3.9 MODE-I FRACTURE TOUGHNESS TEST

Plane-strain fracture toughness tests were performed according to the standard ASTM D5045-99 to determine fracture toughness, K_{IC} , and strain energy release rate, G_{IC} , of the nanocomposite samples [14]. The single edge notch bend (SENB) geometry (see Figure 3.13) was chosen, and testing was performed on a MTS 810 universal testing machine by three-point bending. It is known that the fracture toughness of a material is dependent on the testing rate and temperature [15]. In this study all the tests were done at room temperature with a crosshead speed of 0.2 mm/min.

Two methods were chosen to pre-crack specimens prior to the testing (see Figure 3.14). In the first method a single-sided razor blade was attached to a previously designed jig (please refer to reference [12]), and mounted onto the MTS machine. A SENB specimen was then placed on a flat metal base stationed on the opposite arm of the MTS machine. The razor blade was then vertically inserted inside the machined notch and finally pressed down to a depth of 1 mm at the notch tip at a loading rate of 0.2 mm/min. This generated a blunt crack as shown in Figure 3.15(a). The blunt crack length was kept to a minimum, i.e. not deeper than 1 mm, because further penetration of the razor blade generated a wedge like motion at

the notch walls resulting in specimen failure. The second method involved inserting and repeatedly tapping a razor blade with a hammer into the machined notch, which created a natural sharp crack (see Figure 3.15 (b)). Attempts to generate a sharp crack by fatigue pre-cracking was unsuccessful and resulted in either no crack or complete specimen failure. The crack length was measured by a Zeiss optical microscope at 50x magnification from post-failure fracture surfaces. The average crack length was derived from three measurements done at two positions near the sides and one at the middle of the specimen. The following validity criteria were satisfied by each specimen for dimensional requirements to meet the plane-strain condition and to prevent significant plastic deformation in the ligaments.

$$B, a, (W - a) > 2.5 \left(\frac{K_I}{\sigma_{ys}} \right)^2 \quad (3.5)$$

where B is the specimen thickness, a is the overall crack length, W is the specimen width, stress intensity K_I is the conditional or trial fracture toughness and σ_{ys} is the yield stress considered as the maximum failure load in a uniaxial tensile test (under load control test condition). Also, the following geometric conditions were satisfied for sample width, $W=2B$; crack length, $0.45 < a/W < 0.55$; support span distance, $S=4W$. The three-point bending test fixture with a loaded specimen is shown in Figure 3.16, in which the stationary bottom support spans are equally spaced from the point of application of the imposed loading. The applied load and load-point displacement were recorded directly from the load and displacement transducers of the MTS machine. Fracture toughness was calculated according to linear elastic fracture mechanics from the following formulae [14].

$$K_I = \left(\frac{P}{BW^{1/2}} \right) f(x) \quad \text{with, } x = \frac{a}{W} \quad (3.6)$$

$$f(x) = 6x^{1/2} \frac{[1.99 - x(1-x)(2.15 - 3.93x + 2.7x^2)]}{(1+2x)(1-x)^{3/2}}$$

where P is the maximum load at failure and $f(x)$ is a shape factor. The strain energy release rate was determined from Equation (3.7).

$$G_Q = \frac{U}{BW\phi} \quad (3.7)$$

where U is the energy estimated by integrating the area under the load versus load-point displacement curve and the energy calibration factor ϕ can be expressed as.

$$\phi = \frac{A + 18.64}{\frac{dA}{dx}} \quad (3.8)$$

$$\text{where: } A = \left[\frac{16x^2}{(1-x)^2} \right] [8.9 - 33.717x + 79.616x^2 - 112.952x^3 + 84.815x^4 - 25.672x^5],$$

$$\begin{aligned} \frac{dA}{dx} = & \left[\frac{16x^2}{(1-x)^2} \right] [-33.717 + 159.232x - 338.8562x^2 + 339.26x^3 - 128.36x^4] \\ & + \left[\frac{32x}{(1-x)^3} \right] [8.9 - 33.717x + 79.616x^2 - 112.952x^3 + 84.815x^4 - 25.672x^5] \end{aligned}$$

An alternative to the above procedure is to use the equation, $G_{IC} = (1 - \nu^2)K_{IC}^2/E$; where E and ν are respectively the modulus and Poisson's ratio.

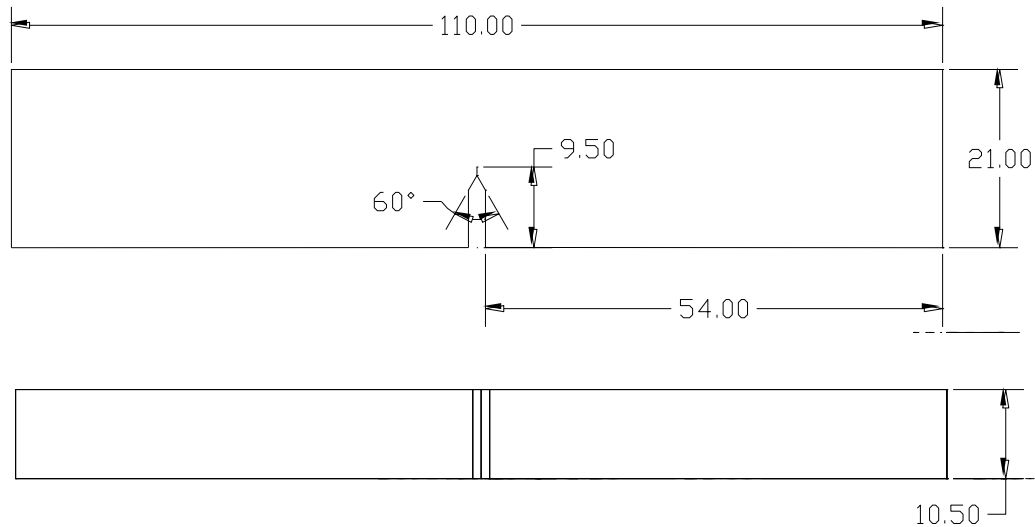


Figure 3.13 A schematic of the single edge notch bend specimen (dimensions in millimeters).

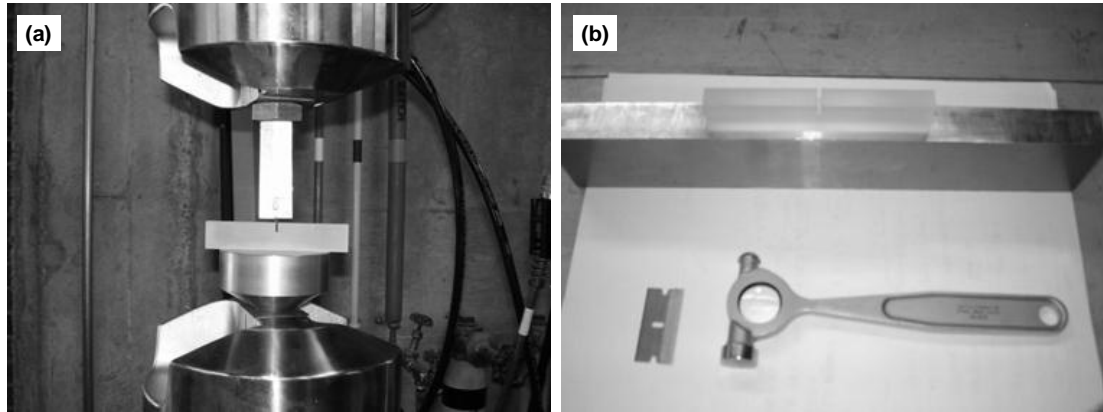


Figure 3.14 Pre-cracking arrangements for (a) blunt crack and (b) sharp crack.

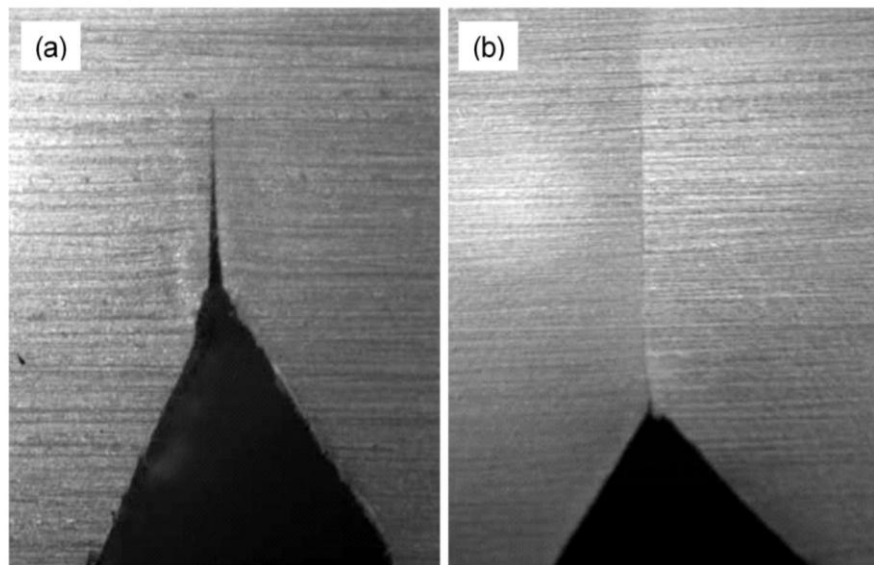


Figure 3.15 Pre-crack configurations: (a) blunt crack and (b) sharp crack.

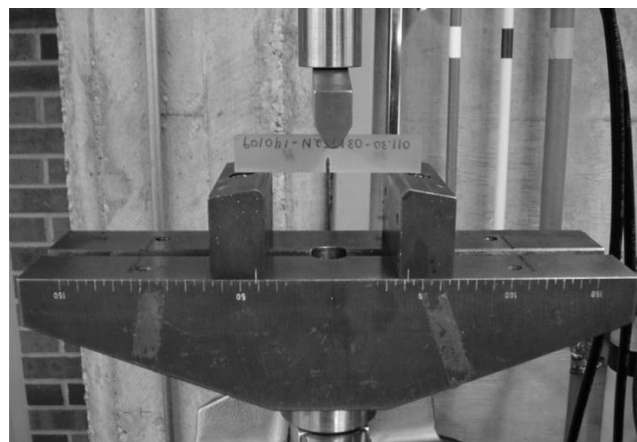


Figure 3.16 Mode-I fracture toughness testing of bulk epoxy nanocomposite.

3.10 MODE-I INTERLAMINAR FRACTURE TOUGHNESS TEST

The mode-I interlaminar fracture toughness, G_{IC} , of double-cantilever beam (DCB) specimens was estimated according to the ASTM D 5528-01 standard [16]. The specimen configuration is shown in Figure 3.17. The specimen thickness and initial delamination length were chosen to satisfy the following criteria specified in the ASTM standard.

$$a_0 \leq 0.042 \sqrt{\frac{h_0^3 E_1}{G_{IC}}} \quad (3.9)$$

$$h_0 \geq 8.28 \left(\frac{G_{IC} a_0^2}{E_1} \right)^{1/3}$$

where a_0 is the initial delamination length, h_0 specimen thickness and E_1 is the longitudinal lamina modulus estimated by strength of materials approach. All tests were performed under displacement control on the MTS 810 universal tester with a constant displacement rate. A specimen was mounted horizontally with both arms of the attached hinges gripped by the hydraulic wedge grips of the MTS machine. To visually measure crack propagation, starting from the insert film edge, one side of each specimen was marked at 1 mm increments for the first 5 mm and subsequently at 5 mm increments for the next 45 mm, see Figure 3.18. Initially, a 5 mm increase in the delamination length was allowed to grow from the edge of the starter film insert at a crosshead speed of 2.5 mm/min followed by unloading at a rate of 25 mm/min. Afterwards, the sample was delaminated to a length of 50 mm from the insert edge at a reloading speed of 2.5 mm/min, and subsequently unloaded at 5 mm/min. During the test, load and opening mode displacement values were recorded, see Figure 3.19 for a neat epoxy laminate. Delamination was visually observed and recorded in the load-displacement data points to measure the initiation value of G_{IC} as well to calculate the energy required for steady-state crack propagation. The strain energy release rate was determined using three different data reduction methods. According to the modified beam theory (MBT) the following formula was used to calculate the strain energy release rate.

$$G_{IC} = \frac{3P_1 \delta_1}{2b(a_1 + |\Delta|)} \quad (3.10)$$

where P_1 is the load, δ_1 is the load-point displacement, b is the specimen width, a_1 is the delamination length and Δ is the delamination correction factor determined as the x-axis intercept of the $C^{1/3}$ versus a_1 plot. The compliance, C , is defined as the ratio of the load-point

displacement to the applied load, δ_l/P_l (see Figure 3.20 (a)). As stated in the compliance calibration (CC) method the opening mode-I interlaminar fracture toughness was determined from the following expression.

$$G_{IC} = \frac{n_1 P_1 \delta_1}{2b a_1} \quad (3.11)$$

where n_1 is the slope of a least square plot of $\log(\delta_l/P_l)$ versus $\log(a_l)$ obtained by using the data points for the delamination onset and propagation values (see Figure 3.20 (b)). In accordance with the modified compliance calibration (MCC) method the mode-I interlaminar fracture toughness was calculated as follows.

$$G_{IC} = \frac{3P_1^2 C^{2/3}}{2A_1 b h_0} \quad (3.12)$$

where h_0 is the thickness of the specimen and A_1 is taken as the slope of a plot of a_l/h_0 with respect to the cube root of compliance $C^{1/3}$ (see Figure 3.20 (c)).

In this study, two crack initiation values were measured for each laminate. One of the crack initiation values, termed ‘NL’, represents the point at which nonlinearity in the load-displacement curve becomes apparent. The visually observed delamination initiation point, termed ‘VIS’, was taken as the point corresponding to a 1 mm crack extension through the laminate. In Figure 3.21, a delamination resistance curve was plotted with fracture energy values calculated from different methods. In the present study the modified beam theory method was ultimately chosen for estimating the mode-I interlaminar fracture toughness of fiber-reinforced laminates.

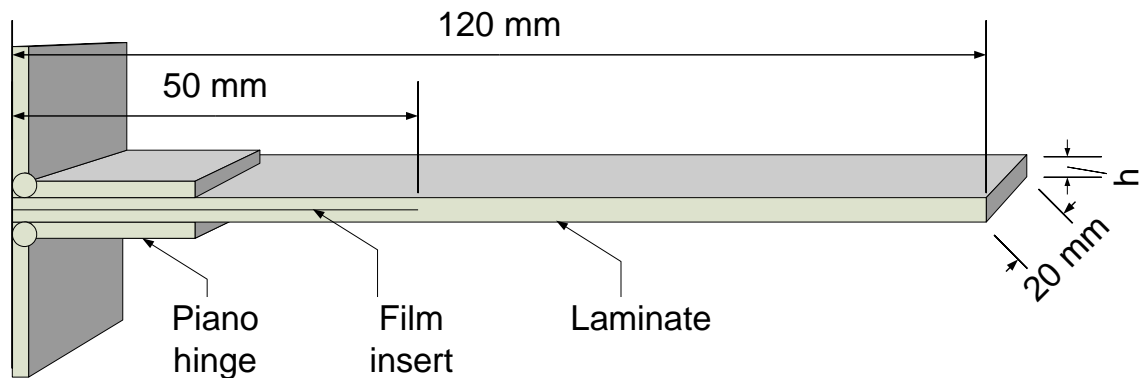


Figure 3.17 A schematic of the double-cantilever beam specimen.

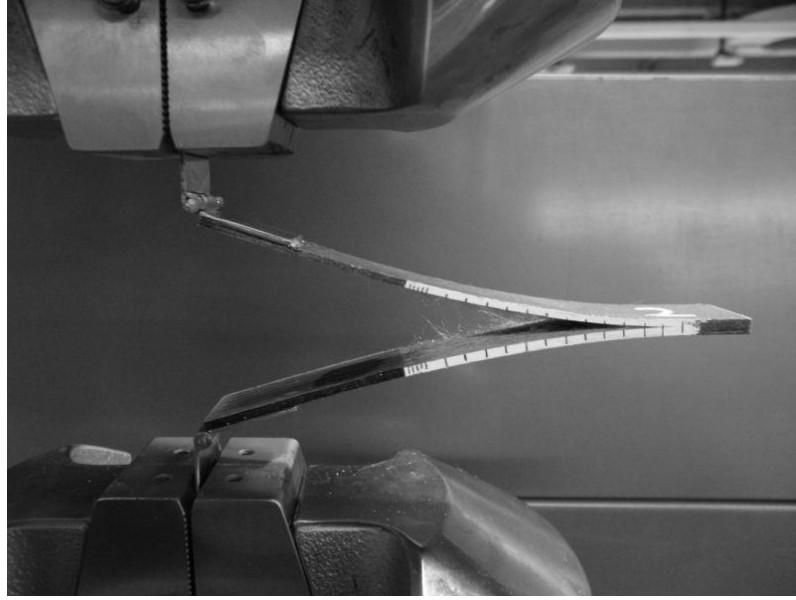


Figure 3.18 Mode-I interlaminar fracture toughness testing of fiber-reinforced nanocomposite laminates.

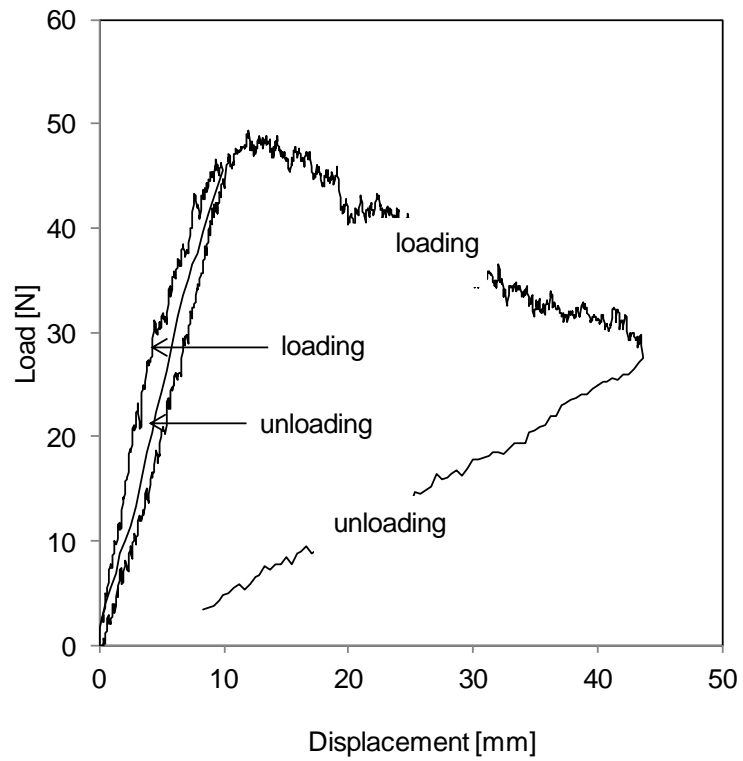


Figure 3.19 Load-displacement curves of the DCB test specimen (neat epoxy).

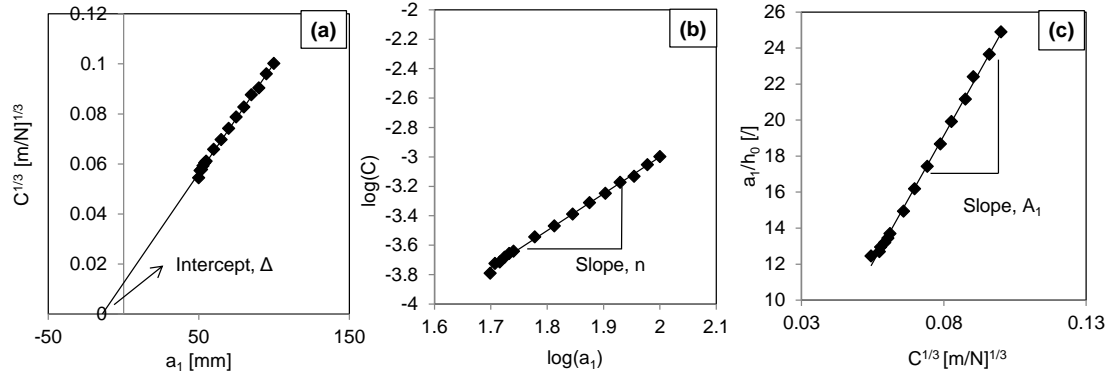


Figure 3.20 Data reduction procedures employed: (a) modified beam theory, (b) compliance calibration and (c) modified compliance calibration.

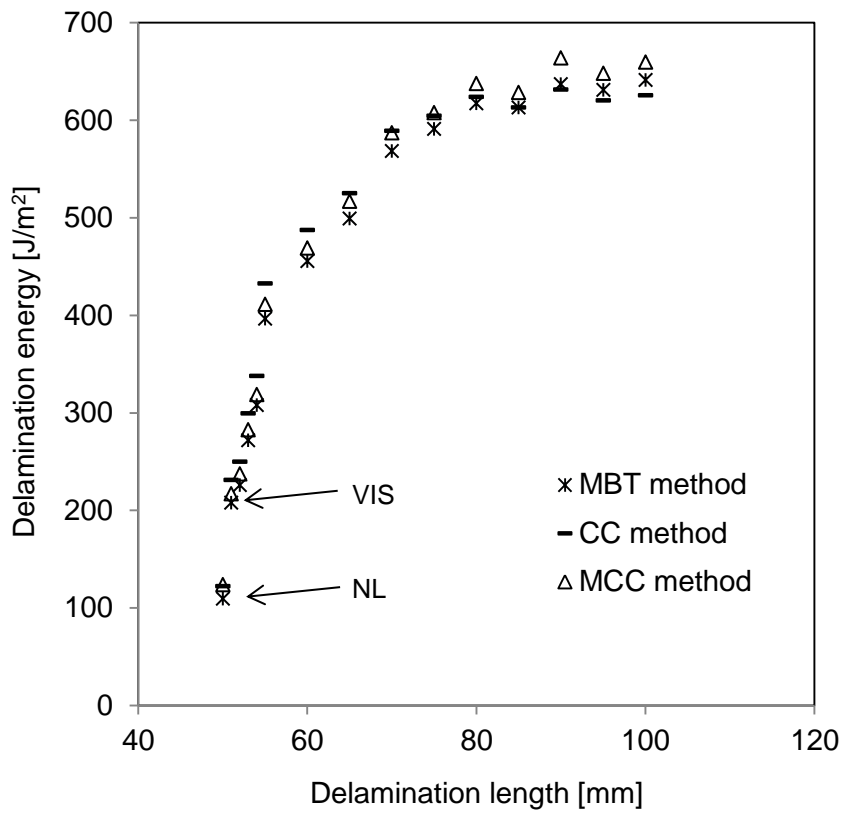


Figure 3.21 Resistance curves obtained from different data reduction methods.

3.11 FIBER VOLUME FRACTION MEASUREMENT

The fiber volume fraction of samples was determined through resin burn-out testing [17]. At least two specimens were taken from different locations of each of the samples. The top and bottom sample surfaces of laminate plates and the outside surface of tubular samples were ground to remove any excess resin. Resin accumulation on the outside surfaces of the samples occurred during fabrication, and its presence was found to obscure the actual fiber volume fraction level inside the composites. The mass of specimens was measured prior to placing them inside a preheated oven maintained at 540°C. The specimens remained in the oven for three hours. During the three-hour burn-out, the resin phase was completely removed leaving behind the reinforcement phases (e.g. fiber and nanoclay) inside the crucibles, which were then weighed to measure the reinforcement mass. By knowing the densities of different components the average fiber volume fraction of the composites was calculated according to Equation (3.13).

$$V_f = \frac{\frac{m_f}{\rho_f}}{\frac{m_f}{\rho_f} + \frac{m_m}{\rho_m} + \frac{m_p}{\rho_p}} \quad (3.13)$$

where m_f , m_m and m_p are the mass and ρ_f , ρ_m and ρ_p are the density of the fiber, matrix and nanoparticle phase, respectively. In the laminates the fiber volume fraction varied within the range of 0.50 to 0.64, and in the composite pipes it varied between 0.59 to 0.68.

3.12 MECHANICAL TESTING OF NANOCOMPOSITE TUBES

Biaxial testing of tubular specimens was performed by applying a monotonic 2-to-1 hoop-to-axial stress loading ratio (“pressure vessel loading”) [18]. Specimens were tested on a custom-built servo-hydraulic machine, which is capable of imposing axial load, internal pressure and torsion upon a specimen (see Figure 3.22). Refer to reference [19] for details on the operation of this testing instrument. At the time of testing, the custom built multi-axial testing machine maintained a constant biaxial stress ratio by simultaneously applying internal pressurization and axial traction. The specimen was clamped to a collar/collet type gripping system and amounted in the testing machine. All tests were performed under load control condition. A pressure intensifier supplied hydraulic fluid (Esso NUTO H-46, Imperial Oil Limited, Calgary, AB, Canada) for specimen pressurization at a rate of 4.63 kPa/s. Loading

was continued until ultimate specimen failure (i.e. structural failure). The data acquisition system permitted recording of hoop and axial strains, axial load and stroke, internal pressure and pressure intensifier volume. Applied hoop and axial stresses were estimated by applying the principle of thin-wall membrane theory [18]. Hoop and axial stresses were calculated according to Equations (3.14) and (3.15).

$$\sigma_H = \frac{D(p_i - p_o) - 2t_0 p_o}{2t_0} \quad (3.14)$$

$$\sigma_A = \frac{D^2(p_i - p_o) - 4t_0 p_o (D + t_0)}{4t_0 (D + t_0)} + \frac{F}{\pi t_0 (D + t_0)} \quad (3.15)$$

where D is the internal pipe diameter, t_0 is the wall thickness, p_i and F are the internal pressure and axial force applied to the pipe, and p_o is the atmospheric pressure.

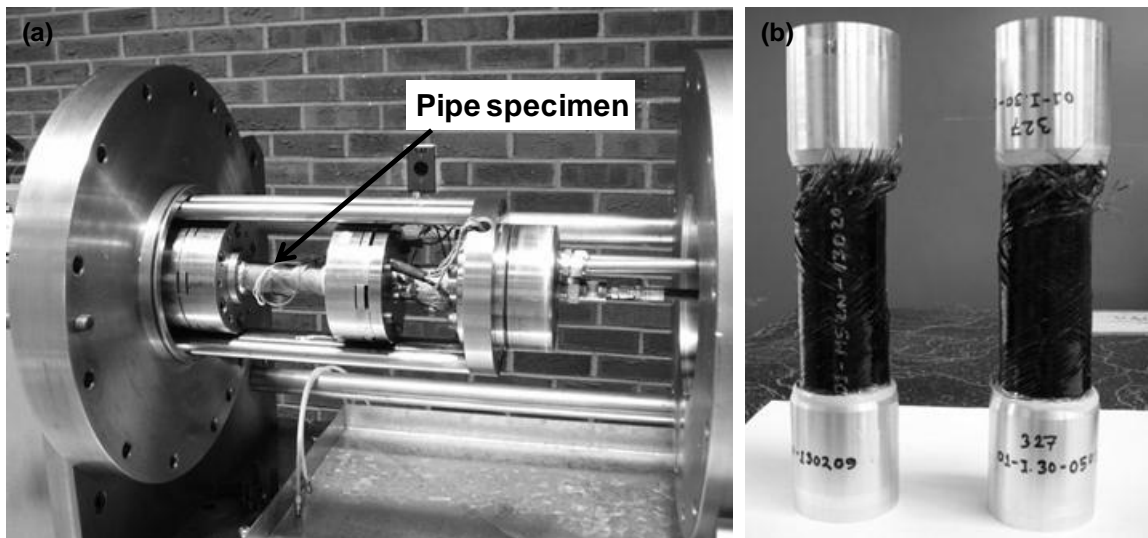


Figure 3.22 (a) Multi-axial testing instrument, and (b) structurally failed tubular test specimens.

Typical stress-strain curves are presented in Figure 3.23 for a tube sample subjected to a biaxial loading condition. The radial stress component was ignored in this study considering its comparatively small magnitude and the use of thin-wall membrane geometry. From the recorded intensifier fluid volume, the cumulative fluid volume loss was calculated that transmitted through the micro-cracked pipes (i.e. fluid volume loss). The fluid volume loss data was corrected for compressibility of the hydraulic fluid and

expansion effects of the specimen and the testing machine's hydraulic system (e.g. hoses). Figure 3.24 shows intensifier fluid volume and fluid volume loss data with corresponding intensifier pressure for a composite pipe made with an epoxy polymer containing 3 wt% of M52N block-copolymer.

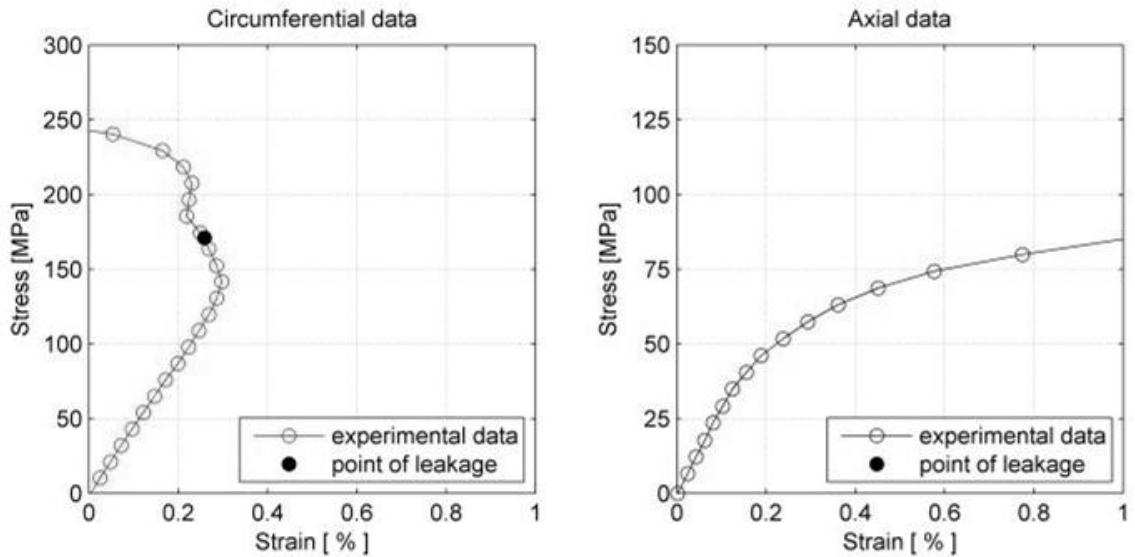


Figure 3.23 Global biaxial stress-strain response of filament-wound tube made with an epoxy polymer containing 3 wt% of M52N block-copolymer.

3.13 DETECTION OF PIPE FAILURES

Quantification of previously mentioned failure events was critical as this would typically standardize the performance of the composite pipes for their intended service condition. To identify functional and structural failure events from the same test setup, each pipe sample was fitted with an internal rubber bladder, which enabled pressurization until catastrophic pipe failure. Prior to testing, the inside of a rubber bladder as well as the annular region in between the pipe and the bladder were filled with hydraulic fluid. Pressurization occurred from inside the bladder. In the course of the experiment, the initiation, accumulation and coalescence of matrix cracks provided pathways for fluid to escape through the composite structure. In this study, functional failure in the form of leakage was characterized by a prescribed fluid loss volume through the tube wall (i.e. a loss corresponding to 1% of the internal pipe volume). After a certain amount of fluid

loss from the annulus, the inflating rubber bladder provides a seal inside the specimen. Pressurization was continued until rapid loss of fluid indicating pipe burst (i.e. structural failure) was ascertained from the hydraulic system.

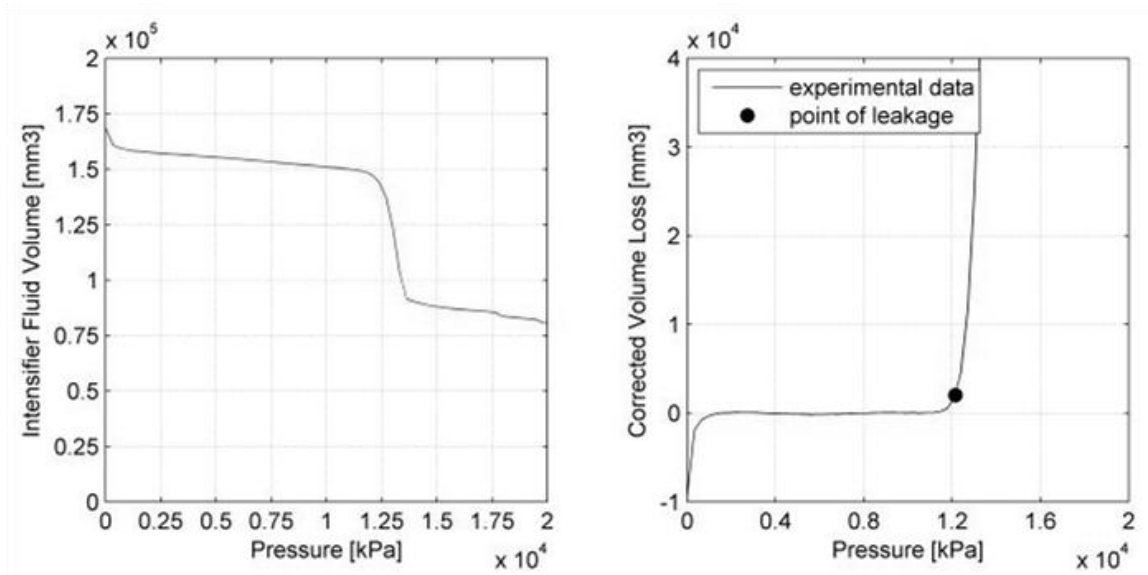


Figure 3.24 Fluid volume versus intensifier pressure for tube tested under biaxial loading.

REFERENCES

1. Utracki, L.A., 2004. *Clay-Containing Polymeric Nanocomposites*. Shawbury: Rapra Technology Limited.
2. EGERTON, R.F., 2005. *Physical principles of electron microscopy: an introduction to TEM, SEM, and AEM*. New York: Springer.
3. Young, R.J. and Lovell, P.A., 2011. *Introduction to polymers*. Boca Raton: CRC press.
4. MERTZEL, E. and KOEING, J.L., 1986. Application of FT-IR and NMR to epoxy resins. *Advances in Polymer Science*, **75**, pp. 73-112.
5. NIKOLIC, G., ZLATKOVIC, S. CAKIC, M., CAKIC, S., LACNJEVAC, C. and RAJIC, Z., 2010. Fast Fourier transform IR characterization of epoxy GY systems crosslinked with aliphatic and cycloaliphatic EH polyamine adducts. *Sensors*, **10**, pp. 684-696.

6. Meyers, M. A. and Chawla, K.K., 2009. *Mechanical Behavior of Materials* (2nd Edition). Cambridge University Press.
7. Product literature (Brochure), DMA 8000 Dynamic Mechanical Analyzer, Perkin Elmer.
8. Standard practice for plastics: dynamic mechanical properties: determination and report of procedures, ASTM D 4065-06, ASTM international, West Conshohocken, PA, USA.
9. Standard test method for tensile properties of plastics, ASTM D 638-10, ASTM international, West Conshohocken, PA, USA.
10. Technical data, MTS 810 & 856 material testing systems, MTS Systems Corporation.
11. Hu, Y., Multiaxial behavior and viscoelastic constitutive modeling of epoxy polymers. *PhD Thesis*, University of Alberta, Edmonton, Alberta, 2002.
12. Brown, G.M., Mechanical properties of Alumina/Epoxy nanocomposites: influence of processing and processing induced inhomogeneities. *MSc Thesis*, University of Alberta, Edmonton, Alberta, 2004.
13. HU, Y., XIA, Z. and ELLYIN, F., 2003. Deformation Behavior of an Epoxy Resin Subject to Multiaxial Loadings. Part I: Experimental Investigations. *Polymer Engineering and Science*, **43**(3), pp. 721-733.
14. Standard test methods for plane-strain fracture toughness and strain energy release rate of plastic materials, ASTM D 5045-99, ASTM international, West Conshohocken, PA, USA.
15. GARG, A.C. and MAI, Y.-W., 1988. Failure mechanisms in toughened epoxy resins-A review. *Composites Science and Technology*, **31**(3), pp. 179-223.
16. Standard test method for mode I interlaminar fracture toughness of unidirectional fibre-reinforced polymer matrix composites, ASTM D 5528-01, ASTM international, West Conshohocken, PA, USA.
17. Mertiny, P. and Ellyin, F., 2002. Influence of the filament winding tension on physical and mechanical properties of reinforced composites. *Composites Part A*, **33**, pp. 1615-1622.

18. SODEN, P.D., KITCHING, R., TSE, P.C., TSAVALAS, Y. and HINTON, M.J., 1993. Influence of winding angle on the strength and deformation of filament-wound composite tubes subjected to uniaxial and biaxial loads. *Composites Science and Technology*, 46(4), pp. 363-378.
19. ELLYIN, F. and WOLODKO, J., 1997. TESTING FACILITIES OF MULTIAXIAL LOADING OF TUBULAR SPECIMENS. *ASTM Special Technical Publication* 1997, pp. 7-24.

Chapter 4

Morphology, Mechanical and Fracture Properties of Epoxy-clay Nanocomposites¹

SYNOPSIS: The effects of organic modifier and processing method on morphology and mechanical properties of epoxy-clay nanocomposites were investigated and discussed in this chapter. Unmodified and alkylammonium-ion-exchanged clay were used to produce nanocomposites involving two different processing methods. In this study, the preparation of nanocomposites by exfoliation-adsorption method was accomplished using an ultrasonic mixing procedure, and mechanical blending was used for in-situ intercalative polymerization. The study of nanocomposite microstructure revealed that the organoclay, which was ultrasonically mixed with the epoxy was partially exfoliated and intercalated inside the polymer matrix. On the other hand, organoclay remained in a phase-separated and flocculated state after the mechanical blending process. The tensile stiffness of resulting nanocomposites increased for both dispersion techniques. Stiffness increased significantly for the ultrasonic dispersion method by realizing the reinforcing potential of exfoliated silicate layers. However, tensile strength decreased slightly and ductility reduced significantly. During plane-strain fracture testing nanocomposites with exfoliated and intercalated nanoclay morphology was found to be ineffective in enhancing the fracture toughness. Nanocomposites with intercalated and phase-separated morphology, on the other hand, had improved crack resistance predominantly by crack deflecting and crack pinning mechanisms.

4.1 INTRODUCTION

Polymer nanocomposites have unique multifunctional properties that distinguish them from traditional polymer microcomposites. Recently it has been demonstrated that nano-scale dispersion of layered silicate in relatively small quantities can significantly enhance the

¹ A version of this chapter has been submitted for publication: BASHAR, M., SUNDARARAJ, U. and MERTINY, P., 2013. Effect of nanoclay structures on fracture behavior of epoxy-clay nanocomposites prepared by different dispersion methods. *Journal of Applied Polymer Science*.

properties of a substrate polymer [1-3]. Having high aspect ratio, large surface area and good interfacial properties, layered silicate clay added to a polymer matrix can contribute to significant cost savings as a property enhancer. Clay-containing polymer nanocomposites may offer beneficial properties, such as good mechanical properties [1-2, 4-9], dimensional stability, barrier properties [2, 4], flame retardancy [4, 10], optical properties and thermal stability [1-2, 4]. In pursuit of optimized property enhancements, this area of nanoscience has been extensively studied with polymers such as epoxy, unsaturated polyester, polystyrene, polyimide, polypropylene and polyurethane [11].

Typically polymer clay nanocomposites exhibit three distinct morphologies, i.e. phase-separated, intercalated and exfoliated structures [3, 11]. Superior mechanical, thermal and barrier properties are usually obtained for an exfoliated architecture, i.e. individual silicate lamellae are homogeneously distributed in the polymer matrix. However, achieving complete exfoliation is difficult because of the layered silicate's tendency to form aggregates due to such forces as electrostatic attraction and van der Waals force [12-13]. Surface modifiers such as alkylammonium ions can promote organophilic characteristics in the layered silicate, thereby making it more compatible with epoxy and the curing agent, which also provides a catalytic influence on the polymerization reaction [10, 12]. The key to a successful formation of exfoliated nanocomposites is faster rates of intragallery polymerization due to the catalytic effect of the surface modifiers compared to rates for competing extragallery reactions [14]. The effect of alkylammonium ion modification on the mechanism of clay intercalation and exfoliation has been studied extensively by several researchers [12, 15-17]. The degree of clay exfoliation and intercalation also depends on the type of clay [8, 12], cation exchange capacity [16, 18], chemical nature of the interlayer cations [7-10, 12], curing agent [6, 15], curing temperature and time [9, 12, 15, 19], resin type [19-20] and dispersion method [21-22]. As mentioned earlier, there are several processing routes that can lead to well dispersed layered silicate nanocomposite; these are in-situ intercalative polymerization [7, 18], exfoliation-adsorption [10, 23] and melt processing [21].

Individual silicate layers provide excellent stiffness and strength in two dimensions due to their high aspect ratio, stiffness and interaction at the molecular level. Lan and Pinnavaia [5] and Pinnavaia et al. [13] attributed the exceptional increase in the stiffness of nanocomposites in an exfoliated state to a reinforcing effect through stress transfer to the rigid individual

silicate nano-sheets. Likewise, Messersmith and Giannelis [6] observed significant improvement in the dynamic storage modulus when dispersing organoclay into an epoxy matrix. Up to now, various researchers have documented similar enhancement in epoxy mechanical properties; notably Kornmann et al. [7, 9], Zilg et al. [8], Xidas et al. [17], Becker et al. [20], Miyagawa and Drzal [23], Zerda and Lesser [24], Yasmin et al. [25] and Kinloch and Taylor [26] all recognized stiffness increase in the epoxy-clay nanocomposites.

Furthermore, nanoclay has the ability to simultaneously increase toughness and stiffness of a polymer. This is highly advantageous compared to, for example, rubber toughened epoxy, where toughness is increased at the expense of other thermo-mechanical properties (i.e. stiffness and glass transition temperature). In a study, Zilg et al. [8] achieved good balance between toughness/stiffness improvements in nanocomposites comprised of anisotropic laminated nanoparticles instead of exfoliated clay platelets. According to these researchers, the intercalated and/or phase-separated clay particles would be more effective in impeding crack propagation than the delaminated isolated clay platelets. Similarly, Kornmann et al. [7] showed that conventionally filled epoxy-clay composites resulted in the best toughening effect, and Miyagawa and Drzal [23] inferred that larger intercalated organoclay particles provided better fracture resistance than the exfoliated platelets. Moreover, Becker et al. [20] and Siddiqui et al. [27] demonstrated increase in polymer fracture toughness with a mixture of mostly intercalated and exfoliated organoclay in epoxy. Studies conducted so far on the fracture and deformation mechanisms of nanoclay-filled epoxy have qualitatively shown evidence of crack deflection, crack pinning, cavitation and matrix deformation phenomena that improved crack propagation resistance in nanocomposites [22, 24, 28-29]. Zerda and Lesser [24] documented crack deflection and branching by intercalated nanoclay diverting cracks in a tortuous path while creating additional fracture surface area. In epoxy-clay nanocomposites, formation of microcracks from within the clay interlayers and subsequent propagation associated with the creation of new surface area due to crack deflection were considered to be the primary energy dissipation mechanism by Wang et al. [28]. Liu et al. [29] identified several crack resistance phenomena, particle-matrix interfacial debonding, microvoiding, matrix shear yielding and crack deflection to work cooperatively in an intercalated nanocomposite. Liu et al. [22] showed crack pinning and crack-tip blunting (e.g.

localized matrix deformation) mechanisms to function together or separately in different nanoclay-filled epoxy systems made by various preparation techniques.

The above literature review clearly demonstrates considerable disagreement and differences in opinion among researchers on the operative crack resistance mechanism in epoxy nanocomposites and its dependence on the nanoclay morphology (i.e. exfoliated, intercalated and particulate). Nanocomposite processing in fact affects the organoclay dispersion and its microstructure, and consequently has pronounced influence on the fracture micromechanism. Therefore, the need for a systematic evaluation from processing to microstructure evolution associated with final mechanical property development of the micro/nano composites derived from organoclay would necessitate further study. In this section of the thesis the effect of the processing/mixing method and the contribution of the organic modifier on the epoxy-clay nanocomposite dispersion were investigated. Different characterization and experimental techniques were involved to study the morphology and mechanical properties of resulting nanocomposites. A correlation between microstructural and mechanical properties of the nanocomposites prepared by in-situ intercalative polymerization and exfoliation adsorption processes was observed.

4.2 RESULTS AND DISCUSSION

4.2.1 Morphology of the Epoxy-clay Nanocomposites

The microstructure of epoxy nanocomposites was studied by WAXD and TEM. The epoxy-clay nanocomposites were prepared according to the synthesis methods described in the Sections 2.2.1.1 and 2.2.1.2. XRD traces of the unmodified clay (PGW) and the primary (I.30E) and quaternary (I.28E) alkylammonium ion treated nanoclays are shown in Figure 4.1. Interlayer spacing of the nanoclay was estimated from the 2θ angle of the peak in the XRD curve. Using the prominent diffraction peak, the d -spacing, d_{001} , was estimated as 1.24 nm, 2.23 nm and 2.39 nm for the PGW, I.30E and I.28E clays respectively. X-ray diffraction patterns of the I.30E organoclay and a mixture of nanoclay-epoxy (by ultrasonic mixing) containing 1 wt% layered silicate are shown in Figure 4.2. Before curing, the blending of epoxy resin with acetone and clay using ultrasonic dispersion promoted interdiffusion of epoxy pre-polymer in between the clay galleries. Swelling of the silicate

layers with epoxy expanded the interlayer distance, thereby shifted the XRD peak to the left, where $d_{001} = 3.15$ nm. However, the reflection completely disappeared in the case of cured I.30E-epoxy nanocomposites.

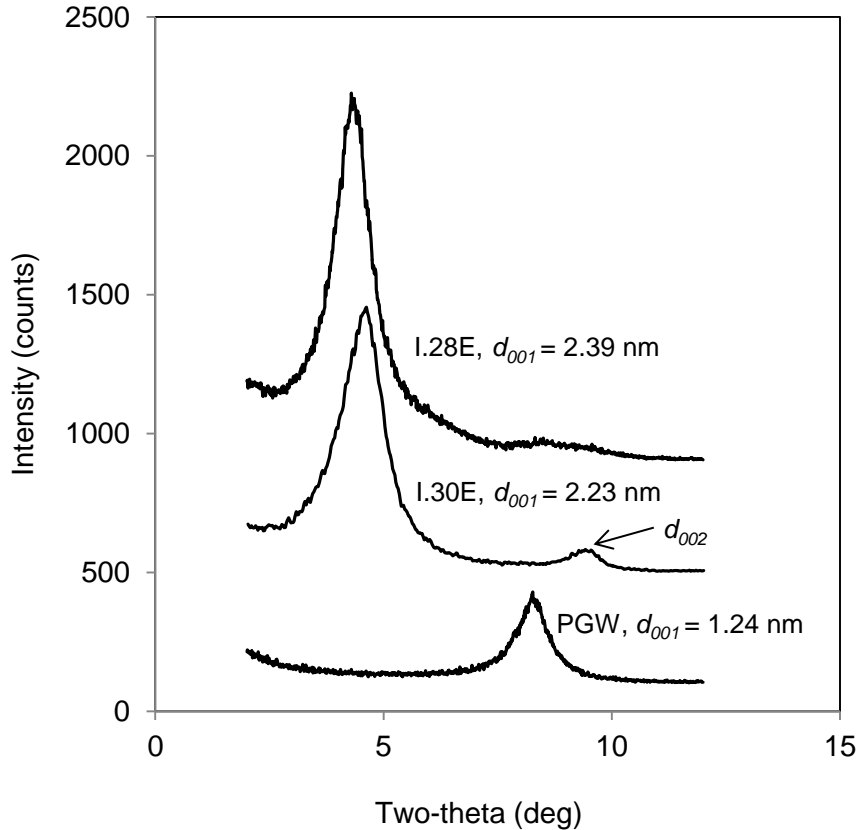


Figure 4.1 Typical X-ray diffraction peaks of the organoclay and unmodified clay.

Figure 4.3 presents XRD traces of the nanocomposites that were prepared by the ultrasonic mixing technique, with each nanocomposite containing 1 wt% of the respective clays. The diffraction peak of the inorganic PGW clay remains unaltered and overlaps with the lower angle scattering peak of the epoxy polymer showing an overall peak broadening effect, but also indicates that this nanocomposite has a phase-separated morphology. A phase-separated morphology implies that the epoxy resin was not able to effectively penetrate between the clay platelets. This type of morphology is normally expected for untreated clays. The absence of a reflection peak for the nanocomposite containing the I.30E clay signifies either an exfoliated or an intercalated structure with interlayer distance exceeding 8.83 nm (which is

the detection limit for WAXD, i.e. $2\theta \geq 1^\circ$). The epoxy nanocomposite that was reinforced with the I.28E clay shows slightly expanded basal spacing of $d_{001} = 2.85$ nm, which was estimated from its diffraction peak. The increase in layer separation from 2.39 nm to 2.85 nm most likely occurred due to epoxy solvation that took place during the ultrasonic blending phase. Pinnavaia et al. [13] reported a d -spacing of $d_{001} = 3.69$ nm when a similar quaternary alkylammonium ion, $\text{CH}_3(\text{CH}_2)_{17}\text{N}(\text{CH}_3)_3^+$, exchanged clay was swollen by the epoxy resin. In that study, the authors assumed that a reorientation of the quaternary onium ion occurred from its usual lateral bilayer orientation to a vertical configuration that maximizes solvation interaction with the epoxy. Initial solvation of the clay galleries is important for later diffusion of the curing agent and the epoxide, and subsequent initiation of the intragallery polymerization. The charge density of the clay and the chain length of the alkylammonium ion are major controlling factors in epoxy solvation that determine migration and the amount of epoxy resin that can occupy the intergallery space [12, 16].

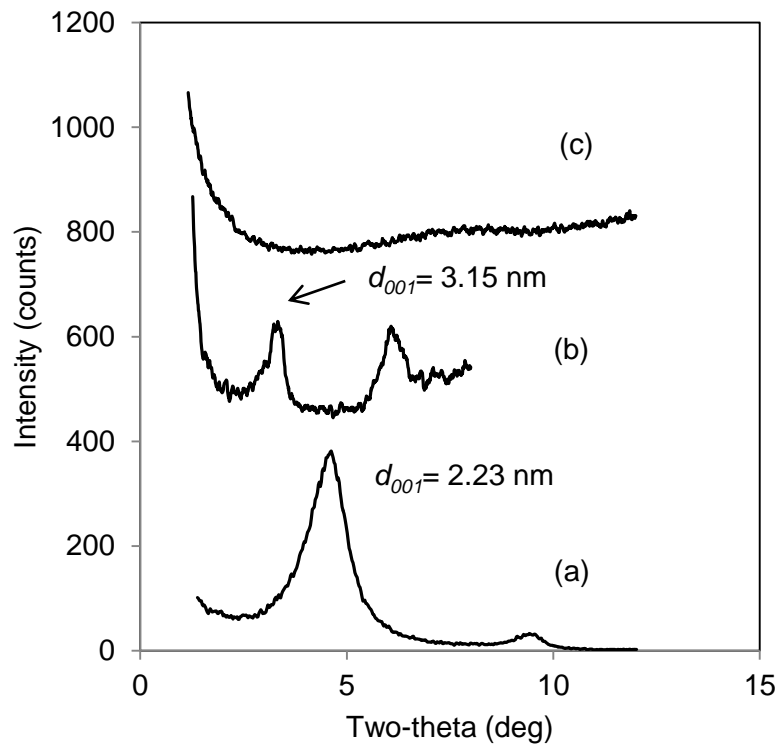


Figure 4.2 XRD analysis results showing interlamellar spacing of nanoclay at various stages of I.30E-epoxy nanocomposite processing: (a) organoclay, (b) organoclay in epoxy resin before curing agent addition and (c) after cure.

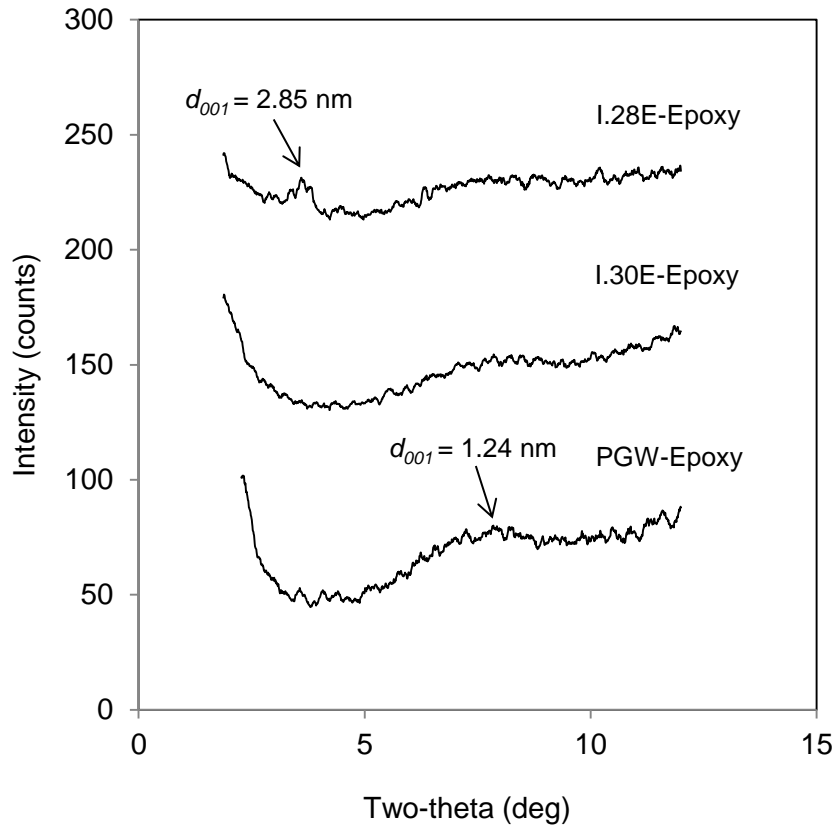


Figure 4.3 X-ray scattering traces of nanocomposites containing 1 wt% nanoclay in epoxy.

Figure 4.4 shows diffraction patterns of the cured epoxy nanocomposites containing various weight fractions of the I.30E clay fabricated by the two different processing techniques. No distinguishable diffraction peak was observed for the nanocomposites produced by ultrasonic mixing containing 1 wt% and 2 wt% I.30E clay, but the composite having 3 wt% clay showed a distinct peak revealing an interlayer spacing of $d_{001} = 2.73 \text{ nm}$. In contrast, mechanical mixing generated a combination of phase-separated and intercalated architectures as evidenced by the broadening of the diffraction peak, which indicates significant variations in the layer spacing among different clay particles. The scattering apex representing interlayer spacing of $d_{001} = 2.68 \text{ nm}$ and 2.63 nm was found respectively for the 1 wt% and 3 wt% I.30E clay loadings. The possibility of an inclined orientation of the exchanged onium ion is probable in these cases, and has been reported previously in the literature [12].

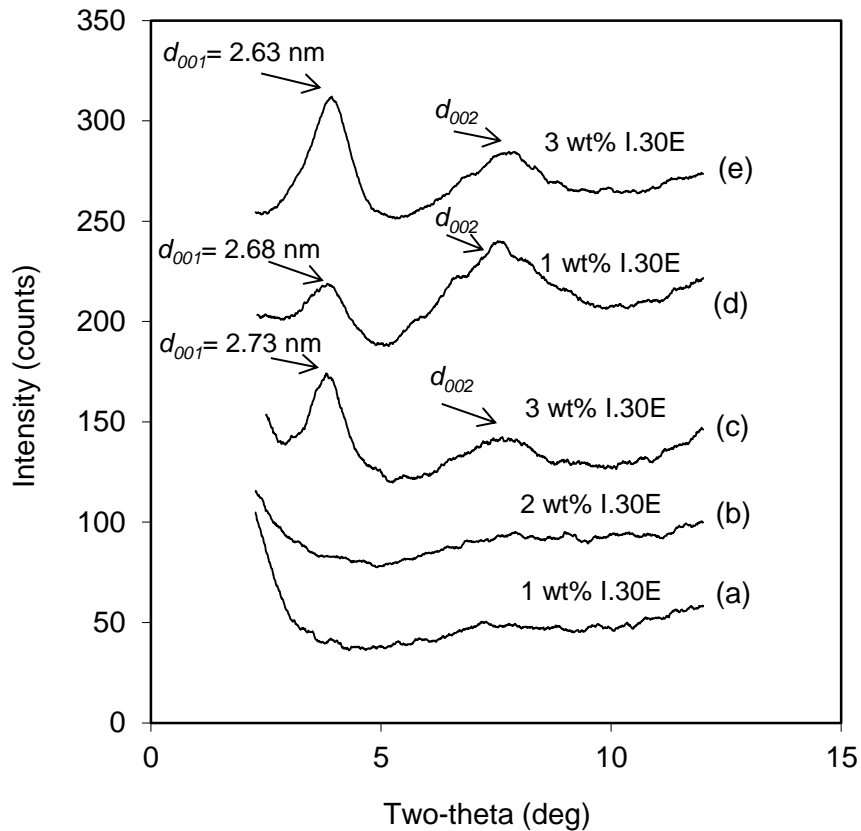


Figure 4.4 X-ray diffraction patterns of nanocomposites: (a), (b) and (c) prepared by ultrasonic dispersion and (d) and (e) by mechanical dispersion of I.30E clay.

Nanocomposites prepared by the ultrasonic dispersion method were transparent after curing as shown in Figure 4.5. This means that the dispersed particles are quite small and/or the concentrations were low enough not to significantly affect the scattering of visible light, which has a wavelength between 380 to 740 nm in the electromagnetic spectrum. From the TEM images in Figures 4.6 and 4.7 it is apparent that the mixing techniques have greatly influenced the degree of the dispersion of I.30E nanoclay, that is, ultrasonic dispersion produced partially exfoliated and intercalated nanocomposites (see Figure 4.6), whereas mechanical dispersion formed mostly phase-separated and intercalated clay agglomerates (see Figure 4.7). The nanocomposites prepared by the ultrasonic technique shown in Figure 4.6(a) displays exfoliated disordered individual 1 nm thick silicate platelets as well as laminated parallel platelets with a layer separation of 10-15 nm for the 1 wt% I.30E-epoxy

nanocomposite. In Figure 4.6(b) the nanocomposite containing 2 wt% I.30E also exhibits an intercalated morphology. For the same nanocomposite system, randomly dispersed submicron-size intercalated particles can be seen at lower magnification (see Figure 4.6(c)). The samples made by mechanical mixing appear to retain its stacked layer structures as tactoids as evidenced in Figure 4.7 for 1 and 2 wt% I.30E concentrations. This morphology resembles the conventional phase-separated structures in clay in which clay tactoids are attached together to form large agglomerates. TEM images in Figure 4.8 show an intercalated morphology and randomly distributed clay tactoids in the epoxy that was modified with the I.28E clay. Phase-separated and larger clay microaggregates are clearly visible in Figure 4.9 for the composite made with the unmodified PGW clay. The white areas shown in Figures 4.7(b) and 4.9(b) were formed during the ultra microtoming process due to severing of the clay particles from the epoxy matrix.

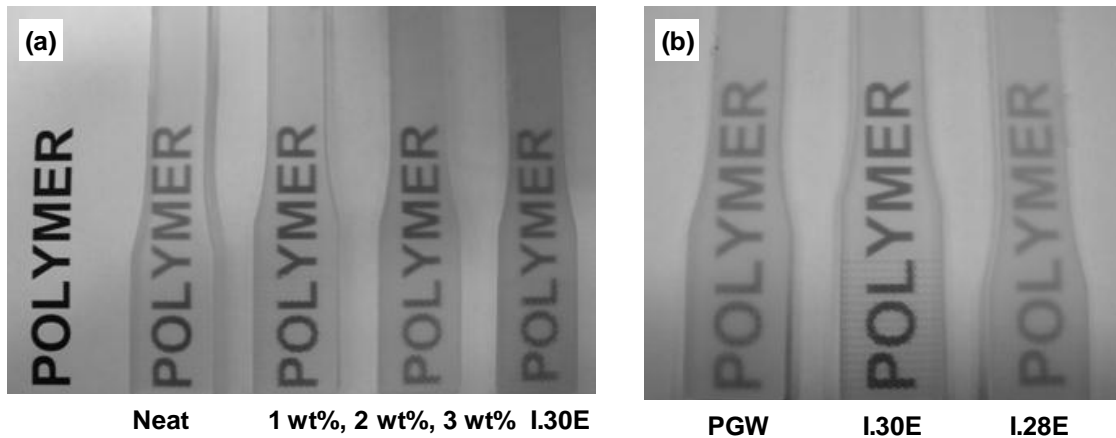


Figure 4.5 Transparency of: (a) neat epoxy and nanocomposites containing 1 wt%, 2 wt% and 3wt% I.30E clay and (b) nanocomposites containing 1 wt% of respective nanoclays, both prepared by ultrasonic dispersion method.

In agreement with the observation made by Zilg et al. [8] and Lan et al. [12], it was also found that the primary ammonium ion is more effective than the quaternary ammonium ion in increasing the interlamellar distance of the layered silicate. According to Lan et al. [12] the apparent differences in the microstructure of the two organoclay systems can be explained by the catalytic influence of the acidic alkylammonium ion on the epoxy-amine curing reaction in the following order; $\text{H}_3(\text{CH}_2)_{17}\text{NH}_3^+ > \text{CH}_3(\text{CH}_2)_{17}\text{N}(\text{CH}_3)\text{H}_2^+ > \text{CH}_3(\text{CH}_2)_{17}\text{N}(\text{CH}_3)_2\text{H}^+$

$\text{CH}_3(\text{CH}_2)_{17}\text{N}(\text{CH}_3)_3^+$. This catalytic effect is primarily due to the acidity of the organic cation in the presence of hydrogen of the ammonium group. Therefore, it was deduced that in the I.30E clay filled epoxy, the intragallery catalytic polymerization rate was relatively higher than the extragallery polymerization, which caused further separation of the clay platelets [10]. Previously it was documented by Wang and Pinnavaia [30] and Kornmann et al. [9] that homopolymerization of the epoxy was facilitated in the presence of the acidic surface modifier of the organosilicate at a sufficiently higher temperature. However, in this study, it is assumed that the present curing conditions do not satisfy the temperature requirement for the DGEBA homopolymerization to be an operative mechanism [10].

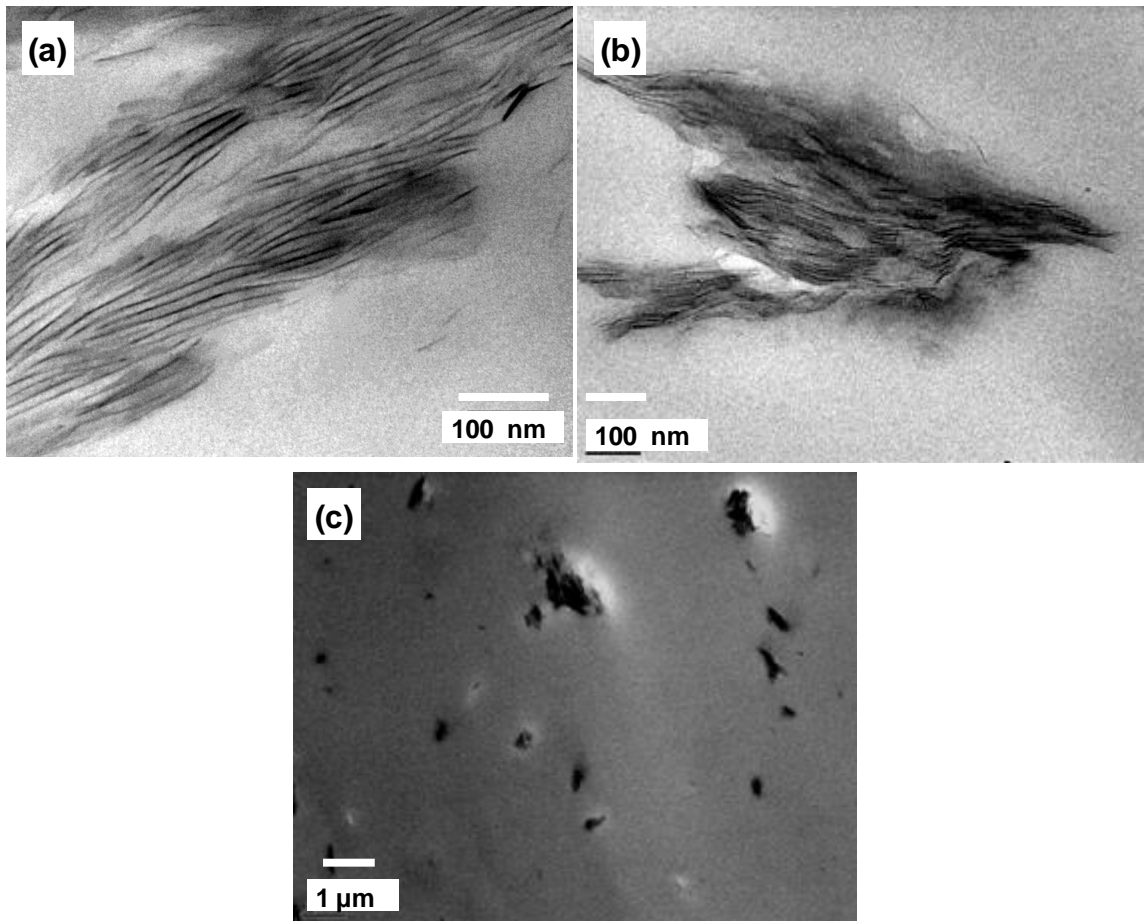


Figure 4.6 TEM micrographs of nanocomposites made by ultrasonic dispersion of epoxy containing (a) 1 wt% I.30E (high magnification) and 2 wt% I.30E clay at (b) high magnification and at (c) low magnification.

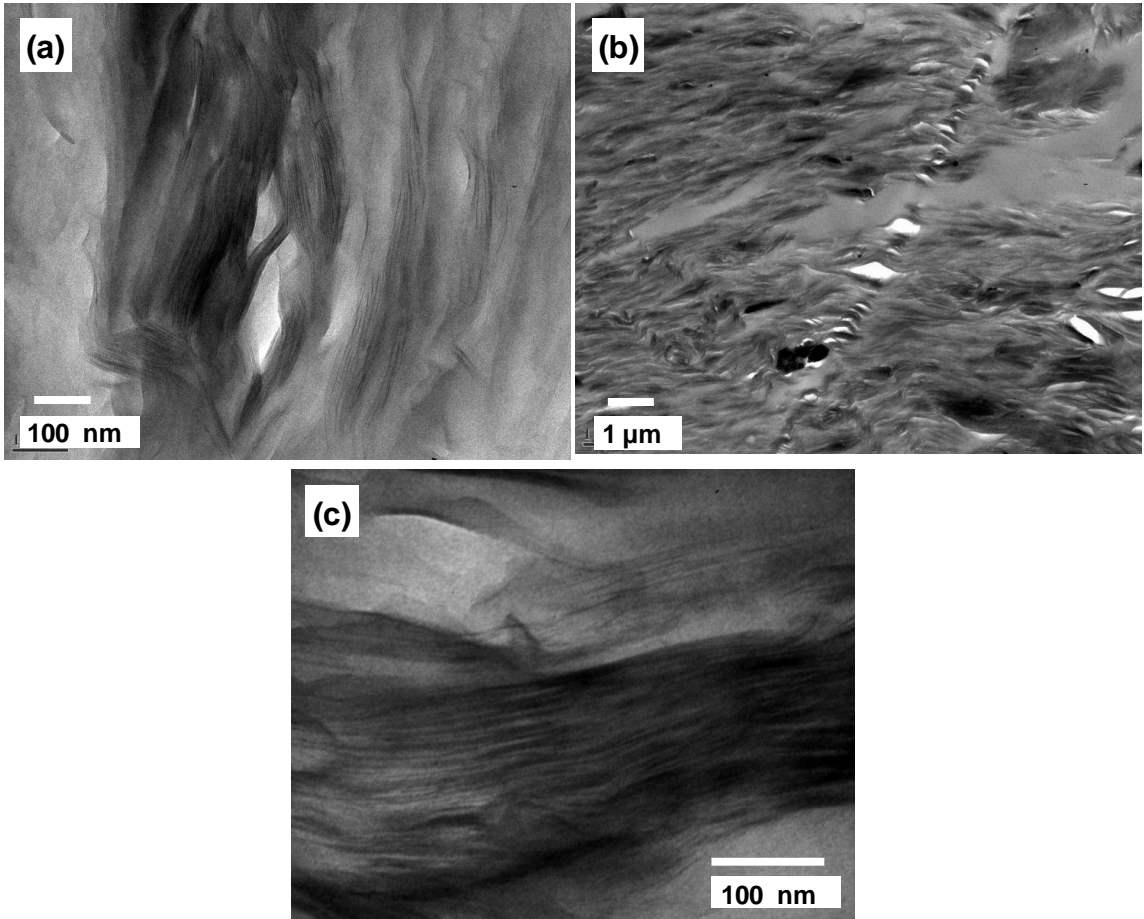


Figure 4.7 TEM micrographs of nanocomposites prepared by mechanical mixing of epoxy containing: 1 wt% I.30E at (a) high and (b) low magnifications and (c) 2 wt% I.30E clay.

Table 4-1 presents the intergallery spacing of the organoclays and their respective nanocomposites composed of 1 wt% of the organoclay. From the XRD and TEM investigations some distinctions can be made between the morphology of the nanocomposites made by the different dispersion methods. On the micro-scale, ultrasonic mixing caused deaggregation of the large layered silicate clusters, and on the nano-scale, it promoted intragallery diffusion of the epoxy prepolymer and the curing agent allowing the development of long range ordered structures (i.e. intercalated clay). In contrast, mechanical mixing produced larger clay aggregates with the formation of predominantly phase-separated clay tactoids. The ultrasonic method caused breaking up of the large clay aggregates into finely dispersed uniformly distributed submicron-size ($< 1 \mu\text{m}$) clay particles as shown in Figure 4.6(c) (see also [21, 23]). Prolonged ultrasonic mixing also influenced the epoxy

solvation into the clay gallery. The importance of epoxy solvation prior to the curing reaction has been well documented in the literature [18]. Therefore, it can be inferred that ultrasonic mixing offered better dispersion. However, neither of the dispersion methods achieved homogeneously dispersed isolated exfoliated platelets resembling a monolithic structure for the nanocomposites. Similar observations have been documented by other researchers based on micro and nano-scale studies on epoxy layered silicate nanocomposites [7, 18].

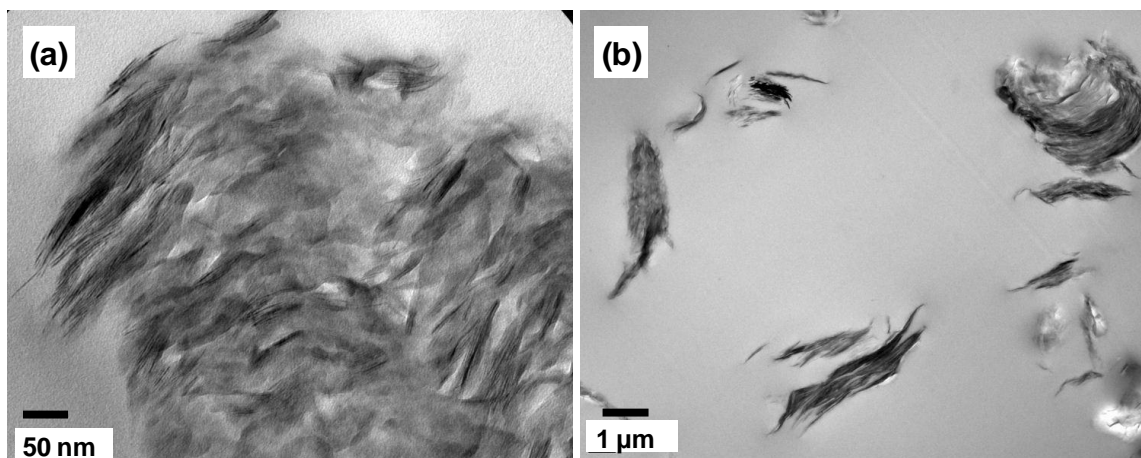


Figure 4.8 TEM images of nanocomposites comprising of 1 wt% I.28E in epoxy at: (a) high magnification and (b) low magnification.

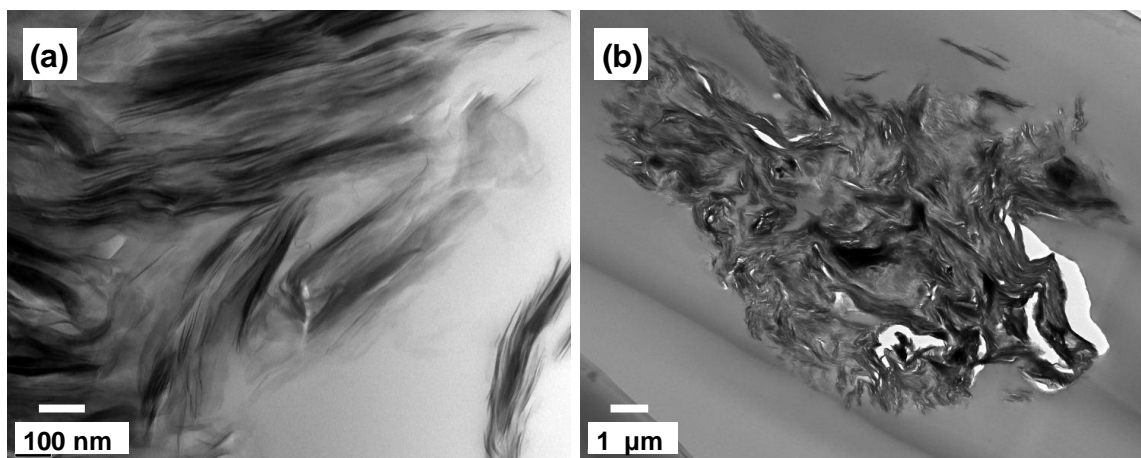


Figure 4.9 TEM images of nanocomposites comprising of 1 wt% PGW in epoxy at: (a) high magnification and (b) low magnification.

Table 4-1 Clay, organic modifier, *d*-spacing and corresponding nanocomposite morphology.

Clay	Organic modifier	<i>d</i> -spacing of the organoclay, d_{001} ^a	<i>d</i> -spacing and morphology of organoclay (1 wt%) in cured epoxy ^{a, b}
I.30E	CH ₃ (CH ₂) ₁₇ NH ₃ ⁺	2.23 nm	10~15 nm, exfoliated/intercalated (U) (measured by TEM)
I.28E	CH ₃ (CH ₂) ₁₇ N(CH ₃) ₃ ⁺	2.39 nm	2.68 nm, phase-separated (M) 2.85 nm, intercalated (U)
PGW	none	1.24 nm	1.24 nm, phase-separated (U)

^a Interlayer spacing was measured using the prominent diffraction peak from XRD traces.

^b U = ultrasonic mixing; M = mechanical mixing.

4.2.2 Tensile Property of the Epoxy-clay Nanocomposites

All nanocomposites prepared by the different blending protocols with varying compositions of the I.30E clay were subjected to uniaxial tensile testing. The average tensile property values are presented in Table 4-2 along with the corresponding standard deviations. The tensile properties of the nanocomposites and the unfilled epoxy resin are presented in Figures 4.10-4.13 with corresponding clay loadings. The lines drawn in the graphs illustrate general trends in the data but are not intended to signify any mathematical correlation. Error bars represent one standard deviation of four tests done on each set of specimens. The tensile modulus and strength of the pristine epoxy were measured to be 2.8 GPa and 82 MPa respectively. The tensile modulus of the nanocomposites prepared by ultrasonic blending increased substantially, i.e. a maximum of 20% increase was observed in response to 3 wt% I.30E nanoclay addition. Stiffness improved slightly in the nanocomposites processed by a mechanical agitator for the same clay loadings. The degree of exfoliation of the high aspect ratio rigid nano-platelets and superior interfacial adhesion of the exfoliated/intercalated nanoclay with the epoxy polymer contributed to the substantial stiffness improvement in the case of the ultrasonic mixed nanocomposites [25]. It can be surmised that well intercalated uniformly dispersed smaller submicron-size I.30E clay particles further influenced the stiffness. In contrast, for the mechanically mixed samples, the modulus increase was

relatively small, probably due in part to the inefficient layer separation of the nanoclay. In addition, the phase-separated clay aggregates formed during the mechanical mixing behaved akin to conventional microparticles that require higher filler concentrations to achieve substantial stiffness enhancement.

Table 4-2 Property of epoxy nanocomposites containing various concentrations of I.30E.

Filler matrix loading (wt%) ^a	Tensile modulus (GPa)	Tensile strength (MPa)	Elongation (%)	Fracture toughness (MPam ^{0.5})	Strain energy (J/m ²)
0 (neat epoxy)	2.82 ± 0.08	82.2 ± 1.56	8.53 ± 0.16	0.78 ± 0.05	235 ± 28
1 wt% I.30E (U)	3.25 ± 0.04	84.7 ± 1.56	6.12 ± 0.5	0.79 ± 0.03	225 ± 11
2 wt% I.30E (U)	3.23 ± 0.04	80.6 ± 2.78	5.51 ± 0.97	0.81 ± 0.05	245 ± 12
3 wt% I.30E (U)	3.36 ± 0.03	76.7 ± 3.51	4.08 ± 0.56	0.77 ± 0.01	230 ± 9
1 wt% I.30E (M)	2.84 ± 0.03	72.8 ± 3.5	4.8 ± 0.75	0.78 ± 0.04	240 ± 26
2 wt% I.30E (M)	2.92 ± 0.02	69.8 ± 0.42	3.96 ± 0.07	0.83 ± 0.04	265 ± 30
3 wt% I.30E (M)	2.97 ± 0.01	69.1 ± 1.19	3.78 ± 0.17	0.93 ± 0.06	320 ± 32

^a U = ultrasonic mixing; M = mechanical mixing.

Tensile strength values remained almost unchanged for samples formulated by ultrasonic mixing (see Figure 4.11). Nanocomposites that were made by the mechanical mixing method exhibited a considerable loss in tensile strength, which is in agreement with the results reported by other researchers [24]. It is assumed that clay aggregates present in the epoxy matrix acted as stress concentrators during the loading process causing the composite to fail at a reduced load level and ductility [7, 24]. Strain values at break reduced significantly with the addition of clay nanoparticles in the epoxy matrix for all of the clay nanocomposites (see Figure 4.12). The reduction in tensile elongation is believed to stem from an embrittlement effect caused by the stiffer clay nanofillers in the epoxy network [17, 24].

Figure 4.13 shows tensile test results of nanocomposites each containing 1 wt% of the PGW, I.30E and I.28E nanoclay respectively. In comparison to the nanocomposites made from PGW and I.28E, I.30E organosilicate generated greater mechanical property enhancement in epoxy. Previously, Pinnavaia et al. [13] reported that in a rubbery epoxy better reinforcing efficiently was achieved with the primary alkylammonium ion (exfoliated nanocomposites)

than the quaternary alkylammonium ion treated montmorillonite (intercalated nanocomposites) at higher clay loadings (>5 wt%).

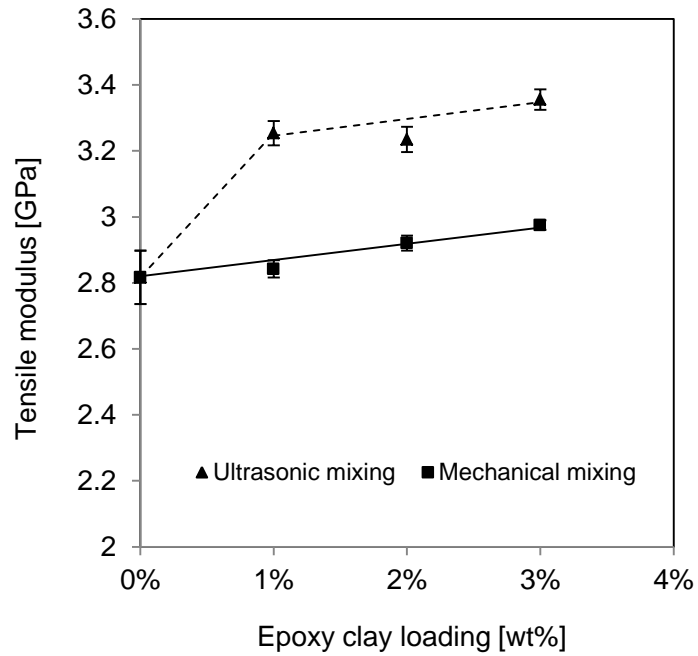


Figure 4.10 Influence of I.30E clay concentration on tensile modulus of nanocomposites.

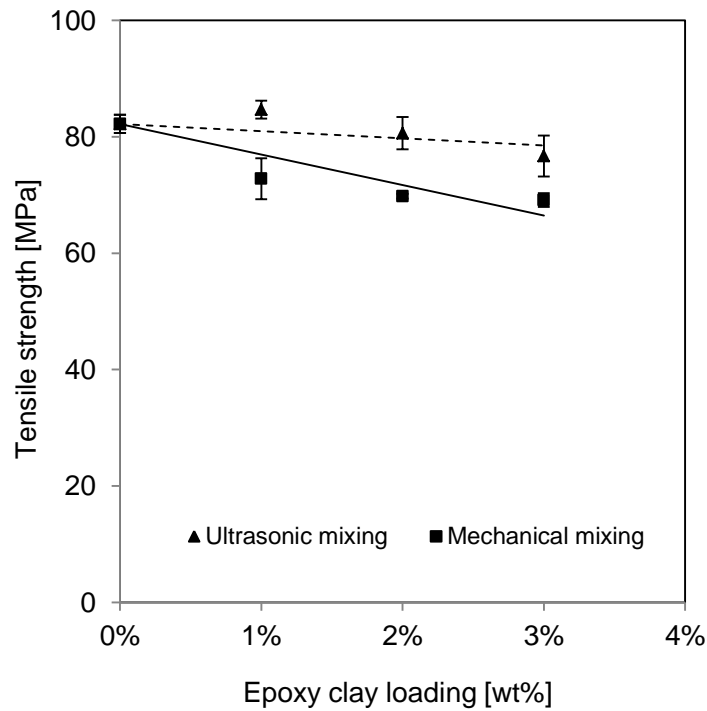


Figure 4.11 Tensile strength of nanocomposites as a function of I.30E clay content.

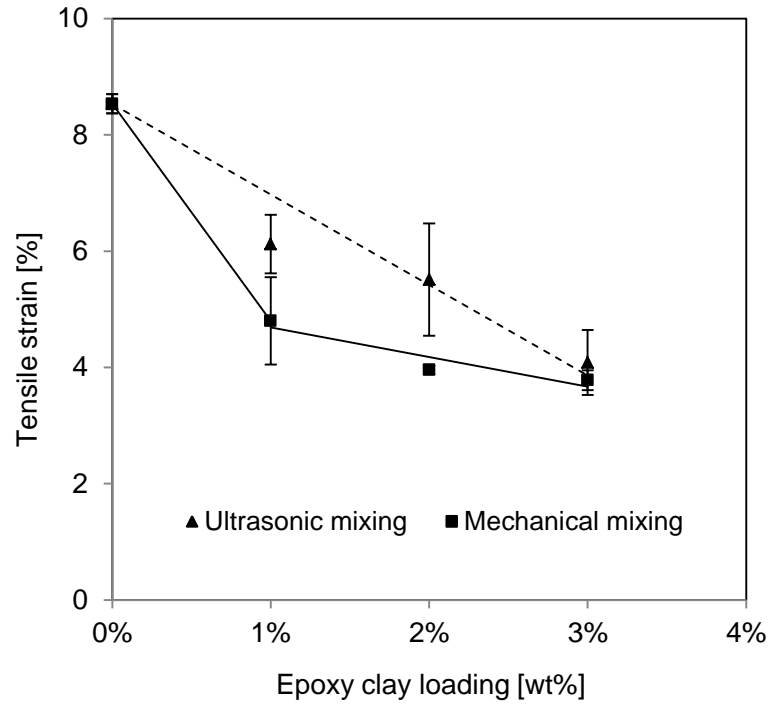


Figure 4.12 Relation between tensile elongation and I.30E clay loading of nanocomposites.

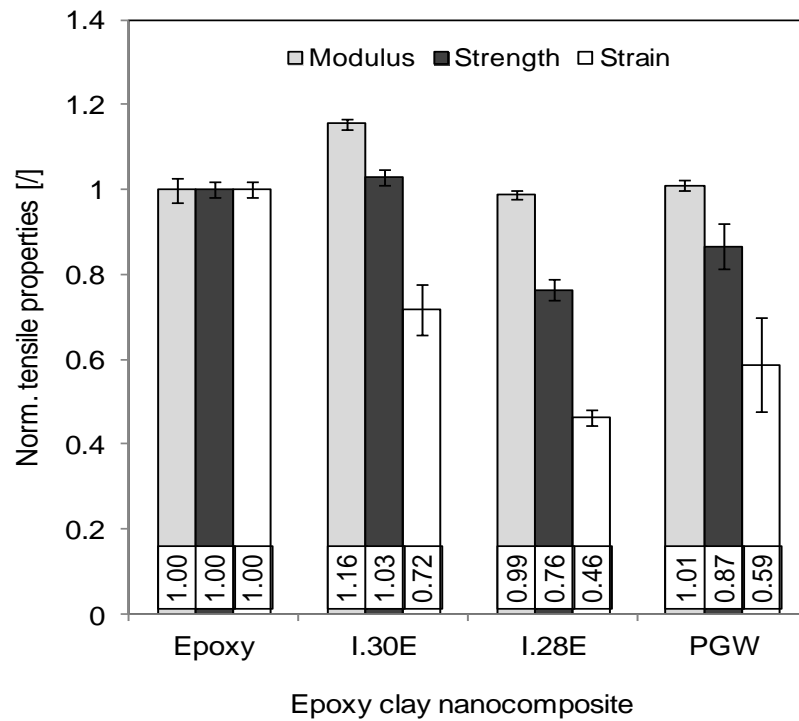


Figure 4.13 Tensile properties of different nanoclay filled epoxy (ultrasonic mixing).

4.2.3 Fracture Property of the Epoxy-clay Nanocomposites

Figures 4.14 and 4.15 depict the fracture energy in the form of the critical stress intensity factor and the strain energy release rate of the neat epoxy and its nanocomposites in relation to the respective nanoclay loadings. The fracture toughness and the strain energy release rate of the neat epoxy were measured as $0.78 \text{ MPa}\cdot\text{m}^{0.5}$ and 235 J/m^2 , respectively. For the ultrasonically produced nanocomposites, the toughness values remained almost identical to that of the pristine epoxy. However, the fracture toughness increased substantially for the mechanical dispersion method. The mechanical dispersion method seems more effective than the ultrasonic mixing method in toughening epoxy by generating phase-separated microparticles. Similar behavior was also observed for the critical energy release rate; for example, by mechanically mixing 3 wt% of I.30E clay with epoxy, an increase of about 35% was observed relative to the unmodified epoxy. Figure 4.16 shows fracture energies of nanocomposites each containing 1 wt% of a specific type of the organosilicate; these nanocomposites were prepared by ultrasonic mixing. It is demonstrated that the quaternary alkylammonium ion (I.28E) exchanged montmorillonite affords a substantial improvement in epoxy toughness compared to the primary alkylammonium ion (I.30E). This finding is in agreement with observations previously made by Zilg et al. [8], who found that conventional composites as well quaternary ammonium ion exchanged fluoromica filled epoxy showed higher toughness than nanocomposites based on protonated primary amines.

In the present investigation, it was concluded that the epoxy-clay microcomposites provided better crack resistance than the nanocomposites. In nanoclay modified epoxy, crack deflection and bifurcation [22, 27, 29], crack pinning [22, 27] and matrix deformation [22, 29] are the most commonly observed crack resistance mechanisms. Matrix deformation and crack pinning are the dominant energy absorption mechanisms since crack deflection phenomenon enhances toughness only to a limited extent. Crack resistance phenomena are further explored with regard to the micromechanisms of the fracture process in the following section.

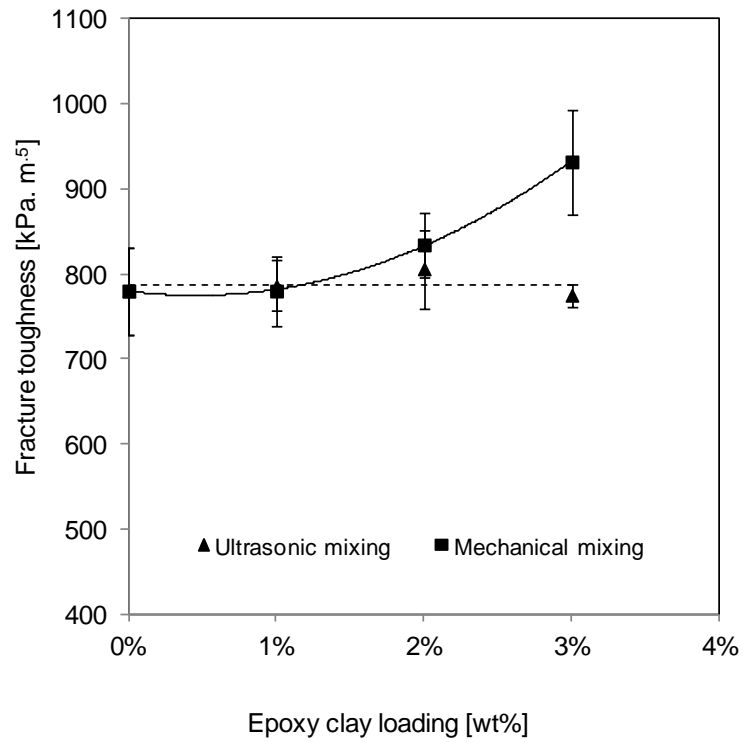


Figure 4.14 Influence of I.30E clay concentration on fracture toughness of nanocomposites.

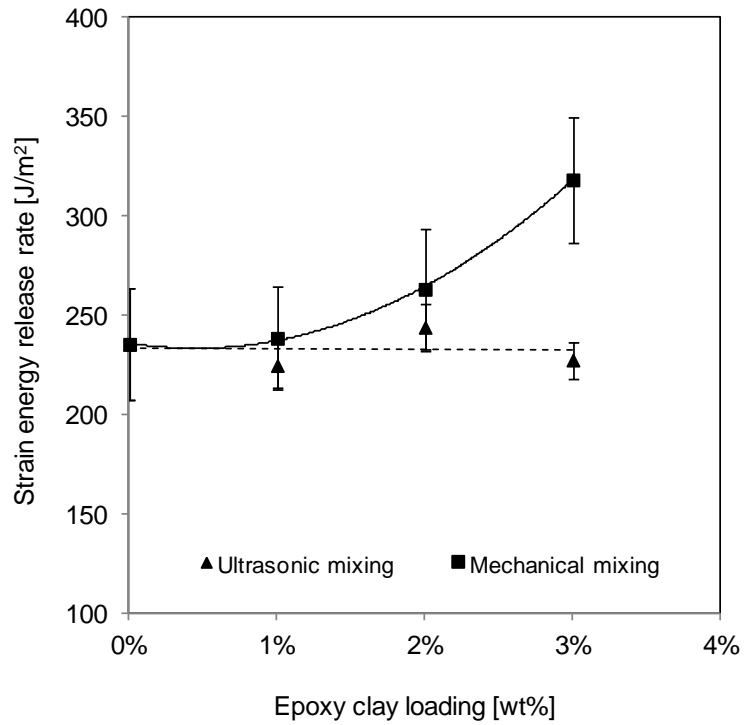


Figure 4.15 The variation of fracture energy of nanocomposites with I.30E clay loading.

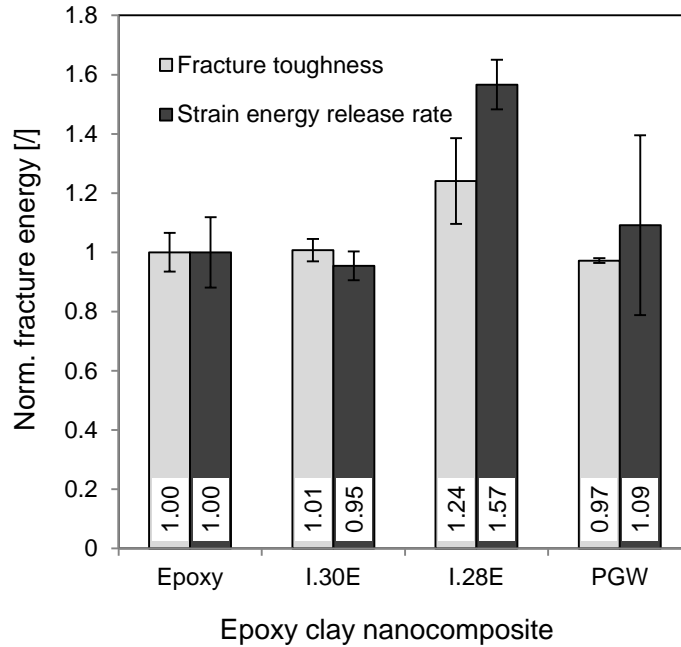


Figure 4.16 Fracture energy of the different nanoclay reinforced nanocomposites.

4.2.4 Fractographic Study of the Epoxy-clay Nanocomposites

Figure 4.17 shows smooth and featureless fracture surfaces of the unfilled epoxy representing insignificant matrix deformation that is usually observed in a homogenous brittle material.

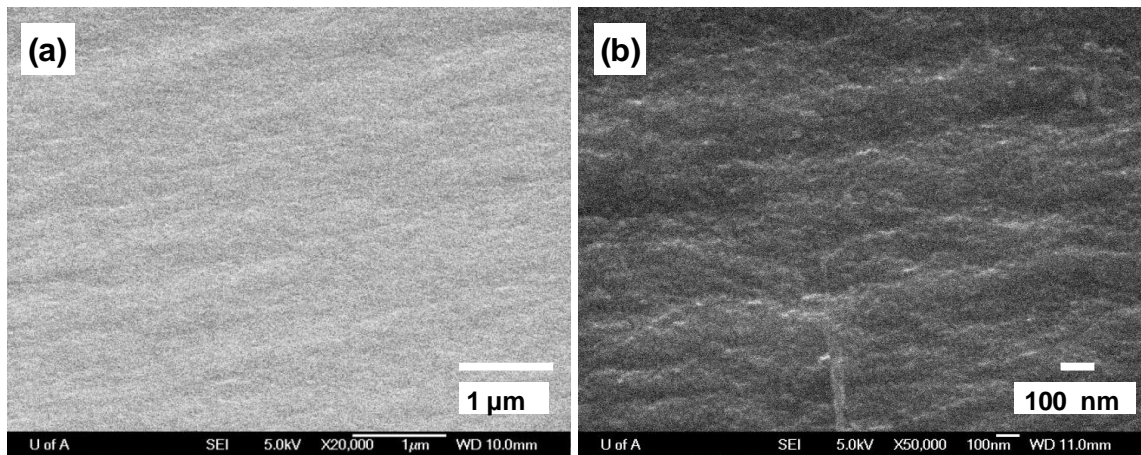


Figure 4.17 SEM micrograph of a neat epoxy fracture surface.

In general, the fracture surface of the modified epoxy was coarse and rough; the result of crack propagation through intricate and perturbed paths. Figure 4.18 shows the fracture

surfaces of the nanocomposites made by blending I.30E clay with epoxy using the ultrasonic probe. Note that arrows in the fractographic images illustrate the crack propagation direction. The higher magnification image in Figure 4.18(b) exhibits epoxy network penetration in between the silicate layers, which correlates well with the intercalated morphology observed by TEM microscopy. Clear evidence of the distorted and perturbed crack path can be seen in lower magnification images of Figures 4.18(a), (c) and (d). These tortuous paths were caused by a crack deflection mechanism when the path of a propagating crack was impeded by the uniformly distributed nanoparticles (i.e. both the intercalated parallel platelets and exfoliated isolated platelets). As this nanocomposite is mostly composed of intercalated clay structures, one would expect to see an increase in fracture toughness, but the smaller submicron-size intercalated clay tactoids behaved akin to exfoliated platelets. This notion was corroborated by the strong increase in modulus values [31]. In Figure 4.18(d), the fracture surface becomes comparatively rough for the clay loading increasing to 3 wt%. In spite of the rough surface texture, river markings are comparatively shallow indicating insignificant matrix deformation. The above observation leads to the inference that in this particular epoxy system, the occurrence of crack deflection mechanism only provided insignificant energy dissipation [32]. In some instances, cracks have penetrated through clay clusters (i.e. interparticle fracture and clay delamination). It is notable from the SEM micrographs that no visual debonding of the particle matrix interface can be observed. This indicates that there is strong interfacial adhesion between the layered silicate and epoxy in an exfoliated and intercalated structure, which also indicates that these rigid well-bonded nanoclay particles restrict the ability of adjacent epoxy polymer to experience matrix deformation.

Figure 4.19 shows SEM images of the fracture surfaces of mechanically mixed nanocomposites showing agglomerated clay of various sizes. The appearance of the textured surface, steps and clusters are indicative of a significant consumption of fracture energy. Figure 4.19(b) depicts a high magnification micrograph of a phase-separated clay structure. Fractographic evidence suggests that at a low clay concentration, agglomerated micron-size I.30E clay resulted in crack deflection and crack pinning mechanisms to be operative. This behavior closely resembles that of conventional microparticles. Characteristic pinning tails can be seen behind the particles. Such step structures form when crack fronts from two different fracture planes meet each other after being blocked by inclusions. Previously,

Moloney et al. [33] observed that the crack-pinning mechanism was responsible for increasing fracture toughness in silica and alumina modified epoxy. In another study, Kinloch et al. [34] discussed crack-pinning mechanism in glass particle filled epoxy citing the fractographic evidence of crack bowing and experimental fracture energy values. In the present study, it was observed that the size of clay aggregates increases with increasing clay concentration, while at the same time the interparticle distance decreases and roughness increases. The fracture surface shown in Figure 4.19(d) for a higher clay content of 3 wt% provides evidence for matrix deformation and particle debonding – this further distinguishes the composites prepared by the mechanical dispersion. At higher concentration, the clay agglomerates may act as stress concentrators during the fracture process and instigate localized matrix shear yielding around the clay inclusions or cause interfacial failure at the epoxy-clay interface.

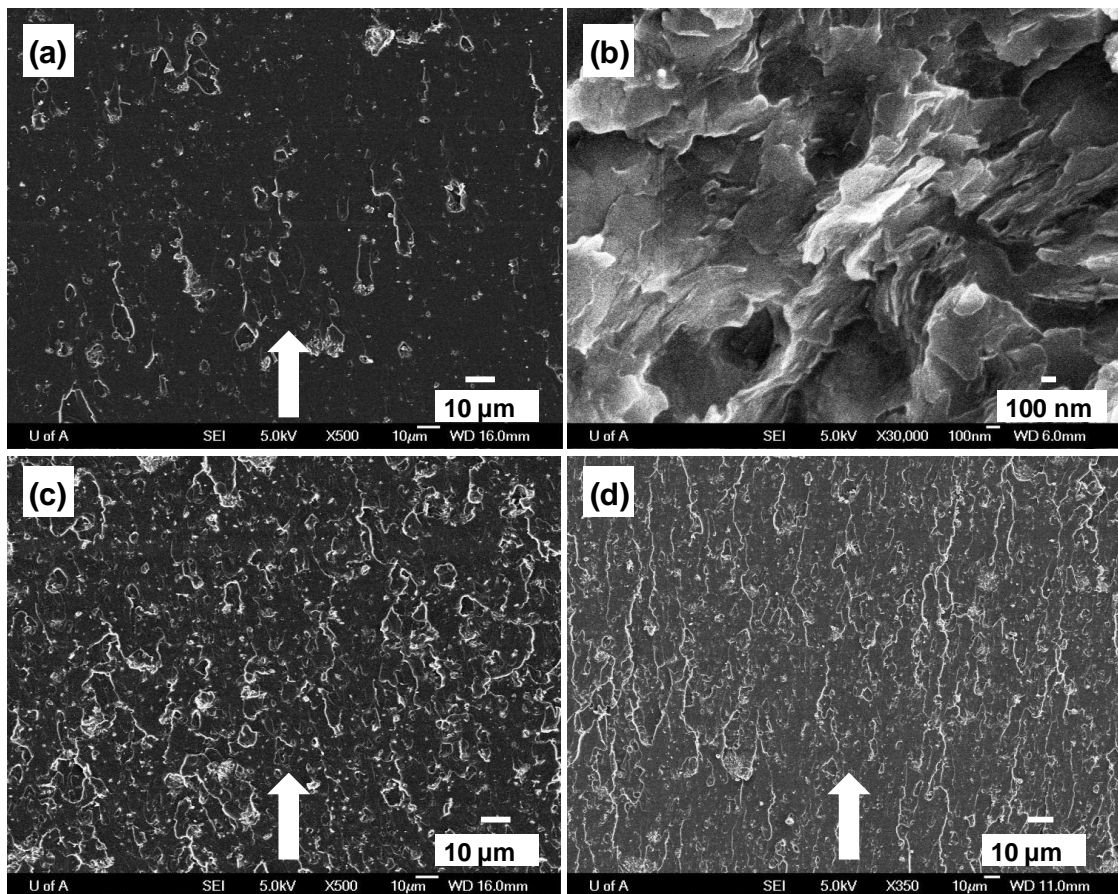


Figure 4.18 Fracture surface micrographs (SEM) of nanocomposites made by ultrasonic dispersion of epoxy containing (a) 1 wt%, (b) 1 wt% (high magnification), (c) 2 wt% and (d) 3 wt% I.30E clay.

The fracture surface topology of the I.28E clay modified epoxy shown in Figure 4.20 is extremely textured and coarse. This convoluted surface morphology confirms the occurrence of the crack deflection and crack pinning operations associated with localized matrix deformation. It appears that I.28E nanoclay assembled into uniformly distributed closely spaced microstructures in the epoxy matrix. It is conjectured that these smaller size intercalated clay assemblies were in fact very efficient in inhibiting the crack propagation by pinning. In the corresponding fracture surface, the pinning tails were overshadowed by interacting secondary crack planes. As expected, the fracture surface of epoxy with PGW clay as shown in Figure 4.21 is relatively featureless and devoid of substantial matrix damage reminiscent of the fracture surface of neat epoxy.

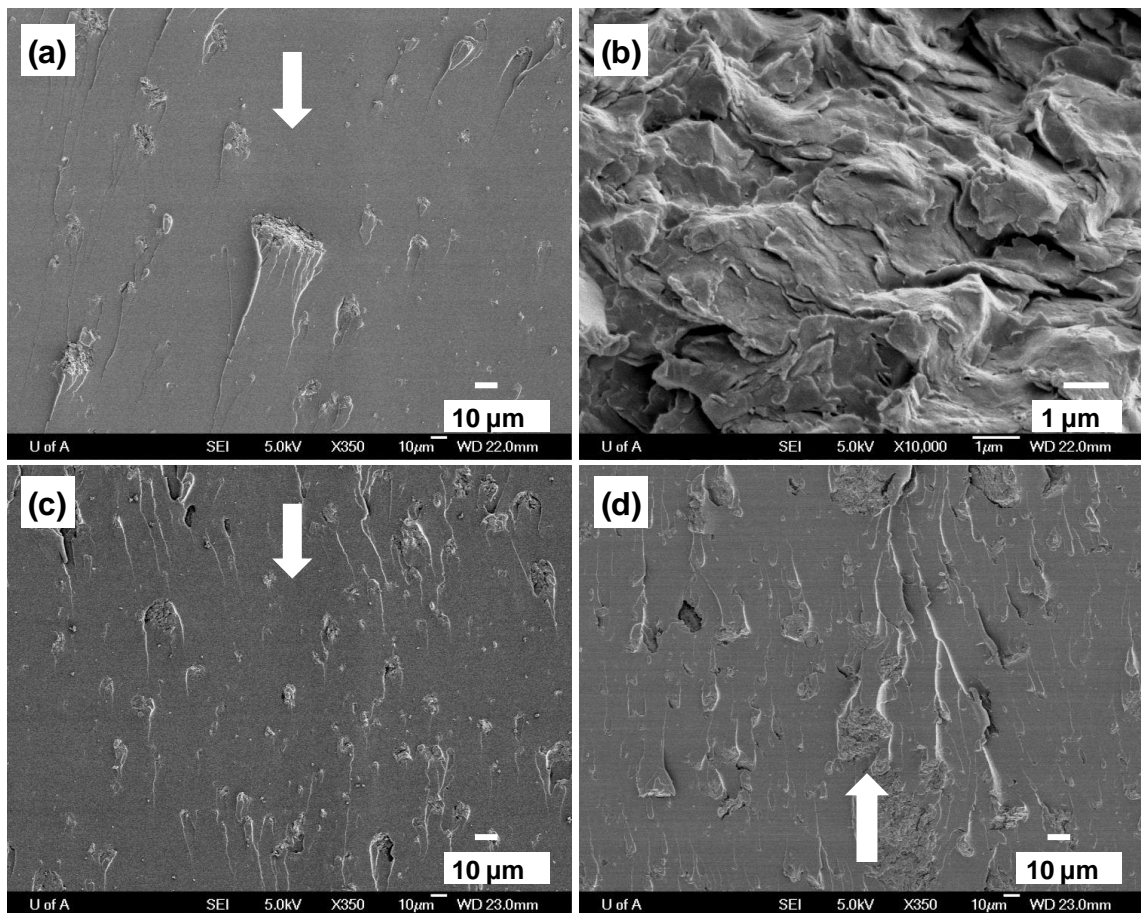


Figure 4.19 Fracture surface micrographs (SEM) of nanocomposites made by mechanical dispersion of epoxy containing (a) 1 wt%, (b) 1 wt% (high magnification), (c) 2 wt% and (d) 3 wt% I.30E clay.

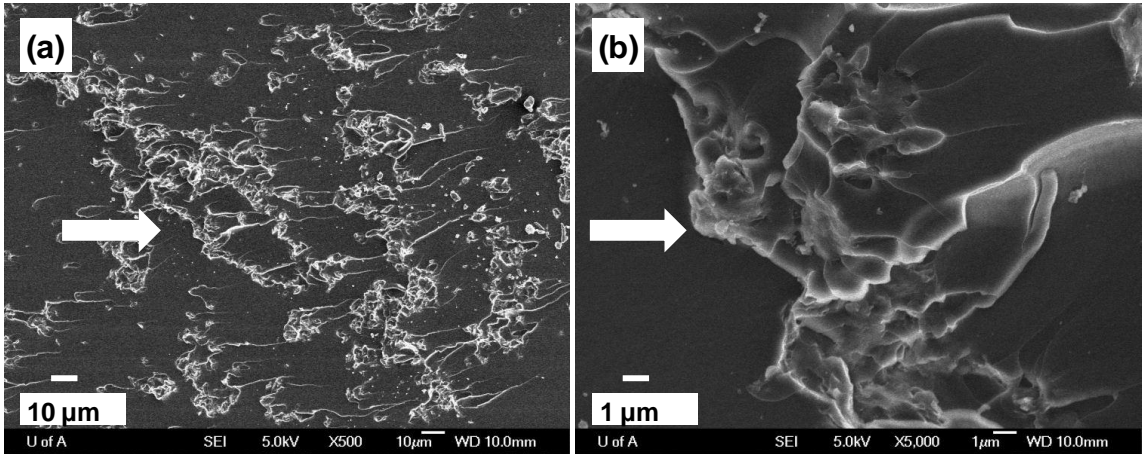


Figure 4.20 Fracture surface micrographs (SEM) of nanocomposites comprised of 1 wt% I.28E clay in epoxy at: (a) low magnification and (b) high magnification.

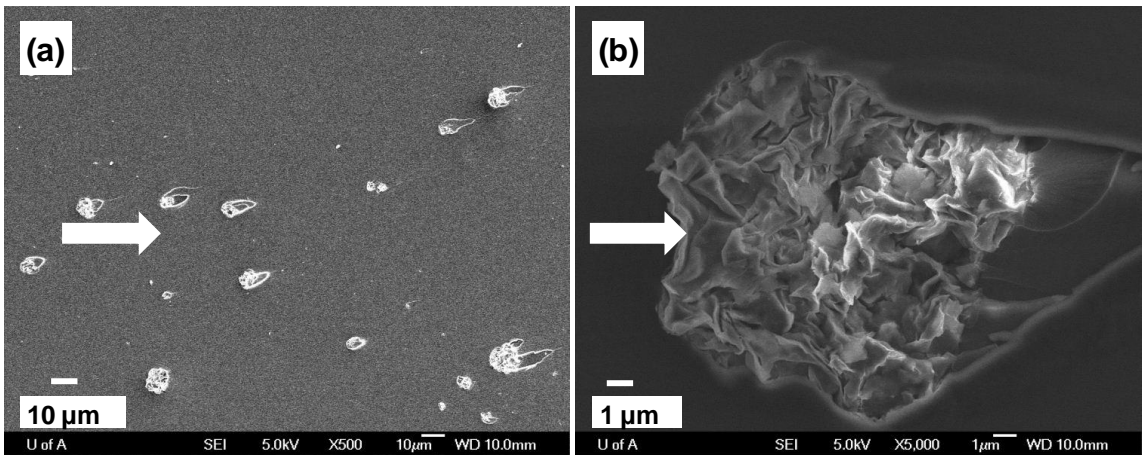


Figure 4.21 Fracture surface micrographs (SEM) of nanocomposites comprised of 1 wt% PGW clay in epoxy at: (a) low magnification and (b) high magnification.

4.2.5 Thermal Property of the Epoxy-clay Nanocomposites

Figure 4.22 delineates the glass transition temperature of the neat epoxy and its nanocomposites as a function of the I.30E organosilicate content, which was determined by DSC tests. The glass transition temperature of the neat epoxy was measured to be 117.5°C. A progressive reduction of the glass transition temperature was observed in the composites produced by the exfoliation-adsorption method. Likewise, the samples that were produced using the intercalative polymerization method showed a decrease without rendering any definite trend in the glass transition temperature. In the literature, there have been reports of

increasing glass transition temperature with nanoclay loading; and restricted segmental mobility due to epoxy being tied down at the polymer-clay interface is thought to be the reason [6, 35]. Others have shown reductions in the glass transition temperature of epoxy-clay nanocomposites [35]. In the past, the plasticizing effect of the free molecules present in the form of untreated resin, hardener and modifier [9, 19-20], homopolymerization of the DGEBA [9, 19-20] and thermal degradation of the organic modifiers at a higher curing temperature [9, 19, 22] have been identified to contribute to the reduction in glass transition temperature. The homopolymerization of the DGEBA resin can occur through catalytic influence of the alkylammonium ion of the organoclay. As a result, an overall reduction of crosslink density within the epoxy network is expected. In this study, phase-separated clay tactoids having limited epoxy solvation during the mechanical mixing and mostly intercalated structures of the ultrasonically dispersed clay showed a decrease in glass transition temperature. For these two dissimilar morphologies, the decline in the glass transition temperature did not originate from homopolymerization of DGEBA or thermal decomposition of the modifier at the curing temperature of 120°C. Therefore, the possible cause may be the plasticization of the intragallery polymer at the epoxy-clay interphase by the long chain primary alkylammonium modifier of the organoclay. Chen et al. [36] contemplated similar effect by a long-chain organic surfactant at the interphase that formed near the surface between the intercalated silicate layers. Triantafillidis et al. [37] reported on plasticizing effects of organic surfactant chains, which reduced the glass transition temperature of an epoxy-clay nanocomposite.

4.3 CONCLUSIONS

The presented study explored how variations in the nanoclay dispersion method can significantly affect the morphology, and hence, the mechanical properties of epoxy nanocomposites. In the case of primary alkylammonium exchanged clay (I.30E), the microscopic study and XRD traces of the nanocomposites revealed the creation of partly exfoliated and laminated silicate layers by ultrasonic dispersion, and phase-separated and intercalated clay agglomerates by mechanical blending. The quaternary alkylammonium treated (I.28E) and unmodified clay (PGW) assembled into intercalated clay tactoids and phase-separated microaggregates in the epoxy matrix respectively.

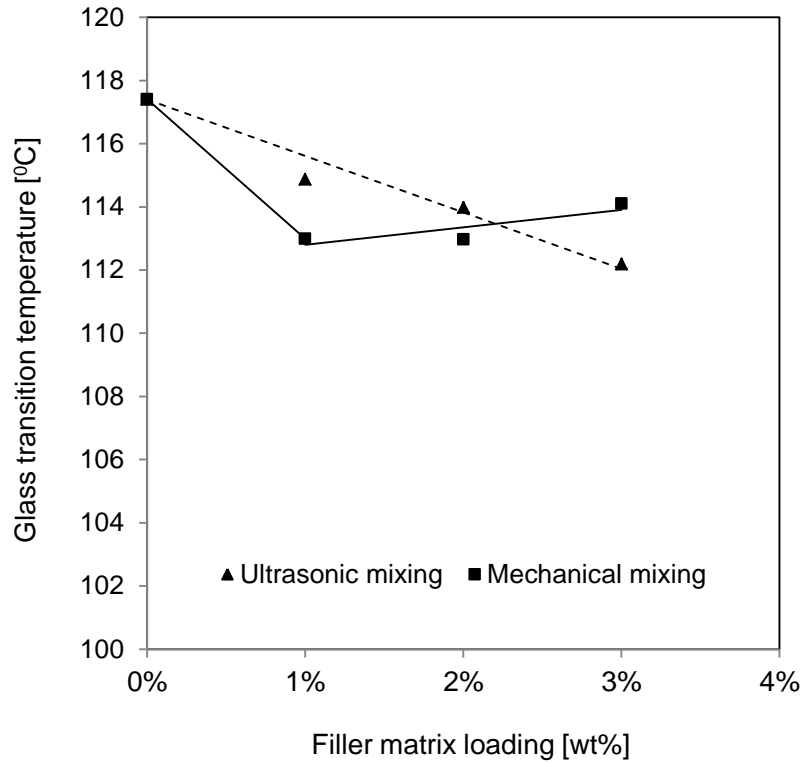


Figure 4.22 Glass transition temperature of nanocomposites as a function of I.30E clay content.

The final properties of the nanocomposites were found to be very much dependent on the macrostructure of the nanoclay inclusion. Although full exfoliation was not achieved in any of the nanocomposite systems, considerable stiffness increase was observed for ultrasonically dispersed I.30E clay. An enhancement in modulus was attributed to a combined reinforcing effect of delaminated clay platelets and intercalated submicron clay tactoids, whereas toughness was found to be independent of silicate layer separation. In contrast, the phase-separated and agglomerated I.30E clay from mechanical dispersion and the intercalated I.28E clay provided substantial fracture resistance. It is speculated that micro-reinforcements through crack deflection and crack pinning and subsequent matrix deformation mechanisms are the key to providing high crack propagation resistance. The nanocomposites fabricated by either dispersion technique resulted in slight reductions in the glass transition temperature, via the plasticizing effect of the organic surfactant present. This study highlights the fact that the

type of organic modifier and the processing method have significant influence on the ultimate properties of the nanocomposites.

REFERENCES

1. KOJIMA, Y., USUKI, A., KAWASUMI, M., OKADA, A., FUKUSHIMA, Y., KURAUCHI, T. and KAMIGAITO, O., 1993. Mechanical properties of nylon 6-clay hybrid. *Journal of Materials Research*, **8**(5), pp. 1185-1189.
2. OKADA, A. and USUKI, A., 1995. The chemistry of polymer-clay hybrids. *Materials Science and Engineering C*, **3**(2), pp. 109-115.
3. HUSSAIN, F., HOJJATI, M., OKAMOTO, M. and GORGA, R.E., 2006. Review article: Polymer-matrix nanocomposites, processing, manufacturing, and application: An overview. *Journal of Composite Materials*, **40**(17), pp. 1511-1575.
4. GIANNELIS, E.P., 1996. Polymer layered silicate nanocomposites. *Advanced Materials*, **8**(1), pp. 29-35.
5. LAN, T. and PINNAVAIA, T.J., 1994. Clay-reinforced epoxy nanocomposites. *Chemistry of Materials*, **6**(12), pp. 2216-2219.
6. MESSERSMITH, P.B. and GIANNELIS, E.P., 1994. Synthesis and characterization of layered silicate-epoxy nanocomposites. *Chemistry of Materials*, **6**(10), pp. 1719-1725.
7. KORNMANN, X., THOMANN, R., MÜLHAUPT, R., FINTER, J. and BERGLUND, L., 2002. Synthesis of amine-cured, epoxy-layered silicate nanocomposites: The influence of the silicate surface modification on the properties. *Journal of Applied Polymer Science*, **86**(10), pp. 2643-2652.
8. ZILG, C., MÜLHAUPT, R. and FINTER, J., 1999. Morphology and toughness/stiffness balance of nanocomposites based upon anhydride-cured epoxy resins and layered silicates. *Macromolecular Chemistry and Physics*, **200**(3), pp. 661-670.
9. KORNMANN, X., BERGLUND, L.A., THOMANN, R., MULHAUPT, R. and FINTER, J., 2002. High performance epoxy-layered silicate nanocomposites. *Polymer Engineering and Science*, **42**(9), pp. 1815-1826.

10. BROWN, J.M., CURLISS, D. and VAIA, R.A., 2000. Thermoset-layered silicate nanocomposites. Quaternary ammonium montmorillonite with primary diamine cured epoxies. *Chemistry of Materials*, **12**(11), pp. 3376-3384.
11. ALEXANDRE, M. and DUBOIS, P., 2000. Polymer-layered silicate nanocomposites: Preparation, properties and uses of a new class of materials. *Materials Science and Engineering R: Reports*, **28**(1), pp. 1-63.
12. LAN, T., KAVIRATNA, P.D. and PINNAVAIA, T.J., 1995. Mechanism of clay tactoid exfoliation in epoxy-clay nanocomposites. *Chemistry of Materials*, **7**(11), pp. 2144-2150.
13. PINNAVAIA, T.J., LAN, T., WANG, Z., SHI, H. and KAVIRATNA, P.D., 1996. CLAY-REINFORCED EPOXY NANOCOMPOSITES: SYNTHESIS, PROPERTIES, AND MECHANISM OF FORMATION. *ACS Symposium Series 622*, 1996, pp. 250-261.
14. KE, Y.C., 2005. *Polymer-layered silicate and silica nanocomposites*. Amsterdam: Elsevier.
15. PARK, J.H. and JANA, S.C., 2003. Mechanism of exfoliation of nanoclay particles in epoxy-clay nanocomposites. *Macromolecules*, **36**(8), pp. 2758-2768.
16. CHEN, C. and CURLISS, D., 2003. Preparation, Characterization, and Nanostructural Evolution of Epoxy Nanocomposites. *Journal of Applied Polymer Science*, **90**(8), pp. 2276-2287.
17. XIDAS, P.I. and TRIANTAFYLLIDIS, K.S., 2010. Effect of the type of alkylammonium ion clay modifier on the structure and thermal/mechanical properties of glassy and rubbery epoxy-clay nanocomposites. *European Polymer Journal*, **46**(3), pp. 404-417.
18. KORNMANN, X., LINDBERG, H. and BERGLUND, L.A., 2001. Synthesis of epoxy-clay nanocomposites: Influence of the nature of the clay on structure. *Polymer*, **42**(4), pp. 1303-1310.
19. BECKER, O., CHENG, Y.-B., VARLEY, R.J. and SIMON, G.P., 2003. Layered silicate nanocomposites based on various high-functionality epoxy resins: The influence of cure temperature on morphology, mechanical properties, and free volume. *Macromolecules*, **36**(5), pp. 1616-1625.

20. BECKER, O., VARLEY, R. and SIMON, G., 2002. Morphology, thermal relaxations and mechanical properties of layered silicate nanocomposites based upon high-functionality epoxy resins. *Polymer*, **43**(16), pp. 4365-4373.
21. HERNANDEZ, M., SIXOU, B., DUCHET, J. and SAUTEREAU, H., 2007. The effect of dispersion state on PMMA-epoxy-clay ternary blends: In situ study and final morphologies. *Polymer*, **48**(14), pp. 4075-4086.
22. LIU, W., HOA, S.V. and PUGH, M., 2005. Organoclay-modified high performance epoxy nanocomposites. *Composites Science and Technology*, **65**(2), pp. 307-316.
23. MIYAGAWA, H. and DRZAL, L.T., 2004. The effect of chemical modification on the fracture toughness of montmorillonite clay/epoxy nanocomposites. *Journal of Adhesion Science and Technology*, **18**(13), pp. 1571-1588.
24. ZERDA, A.S. and LESSER, A.J., 2001. Intercalated clay nanocomposites: Morphology, mechanics, and fracture behavior. *Journal of Polymer Science, Part B: Polymer Physics*, **39**(11), pp. 1137-1146.
25. YASMIN, A., ABOT, J.L. and DANIEL, I.M., 2003. Processing of clay/epoxy nanocomposites by shear mixing. *Scripta Materialia*, **49**(1 SPEC.), pp. 81-86.
26. KINLOCH, A.J. and TAYLOR, A.C., 2003. Mechanical and fracture properties of epoxy/inorganic micro- and nano-composites. *Journal of Materials Science Letters*, **22**(20), pp. 1439-1441.
27. SIDDIQUI, N.A., WOO, R.S.C., KIM, J.-K., LEUNG, C.C.K. and MUNIR, A., 2007. Mode I interlaminar fracture behavior and mechanical properties of CFRPs with nanoclay-filled epoxy matrix. *Composites Part A: Applied Science and Manufacturing*, **38**(2), pp. 449-460.
28. WANG, K., CHEN, L., WU, J., TOH, M.L., HE, C. and YEE, A.F., 2005. Epoxy nanocomposites with highly exfoliated clay: Mechanical properties and fracture mechanisms. *Macromolecules*, **38**(3), pp. 788-800.
29. LIU, T., TJIU, W., TONG, Y., HE, C., GOH, S. and CHUNG, T., 2004. Morphology and fracture behavior of intercalated epoxy/clay nanocomposites. *Journal of Applied Polymer Science*, **94**(3), pp. 1236-1244.

30. WANG, M.S. and PINNAVAIA, T.J., 1994. Clay-polymer nanocomposites formed from acidic derivatives of montmorillonite and an epoxy resin. *Chemistry of Materials*, **6**(4), pp. 468-474.
31. BASHAR, M.T., SUNDARARAJ, U. and MERTINY, P., 2012. Microstructure and mechanical properties of epoxy hybrid nanocomposites modified with acrylic tri-block-copolymer and layered-silicate nanoclay. *Composites Part A: Applied Science and Manufacturing*, **43**, pp. 945-954.
32. GARG, A.C. and MAI, Y.-W., 1988. Failure mechanisms in toughened epoxy resins-A review. *Composites Science and Technology*, **31**(3), pp. 179-223.
33. MOLONEY, A.C., KAUSCH, H.H. and STIEGER, H.R., 1983. The fracture of particulate-filled epoxide resins - Part 1. *Journal of Materials Science*, **18**(1), pp. 208-216.
34. KINLOCH, A.J., MAXWELL, D.L. and YOUNG, R.J., 1985. The fracture of hybrid-particulate composites. *Journal of Materials Science*, **20**(11), pp. 4169-4184.
35. BECKER, O. and SIMON, G.P., 2005. Epoxy layered silicate nanocomposites. *Advances in Polymer Science*, **179**, pp. 29-82.
36. CHEN, J.-S., POLIKS, M.D., OBER, C.K., ZHANG, Y., WIESNER, U. and GIANNELIS, E., 2002. Study of the interlayer expansion mechanism and thermal-mechanical properties of surface-initiated epoxy nanocomposites. *Polymer*, **43**(18), pp. 4895-4904.
37. TRIANTAFILLIDIS, C.S., LEBARON, P.C. and PINNAVAIA, T.J., 2002. Homostructured mixed inorganic-organic ion clays: A new approach to epoxy polymer-exfoliated clay nanocomposites with a reduced organic modifier content. *Chemistry of Materials*, **14**(10), pp. 4088-4095.

Chapter 5

Study of Morphology and Mechanical Property of Acrylic Triblock-copolymer Modified Epoxy²

SYNOPSIS: Acrylic triblock-copolymers of different compositions and constituents were used to modify epoxy resin. In epoxy the block-copolymers self-assembled to generate different nanostructured phases. Spherical micelles and vesicles were formed due to preferential interactions among constituents of the blends. The effect of modifier concentration and morphology on the resulting mechanical properties was investigated. At a modifier content of 5 wt% a more than threefold increase in critical strain energy was observed relative to the unfilled epoxy for the block-copolymer/epoxy systems studied. This improvement was accompanied by slight reductions in the tensile stiffness, strength and glass transition temperature of developed epoxy blends. Microstructure studies revealed that during crack propagation, vesicle and micelle structures respectively underwent debonding and cavitation followed by shear yielding of the substrate matrix.

5.1 INTRODUCTION

Thermosetting polymer epoxy has been recognized as one of the materials of choice for structural adhesives, thin film coatings and matrix materials for fiber-reinforced polymer composites. Compared to other engineering polymers, epoxy resins generally provide better stiffness, creep resistance, chemical inertness and high temperature applicability. Unfortunately they are also subject to certain shortcomings, such as having high brittleness and notch sensitivity. To date, significant research has been conducted to increase the toughness of epoxy resin by reinforcing with dispersed micro-particles. Blending epoxy with a liquid-rubber phase [1-12] is a rather established method, and incorporating thermoplastic [13-16] and core-shell [17-22] particles are known to have

² A version of this chapter has been published as: BASHAR, M.T., SUNDARARAJ, U. and MERTINY, P., 2013. Morphology and mechanical properties of nanostructured acrylic tri-block-copolymer modified epoxy, *Polymer Engineering and Science*, DOI: 10.1002/pen.23648.

improved epoxy toughness. These micron size particles can distinctly enhance epoxy toughness, but at the same time degrade important mechanical and thermal properties (e.g. stiffness and service temperature). Also, many of these particles pose considerable mixing and dispersion problems.

Toughening thermosets by elastomeric/thermoplastic particles is an extensively studied topic, and numerous toughening mechanisms have been observed thus far. Particle cavitation [5-8, 23], matrix shear yielding [4-9, 22-24], crazing [1-2, 23-24], rubber stretching [3, 23-24], crack pinning [23-24] and crack deflection [23-24] are some of the toughening concepts well recognized in rubber modification of polymer. Depending on the material systems and operating conditions (e.g. applied loading), desired toughening is achieved by the function of a single mechanism or through a complex combination of simultaneous and successive actions of different processes. It is therefore of great importance to thoroughly understand the principles and fundamentals of different toughening mechanisms to effectively apply the appropriate toughener phase in order to meet the intended toughness requirement of a polymer. Material properties such as matrix cross-link density [7, 11-12], particle morphology [21-22, 25] and size [1, 8, 19-20], degree of dispersion [20] and interfacial property [24] also influence the toughness of rubber modified epoxy. It was observed that lightly cross-linked epoxies can easily deform and shear yield [26], and for effective toughening the optimal particle size was located within the range of 0.2 to 5 μm .

Recently it has been demonstrated that nanostructured block-copolymers can be an attractive alternative to the conventional micro-particles. Self-assembling amphiphilic block-copolymers provide a highly efficient way of improving epoxy toughness with a relatively low amount of additive loading [26-41]. Typically, block-copolymers are distinct and chemically dissimilar polymer blocks linked together by covalent bonds. Up until very recently, the application of block-copolymer has been mainly concentrated as compatibilizing agents and surfactants. The unique toughness property of block-copolymer modified thermosets stem from their characteristic self-ordering micro/nano domain configurations inside the thermoset. According to the dilute disordered phase behavior in a selective solvent such as epoxy, the block-copolymers can spontaneously self-assemble mainly into three equilibrium morphologies, i.e. spherical micelles,

cylindrical micelles and vesicles [28, 31-35]. Organization to the nanostructured morphologies is dictated by chemical interactions (block-block, block-solvent), polymer molecular weight, copolymer/solvent composition and concentration [32-34, 36].

It should be mentioned that there are alternative ways to toughen epoxy, which require chemical flexibilization/functionalization of epoxy backbone, increasing molecular weight of the epoxy monomer and reducing density of the epoxy cross-link network [24]. Modification of the epoxy resin chemistry or changed to a different polymer system was not within the scope of this research. Therefore, toughening by dispersion of a second-phase material was chosen as the preferred method for this study. The intent of the present research is to study the toughening effect of two ABA type triblock-copolymers on the epoxy system under investigation. These ABA triblock-copolymers are expected to easily dissolve in epoxy and self-organize on the nano-level due to the affinity between epoxy monomer and poly(methylmethacrylate) and the repulsion between epoxy and the middle poly(n-butylacrylate) block. A miscibility study and morphology characterization of the block-copolymers in epoxy was performed by different analytical techniques. Tensile properties, fracture toughness and associated crack resistance micromechanisms of the fully cured block-copolymer/epoxy blends were investigated.

5.2 RESULTS AND DISCUSSION

5.2.1 Miscibility of Block-copolymer/Epoxy Blends

In the M52 and M52N block-copolymers P BuA is the immiscible block causing segregation in epoxy and PMMA and P(MMA-*co*-DMA) are the miscible blocks giving compatibility towards epoxy. Binary mixtures containing DGEBA resin and any of the M52 and M52N block-copolymers appeared transparent preceding curing, indicating no macroscopic phase separation and complete miscibility with the epoxy precursor. Preparation of different block-copolymer/epoxy blends are presented in Section 2.2.2. Previously, Ritzenthaler et al. [42] and Woo and Wu [43] reported formation of homogenous solutions between different compositions of poly(methylmethacrylate) (PMMA) with DGEBA. Their inference was based on the transparency of the solutions and the detection of a single glass transition temperature that is dependent on the

composition of the blends. However, in the reactive mixtures (DGEBA and the curing agent), Ritzenthaler et al. [42] observed that the PMMA miscibility and consequently final morphology of the cured blends depends on the nature of the curing agent used. In the present study, it was noticed that M52-epoxy blends became opaque, but M52N-epoxy blends preserved transparency up to the end of epoxy-amine cross-link reaction. This observation suggests improved M52N block-copolymer compatibility by the P(MMA-*co*-DMA) random copolymer. It has been shown previously in the literature that the DMA units in P(MMA-*co*-DMA) copolymer increased the miscibility and stability of block-copolymer nanostructures in thermosets (e.g. epoxy, unsaturated polyester) until completion of the polymerization reaction [28-29, 41]. In the case of M52-epoxy blends it is conjectured that the block-copolymers rearranged themselves during progression of the curing reaction that changed the equilibrium of the system due to an increase in epoxy molar mass. Therefore, a dependence of the final nanostructures on the constituents of the block-copolymers was observed.

Fourier transform infrared spectroscopy (FTIR) was performed to identify any specific interactions between epoxy and the block-copolymers. Figure 5.1 shows absorbance spectra between 650 cm^{-1} and 4000 cm^{-1} for neat epoxy and blends of epoxy having 5 wt% M52 and M52N block-copolymers, respectively. Careful examination of FTIR spectra of Figure 5.1 reveal shifting and/or broadening of the O-H (3411 cm^{-1}) and C=O (1709 cm^{-1}) stretching absorption peak of the epoxy blends relative to the neat epoxy. Earlier, Janarthanan and Thyagarajan [44] speculated that the alteration of C=O and O-H absorption bands is due to the hydrogen bonding between carbonyl groups of PMMA and hydroxyl groups of DGEBA [45]. The increased level of molecular interaction is reflective of the outstanding miscibility of M52 and M52N block-copolymers with epoxy. Thus, this specific interaction of PMMA and P(MMA-*co*-DMA) with epoxy is thought to have influenced the nanostructure development and afterwards its stabilization at the time of epoxy polymerization.

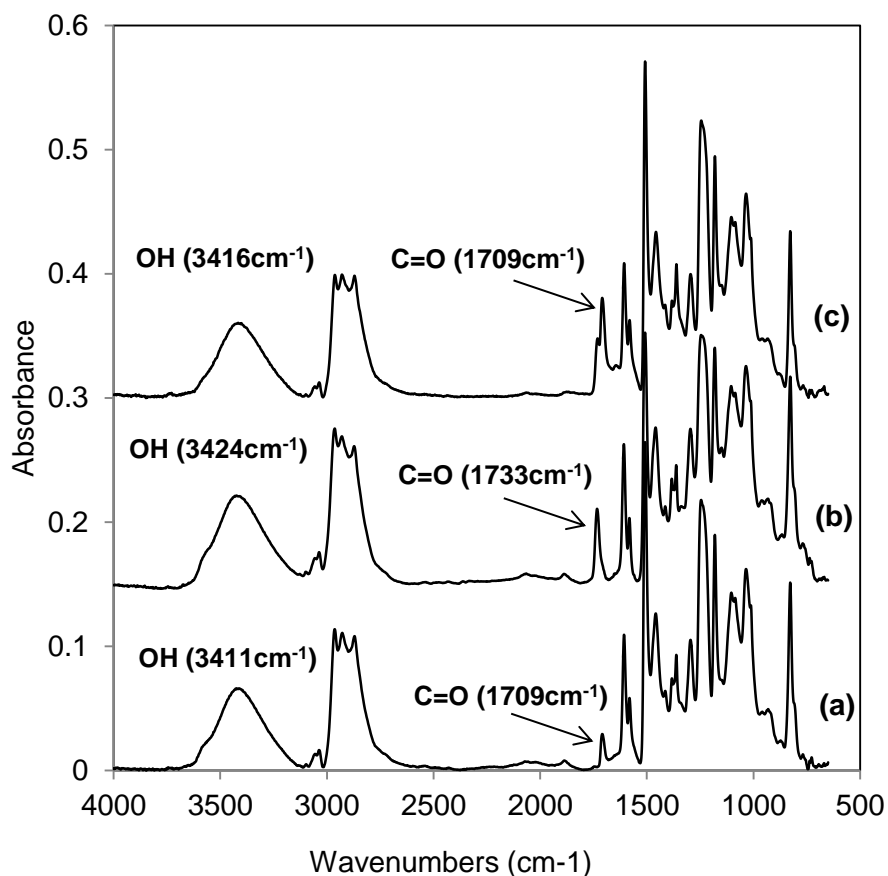


Figure 5.1 FTIR spectra of cured (a) neat epoxy and (b) 5 wt% M52 and (c) 5 wt% M52N modified epoxy blends.

5.2.2 Microstructure of Cured Block-copolymer/Epoxy Blends

The epoxy blends that were modified with M52 block-copolymer are opaque, and the ones containing M52N block-copolymer are transparent after cure as shown in Figure 5.2. This observation suggests that in M52 modified epoxy the dispersed phases are probably large enough to scatter visible light; this interpretation has been further supported by TEM microscopy. TEM micrographs shown in Figure 5.3 and 5.4 reveal a two-phase morphology of the block-copolymer modified epoxy, where the epoxy domain appears gray and block-copolymer phase seems black. Randomly dispersed bilayer vesicles with size ranging between 200~400 nm are visible in the M52-epoxy blend (see Figure 5.3). In Figure 5.4, samples made with M52N exhibit disordered spherical micelles with diameter of approximately 20~30 nm and without any sharp interface (i.e.

diffused boundary) between the matrix and block-copolymers. Similar nanostructured morphologies have been reported earlier by Gerard et al. [28] and Maiez-Tribut et al. [41] between epoxy and P[(MMA-*co*-DMA)-*b*-BuA-*b*-(MMA-*co*-DMA)] block-copolymer. Gerard et al. [28] reported a reaction-induced phase separation of PMMA homopolymers and P[MMA-*b*-BuA-*b*-MMA] block-copolymers in epoxy, but when a random copolymer of methylmethacrylate (MMA) and *N,N*-dimethylacrylamide (DMA) was introduced in epoxy, a miscible mixture was achieved. Therefore, it is presumed in this study that the existence of P(MMA-*co*-DMA) block in the M52N block-copolymer stabilizes the micelle configurations during the time of epoxy curing. Spherical micelles have a structure consisting of a rubbery core encircled by a spherical hard shell. On the other hand, vesicles are made of a bilayer spherical shell enclosing an epoxy core. Previous studies on amphiphilic block-copolymers in epoxy systems documented transitions from spherical to cylindrical micelles to vesicles with decreasing volume fraction of the miscible block [31-34]. The TEM micrographs also evidence the absence of macroscopic phase-separation of different polymer phases.

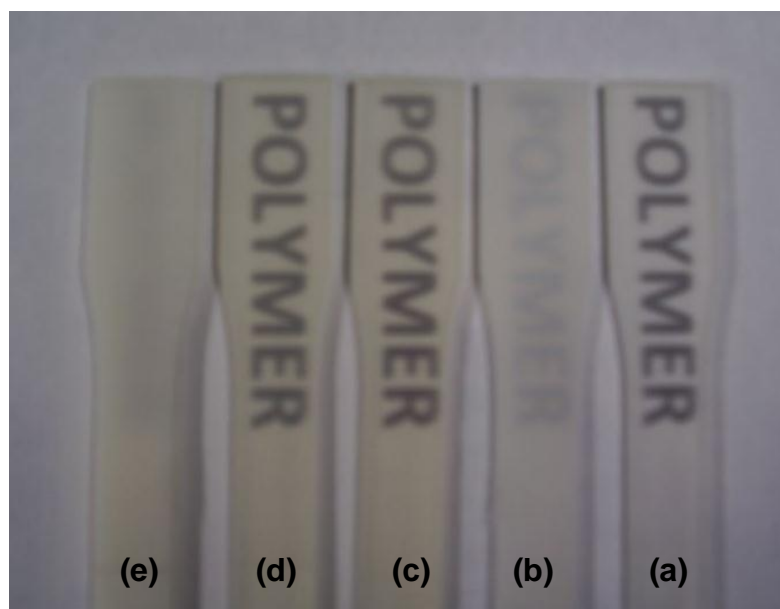


Figure 5.2 Transparency of (a) neat epoxy and (b) 3 wt% M52, (c) 3 wt% M52N, (d) 5 wt% M52N and (e) 5 wt% M52 modified epoxy blends.

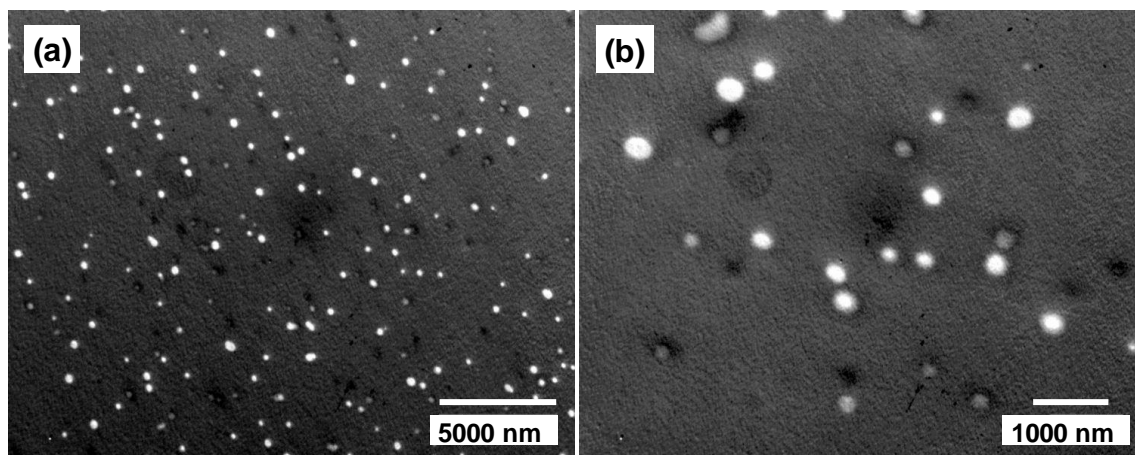


Figure 5.3 TEM micrographs of 3 wt% M52 block-copolymer modified epoxy blends at (a) low and (b) high magnifications.

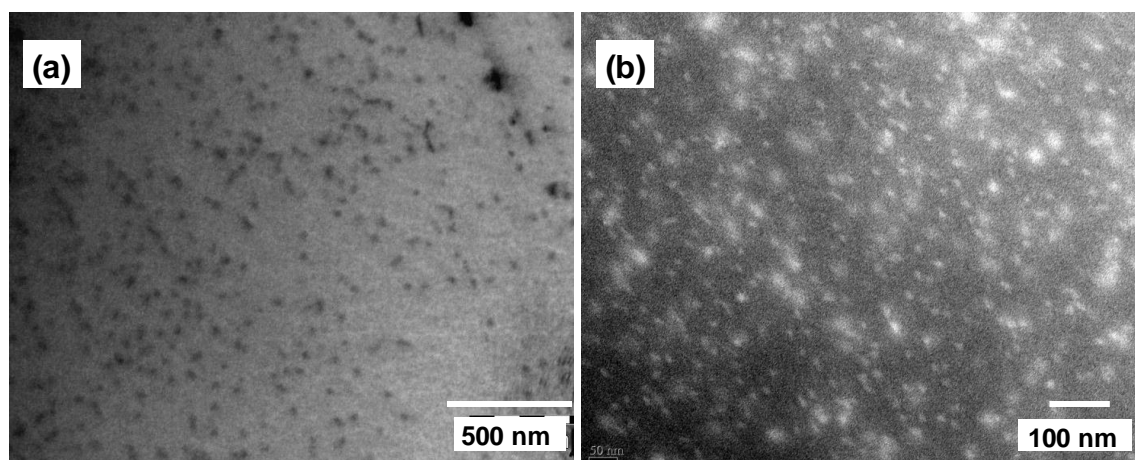


Figure 5.4 TEM micrographs: (a) 3 wt% M52N (without osmic acid staining) and (b) 5 wt% M52N (with osmic acid staining) block-copolymer modified epoxy blends.

Figure 5.5 shows the DSC traces of pure epoxy and its blends with 5 wt% M52 and M52N block-copolymers respectively. The evolution of a single glass transition temperature (T_g) slightly lower than the T_g of neat epoxy indicates a uniform dispersion of block-copolymer to a very small scale (i.e. nano-scale) and good compatibility with epoxy [34, 37, 42]. In Figure 5.6 dynamic mechanical-thermal spectra from DMA test are compared between 5 wt% block-copolymer/epoxy blends and neat epoxy. From the $\tan \delta$ versus temperature plot maximum peak values were taken as the α -relaxation peak representing the glass transition temperature. In the fully cured epoxy blends, a single

relaxation peak near the pure epoxy relaxation is located. This observation further corroborates previous TEM and DSC results that macrophase phase-separation did not take place during thermoset network formation, but rather that dispersed nanostructured domains randomly distributed in the epoxy substrate. It was noticed that the T_g values measured for neat epoxy are 117°C and 119°C according to the DSC and DMTA methods, which indeed are quite close. The T_g values estimated for the block-copolymer modified epoxy demonstrated some variability among different measurement methods, which again can be considered well within the experimental uncertainty of these techniques. Furthermore, it was observed that the relaxation time was shortened in the case of the modified systems with respect to the neat resin, yet this observation is not very conclusive. It was also ascertained from the DMTA results that the modified epoxies exhibited a lower storage modulus value compared to the neat epoxy in the 30°C to 100°C temperature range.

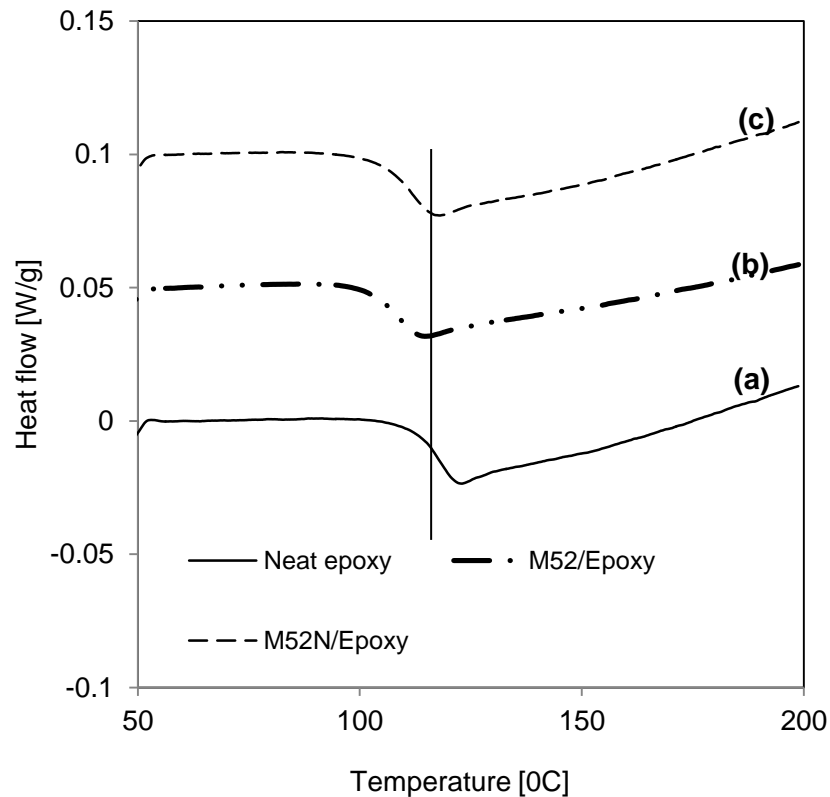


Figure 5.5 DSC thermograms of cured (a) neat epoxy and (b) 5 wt% M52 and (c) 5 wt% M52N block-copolymer modified epoxy.

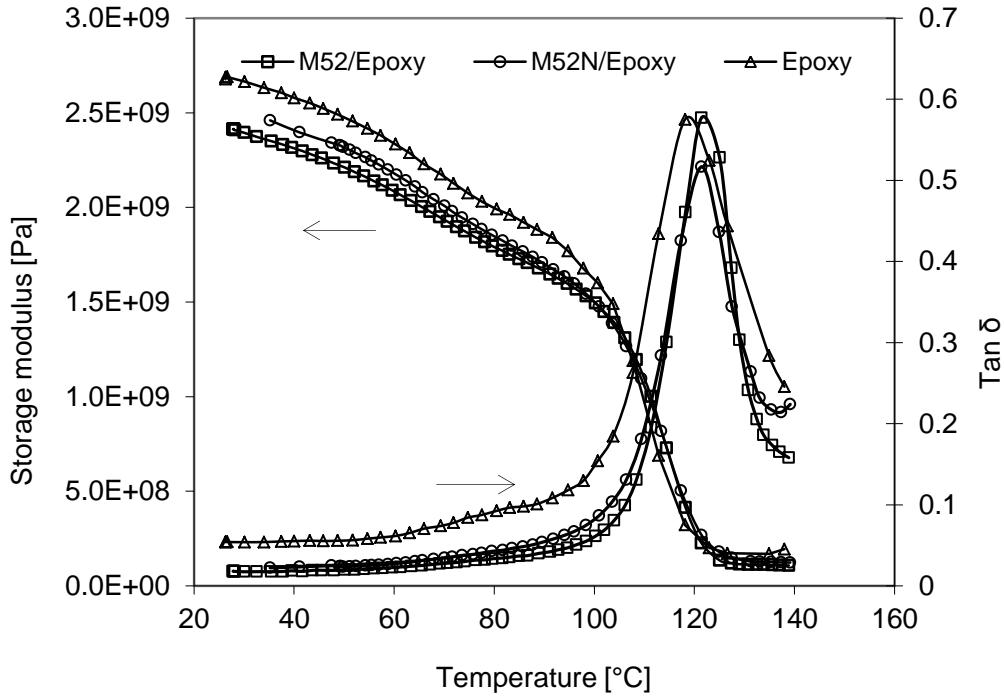


Figure 5.6 DMTA plot showing storage modulus and $\tan \delta$ curves of neat and 5 wt% block-copolymer modified epoxy.

5.2.3 Tensile Properties of Block-copolymer/Epoxy Blends

Average tensile property values are reported in Table 5-1 along with the corresponding standard deviations. At least four specimens were tested for each epoxy blends except that the 3 wt% M52N modified epoxy data is based on only two tests. The influence of the block-copolymer weight percentages on mechanical properties of the cured epoxy is shown in Figures 5.7 and 5.8. Tensile modulus of M52 and M52N modified epoxy systems are compared in Figure 5.7 for various block-copolymer concentrations. It was observed that stiffness remained almost unchanged with increasing M52 content, while the addition of M52N caused a slight reduction in modulus [38]. Tensile strength results are presented in Figure 5.8 for the modified epoxy blends. As expected, strength values decreased only marginally for the whole range of modifier concentrations studied. Pearson and Yee [6] and Bagheri and Pearson [9, 22] reported that increasing rubber content caused reduction of the modulus and yield strength of modified epoxies. It has been discussed in the literature [6, 9, 10, 15] that the application of tensile loading resulted in stress concentrations around the particle inclusions until dissipation of this

energy by matrix deformation, leading to a reduction in the yield stress of the material. A similar tendency is observed in the present study for the block-copolymer/epoxy blends with a minor reduction in strength and stiffness. It was also inferred that with increasing block-copolymer concentration, more dispersed particles with interacting/overlapping stress fields would further decrease composite failure strength [6]. It is thought that the particle size and distribution, morphology (e.g. micelles and vesicles) and interfacial adhesion all played an important role in the stress distribution around the particles. It should be noted that the vesicles are made of spherical structures of hard and rubbery shells and an enclosed epoxy domain. It is presumed that a complex stress state exists associated with the vesicles, which will require further investigation of the stress distribution in epoxy to fully understand the mechanism of failure. In general, retention of both tensile modulus and strength is an indication of good compatibility (e.g. interface property) and stability of the nanostructured block-copolymers with epoxy. Room temperature modulus values normalized with respect to the unmodified epoxy are plotted in Figure 5.9, presenting both tensile and DMTA (see also Figure 5.6) test data. These results indicate consistency and good agreement among different test methods regarding measurement of modulus. The block-copolymer addition resulted in a modest drop in epoxy stiffness, irrespective of the test method used.

Table 5-1 Property of modified epoxy blends constraining various types and concentrations of block-copolymers.

Filler matrix loading (wt%)	Tensile modulus (GPa)	Tensile strength (MPa)	Fracture toughness (MPam ^{0.5})	Strain energy (J/m ²)	Glass transition temp (°C)
0 (neat epoxy)	2.82 ± 0.08	82.2 ± 1.56	0.78 ± 0.05	235 ± 28	117
1 wt% M52	2.81 ± 0.11	79.6 ± 1.07	0.99 ± 0.06	350 ± 46	104
3 wt% M52	2.73 ± 0.03	76.7 ± 2.35	1.28 ± 0.07	605 ± 44	110
5 wt% M52	2.78 ± 0.03	75.6 ± 0.4	1.51 ± 0.06	865 ± 55	108
1 wt% M52N	2.71 ± 0.04	78.8 ± 0.6	0.87 ± 0.04	285 ± 37	115
3 wt% M52N	2.68 ± 0.01	74.1 ± 2.89	1.26 ± 0.12	495 ± 78	99
5 wt% M52N	2.64 ± 0.05	77.7 ± 0.38	1.48 ± 0.03	765 ± 60	111

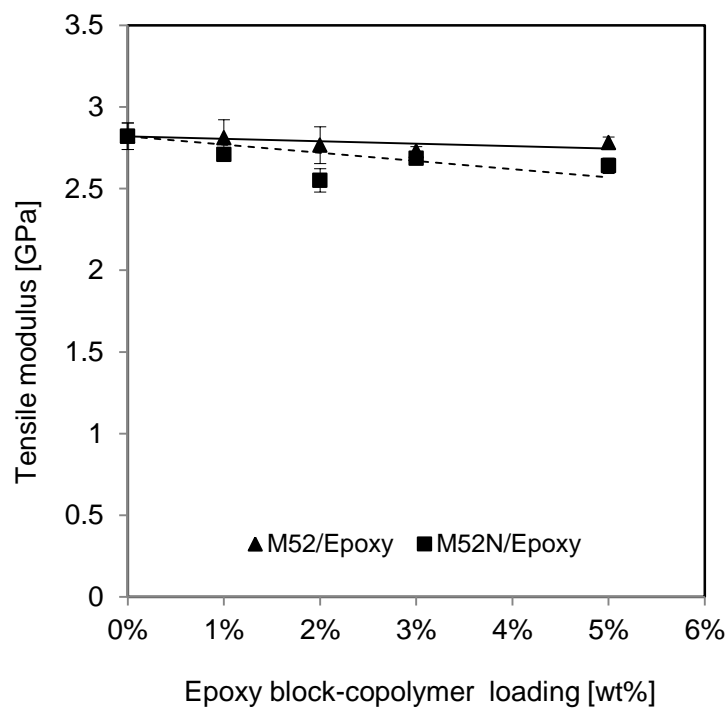


Figure 5.7 Tensile modulus of modified epoxy as a function of block-copolymer content.

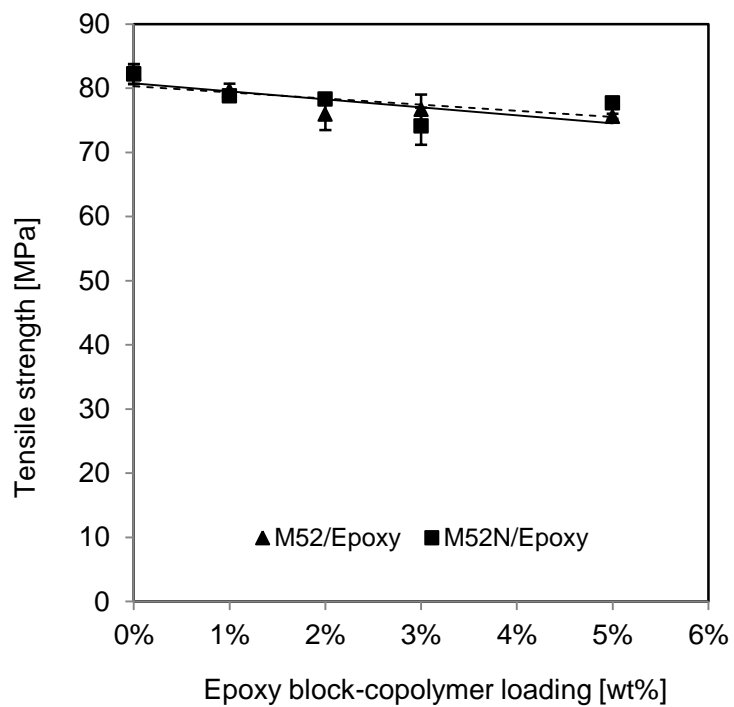


Figure 5.8 Influence of block-copolymer concentration on tensile strength of modified epoxy.

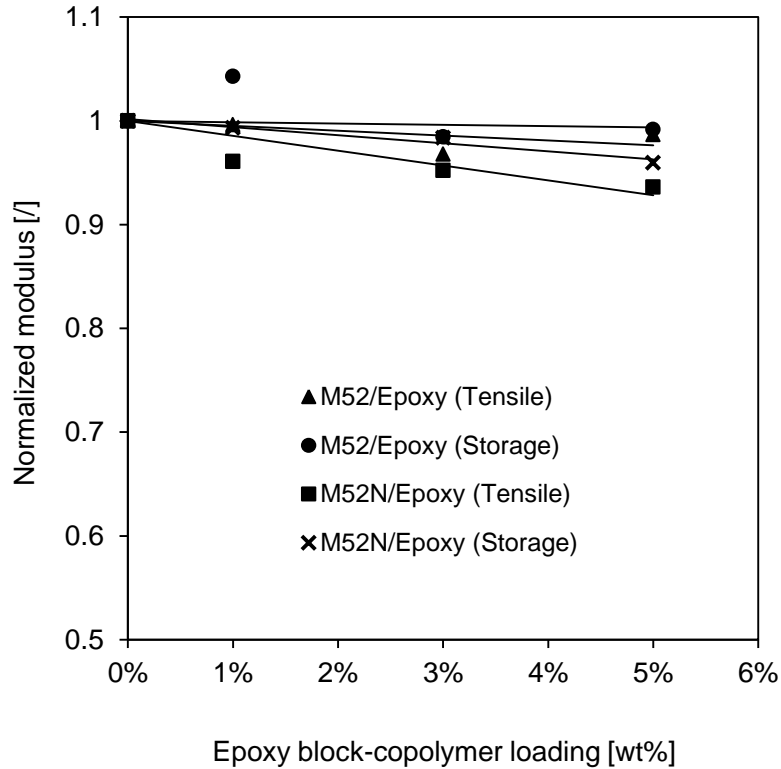


Figure 5.9 Effect of block-copolymer content on modulus of modified epoxy.

5.2.4 Fracture Properties of Block-copolymer/Epoxy Blends

Figure 5.10 illustrates fracture toughness of modified epoxy as a function of block-copolymer content. All the epoxy blends greatly enhanced epoxy fracture toughness approximately proportional to modifier loading, that is, the data points for the fracture toughness of the modified epoxy in Figure 5.10 follow a linear relationship with block-copolymer concentration. But, it is expected that at significantly higher concentrations the initial linear trend will eventually reach a plateau, similar to the behavior what was observed in the case of rubber modified epoxy [9, 18]. An approximately two-fold increase for both the M52 and M52N blends was the observed maximum for a modifier loading of 5 wt%. Critical strain energy release rate values are presented in Figure 5.11. As expected, the strain energy for the blends containing 5 wt% block-copolymers improved remarkably by a factor of 3.5 for the M52 and about 3.2 for the M52N over the base epoxy. The vesicles in M52 modified epoxy generated marginally higher fracture toughness than the spherical micelles of M52N block-copolymer. Comparable

improvements in the fracture energy for vesicles and spherical micelles toughened epoxy systems have been reported before in the published literature [30, 33-34]. It is thought that the cavitation/debonding of the block-copolymer inclusions and subsequent matrix shear deformation are the main energy dissipation modes for the modified epoxy blends [27, 36], which has been discussed further in light of the micromechanisms of the fracture process in the following.

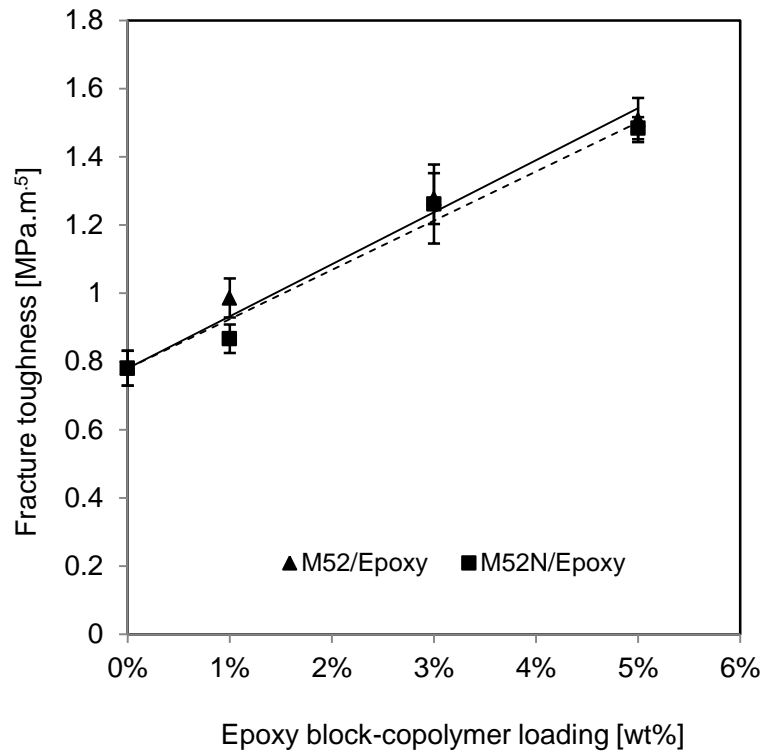


Figure 5.10 Fracture toughness of modified epoxy plotted against corresponding block-copolymer concentration.

Fracture surface micrographs (using SEM) of pure epoxy and block-copolymer toughened epoxy are displayed in Figures 4.16 (see Chapter 4), 5.12 and 5.13. The neat epoxy fracture surface shown in Figure 4.16 is clearly plain and featureless, which is typical of a brittle failure in an amorphous material. In comparison to the neat resin, the fracture surface of M52 modified epoxy shown at low magnification in Figure 5.12(a) is extensively uneven, more convoluted and coarse, which are definite signs of significant crack resistance. Morphological evidence from the higher magnification image of Figure

5.12(b) exhibits vesicle pullout, spherical craters, cleaved edges and matrix deformation. These visible markings on the cracked surface correlate well with the large fracture toughness increase observed with the vesicles morphology. Therefore, from the above illustrations, it may be hypothesized that in the M52 modified epoxy, crack propagation is predominantly by particle-matrix interfacial debonding followed with matrix shear deformation and/or by crack deflection, which are all energy absorption phenomena [32, 34]. As the opposite fracture surfaces detached by ligament breaking, the vesicles either extracted or remained embedded in the same position to the matrix. It becomes apparent that vesicle cavitation did not take place because of an encased inner core made of a rigid cross-linked epoxy network having high cavitation resistance. Also from Figure 5.12(b) uniform dispersion of vesicles is clearly evident.

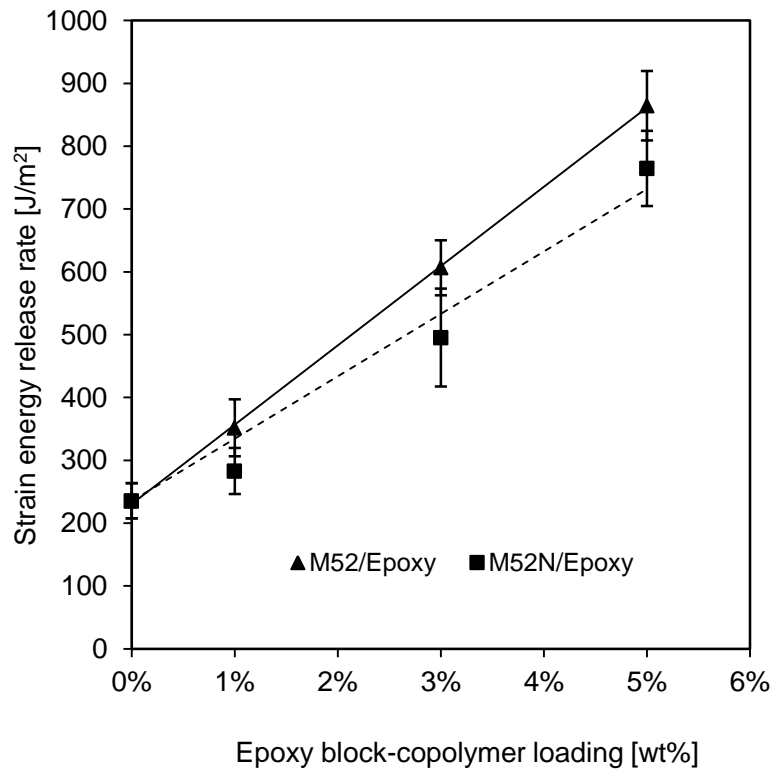


Figure 5.11 Strain energy release rate of modified epoxy plotted against corresponding block-copolymer concentration.

It is apparent from the low magnification image in Figure 5.13(a) that the spherical micelles in M52N modified epoxy generated matrix rich regions and relatively plain

surface features devoid of significant matrix damage that is reminiscent of pure epoxy. Figures 5.13(b)-(c) (at high magnification) shows some interesting surface morphology of the epoxy matrix that contains spherical micelles, such as minute spherical nano-cavities and microscopic fine surface roughness. It is surprising to note that the size and morphology of the spherical micelles and vesicles have marked differences, but are still able to yield equivalent toughness. Several researchers have documented the importance of the reinforcement size in rubber toughened [1, 8, 19-20] and block-copolymer [34] modified epoxies. The vesicles studied are well within the optimal size ranges of 0.2 to 5 μm , but the micelles size fall below that reported previously for efficient toughening of epoxy. Pearson and Yee [8] showed that smaller rubber particles were more effective in toughening epoxy than the larger particles, and their smallest particles were about 0.2 μm in size. According to Pearson and Yee [8], the particle size effect on toughening can be realized based on its behavior at the crack-tip plastic zone, i.e. smaller particles cavitate, while larger particles play the role of bridging sites. Recently, Liu et al. [38] showed evidence of nano-scale cavitation processes in spherical micelles as small as 15 nm in size by relieving the hydrostatic stress state at the crack-tip. Similar toughening mechanisms are well established in the field of rubber modified epoxy [5-8].

In agreement with the hypothesis presented by Wu et al. [32] and Liu et al. [38], the present author speculates that during plane-strain fracture testing the triaxial stress state at the crack front dilates/cavitates the poly(n-butylacrylate) rubbery core of the micelles, thereby modifying the stress condition to initiate matrix shear yielding. Hence, for the spherical micelles, the crack resistance mechanism is equivalent of particle cavitation (debonding), which alters the stress field ahead of the crack-tip and promotes matrix shear yielding. The above observation is also supported by tensile and fracture toughness results. Wu et al. [32] and Gerard et al. [28] respectively showed worm-like (cylindrical) micelles and micro-clustered block-copolymer structures (i.e. interconnected/co-continuous structures), which demonstrated the highest fracture toughness improvements. Therefore, it can be presumed that in the present study even greater toughness enhancement would be achieved if a worm-like micelle structure or an interconnected morphology [21-22] was obtained.

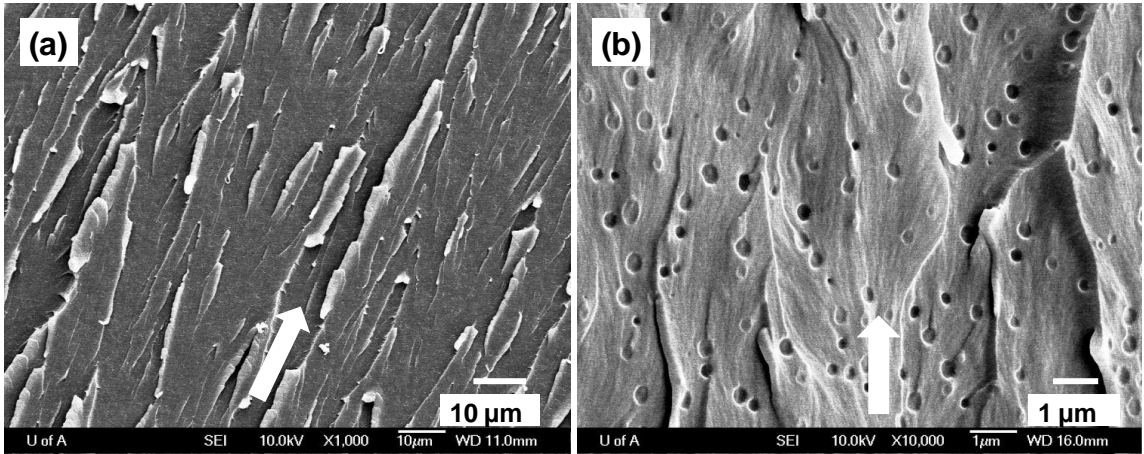


Figure 5.12 Fracture surface micrographs (SEM) of modified epoxy comprised of 3 wt% M52 block-copolymer at (a) low (1000x) and (b) high (10000x) magnifications.

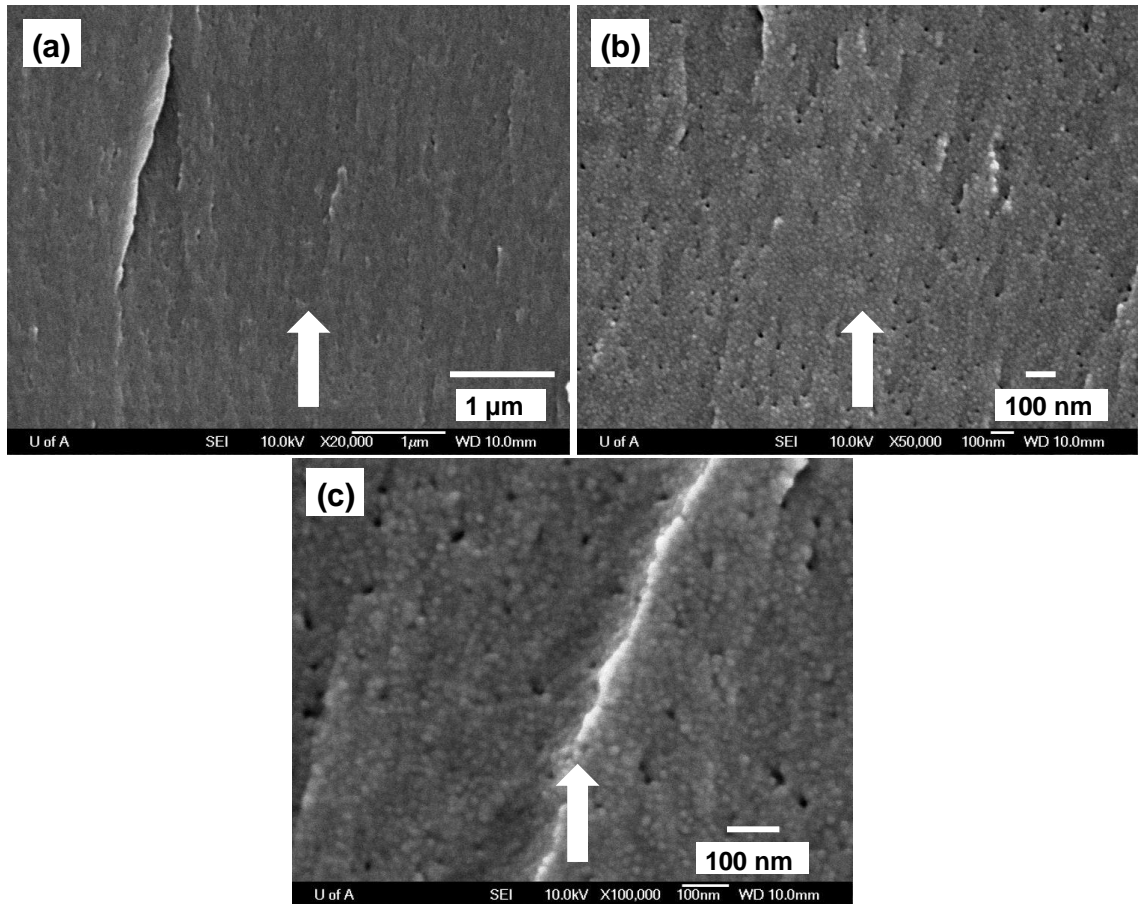


Figure 5.13 Fracture surface micrographs (SEM) of modified epoxy comprised of 3 wt% M52N block-copolymer: (a) low magnification of 20000x and high magnification of (b) 50000x and (c) 100000x.

5.3 CONCLUSIONS

The present chapter documents the formation of well dispersed nanostructured phases by self-assembly of block-copolymers within the epoxy polymer. The constituents of the block-copolymer were found to be very important for the initial nanostructuring of the epoxy; especially the epoxy miscible blocks have shown pronounced influence over the formation of nano-domains, i.e. spherical micelles and vesicles. The modified epoxy showed improved toughness, which is dependent on filler concentrations and morphology. In the investigated DGEBA epoxy system improvements in toughness were achieved without any significant reductions in other desirable mechanical (e.g. structural stiffness and strength) properties. A causal relationship between the modifier morphology and resulting property enhancement of the block-copolymer/epoxy system was presented. In the developed epoxy systems, the dispersed block-copolymer modifiers act to induce shear yielding of the matrix by relieving the triaxial stress condition at the crack-tip with mechanisms such as cavitation and/or debonding of the toughener phase. These are all accepted crack resistance mechanisms for rubber toughened epoxy, and have been reported recently in the literature [27-28, 30-36, 38-40] concerning amphiphilic block-copolymer modified epoxy. It is surprising to note that despite differences in block-copolymer compositions, particle morphology and size-scale, both spherical micelles and vesicles resulted in equivalent mechanical properties. The above observation would require more investigation to further elucidate these phenomena. It is presumed that final properties are greatly influenced by the constituents of the block-copolymers, their self-assembling morphology and the induced deformation mechanics under applied loading. The greater advantages of using block-copolymers in epoxy are improved toughness with far lower additive requirement (for example in comparison to the CTBN rubber loading), chemical compatibility between the dispersed and continuous phases providing strong interfacial properties, and the retention of important thermo-mechanical properties.

REFERENCES

1. SULTAN, J. and MCGARRY, F., 1973. Effect of Rubber Particle-Size on Deformation Mechanisms in Glassy Epoxy. *Polymer Engineering and Science*, **13**(1), pp. 29-34.
2. C.B. BUCKNALL, 1977. *Toughened Plastics*. London: Applied Science Publishers LTD.
3. KUNZDOUGLASS, S., BEAUMONT, P. and ASHBY, M., 1980. A Model for the Toughness of Epoxy-Rubber Particulate Composites. *Journal of Materials Science*, **15**(5), pp. 1109-1123.
4. BASCOM, W., COTTINGTON, R., JONES, R. and PEYSER, P., 1975. Fracture of Epoxy-Modified and Elastomer-Modified Epoxy Polymers in Bulk and as Adhesives. *Journal of Applied Polymer Science*, **19**(9), pp. 2545-2562.
5. KINLOCH, A.J., SHAW, S.J., TOD, D.A. and HUNSTON, D.L., 1983. Deformation and fracture behaviour of a rubber-toughened epoxy: 1. Microstructure and fracture studies. *Polymer*, **24**(10), pp. 1341-1354.
6. YEE, A.F. and PEARSON, R.A., 1986. Toughening mechanisms in elastomer-modified epoxies - Part 1 Mechanical studies. *Journal of Materials Science*, **21**(7), pp. 2462-2474.
7. PEARSON, R.A. and YEE, A.F., 1989. Toughening mechanisms in elastomer-modified epoxies - Part 3 The effect of cross-link density. *Journal of Materials Science*, **24**(7), pp. 2571-2580.
8. PEARSON, R.A. and YEE, A.F., 1991. Influence of particle size and particle size distribution on toughening mechanisms in rubber-modified epoxies. *Journal of Materials Science*, **26**(14), pp. 3828-3844.
9. BAGHERI, R. and PEARSON, R.A., 1996. Role of particle cavitation in rubber-toughened epoxies: 1. Microvoid toughening. *Polymer*, **37**(20), pp. 4529-4538.
10. GUILD, F.J. and YOUNG, R.J., 1989. A predictive model for particulate filled composite materials - Part 2 Soft particles. *Journal of Materials Science*, **24**(7), pp. 2454-2460.

11. LEVITA, G., DE PETRIS, S., MARCHETTI, A. and LAZZERI, A., 1991. Crosslink density and fracture toughness of epoxy resins. *Journal of Materials Science*, **26**(9), pp. 2348-2352.
12. KANG, B.U., JHO, J.Y., KIM, J., LEE, S.-S., PARK, M., LIM, S. and CHOE, C.R., 2001. Effect of molecular weight between crosslinks on the fracture behavior of rubber-toughened epoxy adhesives. *Journal of Applied Polymer Science*, **79**(1), pp. 38-48.
13. KINLOCH, A.J., YUEN, M.L. and JENKINS, S.D., 1994. Thermoplastic-toughened epoxy polymers. *Journal of Materials Science*, **29**(14), pp. 3781-3790.
14. GIRODET, C., ESPUCHE, E., SAUTEREAU, H., CHABERT, B., GANGA, R. and VALOT, E., 1996. Influence of the addition of thermoplastic preformed particles on the properties of an epoxy/anhydride network. *Journal of Materials Science*, **31**(11), pp. 2997-3002.
15. HÖFFLIN, F., KÖNCZÖL, L., DÖLL, W., MORAWIEC, J. and MÜLHAUPT, R., 2000. Toughening of epoxy resins modified with polyetherester block copolymers: the influence of modifier molecular architecture on mechanical properties. *Journal of Applied Polymer Science*, **76**(5), pp. 623-634.
16. ZHENG, S., WANG, J., GUO, Q., WEI, J. and LI, J., 1996. Miscibility, morphology and fracture toughness of epoxy resin/poly(styrene-co-acrylonitrile) blends. *Polymer*, **37**(21), pp. 4667-4673.
17. LIN, K.-F. and SHIEH, Y.-D., 1998. Core-shell particles designed for toughening the epoxy resins. II. Core-shell-particle-toughened epoxy resins. *Journal of Applied Polymer Science*, **70**(12), pp. 2313-2322.
18. HE, J., RAGHAVAN, D., HOFFMAN, D. and HUNSTON, D., 1999. The influence of elastomer concentration on toughness in dispersions containing preformed acrylic elastomeric particles in an epoxy matrix. *Polymer*, **40**(8), pp. 1923-1933.
19. KIM, D.S., CHO, K., KIM, J.K. and PARK, C.E., 1996. Effects of particle size and rubber content on fracture toughness in rubber-modified epoxies. *Polymer Engineering and Science*, **36**(6), pp. 755-768.
20. BÉCU-LONGUET, L., BONNET, A., PICHOT, C., SAUTEREAU, H. and MAAZOUZ, A., 1999. Epoxy Networks Toughened by Core-Shell Particles: Influence of

the Particle Structure and Size on the Rheological and Mechanical Properties. *Journal of Applied Polymer Science*, **72**(6), pp. 849-858.

21. QIAN, J.Y., PEARSOR, R.A., DIMONIE, V.L., SHAFFER, O.L. and EL-AASSER, M.S., 1997. The role of dispersed phase morphology on toughening of epoxies. *Polymer*, **38**(1), pp. 21-30.
22. BAGHERI, R. and PEARSON, R.A., 1996. Role of blend morphology in rubber-toughened polymers. *Journal of Materials Science*, **31**(15), pp. 3945-3954.
23. GARG, A.C. and MAI, Y.-W., 1988. Failure mechanisms in toughened epoxy resins-A review. *Composites Science and Technology*, **31**(3), pp. 179-223.
24. SUE, H.-J., GARCIA-MEITIN, E.I. and PICKELMAN, D.M., 1993. Toughening concept of rubber-modified high performance epoxies. In: CHEREMISINOFF, N.P. and CHEREMISINOFF, P.N., ed, *Elastomer Technology Handbook*. Boca Raton: CRC Press, pp. 661.
25. DAY, R.J., LOVELL, P.A. and PIERRE, D., 1997. Toughening of epoxy resins using particles prepared by emulsion polymerization: Effects of particle surface functionality, size and morphology on impact fracture properties. *Polymer International*, **44**(3), pp. 288-299.
26. THOMPSON, Z.J., HILLMYER, M.A., LIU, J., SUE, H.-J., DETTLOFF, M. and BATES, F.S., 2009. Block copolymer toughened epoxy: Role of cross-link density. *Macromolecules*, **42**(7), pp. 2333-2335.
27. HYDRO, R.M. and PEARSON, R.A., 2007. Epoxies toughened with triblock copolymers. *Journal of Polymer Science, Part B: Polymer Physics*, **45**(12), pp. 1470-1481.
28. GERARD, P., BOUPAT, N.P., FINE, T., GERVAT, L. and PASCAULT, J.-P., 2007. Toughness properties of lightly crosslinked epoxies using block copolymers. *Macromolecular Symposia*, **256**, pp. 55-64.
29. SERRANO, E., GERARD, P., LORTIE, F., PASCAULT, J.-P. and PORTINHA, D., 2008. Nanostructuring of unsaturated polyester by all-acrylic block copolymers, 1 - use of high-molecular-weight block copolymers. *Macromolecular Materials and Engineering*, **293**(10), pp. 820-827.

30. RUIZ-PÉREZ, L., ROYSTON, G.J., FAIRCLOUGH, J.P.A. and RYAN, A.J., 2008. Toughening by nanostructure. *Polymer*, **49**(21), pp. 4475-4488.
31. THIO, Y.S., WU, J. and BATES, F.S., 2006. Epoxy toughening using low molecular weight poly(hexylene oxide)-poly(ethylene oxide) diblock copolymers. *Macromolecules*, **39**(21), pp. 7187-7189.
32. WU, J., THIO, Y.S. and BATES, F.S., 2005. Structure and properties of PBO-PEO diblock copolymer modified epoxy. *Journal of Polymer Science, Part B: Polymer Physics*, **43**(15), pp. 1950-1965.
33. DEAN, J.M., LIPIC, P.M., GRUBBS, R.B., COOK, R.F. and BATES, F.S., 2001. Micellar structure and mechanical properties of block copolymer-modified epoxies. *Journal of Polymer Science, Part B: Polymer Physics*, **39**(23), pp. 2996-3010.
34. DEAN, J.M., GRUBBS, R.B., SAAD, W., COOK, R.F. and BATES, F.S., 2003. Mechanical properties of block copolymer vesicle and micelle modified epoxies. *Journal of Polymer Science, Part B: Polymer Physics*, **41**(20), pp. 2444-2456.
35. DEAN, J.M., VERGHESE, N.E., PHAM, H.Q. and BATES, F.S., 2003. Nanostructure toughened epoxy resins. *Macromolecules*, **36**(25), pp. 9267-9270.
36. KISHI, H., KUNIMITSU, Y., IMADE, J., OSHITA, S., MORISHITA, Y. and ASADA, M., 2011. Nano-phase structures and mechanical properties of epoxy/acryl triblock copolymer alloys. *Polymer*, **52**(3), pp. 760-768.
37. LARRAÑAGA, M., SERRANO, E., MARTIN, M.D., TERCJAK, A., KORTABERRIA, G., DE LA CABA, K., RICCARDI, C.C. and MONDRAGON, I., 2007. Mechanical properties-morphology relationships in nano-/microstructured epoxy matrices modified with PEO-PPO-PEO block polymers. *Polymer International*, **56**(11), pp. 1392-1403.
38. LIU, J., SUE, H.-J., THOMPSON, Z.J., BATES, F.S., DETTLOFF, M., JACOB, G., VERGHESE, N. and PHAM, H., 2008. Nanocavitation in self-assembled amphiphilic block copolymer-modified epoxy. *Macromolecules*, **41**(20), pp. 7616-7624.
39. BASHAR, M.T., SUNDARARAJ, U. and MERTINY, P., 2011. Study of Matrix Micro-cracking in Nanoclay and Acrylic Tri-block-copolymer Modified Epoxy/basalt Fiber-reinforced Pressure-retaining Structures. *Express polymer letters*, **5**, pp. 882-896.

40. BASHAR, M.T., SUNDARARAJ, U. and MERTINY, P., 2012. Microstructure and mechanical properties of epoxy hybrid nanocomposites modified with acrylic tri-block-copolymer and layered-silicate nanoclay. *Composites Part A: Applied Science and Manufacturing*, **43**, pp. 945-954.
41. MAIEZ-TRIBUT, S., PASCAULT, J.P., SOULÉ, E.R., BORRAJO, J. and WILLIAMS, R.J.J., 2007. Nanostructured epoxies based on the self-assembly of block copolymers: A new miscible block that can be tailored to different epoxy formulations. *Macromolecules*, **40**(4), pp. 1268-1273.
42. RITZENTHALER, S., GIRARD-REYDET, E. and PASCAULT, J.P., 2000. Influence of epoxy hardener on miscibility of blends of poly(methyl methacrylate) and epoxy networks. *Polymer*, **41**(16), pp. 6375-6386.
43. WOO, E.M. and WU, M.N., 1996. Blends of a diglycidylether epoxy with bisphenol-A polycarbonate or poly(methyl methacrylate): Cases of miscibility with or without specific interactions. *Polymer*, **37**(12), pp. 2485-2492.
44. JANARTHANAN, V. and THYAGARAJAN, G., 1992. Miscibility studies in blends of poly(N-vinyl pyrrolidone) and poly(methyl methacrylate) with epoxy resin: a comparison. *Polymer*, **33**(17), pp. 3593-3597.
45. KWEL, T.K., 1984. EFFECT OF HYDROGEN BONDING ON THE GLASS TRANSITION TEMPERATURES OF POLYMER MIXTURES. *Journal of polymer science. Polymer letters edition*, **22**(6), pp. 307-313.

Chapter 6

Microstructure and Mechanical Properties of Epoxy Hybrid Nanocomposites³

SYNOPSIS: In this chapter the morphology and mechanical properties of acrylic triblock-copolymer and organophilic layered silicate nanoclay modified epoxy hybrid nanocomposites were investigated. Three-phase ternary nanocomposites showed coexistence of both intercalated nanoclay and nanostructured block-copolymer (i.e. spherical micelles) in epoxy. Experimental results revealed that the block-copolymer significantly enhanced fracture toughness. Increased toughness coincided with a slight reduction of tensile stiffness and strength in the case of block-copolymer modified epoxy. The nanoclay filled nanocomposites exhibited superior stiffness and slight improvement in tensile strength while compromising ductility. Optimum property enhancement was observed in the case of epoxy hybrid nanocomposites. Mechanical properties of the hybrid nanocomposites depend on microstructure, dispersion state and the ratio between organic and inorganic nanofiller contents.

6.1 INTRODUCTION

Polymer nanocomposites are emerging as a new breed of high performance materials, exceeding many of the properties of the conventional polymer composites [1-5]. Sometimes a compromise between properties must be tolerated because multifunctionality in all three dimensions and different length scales is difficult to achieve. However, by incorporating two or more different types of nanoparticles, and combining their useful properties in a matrix substrate may effectively circumvent the above situation. Thereby a material possessing various favorable characteristics necessary for certain high-performance applications can be produced.

³ A version of this chapter has been published as: BASHAR, M., SUNDARARAJ, U. and MERTINY, P., 2012. Microstructure and mechanical properties of epoxy hybrid nanocomposites modified with acrylic tri-block-copolymer and layered-silicate nanoclay. *Composites A*, **43**(6), pp. 945-954.

Epoxy is preferred for many applications in the aerospace, marine and automobile industries. But, the inherent brittleness of epoxy resulted in limited resistance against crack propagation. Several methods have been frequently employed to provide excellent toughening to epoxy. Among these, incorporating a second rubbery phase is a commonly recognized practice. General wisdom about rubbery and rigid particulate inclusions is that soft particles increase ductility and toughness, and conversely, hard particles enhance stiffness and strength of the polymer matrix. The above statement was found justified also for the present study as revealed by the subsequently presented results.

Extensive research has been conducted by incorporating a diverse range of dispersed phases into the epoxy matrix, i.e. liquid rubbers [6-9], thermoplastic spheres [10-12], core-shell particles [13-16] and nanostructured block-copolymers [17-21]. In most of these cases, improved toughness was achieved whilst lowering the stiffness and strength of epoxy. Inorganic particles such as silica [22-23], glass beads [8], alumina [22] and nanoclay [1-5, 12, 14-16, 24-26] are known to enhance stiffness, strength and in some instances toughness of the thermoset epoxy while compromising ductility.

Thus, blending both rigid and rubbery nanoparticles in a thermosetting polymer would be an interesting alternative. Previous studies have successfully incorporated two or more particulate reinforcements in an epoxy, thereby generating so-called hybrid composites [4-5, 8, 12, 14-16, 24-25]. A recent study conducted by Marouf et al. [16] provided an excellent and brief review on nanoclay-filled/rubber-modified epoxy hybrid nanocomposites. Most of the publications documented significant improvements in fracture energy while maintaining stiffness, strength and ductility of the unmodified epoxy through formation of a ternary nanocomposite [14, 24-25]. The synergistic effects of both rubber and nanoclay on thermosetting epoxy were cited as the reason for these enhancements. Rubber particle cavitation [14, 16, 25], matrix shear yielding [14, 25], crack bifurcation and deflection by clay particles [5, 14, 16, 25] were attributed to be the predominant crack resistance phenomena in epoxy hybrid nanocomposites. In contrast to the single-additive system, a reduction in fracture energy of the hybrid epoxy was also observed [15-16]. Marouf et al. [16] speculated that in a hybrid nanocomposite, the occurrence of competing micromechanisms associated with dispersed rubber and nanoclay were responsible for this behavior.

Much of the literature on epoxy hybrid composites focused either on two different micro particles [8] or micro-nano combinations containing micron size rubber particles [15, 23-25]. Previous chapters already described the significant improvements in fracture energy by dispersing acrylic based block-copolymer in epoxy, and the considerable increase of stiffness imparted by nanoclay addition. Therefore, in an effort to synergistically combine favorable properties of various nano-reinforcements in a thermosetting epoxy, the current study incorporated two different nano-phases, i.e. acrylic triblock-copolymer M52N and layered silicate I.30E nanoclay into the epoxy polymer. It has been reported in the technical literature [17-19] that significant improvement in epoxy toughness can be achieved with relatively minor reductions in strength and elastic modulus when a small amount of block-copolymer was added as a modifier. The significant enhancement of fracture resistance was primarily attributed to the nanostructuring of block-copolymers within epoxy matrix, which is very much dependent on the specific morphology of the nano-inclusions (i.e. spherical micelles, cylindrical micelles and vesicles). On the other hand, nanoclay is well known for developing a marked increase in epoxy stiffness with the formation of nanocomposites [1-3, 27-29], and several investigators have demonstrated improved toughness mainly with conventional and intercalated clay morphologies [27-29].

The focus of this work was to synergistically enhance mechanical properties (such as tensile stiffness, strength and fracture toughness) of the resulting hybrid nanocomposites. The current study involved characterizing the nanocomposites by various morphological examinations. Toughening mechanisms and tensile yield behaviors were explored with respect to the associated modifier compositions. The formulations of the single-component epoxy systems and hybrid nanocomposites as evaluated and compared in this chapter are summarized in Table 6-1.

6.2 RESULTS AND DISCUSSION

6.2.1 X-ray Diffraction Analysis of Hybrid Nanocomposites

Figure 6.1 compares X-ray diffraction results of the single-component epoxy-clay nanocomposites with hybrid nanocomposites containing both block-copolymer and clay

nanoparticles. The preparation methods of single-component and hybrid nanocomposites are described in the Sections 2.2.1.2, 2.2.2 and 2.2.3. XRD traces of I.30E-epoxy nanocomposites revealed that the prominent diffraction peak was absent when 1 wt% and 2 wt% I.30E were incorporated in epoxy. Hybrid nanocomposites (i.e. 3B&1C and 1B&3C) examined by X-ray diffraction also did not exhibit any well-defined peak [24]. The absence of the diffraction peak is indicative of either an exfoliated morphology or highly intercalated structure for the prepared nanocomposites. Even coexistence of an exfoliated and intercalated morphology cannot be fully discerned, so further investigation by TEM microscopy was required. Therefore, from the XRD results, it was confirmed that the epoxy polymer was able to effectively penetrate between the clay interlayers. It has been assumed that during the curing, catalytic effect of the primary alkylammonium ions of the nanoclay influenced the epoxy-amine curing reaction, and increased the clay interlamellar distance. It can also be inferred from the XRD curves in Figure 6.1 that the individual clay platelets are at least 8.8 nm apart from each other, which is the detection limit of the WAXD.

Table 6-1 Compositions of different single-component and hybrid nanocomposites.

Material system	Clay content (wt%)	Block-copolymer content (wt%)
0 (neat epoxy)	0	0
1C	1.0	0
3C	3.0	0
1B	0	1.0
3B	0	3.0
1B&1C	1.0	1.0
1B&3C	3.0	1.0
3B&1C	1.0	3.0

6.2.2 Microstructure Study of Hybrid Nanocomposites

TEM micrographs of Figure 6.2 show microstructures and nanoparticle dispersions in cured epoxy. These micrographs provided additional information on particle dimensions

and interlayer distances of the layered silicate. Composites prepared by combining different compositions of I.30E and M52N additive mixtures with epoxy were found to be transparent under visible light. As shown before in Chapter 4, nanocomposites prepared by ultrasonic mixing of layered silicate with epoxy mainly had intercalated and few exfoliated nanostructures. Characteristic ordered layer structures of clay are shown in Figure 6.2 (a) having an average layer separation of about 10~15 nm. The TEM micrograph in Figure 6.2 (b) shows randomly dispersed spherical micelles with diameter of about 20~30 nm (see Chapter 5 for more information on block-copolymer modified epoxy). In a previous study, Dean et al. [17] identified the presence of spherical micelles in epoxy by analyzing the small-angle X-ray scattering and TEM results of a blend containing block-copolymer (e.g. PEO-PEP or PEO-PI) and epoxy. Formation of the two-phase morphology is crucial for toughness improvement as well as for preserving other important mechanical properties of epoxy.

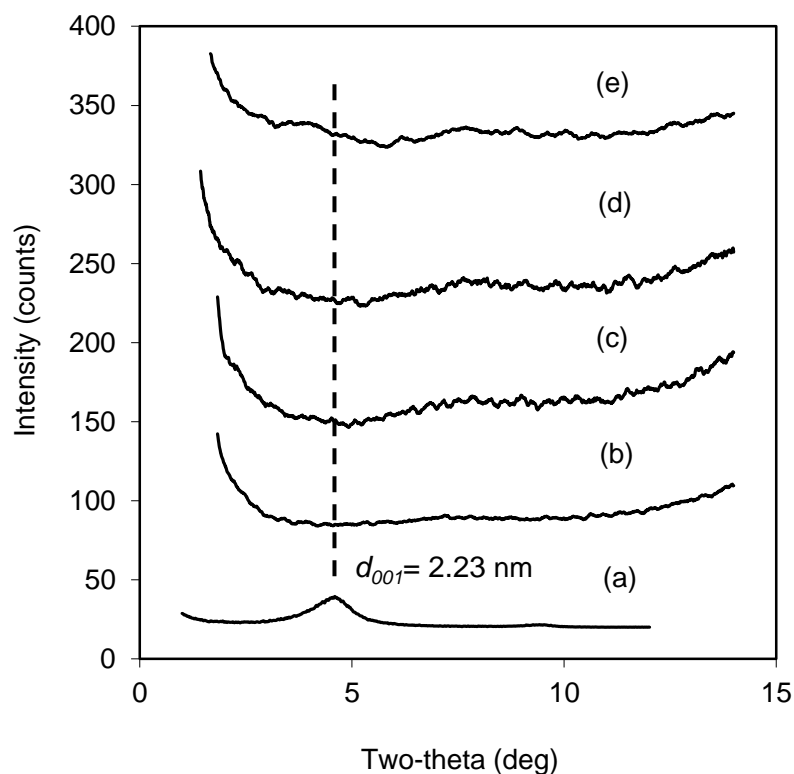


Figure 6.1 X-ray diffraction patterns of (a) organoclay and cured nanocomposites: (b) 1 wt% and (c) 2 wt% I.30E nanoclay filled epoxy, (d) 3B&1C and (e) 1B&3C hybrid compounds.

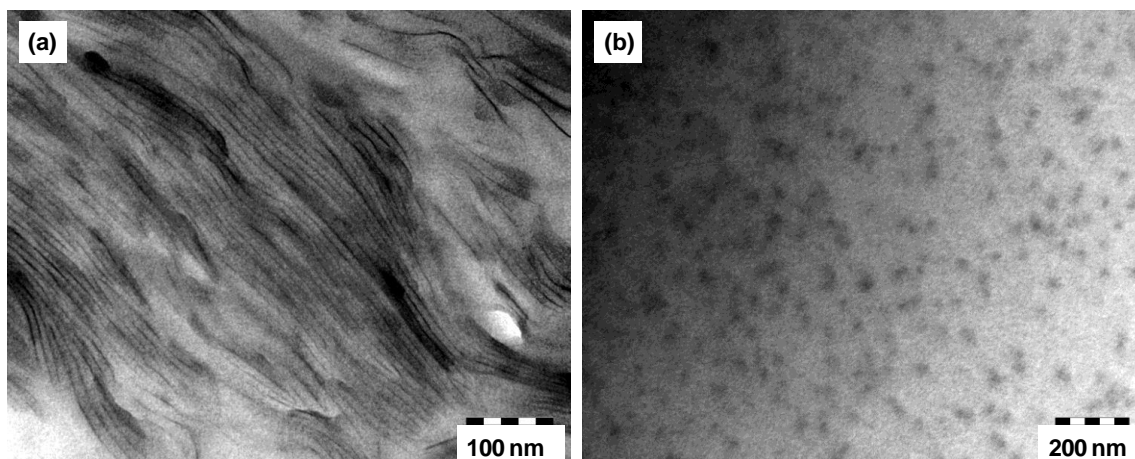


Figure 6.2 TEM images of (a) sample 1C a nanoclay filled epoxy and (b) sample 3B a block-copolymer dispersed epoxy.

A combination of intercalated nanoclay and nanostructured block-copolymer morphology is shown for the 3B&1C hybrid nanocomposite in Figure 6.3, which correlates well with the XRD results. It is evident from Figure 6.3 (a) that some of the block-copolymers were able to infiltrate amid the clay interlayers. This has been reported before by Frohlich et al. [5] who observed that liquid rubber diffused between the silicate galleries. Likewise, Balakrishnan et al. [25] noticed clay particles preferentially attaching themselves on the rubber surface. Figure 6.3 (b) shows the same hybrid nanocomposite sample after straining with osmic acid. Clearly osmic acid has dissolved the block-copolymer in the hybrid nanocomposite specimen. Finely dispersed, randomly distributed, mostly submicron-size intercalated clay tactoids have been observed in the low magnification TEM micrograph of Figure 6.3 (c). The straight lines in Figure 6.3 (c) are knife marks left from the microtoming process. It has been ascertained that sonication caused a breakdown of larger clay agglomerates into smaller particles, and similar observation has been previously reported by Hernandez et al. [12].

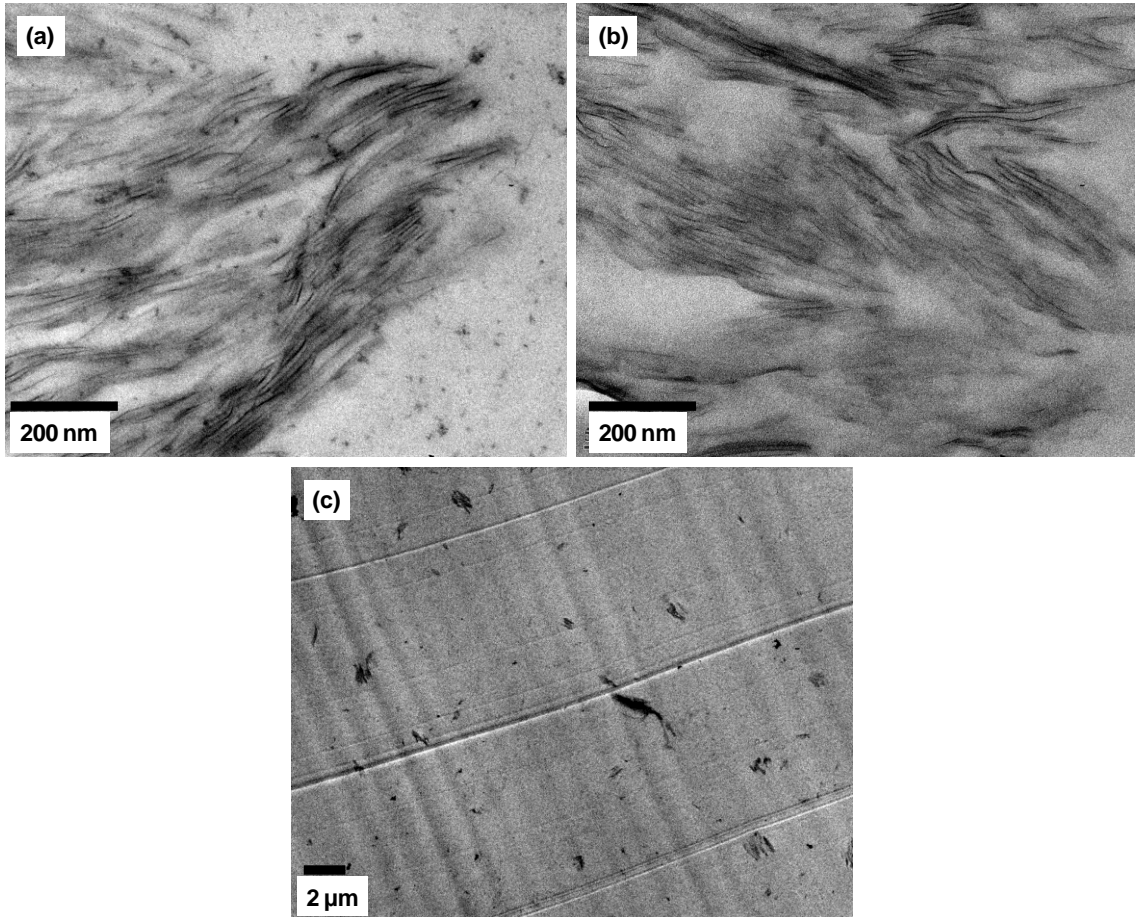


Figure 6.3 TEM images of 3B&1C a hybrid nanocomposite: pictures are taken at high magnification for specimens (a) without and (b) with osmic acid staining and (d) at low magnification.

6.2.3 Tensile Properties of Hybrid Nanocomposites

Typical tensile stress-strain curves of the neat epoxy and its nanocomposites are shown in Figure 6.4. The figure illustrates that the stress increased almost linearly with strain for acrylic block-copolymer dispersed epoxy until it reached a maximum value. Subsequent yielding of the specimen was followed by ultimate failure. The clay nanocomposite demonstrated an apparent loss of DGEBA ductility, and did not yield before ultimate failure of the specimen. The behavior of hybrid nanocomposites was dictated by the relative amount of block-copolymer and clay contents.

Table 6-2 lists tensile properties of the hybrid and single-component systems and corresponding standard deviations. Tensile test results represent average values from

three or more test samples. Normalized tensile moduli of the hybrid nanocomposites along with the single-additive composites are shown in Figure 6.5. Error bars correspond to one standard deviation. For layered silicate nanocomposites, Lan and Pinnavaia [1] showed that the stiffness increased significantly due to the presence of exfoliated high aspect ratio rigid clay platelets. To a lesser extent, this was observed in the current study as stiffness increased with increasing I.30E concentration for the predominantly intercalated nanocomposites [27]. When 3 wt% nanoclay was incorporated in epoxy (i.e. sample 3C), the value of modulus increased by 16%. As expected, addition of acrylic block-copolymer caused a slight reduction in modulus [4]. Stiffness of 1B&3C hybrid nanocomposite containing 1 wt% M52N and 3 wt% I.30E generated similar improvement as with only 3 wt% I.30E in epoxy. Therefore, for hybrid materials, the stiffness enhancement is directly dependent on silicate content [5], while the block-copolymer additive has only limited influence on modulus. Superior interfacial properties of intercalated nanoclay may also have contributed to the stiffening effect.

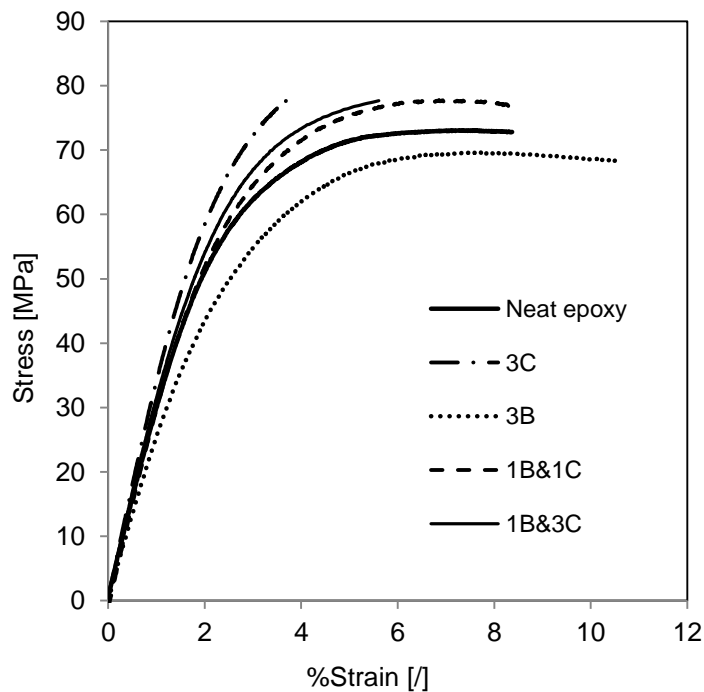


Figure 6.4 Tensile stress-strain response of modified epoxy with respect to nanofiller contents.

Table 6-2 Mechanical properties of modified epoxy containing various types and compositions of nanofiller.

Material system	Tensile modulus (GPa)	Tensile strength (MPa)	Elongation (%)	Fracture toughness (MPa.m ^{0.5})	Strain energy (J/m ²)
0 (neat epoxy)	2.88 ± 0.04	73.3 ± 0.9	8.50 ± 0.39	0.78 ± 0.05	235 ± 28
1C	3.15 ± 0.08	78.5 ± 0.73	7.21 ± 0.66	0.79 ± 0.03	225 ± 11
3C	3.33 ± 0.04	77.2 ± 2.31	3.77 ± 0.34	0.77 ± 0.01	230 ± 9
1B	2.67 ± 0.01	72.8 ± 0.15	9.41 ± 0.2	0.87 ± 0.04	285 ± 37
3B	2.63 ± 0.05	69.5 ± 0.07	9.64 ± 1.22	1.26 ± 0.12	495 ± 78
1B&1C	3.06 ± 0.05	77.6 ± 0.5	8.34 ± 0.56	0.85 ± 0.04	275 ± 27
1B&3C	3.31 ± 0.05	76.4 ± 2.32	4.75 ± 0.73	0.8 ± 0.06	235 ± 23
3B&1C	2.96 ± 0.07	81.2 ± 1.49	8.35 ± 0.57	1.24 ± 0.03	560 ± 33

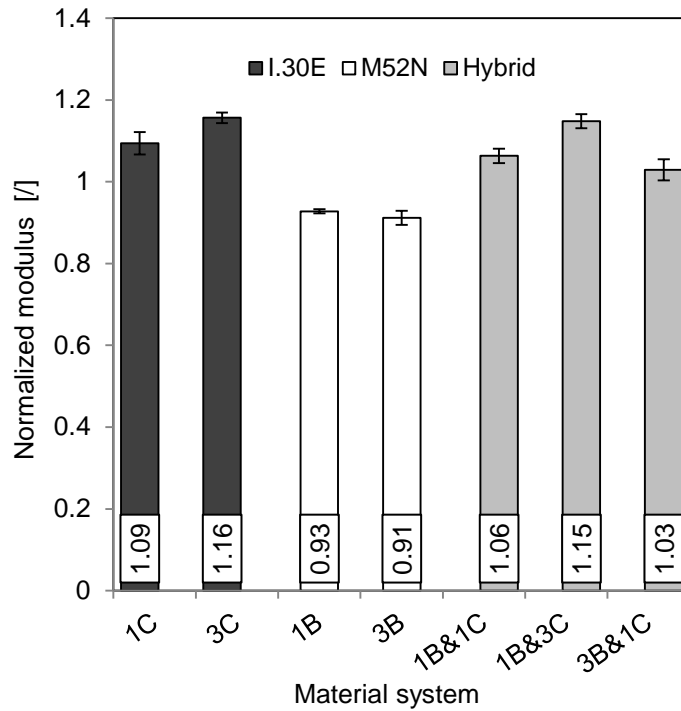


Figure 6.5 Tensile modulus of composites in reference to different nanofiller compositions.

When acrylic block-copolymer was incorporated as an additive, tensile strength decreased by 5% as illustrated in Figure 6.6, while nanoclay enhanced tensile strength of the epoxy [25]. Indeed, for hybrid nanocomposites incorporating both M52N block-copolymer and I.30E nanoclay, the strength increased in response to nanoclay concentration.

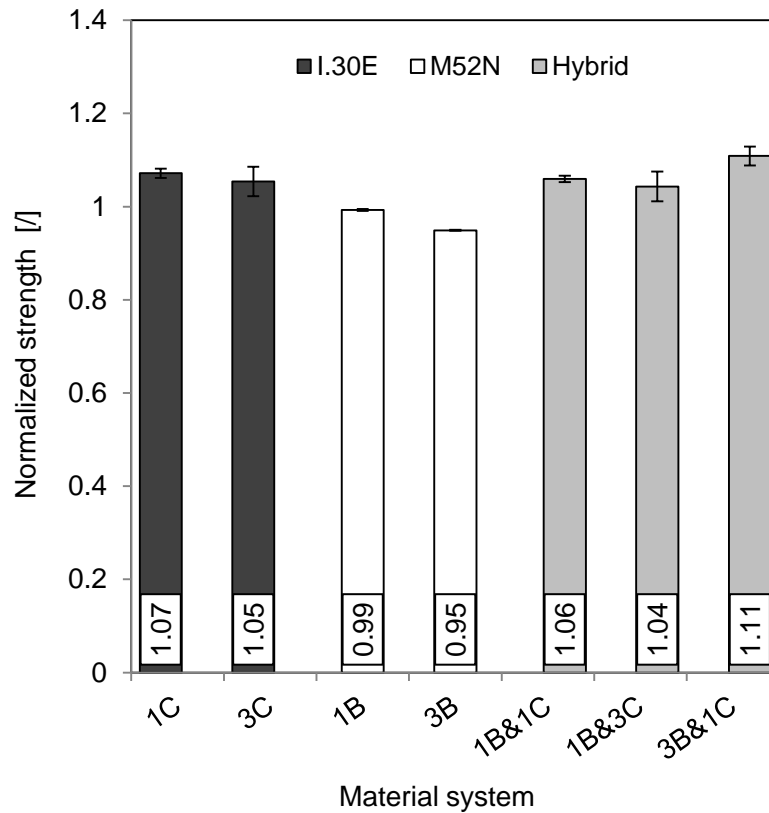


Figure 6.6 Tensile strength of composites as a function of different nanofiller compositions in epoxy.

Figure 6.7 shows the results for tensile elongation. The tensile elongation for samples with nanoclay decreased substantially by 15-56%. Higher rigidity and stiffness of the clay particles caused a reduction in ductility by matrix embrittlement, hence affecting the deformation behavior of matrix, which is commonly observed in stiff particulate reinforced epoxy [14, 27]. However, elongation increased for M52N-epoxy samples with addition of acrylic block-copolymer, which formed spherical nanostructures consisting of a softer rubbery core [25]. As predicted, in the case of hybrid nanocomposites (except

1B&3C), strain at break was close to the value for neat epoxy. Enhancement of modulus and strength and retention of ductility indicates that the strengthening effect of the nanoclay and the ductility enhancement of block-copolymer are simultaneously operative in the hybrid nanocomposites.

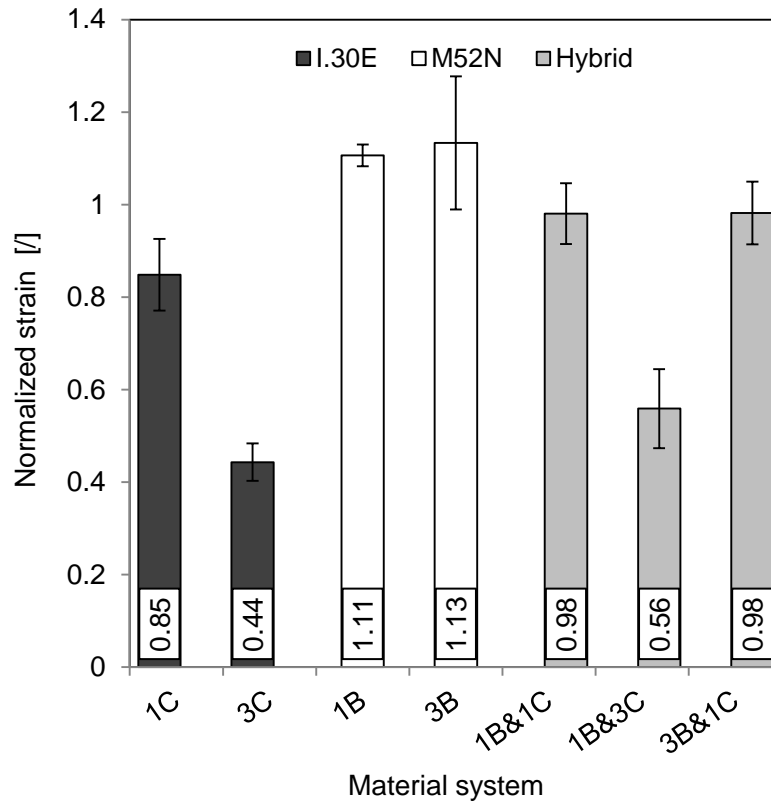


Figure 6.7 Dependence of composite tensile elongation on various nanofiller compositions in modified epoxy.

6.2.4 Fracture Properties of Hybrid Nanocomposites

Figures 6.8 (a-c) display load-displacement behavior of the fracture process of SENB specimens for both filled and unfilled epoxies. As depicted in Figure 6.8 (a), unmodified epoxy shows unstable brittle crack growth behavior where the crack propagates by the characteristic slip/stick mechanism. Modified epoxy fracture behavior is dependent on the specific filler compositions. The simple composite with 3 wt% I.30E (i.e. sample 3C) and the hybrid composite 1B&3C in Figure 6.8 (b) manifest a stable brittle crack growth characteristic where the load increases linearly to a maximum followed by steady and

controlled crack propagation. The appearance of the fracture surface is characterized as a distinct brittle failure, and this kind of fracture process correlates well with the insignificant toughening effect of nanoclay as will be shown later in this chapter. It can be observed from Figure 6.8 (c) that 3 wt% M52N modified epoxy (i.e. sample 3B) and 3B&1C composite exhibited significant increase in load up to certain higher value at which point fast unstable crack growth took place. This sudden failure mechanism occurred because, in the process of load increment, a substantial amount of elastic energy was stored, until finally a sudden release of this energy is accompanied by instantaneous unstable crack propagation.

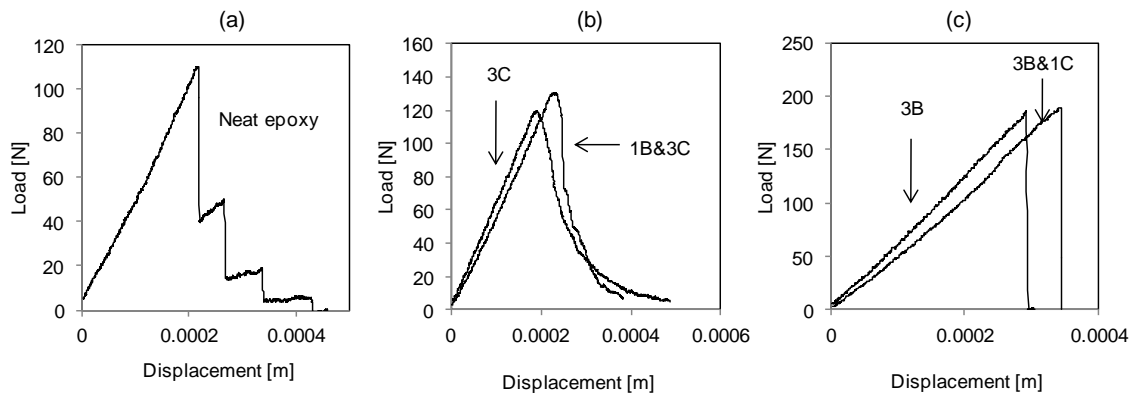


Figure 6.8 Crack initiation and crack growth behavior of SENB specimens made with: (a) neat epoxy, (b) sample 3C a nanoclay filled epoxy and 1B&3C a hybrid nanocomposite and (c) sample 3B a block-copolymer modified epoxy and 3B&1C a hybrid nanocomposite.

Fracture toughness of the modified epoxy in terms of critical stress intensity factor was measured at room temperature. Table 6-2 summarizes dissipated fracture energies associated with propagating a sharp crack through the SENB specimens made from neat epoxy and its nanocomposites. The values of pristine epoxy fracture toughness and strain energy were calculated to be $0.78 \text{ MPa}\cdot\text{m}^{0.5}$ and 235 J/m^2 respectively, which are typical for an unmodified, highly cross-linked brittle epoxy. Figure 6.9 illustrates the effect of nanoparticle concentration on fracture toughness of different nanocomposite systems. In I.30E-epoxy nanocomposites, addition of layered silicate did not introduce any

considerable change to epoxy fracture toughness. Even though the nanoclay concentration was increased from 1 wt% to 3 wt%, the toughness remained almost constant relative to the unmodified epoxy. Similar observation was made by Balakrishnan et al. [25] and Gam et al. [14]. Frohlich et al. [5] identified crack deflection and crack branching as the main fracture modes in nanocomposites containing organoclay, and observed minor/insignificant improvements in fracture toughness. Kinloch and Taylor [28] studied mechanical and fracture properties of I.30E modified epoxy samples. Similar to present findings, these researchers also observed only a small toughening effect of this organoclay in epoxy. Others have inferred intercalated structures provide better crack resistance than exfoliated clay [27, 29].

However, incorporating M52N block-copolymer in epoxy matrix greatly increased fracture toughness and strain energy relative to the neat epoxy, as has been previously observed for rubber toughened thermosets [7, 9]. Increases of approximately 60% and 110% were observed in fracture toughness and strain energy respectively by adding 3 wt% M52N (i.e. sample 3B). It is believed that during the fracture process, the stress field ahead of the crack-tip caused the rubbery poly(*n*-butylacrylate) core of the triblock-copolymer to cavitate. These cavitated particles initiate and facilitate subsequent matrix shear yielding, which has been previously reported by Liu et al. [19] for block-copolymer micelle structures in epoxy.

As expected, toughness of the hybrid nanocomposites was higher and closer to the toughness of M52N-epoxy composites. It was ascertained from these results that the fracture toughness of the hybrid epoxy improved significantly mainly because of the presence of block-copolymer dispersant. As noted, the contribution of nanoclay to the fracture process of the hybrid materials was insignificant. For example, 3B&1C hybrid nanocomposite containing 3 wt% M52N block-copolymer and 1 wt% I.30E clay generated 60% increase in fracture toughness, which is the same order of magnitude as that of 3 wt% M52N in epoxy (i.e. sample 3B). Similar improvements for hybrid nanocomposites have been documented before in the literature [14]. The strain energy values in Table 6-2 for different nanocomposites show the same trend as fracture toughness. It has been observed that the fracture mechanisms and their associated fracture energies are significantly different for the block-copolymer and clay modified epoxies. It

is also surmised that the low ductility and high cross-link density of the epoxy polymer has an influence on the fracture properties of the reinforced epoxy [14].

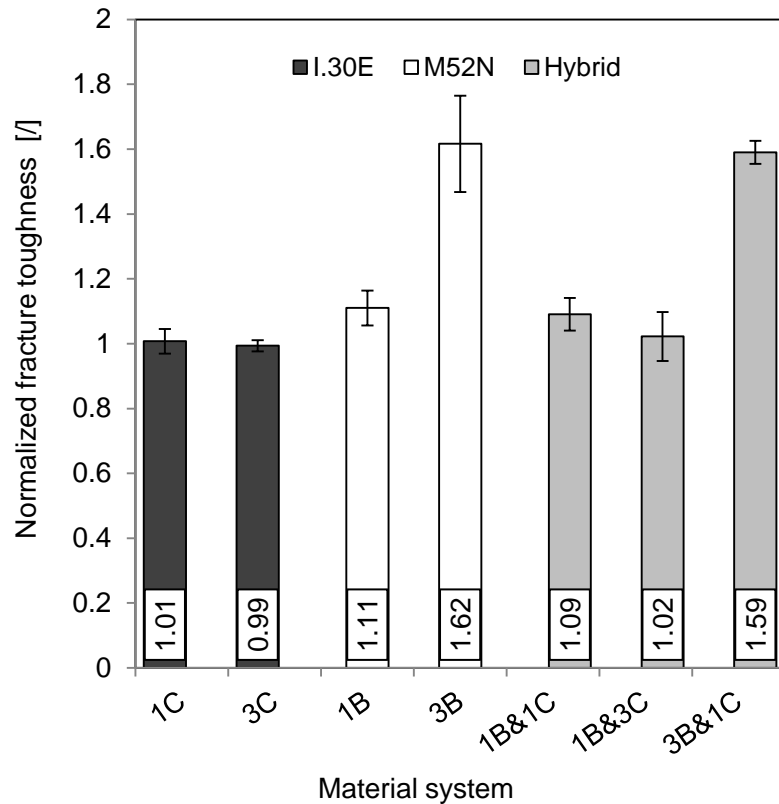


Figure 6.9 Fracture toughness of epoxy composites as a function of different nanofiller compositions.

6.2.5 Fracture Surface Study of Hybrid Nanocomposites

Fracture surfaces of the neat epoxy and its nanocomposites were examined by SEM, and the images are displayed in Figures 6.10 through 6.12. The arrow indicates crack propagation direction.

The fracture surface of nanoclay filled epoxy in Figure 6.10 (a) is extensively textured and the morphology is coarser and the surface is rougher. It is remarkable that the extensively convoluted morphology of the I.30E-epoxy fracture surface did not generate the expected toughness that was reported by various authors for intercalated clay architecture [27, 29]. It is speculated that intercalated submicron-size clay tactoids and exfoliated clay platelets are responsible for this behavior. It can be seen that the

intercalated structures only resulted in perturbation of the natural crack path by deflection and branching, which are known to be a less effective toughening mechanism [30]. The smaller dimension intercalated clay particles shown in Figure 6.10 (a) did not provide effective resistance to crack propagation through such mechanism as crack pinning, even though few clay clusters and aggregates were present in the nanocomposites. Based on these observations the present author speculates that without the occurrence of prominent energy dissipating toughening mechanisms (e.g. matrix shear yielding and crack pinning), the fracture toughness of nanoclay filled epoxy remained unchanged. The high magnification image in Figure 6.10 (b) shows laminated clay layers with epoxy penetrating in between adjacent clay sheets.

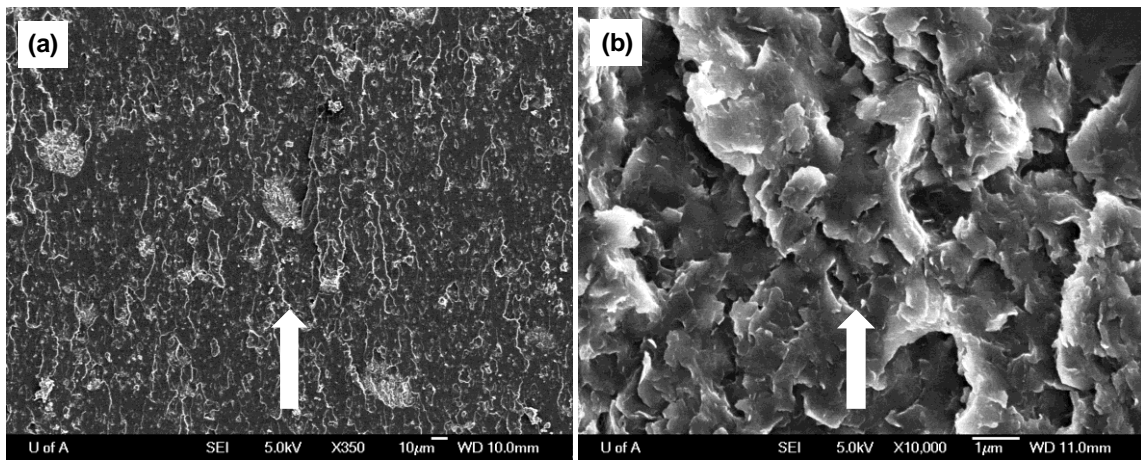


Figure 6.10 SEM images of SENB fracture surfaces of sample 3C a nanoclay filled epoxy nanocomposite at (a) low magnification and (b) high magnification.

In contrast, the block-copolymer modified epoxy surface as shown in the low magnification image of Figure 6.11 (a) exhibits no visible sign of extensive roughness, and areas of matrix rich domains are also evident, similar to pure epoxy (see Figure 4.17). It is apparent from Figure 6.11 (b) that the spherical micelles in M52N modified epoxy created a significant number of spherical cavities. In accordance with present findings on M52N block-copolymer dispersed epoxy, it can be concluded that voiding of the rubbery core of the spherical micelles in front of a propagating crack aided subsurface matrix shear deformation (see Chapter 5). This implies that a large amount of energy was

dissipated during the fracture process. Figure 6.11 (b) further illustrates homogenous but random distribution of the acrylic block-copolymer additive.

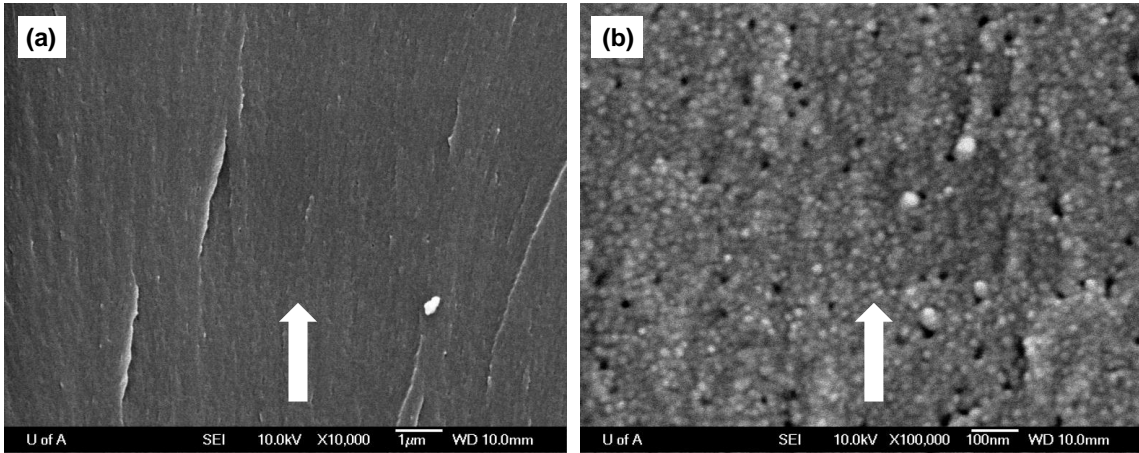


Figure 6.11 SEM images of SENB fracture surfaces of sample 3B a block-copolymer modified epoxy at (a) low magnification and (c) high magnification.

The fracture surface of the hybrid nanocomposite 1B&1C is shown in Figure 6.12. The 1B&1C fracture surfaces exhibit a flat and plane surface morphology, identical to the block-copolymer fracture surface. It is also noteworthy that the evidence of three-phase morphology of the hybrid nanocomposites is clearly visible in Figure 6.12 (a), i.e. discrete nanoscopic holes formed by cavitated block-copolymers marked by white circles and intercalated nanoclay in epoxy substrate. The toughness enhancement is thought to be by void formation followed by matrix yielding due to the presence of dispersed spherical block-polymer nanostructures. Confirming what was observed previously for nanoclay reinforced epoxy, the crack resistance effect of the nanoclay was not seen in the hybrid nanocomposites.

6.3 CONCLUSIONS

The present investigation successfully demonstrated the strategy of simultaneously incorporating both triblock-copolymer and nanoclay as a significant property enhancer by generating nanostructured domains in thermosetting epoxy. This study substantiated that the epoxy modified with a small amount of particular type of nano-additive resulted in

significant increase in specific mechanical property. Furthermore, the hybrid nanocomposites illustrated the potential of generating optimal mechanical property by taking advantage of the favorable properties of different nanoparticles.

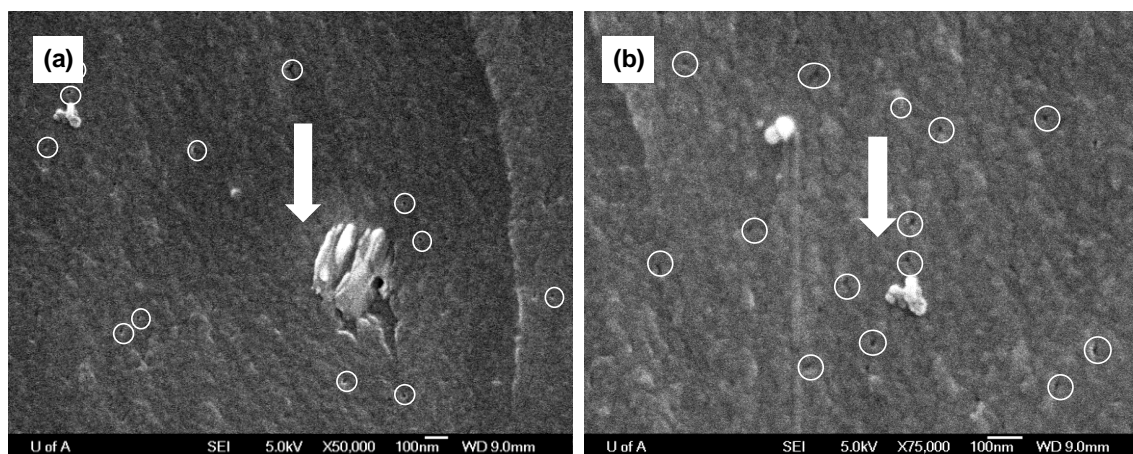


Figure 6.12 SEM images of SENB fracture surfaces of 1B&1C a hybrid nanocomposite at (a)-(b) high magnification.

Dispersed spherical micelles in acrylic block-copolymer modified epoxy and intercalated silicate layers in nanoclay filled epoxy were observed by various characterization methods. In an epoxy hybrid nanocomposite, when both particles are present, a three-phase morphology was observed. Addition of acrylic triblock-copolymer M52N greatly enhanced toughness of the thermosetting epoxy, and this increase in toughness was attributed to a mechanism of particle cavitation and subsequent matrix shear deformation. Organoclay I.30E significantly improved stiffness of the epoxy nanocomposites while maintaining fracture toughness constant through a less efficient failure mode of crack diversion and branching, presumably by the presence of submicron-size intercalated clay tactoids. A hybrid nanocomposite prepared by combining block-copolymer with nanoclay in a thermosetting epoxy achieved enhanced toughness and stiffness over the neat epoxy. From the results of this work, it can be inferred that the 3B&1C hybrid nanocomposite made with 3 wt% M52N and 1 wt% I.30E introduced a significant improvement in toughness while slightly enhancing tensile stiffness and strength of the epoxy. Results also indicate an influence of both nanoclay and block-copolymer on the fracture and tensile properties of the epoxy nanocomposites. Therefore, the general conclusion is that

the mechanical property enhancement in hybrid nanocomposites depends on the specific combination of different dispersants and their nanostructured morphology in a composite system, and thus, optimization of the type and concentration of different dispersants and their interactions is critical to obtain multi-functional properties.

REFERENCES

1. LAN, T. and PINNAVAIA, T.J., 1994. Clay-reinforced epoxy nanocomposites. *Chemistry of Materials*, **6**(12), pp. 2216-2219.
2. LAN, T., KAVIRATNA, P.D. and PINNAVAIA, T.J., 1995. Mechanism of clay tactoid exfoliation in epoxy-clay nanocomposites. *Chemistry of Materials*, **7**(11), pp. 2144-2150.
3. MESSERSMITH, P.B. and GIANNELIS, E.P., 1994. Synthesis and characterization of layered silicate-epoxy nanocomposites. *Chemistry of Materials*, **6**(10), pp. 1719-1725.
4. FRÖHLICH, J., THOMANN, R. and MÜLHAUPT, R., 2003. Toughened epoxy hybrid nanocomposites containing both an organophilic layered silicate filler and a compatibilized liquid rubber. *Macromolecules*, **36**(19), pp. 7205-7211.
5. FRÖHLICH, J., THOMANN, R., GRYSCHUK, O., KARGER-KOCSIS, J. and MÜLHAUPT, R., 2004. High-performance epoxy hybrid nanocomposites containing organophilic layered silicates and compatibilized liquid rubber. *Journal of Applied Polymer Science*, **92**(5), pp. 3088-3096.
6. SULTAN, J. and MCGARRY, F., 1973. Effect of Rubber Particle-Size on Deformation Mechanisms in Glassy Epoxy. *Polymer Engineering and Science*, **13**(1), pp. 29-34.
7. KINLOCH, A.J., SHAW, S.J., TOD, D.A. and HUNSTON, D.L., 1983. Deformation and fracture behaviour of a rubber-toughened epoxy: 1. Microstructure and fracture studies. *Polymer*, **24**(10), pp. 1341-1354.
8. KINLOCH, A.J., MAXWELL, D.L. and YOUNG, R.J., 1985. The fracture of hybrid-particulate composites. *Journal of Materials Science*, **20**(11), pp. 4169-4184.

9. YEE, A.F. and PEARSON, R.A., 1986. Toughening mechanisms in elastomer-modified epoxies - Part 1 Mechanical studies. *Journal of Materials Science*, **21**(7), pp. 2462-2474.
10. KINLOCH, A.J., YUEN, M.L. and JENKINS, S.D., 1994. Thermoplastic-toughened epoxy polymers. *Journal of Materials Science*, **29**(14), pp. 3781-3790.
11. HÖFFLIN, F., KÖNCZÖL, L., DÖLL, W., MORAWIEC, J. and MÜLHAUPT, R., 2000. Toughening of epoxy resins modified with polyetherester block copolymers: the influence of modifier molecular architecture on mechanical properties. *Journal of Applied Polymer Science*, **76**(5), pp. 623-634.
12. HERNANDEZ, M., SIXOU, B., DUCHET, J. and SAUTEREAU, H., 2007. The effect of dispersion state on PMMA-epoxy-clay ternary blends: In situ study and final morphologies. *Polymer*, **48**(14), pp. 4075-4086.
13. BÉCU-LONGUET, L., BONNET, A., PICHOT, C., SAUTEREAU, H. and MAAZOUZ, A., 1999. Epoxy Networks Toughened by Core-Shell Particles: Influence of the Particle Structure and Size on the Rheological and Mechanical Properties. *Journal of Applied Polymer Science*, **72**(6), pp. 849-858.
14. GAM, K.T., MIYAMOTO, M., NISHIMURA, R. and SUE, H.-J., 2003. Fracture Behavior of Core-Shell Rubber-Modified Clay-Epoxy Nanocomposites. *Polymer Engineering and Science*, **43**(10), pp. 1635-1645.
15. SUBRAMANIYAN, A.K. and SUN, C.T., 2007. Toughening polymeric composites using nanoclay: Crack tip scale effects on fracture toughness. *Composites Part A: Applied Science and Manufacturing*, **38**(1), pp. 34-43.
16. MAROUF, B.T., PEARSON, R.A. and BAGHERI, R., 2009. Anomalous fracture behavior in an epoxy-based hybrid composite. *Materials Science and Engineering A*, **515**(1-2), pp. 49-58.
17. DEAN, J.M., LIPIC, P.M., GRUBBS, R.B., COOK, R.F. and BATES, F.S., 2001. Micellar structure and mechanical properties of block copolymer-modified epoxies. *Journal of Polymer Science, Part B: Polymer Physics*, **39**(23), pp. 2996-3010.
18. DEAN, J.M., GRUBBS, R.B., SAAD, W., COOK, R.F. and BATES, F.S., 2003. Mechanical properties of block copolymer vesicle and micelle modified epoxies. *Journal of Polymer Science, Part B: Polymer Physics*, **41**(20), pp. 2444-2456.

19. LIU, J., SUE, H.-J., THOMPSON, Z.J., BATES, F.S., DETTLOFF, M., JACOB, G., VERGHESE, N. and PHAM, H., 2008. Nanocavitation in self-assembled amphiphilic block copolymer-modified epoxy. *Macromolecules*, **41**(20), pp. 7616-7624.
20. GERARD, P., BOUPAT, N.P., FINE, T., GERVAT, L. and PASCAULT, J.-P., 2007. Toughness properties of lightly crosslinked epoxies using block copolymers. *Macromolecular Symposia*, **256**, pp. 55-64.
21. HYDRO, R.M. and PEARSON, R.A., 2007. Epoxies toughened with triblock copolymers. *Journal of Polymer Science, Part B: Polymer Physics*, **45**(12), pp. 1470-1481.
22. MOLONEY, A.C., KAUSCH, H.H. and STIEGER, H.R., 1983. The fracture of particulate-filled epoxide resins - Part 1. *Journal of Materials Science*, **18**(1), pp. 208-216.
23. HSIEH, T.H., KINLOCH, A.J., MASANIA, K., SOHN LEE, J., TAYLOR, A.C. and SPRENGER, S., 2010. The toughness of epoxy polymers and fibre composites modified with rubber microparticles and silica nanoparticles. *Journal of Materials Science*, **45**(5), pp. 1193-1210.
24. LIU, W., HOA, S.V. and PUGH, M., 2004. Morphology and performance of epoxy nanocomposites modified with organoclay and rubber. *Polymer Engineering and Science*, **44**(6), pp. 1178-1186.
25. BALAKRISHNAN, S., START, P.R., RAGHAVAN, D. and HUDSON, S.D., 2005. The influence of clay and elastomer concentration on the morphology and fracture energy of preformed acrylic rubber dispersed clay filled epoxy nanocomposites. *Polymer*, **46**(25), pp. 11255-11262.
26. BASHAR, M.T., SUNDARARAJ, U. and MERTINY, P., 2011. Study of Matrix Micro-cracking in Nanoclay and Acrylic Tri-block-copolymer Modified Epoxy/basalt Fiber-reinforced Pressure-retaining Structures. *Express polymer letters*, **5**, pp. 882-896.
27. ZERDA, A.S. and LESSER, A.J., 2001. Intercalated clay nanocomposites: Morphology, mechanics, and fracture behavior. *Journal of Polymer Science, Part B: Polymer Physics*, **39**(11), pp. 1137-1146.

28. KINLOCH, A.J. and TAYLOR, A.C., 2003. Mechanical and fracture properties of epoxy/inorganic micro- and nano-composites. *Journal of Materials Science Letters*, **22**(20), pp. 1439-1441.
29. ZILG, C., MÜLHAUPT, R. and FINTER, J., 1999. Morphology and toughness/stiffness balance of nanocomposites based upon anhydride-cured epoxy resins and layered silicates. *Macromolecular Chemistry and Physics*, **200**(3), pp. 661-670.
30. GARG, A.C. and MAI, Y.-W., 1988. Failure mechanisms in toughened epoxy resins-A review. *Composites Science and Technology*, **31**(3), pp. 179-223.

Chapter 7

Interlaminar Fracture Behaviour of Nanoparticle Modified Epoxy/Basalt Fiber-reinforced Laminates⁴

SYNOPSIS: The effect of nano-reinforcements on mode-I interlaminar fracture toughness of filament-wound basalt fiber-reinforced laminates was studied. It was found that delamination fracture toughness was not influenced by the presence of nanoparticles in the matrix. Decreasing fiber volume fraction, on the other hand, significantly improved interlaminar fracture energy. Rigid fibers in these composites constrict the stress field ahead of the crack-tip. Hence, increasing resin content enhanced composite delamination energy by increasing the capacity for matrix deformation. Interlaminar crack propagation through the composite was observed to occur mainly by interfacial failure and matrix cracking.

7.1 INTRODUCTION

Intrinsic heterogeneity and anisotropy in fiber-reinforced polymer (FRP) structures often introduce significant complexity, which obscures the appreciation of distinct failure mechanisms. In high-pressure applications, fluid leakage through the wall of a composite pipe or vessel as a result of transverse matrix cracking usually constitutes failure and thus terminates service life [1-3]. This particular failure event, which is frequently termed functional failure, severely degrades performance of pressure-bearing composite structures even though the material may still be able to sustain applied mechanical loads. It is widely believed that transverse micro-cracking is a matrix dominated phenomenon but there are various other factors that contribute to the initiation and propagation of micro-cracks (e.g. fiber volume fraction, fiber architecture and applied loading conditions). Micro-cracking in

⁴ A version of this chapter has been published as: BASHAR, M., SUNDARARAJ, U. and MERTINY, P., 2013. Mode-I interlaminar fracture behavior of nanoparticle modified epoxy/basalt fibre-reinforced laminates. *Polymer Testing*, **32**(2), pp. 402-412.

pressure-bearing composite structures frequently occurs in conjunction with interlaminar cracking between adjacent plies, i.e. delamination. The occurrence of transverse matrix micro-cracking in conjunction with delamination greatly increases the possibility of fluid leakage through the wall of a pipe or vessel [1-2].

Advances in nanotechnology have generated considerable optimism regarding significant improvements in mechanical, thermal, electrical and barrier properties of nano-reinforced materials. Lately, substantial efforts have been made towards improving polymer toughness by incorporating nanoparticles in brittle matrix systems such as epoxy [4-6]. Traditionally, epoxy is toughened through techniques such as flexibilization of the epoxy backbone, lowering polymer cross-link density and addition of dispersed micro-particles. In contrast, nano-scale particles have been shown to impart considerable improvements in polymer toughness relative to their micro-scale counterparts while maintaining important mechanical properties at comparatively low filler contents. Several studies on the fracture behaviour of nanoparticle reinforced laminated composites have shown improvements in interlaminar fracture toughness [7-10], interlaminar shear strength [11-12], flexural strength [11] and micro-crack density [12].

An organically modified sodium-montmorillonite (Na-MMT) nanoclay and an acrylic based triblock-copolymer were chosen for this study. Inside a polymer the transformation of lamellar tactoids of sodium-montmorillonite into intercalated clay nanostructures are known to increase epoxy toughness [8-11, 13]. Acrylic block-copolymers have the ability to self-assemble to form nanostructures (e.g. micelles, vesicles) through selective chemical interactions with the epoxy matrix [6, 14-15]. It has been demonstrated in the technical literature that nanoclay has the ability to improve epoxy fracture behaviour by crack pinning, crack deflection and matrix deformation mechanisms [6, 9]. In block-copolymer toughened epoxy, particle cavitation, debonding and matrix shear yielding are recognized toughening mechanisms for resisting crack propagation [14]. Matrix deformation [16-20], fiber pull-out, fiber bridging, fiber breakage [16] and interfacial debonding [18-19] are the major forms of delamination energy dissipation processes occurring in fiber composites. Moreover, factors such as fiber volume fraction [19, 21-25], ply thickness [18], fiber type and orientation [24-26], residual stress state [16] and material uniformity [17] are also known to affect mode-I interlaminar fracture toughness. It has generally been agreed upon that in a fiber composite

increasing the neat resin toughness above a certain limiting value cannot effectively be translated into interlaminar fracture toughness [16-19]. Therefore, for fiber composite systems the question remains, is it worthwhile to enhance the resin toughness beyond a certain trade-off value. A thorough understanding of the relationship between the composite delamination fracture toughness with the corresponding resin toughness would provide insight into this question.

In this part of a thesis the influence of resin toughness associated with different nanoparticle incorporation and fiber volume fraction on fracture properties of the given epoxy system was investigated. Delamination resistance of filament-wound fiber-reinforced composites were evaluated. Fracture energies of modified epoxies and their corresponding fiber composites were contrasted providing a quantitative analysis.

7.2 RESULTS AND DISCUSSION

7.2.1 Mode-I Interlaminar Fracture Toughness of the Fiber Composites

The sample preparation and measurement methods of mode-I interlaminar fracture toughness testing of fiber composites are elaborated in Sections 2.2.5 and 3.10, respectively. Specimens were tested at least in quadruplicate for each laminate system with a specific matrix composition. Figure 7.1 presents characteristic load-displacement graphs of unidirectional basalt fiber laminates obtained from opening mode delamination tests. The data relate to a delamination growth approaching 50 mm from the edge of starter crack film. All load-displacement curves shown in Figure 7.1 were found to be linear up to the onset of crack initiation, after which stable crack growth behaviour was observed. The crack opening displacement of the laminates made with the nanoclay containing resin formulation was found to be smaller than that of neat epoxy laminates. This was attributed to an embrittlement effect of the rigid nanoclay fillers on the epoxy matrix [20]. The unloading curves in Figure 7.1 clearly demonstrate that extending the crack by 5 mm through the composite followed by unloading to zero displacement did not introduce any appreciable permanent deformation in the specimens as the load prior to reloading was found to be zero.

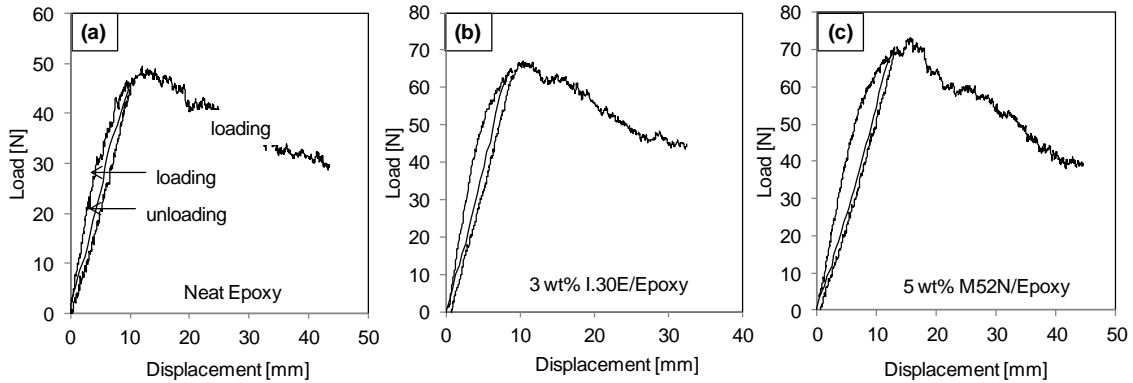


Figure 7.1 Load-displacement curves of the DCB test specimens made with: (a) neat epoxy and modified epoxy containing (b) 3 wt% I.30E and (c) 5 wt% M52N respectively.

The crack growth resistance curves (R-curves) shown in Figure 7.2 delineate the variations in critical strain energy release rate as a function of delamination length for different fiber composites fabricated under identical conditions. Initially, delamination fracture energy increased monotonically until at a later stage in the experiment steady-state crack propagation associated with significant fiber bridging became effective. It is presumed here that a substantial amount of energy was dissipated due to fiber bridging, and strain energy reached a plateau as shown by the resistance curves. The steady-state plateau value was reached after a crack growth of roughly 35 mm, with the nanoparticle filled composites showing a steeper rise in the resistance curve in the earlier stages of delamination. R-curves shown in Figure 7.2 also indicate that adding I.30E and M52N into epoxy polymer increased both the onset of interlaminar crack initiation and propagation energy. It is important to note though that nanofiller addition was also accompanied by a decrease in fiber volume fraction as recorded in Table 7-1. Also tabulated in Table 7-1 are the fracture energies and fiber volume fractions of the fiber composites and corresponding bulk nanocomposites, along with standard deviations. The composite made with unmodified epoxy, G_{IC} at initiation was measured to be 120 J/m^2 and 240 J/m^2 , respectively for NL and VIS (according to the definition given in Chapter 3); this composite has a fiber volume fraction of 0.64. It is interesting to note that the visually observed crack initiation value (VIS) of fiber composite closely matches the G_{IC} of the neat resin of 240 J/m^2 . Identical fracture energy values may be interpreted as the existence of a representative plastic zone size for the bulk neat epoxy and associated fiber composite

[15]. However, this deduction is disputable in the present context as the visual crack initiation value (VIS) is associated with an appreciable crack growth of 1 mm through the laminate interlayer, and other fiber dominated energy dissipation phenomena were thereby operative. It was shown previously by Hsieh et al. [7] in a study on fiber composites modified with CTBN rubber microparticles and silica nanoparticles that delamination initiation energy exceeded bulk polymer fracture energy due to contributions from additional toughening mechanisms, i.e. fiber debonding, fiber pull-out and fiber bridging. Nevertheless, being a function of matrix toughness, crack initiation energy may be regarded as a conservative minimum value in composite interlaminar fracture toughness testing [26]. Considering the importance of crack initiation data for the composite structures under consideration, the fracture energy associated with the point of deviation from linearity (NL) was herein chosen as the interlaminar crack initiation value.

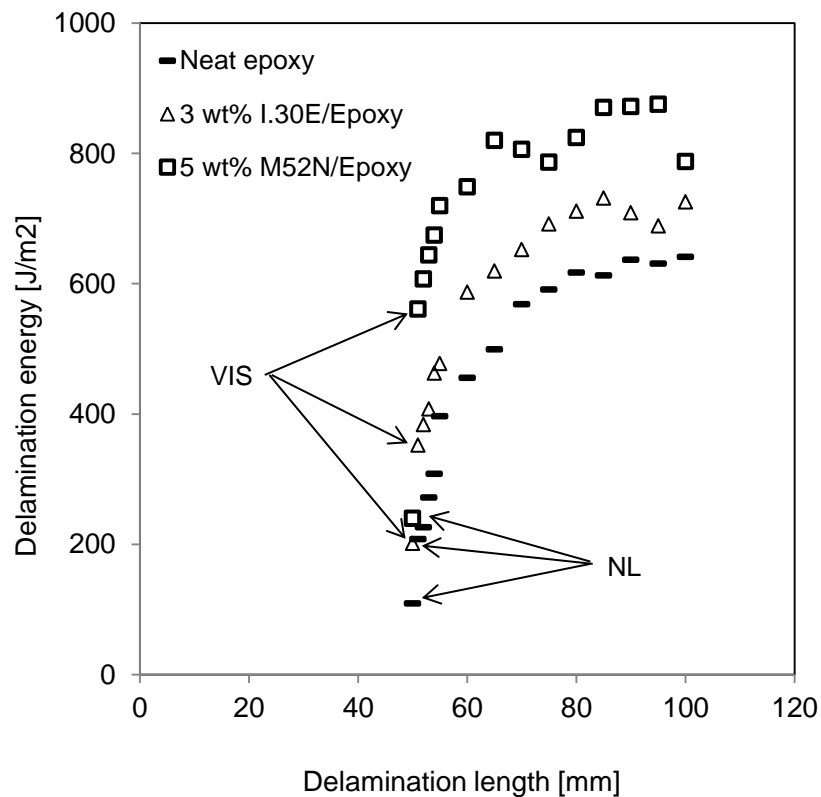


Figure 7.2 Variations in strain energy release rate with delamination length of different fiber composites.

Table 7-1 Fracture energy of bulk epoxy and its nanocomposites and corresponding fiber-reinforced composites.

Particle- matrix loading	Fiber volume fraction	Fracture energy, J/m ²			
		Fiber composite		Bulk composite	
		Initiation		Propagation	
		NL	VIS		
0 wt% (Neat)	0.64	120 ± 8	240 ± 33	600 ± 33	235 ± 28
0 wt% (Neat)	0.55	230 ± 17	410 ± 63	795 ± 91	
1 wt% M52N	0.59	175 ± 33	370 ± 37	595 ± 65	280 ± 37
3 wt% M52N	0.63	150 ± 18	355 ± 31	610 ± 69	495 ± 78
5 wt% M52N	0.56	255 ± 32	535 ± 35	785 ± 53	765 ± 60
1 wt% I.30E	0.58	155 ± 22	290 ± 39	490 ± 51	225 ± 11
3 wt% I.30E	0.5	195 ± 7	365 ± 23	645 ± 95	230 ± 9

Figure 7.3 presents interlaminar fracture toughness as a function of laminate fiber volume fraction. This figure highlights the fact that decreasing fiber volume fraction of the laminate made of neat epoxy resin from 0.65 to 0.55 significantly improved composite delamination fracture energy. Similarly, interlaminar fracture energy values for composites fabricated with modified polymer matrices increased at higher resin contents. Jordan et al. [19] also reported a rise in steady-state delamination resistance energy from 620 J/m² to 1015 J/m² by lowering fiber volume fraction from 0.71 to 0.60 in a rubber toughened epoxy composite. Their microscopic study further revealed that the resin-rich interlaminar region between plies in the composite with the lowest fiber volume fraction doubled in thickness compared to the lowest resin content composite. Lee [25] also observed higher delamination initiation energy with increasing resin content (from 0.27 to 0.40) in glass and graphite fiber epoxy laminates. Davies et al. [23] presented evidence of increasing mode-II interlaminar fracture toughness (both initiation and propagation) with decreasing fiber content (from 0.65 to 0.42) in quasi-unidirectional glass fiber epoxy composites. They prescribed this effect to stem from increased plastic deformation in a thicker resin-rich interlaminar region. The above literature findings support the premise that matrix dominated fracture processes such as delamination initiation are strongly influenced by the resin content [26]. It was postulated by Hunston [16]

and others [17-19, 27] with regards to interlaminar fracture in fiber composites that the rigid fibers restrict the development of a plastic zone at the crack-tip. In the present study, the improvement in the fiber composite strain energy with increasing resin concentration implicates the presence of such a constraining influence by the fibers. In other words, with decreasing fiber volume fraction the resin occupied region between adjacent fibers became larger, which reduces the constraining effect of the fiber. To further support this conjecture an analysis of the plastic zone size was conducted. According to linear elastic fracture mechanics the plastic zone size in neat epoxy under plane-strain condition was approximated to be $6 \mu\text{m}$ from Equation (7.1) [28].

$$r_y = \frac{1}{6\pi} \left(\frac{K_I}{\sigma_{ys}} \right)^2 \quad (7.1)$$

where r_y is the radius of the plastic zone and K_I is the stress intensity factor ($0.78 \text{ MPa}\cdot\text{m}^{0.5}$). The tensile yield stress $\sigma_{ys} = 73.25 \text{ MPa}$ of the neat epoxy was determined by uniaxial tensile testing. Figure 7.4 displays cross-section views from the middle portion of the specimen thickness for a laminate made with pure epoxy having a fiber volume fraction of 0.64. Note that broken fiber edges visible in Figure 7.4 are merely artifacts produced during polishing of the sample surface. Figure 7.4 displays a closely packed fiber arrangement with diminutive fiber-fiber spacing of typically less than $\sim 6 \mu\text{m}$. This observation in conjunction with the theoretical plastic zone size substantiates the notion that the influence of matrix ductility was restricted during interlaminar fracture, and that rigid fibers affected the stress field away from the crack-tip. Critical failure stresses were thus ascertained at lower loads than suggested from bulk polymer fracture testing. This deduction is supported by work of Bradley [18] who stated that if interlayer spacing between plies (i.e. fiber-fiber spacing) matches or exceeds the damage zone size in the bulk polymer, interlaminar fracture toughness would at least be equivalent to the matrix toughness. Conversely, resin toughness does not effectively translate into delamination fracture toughness if the fiber-fiber spacing is smaller than the bulk composite deformation zone. The phenomena described above are assumed to have been operative for the fiber-reinforced epoxy composites under investigation.

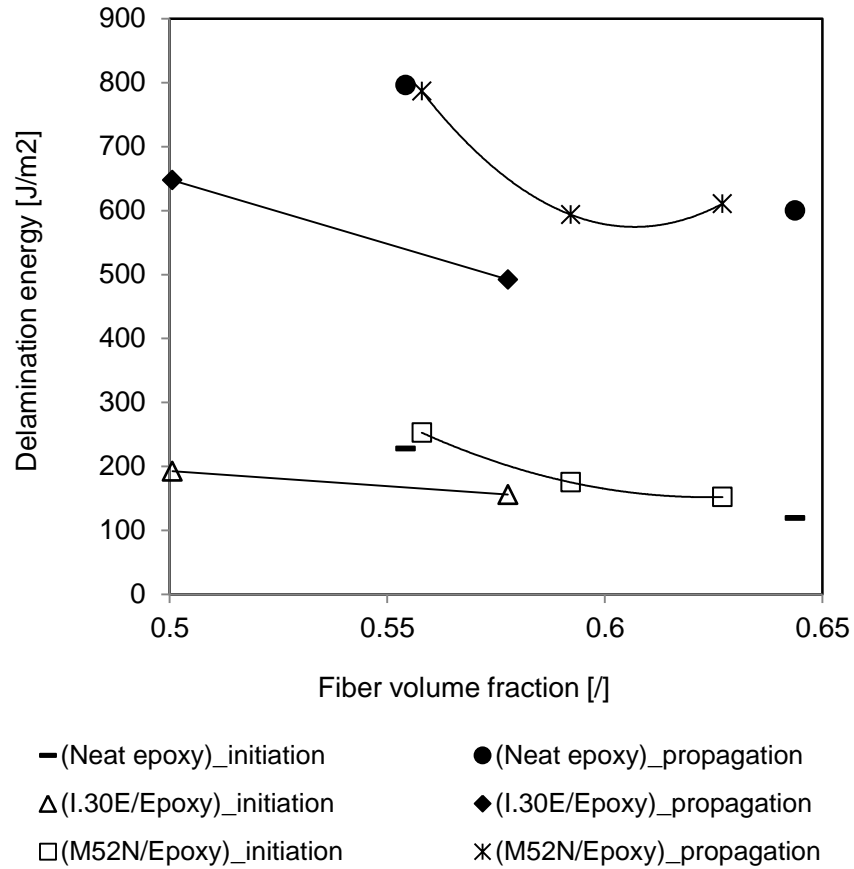


Figure 7.3 Dependence of delamination energy on fiber volume fraction of different fiber composites.

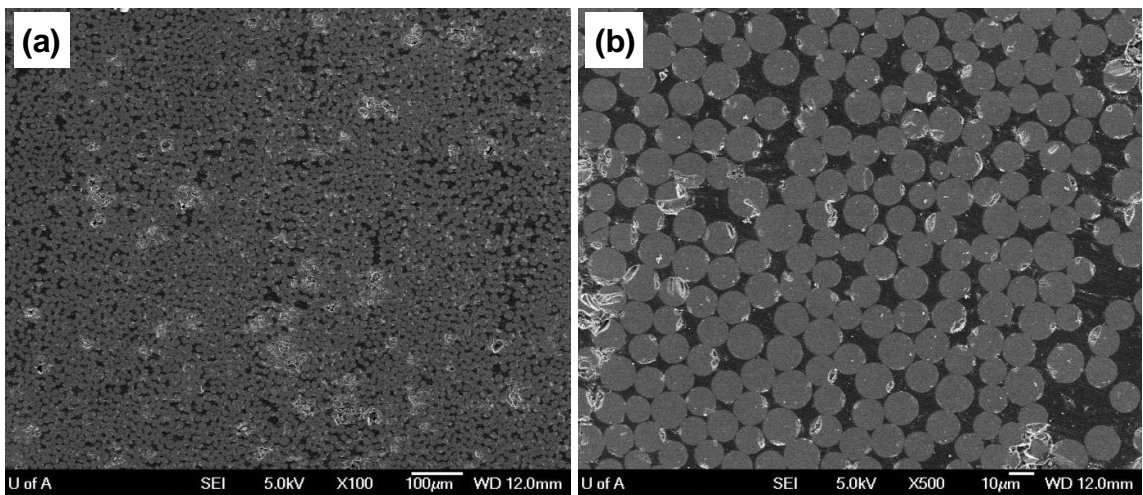


Figure 7.4 SEM pictures of the cross-section of laminate made with neat epoxy taken at: (a) low and (b) high magnifications.

7.2.2 Comparison of Bulk Polymer and Fiber Composite Fracture Energy

In Figures 7.5 and 7.6, interlaminar crack initiation energy (NL) of the fiber composites and the fracture energy of corresponding bulk polymers were plotted against the respective I.30E and M52N nanofiller loadings. From Figure 7.5, it is observed that nanoclay dispersants enhanced interlaminar crack initiation energy (NL); yet, this improvement was lower when compared to the composite made with neat epoxy having a fiber volume fraction of 0.55. This behaviour can be explained by the earlier findings for nanoclay filled bulk nanocomposites where resistance to crack growth values remained almost unchanged with nanoclay addition. Previously, Kim et al. [20] considered an embrittling effect of rigid silica fillers to lead to reduced epoxy matrix deformation. Embrittlement of the epoxy matrix was presumably responsible for the unaltered fracture energy of their modified epoxy even though additional toughening mechanisms associated with the rigid fillers may have been operative. In a separate study, Subramanian and Sun [13] documented the alignment of nanoclay along the fiber axis (i.e. crack propagation direction) causing reduction in composite delamination propagation energy relative to unmodified laminates. Therefore, it may be hypothesized that the existence of few nanoclay aggregates (as shown in Chapter 6 and reference [6]) may have acted as stress concentration points causing micro-cracks to initiate instead of resisting crack propagation. Contrary to the above observation a moderate improvement in initial fracture energy was observed by Becker et al. [8] and Siddiqui et al. [9] in carbon fiber-reinforced epoxy-clay nanocomposites. In these studies, fiber volume fractions were considerably lower, so it can be assumed that constraining effects of the fibers would be of less significance compared to the present study. Also, the authors in [8-9] mentioned improvements in the bulk composite fracture energies with nanoclay loading (which was not the case in the present study).

As shown in Figure 7.6 for block-copolymer modified epoxy the interlaminar crack initiation energy of the fiber composites was substantially less than the fracture energy of the corresponding bulk polymers. This result can be explained by fibers constricting the development of the crack-tip plastic zone. No significant effect of nano-reinforcements on interlaminar fracture toughness values was observed because the range of fiber volume fractions studied herein was too high for full utilization of the modified epoxy fracture toughness. This notion is substantiated considering the laminates made with neat and 5 wt%

block-copolymer toughened epoxy with comparable fiber volume fractions of ~ 0.55 , in which case practically identical crack growth resistance values were recorded. Also, these laminates exhibited initial delamination resistance (NL) values of 230 J/m^2 and 255 J/m^2 which are representative of the bulk epoxy fracture energy of 235 J/m^2 . Therefore, for the fiber composites it is surmised that full utilization of neat epoxy toughness could only be achieved for the low fiber volume fractions of ~ 0.55 .

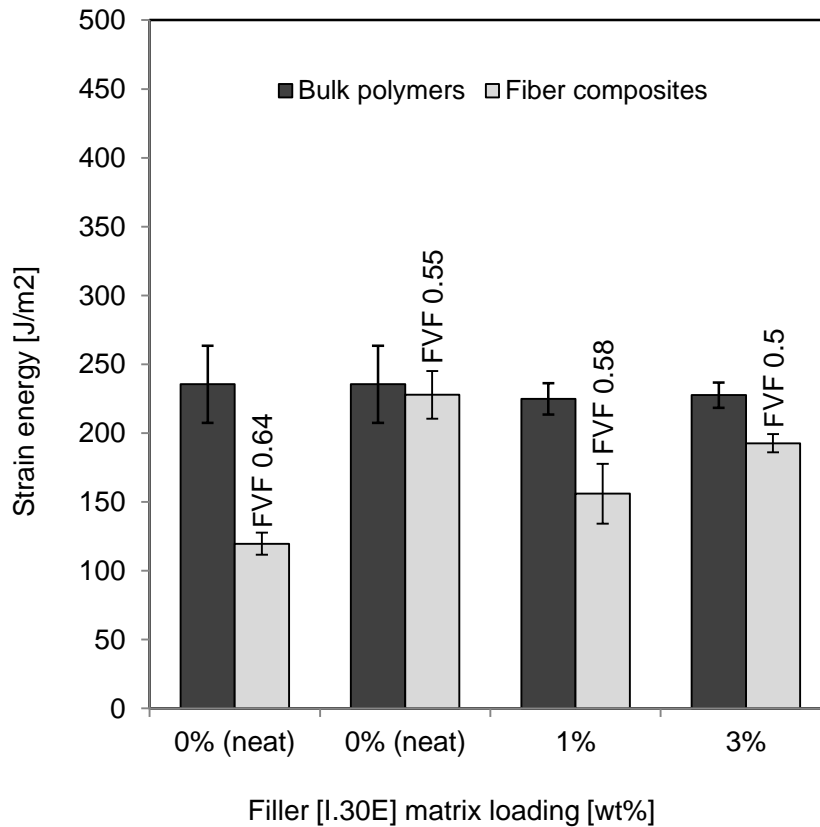


Figure 7.5 Crack initiation energy (NL) of the fiber composites with corresponding fracture energy of the bulk polymers as a function of I.30E content.

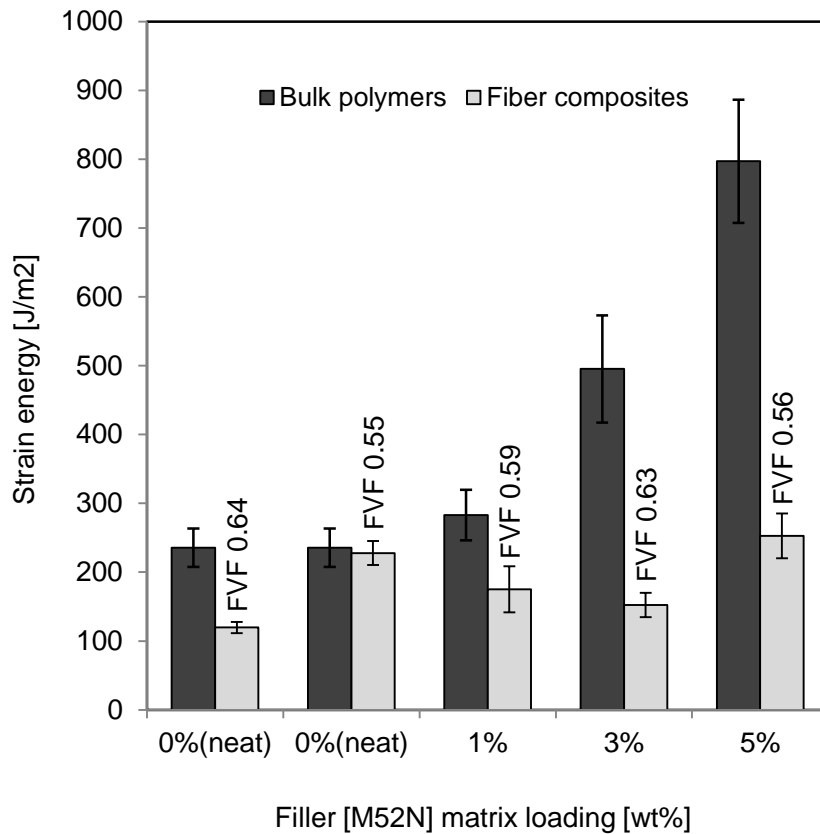


Figure 7.6 Crack initiation energy (NL) of the fiber composites with corresponding fracture energy of the bulk polymers as a function of M52N content.

In Figure 7.7, steady-state delamination energies of the fiber composites are plotted against the fracture energies of the corresponding bulk polymers for respective nanofiller compositions. It can be observed that for a brittle epoxy system (i.e. nanoclay modified epoxy) the delamination fracture toughness is greater than the resin fracture energy as previously documented by Hunston et al. [16]. In the present study, laminates were produced by the filament winding process, which introduced significant fiber intermingling (e.g. fiber nesting) and misalignment between adjacent plies. As a result of considerable debonding of the fibers from the matrix and subsequent crack propagation, a region of bridged fibers formed stretching behind the crack-tip before ultimate fiber breakage occurred (see Figure 7.8). Consequently, toughening mechanisms such as fiber pull-out, fiber bridging and fiber breakage accounted for further dissipation of energy in the fiber composites. Note also that in

unidirectional composites fiber bridging during delamination crack growth is considerably more prevalent compared to angle-ply or woven fiber laminates. In contrast, in a ductile polymer the higher fracture toughness corresponds to the formation of a larger deformation zone at the crack-tip. For the fiber composites made with the ductile resin system (i.e. block-copolymer modified epoxy) limited transfer of neat resin fracture energy into composite steady-state delamination energy signifies the restraining influence of the fibers. Clearly, this effect is more pronounced in a tougher polymer than in a brittle polymer [16-19, 27]. According to the literature [9, 16, 19] cited, the general consensus is that for resin fracture energies exceeding 700 J/m^2 the improvement in fiber composite interlaminar fracture toughness is only moderate, and increasing the resin G_{IC} further to values over 2000 J/m^2 would have a rather insignificant effect on fiber composite fracture toughness.

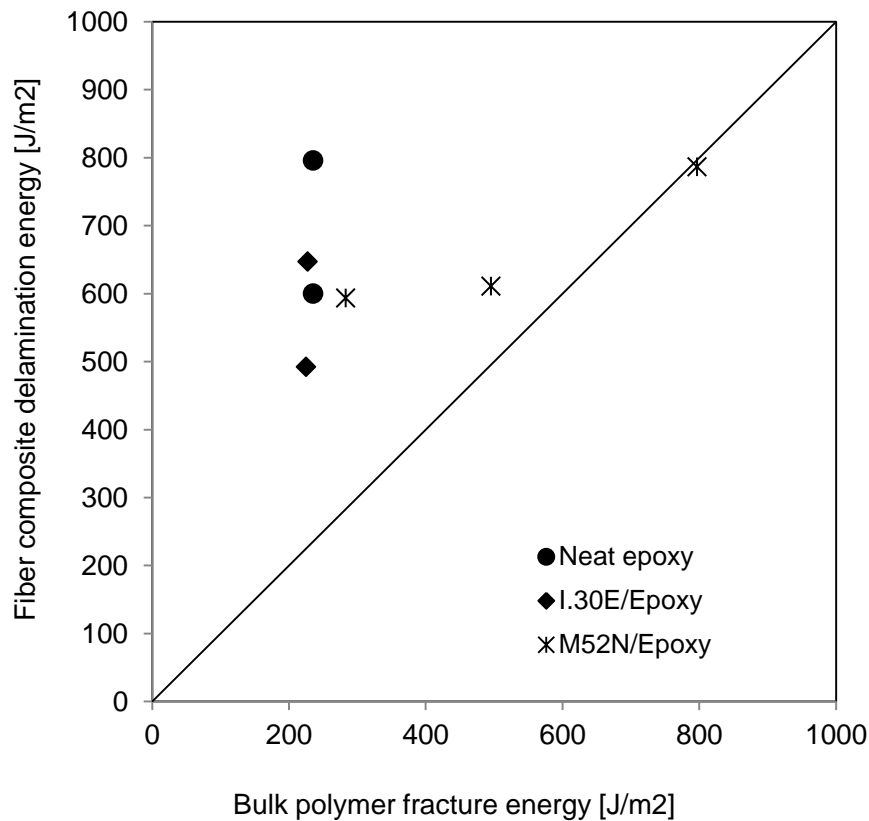


Figure 7.7 Comparison between steady-state delamination energy of fiber composites and strain energy of bulk polymers.

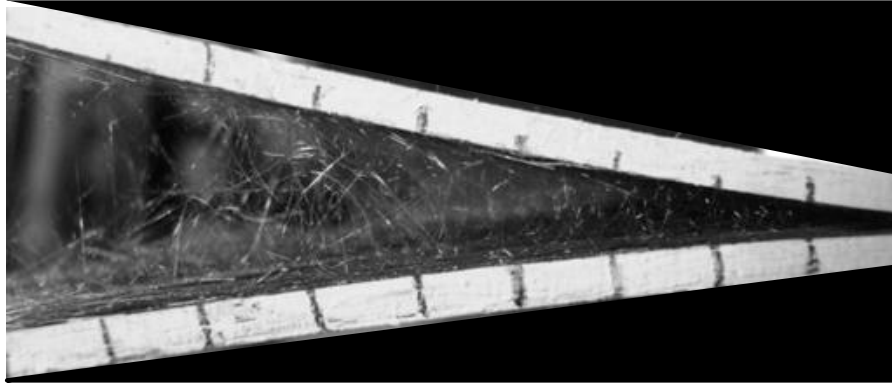


Figure 7.8 Fiber bridging that took place during delamination in a laminate made of neat resin and basalt fiber.

7.2.3 Fracture Surface Analysis

In the neat epoxy laminates planar crack growth proceeded mainly by debonding along the fiber-matrix interface as revealed by SEM examination of cracked surfaces as shown in Figure 7.9. Fiber-matrix interfacial failure is known also to influence delamination fracture toughness, since improving neat resin toughness without strong enough interfacial bonding would not adequately enhance fiber composite fracture toughness. Visual observation suggests little matrix deformation, as has been assumed for the densely packed fiber arrangements. For nanoclay modified laminates the fractographic evidence of Figure 7.10 shows crack extension along the fiber-matrix interface with the absence of appreciable matrix deformation, which is reminiscent of brittle fracture behaviour. Nanoclays can be seen embedded in the epoxy matrix providing little resistance to crack propagation.

Figure 7.11 exhibits fracture surfaces of a block-copolymer toughened composite illustrating that fracture clearly occurs along or close to the interface rather than by cohesive failure through the matrix. The SEM pictures also suggest that the morphology of the fiber composite fracture surface is significantly different from samples with block-copolymer modified epoxy resin shown in Figure 5.13 (in Chapter 5). The bulk polymer showed random distribution of nanostructured micelles, while in fiber composite coated fibers and nodular interface structures are apparent. Again, no sign of significant matrix deformation is noticeable. The differences in morphology may manifest that the matrix behaved differently in the fracture process of the fiber composites. Li et al. [29] studied interfacial structures of

glass fiber-reinforced polystyrene composites, where triblock-copolymer coupling agents polystyrene-*b*-poly(*n*-butylacrylate)-*b*-poly(γ -methacryloxypropyltrimethoxysilane) were chemically grafted on the fiber surface. They observed so-called hemispherical domain morphology at the fiber interface where PBuA blocks collapsed onto the glass surface surrounded by a layer of polystyrene blocks interdiffused with the polystyrene matrix melt. In the present study it is hypothesized that a similar but nodular domain structure was composed of a PBuA core and a PMMA corona due to the preferential interaction between different block segments towards epoxy and fiber reinforcement. This convoluted morphology seen at the epoxy-glass interface possibly substantiates stronger interfacial adhesion between the matrix and the fibers; however, this postulate requires further corroboration. In summary, for the various fiber composite systems studied herein the crack growth was mainly by a combination of fiber-matrix interfacial debonding and matrix cracking notwithstanding differences in the resin formulation. It was also noticed visually that fracture surfaces of filament-wound composites are not as plane as commonly observed in laminated composites. Furthermore, corrugated features of the fracture surface in fiber composites generally suggest the creation of additional surface area with the expense of more fracture energy. Similar to the idea proposed before, at the time of laminate fabrication intermingling of fibers between adjacent plies resulted in fiber nesting. Hence, for the crack propagation to occur the nested fibers needed to be pulled out from adjacent plies by changing the planar crack front to meander along the fibers causing greater energy dissipation.

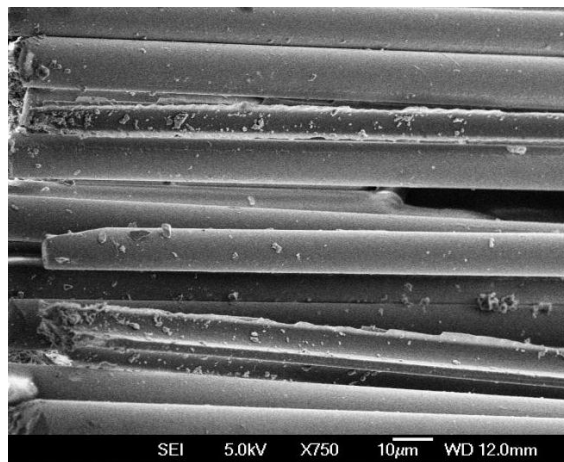


Figure 7.9 SEM image of a DCB fracture surface of a laminate made with neat epoxy.

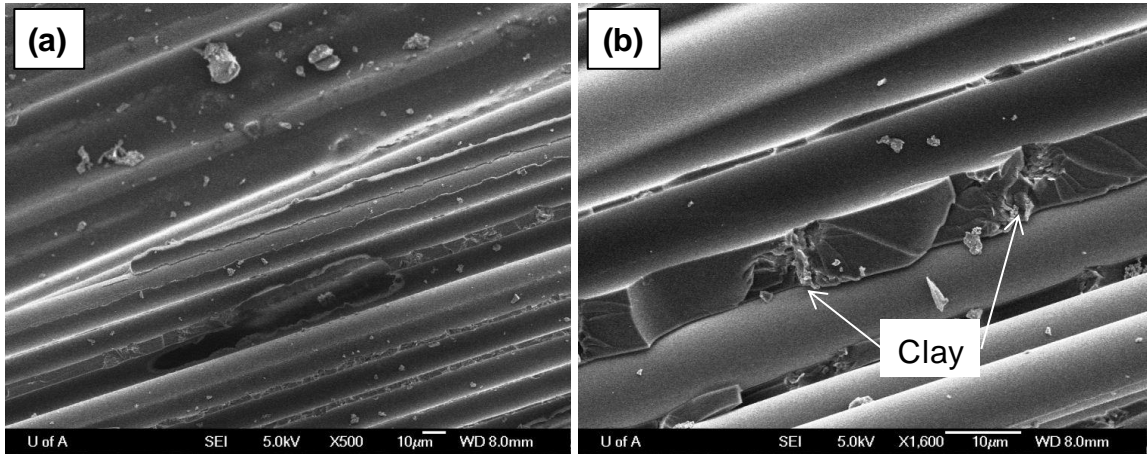


Figure 7.10 SEM images of DCB fracture surface of 3 wt% I.30E modified epoxy laminate taken at (a) low and (b) high magnifications.

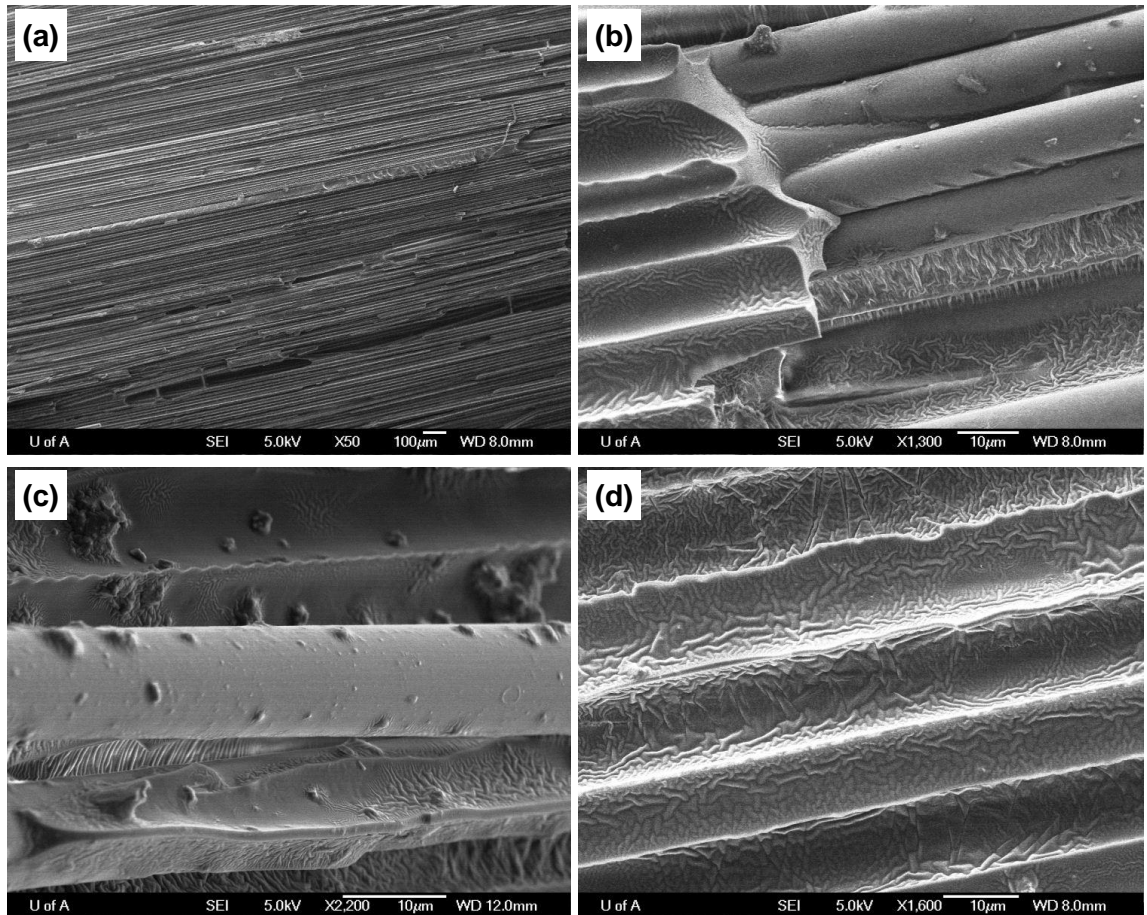


Figure 7.11 SEM images of the DCB fracture surface of 3 wt% M52N modified epoxy laminate taken at (a) low and (b)-(d) high magnifications.

7.3 CONCLUSIONS

A qualitative correlation can be derived from the present results regarding the translation of bulk epoxy fracture energy into fiber composites. Based on the above observations it can be inferred that the main governing factor in delamination crack initiation was matrix ductility, provided that firstly the crack-tip plastic zone was not affected by a restraining effect from adjacent fibers, and secondly, fiber-matrix bonding strength was sufficiently high. Steady-state crack propagation values of nanoclay filled epoxy composites were found to surpass the bulk polymer fracture energy. In this type of fiber composite, matrix toughness as well as other crack resistance phenomena commonly associated with the presence of fibers (e.g. fiber pull-out, fiber bridging and fiber breakage) substantially increased delamination fracture toughness. On the other hand, in the block-copolymer modified epoxy composites the equivalent improvement of delamination energy to the fullest extent of bulk polymer fracture energy was not realized as fibers restricted crack-tip plastic zone size. It was further found that reductions in fiber volume fraction enhanced interlaminar fracture toughness in the fiber composites, which was attributed to the formation of a matrix deformation zone with less interference from rigid fibers. In accord with other published works this investigation showed that for strain energy values exceeding 700 J/m^2 an increase in resin toughness does not adequately transfer into composite interlaminar fracture toughness when fiber volume fractions are maintained at comparable levels.

REFERENCES

1. JONES, M.L.C. and HULL, D., 1979. Microscopy of failure mechanisms in filament-wound pipe. *Journal of Materials Science*, **14**(1), pp. 165-174.
2. MARTENS, M. and ELLYIN, F., 2000. Biaxial monotonic behavior of a multidirectional glass fiber epoxy pipe. *Composites Part A: Applied Science and Manufacturing*, **31**(9), pp. 1001-1014.
3. MERTINY, P. and ELLYIN, F., 2002. Influence of the filament winding tension on physical and mechanical properties of reinforced composites. *Composites Part A: Applied Science and Manufacturing*, **33**(12), pp. 1615-1622.
4. BASHAR, M.T., SUNDARARAJ, U. and MERTINY, P., 2012. Microstructure and mechanical properties of epoxy hybrid nanocomposites modified with acrylic tri-

block-copolymer and layered-silicate nanoclay. *Composites Part A: Applied Science and Manufacturing*, **43**, pp. 945-954.

5. MILLER, S.G. and MEADOR, M.A., 2007. POLYMER- LAYERED SILICATE NANOCOMPOSITES FOR CRYOTANK APPLICATIONS, *Collection of Technical Papers - AIAA/ASME/ASCE/AHS/ASC Structures, Structural Dynamics and Materials Conference 2007*, pp. 7530-7538.

6. BASHAR, M.T., SUNDARARAJ, U. and MERTINY, P., 2011. Study of Matrix Micro-cracking in Nanoclay and Acrylic Tri-block-copolymer Modified Epoxy/basalt Fiber-reinforced Pressure-retaining Structures. *Express polymer letters*, **5**, pp. 882-896.

7. HSIEH, T.H., KINLOCH, A.J., MASANIA, K., SOHN LEE, J., TAYLOR, A.C. and SPRENGER, S., 2010. The toughness of epoxy polymers and fibre composites modified with rubber microparticles and silica nanoparticles. *Journal of Materials Science*, **45**(5), pp. 1193-1210.

8. BECKER, O., VARLEY, R.J. and SIMON, G.P., 2003. Use of layered silicates to supplementary toughen high performance epoxy-carbon fiber composites. *Journal of Materials Science Letters*, **22**(20), pp. 1411-1414.

9. SIDDIQUI, N.A., WOO, R.S.C., KIM, J.-K., LEUNG, C.C.K. and MUNIR, A., 2007. Mode I interlaminar fracture behavior and mechanical properties of CFRPs with nanoclay-filled epoxy matrix. *Composites Part A: Applied Science and Manufacturing*, **38**(2), pp. 449-460.

10. XU, Y. and HOA, S.V., 2008. Mechanical properties of carbon fiber reinforced epoxy/clay nanocomposites. *Composites Science and Technology*, **68**(3-4), pp. 854-861.

11. HAQUE, A., SHAMSUZZOHA, M., HUSSAIN, F. and DEAN, D., 2003. S2-glass/epoxy polymer nanocomposites: Manufacturing, structures, thermal and mechanical properties. *Journal of Composite Materials*, **37**(20), pp. 1821-1838.

12. TIMMERMAN, J.F., HAYES, B.S. and SEFERIS, J.C., 2002. Nanoclay reinforcement effects on the cryogenic microcracking of carbon fiber/epoxy composites. *Composites Science and Technology*, **62**(9), pp. 1249-1258.

13. SUBRAMANIYAN, A.K. and SUN, C.T., 2008. Interlaminar fracture behavior of nanoclay reinforced glass fiber composites. *Journal of Composite Materials*, **42**(20), pp. 2111-2122.

14. WU, J., THIO, Y.S. and BATES, F.S., 2005. Structure and properties of PBO-PEO diblock copolymer modified epoxy. *Journal of Polymer Science, Part B: Polymer Physics*, **43**(15), pp. 1950-1965.
15. BASHAR, M.T., SUNDARARAJ, U. and MERTINY, P., 2011. STUDY OF FRACTURE BEHAVIOR OF NANOCLAY FILLED EPOXY/BASALT FIBER-REINFORCED NANOCOMPOSITES, *Proceedings of the 26th ASC Technical Conference 2011*, pp. 1-12.
16. HUNSTON, D.L., 1984. Composite interlaminar fracture: effect of matrix fracture energy. *Composites technology review*, **6**(4), pp. 176-180.
17. HUNSTON, D.L., MOULTON, R.J., JOHNSTON, N.J. and BASCOM, W.D., 1987. MATRIX RESIN EFFECTS IN COMPOSITE DELAMINATION: MODE I FRACTURE ASPECTS. *ASTM Special Technical Publication 1987*, pp. 74-94.
18. BRADLEY, W.L., 1989. Understanding the translation of neat resin toughness into delamination toughness in composites. *Mechanical and corrosion properties. Series A, Key engineering materials*, **37**, pp. 161-198.
19. JORDAN, W., BRADLEY, W. and MOULTON, R., 1989. Relating Resin Mechanical-Properties to Composite Delamination Fracture-Toughness. *Journal of Composite Materials*, **23**(9), pp. 923-943.
20. KIM, J., BAILLIE, C., POH, J. and MAI, Y.-W., 1992. Fracture toughness of CFRP with modified epoxy resin matrices. *Composites Science and Technology*, **43**(3), pp. 283-297.
21. COMPSTON, P. and JAR, P.-Y.B., 1999. Influence of fibre volume fraction on the mode I interlaminar fracture toughness of a glass-fibre/vinyl ester composite. *Applied Composite Materials*, **6**(6), pp. 353-368.
22. LEE, S., 1986. A Comparison of Fracture-Toughness of Matrix Controlled Failure Modes - Delamination and Transverse Cracking. *Journal of Composite Materials*, **20**(2), pp. 185-196.
23. DAVIES, P., CASARI, P. and CARLSSON, L.A., 2005. Influence of fibre volume fraction on mode II interlaminar fracture toughness of glass/epoxy using the 4ENF specimen. *Composites Science and Technology*, **65**(2), pp. 295-300.

24. MAROM, G., ROMAN, I., HAREL, H., ROSENSAFT, M., KENIG, S. and MOSHONOV, A., 1988. The strain energy release rate of delamination in fabric-reinforced composites. *International Journal of Adhesion and Adhesives*, **8**(2), pp. 85-91.
25. JORDAN, W.M. and BRADLEY, W.L., 1984. EFFECT OF RESIN CONTENT ON THE DELAMINATION FRACTURE BEHAVIOR OF GRAPHITE EPOXY LAMINATES. *National SAMPE Symposium and Exhibition (Proceedings)* 1984, pp. 1422-1437.
26. RUSSELL, A.J. and STREET, K.N., 1982. FACTORS AFFECTING THE INTERLAMINAR FRACTURE ENERGY OF GRAPHITE/EPOXY LAMINATES. *Proceedings of the ICCM-IV conference on Progress in Science and Engineering in Composites* 1982, pp. 279-286.
27. JORDAN, W.M. and BRADLEY, W.L., 1987. MICROMECHANISMS OF FRACTURE IN TOUGHENED GRAPHITE-EPOXY LAMINATES. *ASTM Special Technical Publication* 1987, pp. 95-114.
28. Anderson, T.L., 2005. *Fracture Mechanics Fundamentals and Applications*. Boca Raton: CRC Press.
29. LI, Y., LIN, Q., CHEN, L. and ZHOU, X., 2009. Assembly of triblock copolymer brush at glass fiber/polystyrene interface and its effect on interfacial shear strength. *Composites Science and Technology*, **69**(11-12), pp. 1919-1924.

Chapter 8

Study of Matrix Micro-cracking in Nanoclay and Acrylic Triblock-copolymer Modified Epoxy/Basalt Fiber-reinforced Pressure-retaining Structures⁵

SYNOPSIS: In fiber-reinforced polymer pressure-retaining structures, such as pipes and vessels, micro-level failure commonly causes fluid permeation due to matrix cracking. This chapter explores the effect of nano-reinforcements on matrix cracking in filament-wound basalt fiber/epoxy composite structures. The mechanical properties and micromechanism of fracture processes in bulk epoxy nanocomposites and hybrid fiber-reinforced composite tubes modified with acrylic triblock-copolymer and organophilic layered silicate clay were investigated. It has been confirmed in the previous chapters of the thesis that block-copolymer addition significantly enhances epoxy fracture toughness by a mechanism of particle cavitation and matrix shear yielding, whereas toughness remained unchanged in nanoclay filled nanocomposites due to the occurrence of lower energy resistance phenomena such as crack deflection and branching. Composite tubes modified with either the organic and inorganic nanoparticles exhibited moderate improvements in leakage failure strain (i.e. matrix cracking strain); however, reductions in functional and structural failure strength were observed.

8.1 INTRODUCTION

Filament winding is known to be one of the most economic and efficient methods for producing fiber-reinforced polymer (FRP) structures such as pipes and vessels. Pressure-retaining structures made from FRP are becoming increasingly popular, and are frequently considered as an alternative to conventional metallic structures. Improved performance in

⁵ A version of this chapter has been published as: BASHAR, M., SUNDARARAJ, U. and MERTINY, P., 2011. Study of matrix micro-cracking in nanoclay and acrylic tri-block-copolymer modified epoxy/basalt fiber-reinforced pressure-retaining structures. *eXPRESS Polymer Letters*, **5**(10), pp. 882-896.

terms of high specific strength and corrosion resistance can be achieved with FRP pressure structures. However, the performance of these structures is dependent on the diverse and sustained loading conditions throughout their service life. It is therefore of great importance to understand their complex material behavior and damage mechanisms under different loading conditions and environmental effects.

In the design and application of composite pressure piping, functional and structural failure mechanisms must be considered [1-6]. In the case of functional failure (e.g. leakage) the structure is unable to contain the pressurized fluid, even though it is still able to sustain the applied mechanical loading. Leakage in composite tube or pressure vessel is attributed to the phenomenon causing fluid permeation through multiple pathways in the tube wall. Structural failure (e.g. burst failure) is thus characterized by the pipe's inability to carry the applied loading. These types of failure usually occur as separate events, but can happen as concomitant damage events depending on the applied loading situation. Functional failure is typically distinguished by fluid weepage and wetting of the outer wall. Due to fluid transmission through the wall, composite pressure structures have restricted application without any ancillary support medium (e.g. liner). Leakage is directly related to transverse matrix micro-cracking which is characterized by a reduction of composite stiffness as well as nonlinear stress-strain behavior. Functional failure is known to occur when transverse tensile loading normal to the fibers exceeds a certain threshold value [6].

On the basis of experimental evidence presented in the preceding chapters it can be inferred that thermosetting polymers such as epoxies are particularly prone to matrix cracking. One possible route to enhance crack resistance of thermosets is by dispersing a second particulate phase inside the polymer matrix. In case of the dispersed particulate/epoxy system, the mechanism of toughening can be as diverse as the multifarious reinforcements available [7]. Irrespective of the operative crack resistance mechanism, the sole purpose of the dispersant is to aid the deformation process for dissipating energy. In FRP structures the presence of a fibrous reinforcement phase introduced additional complexity to polymer toughening. It is known that toughness enhancements as observed in bulk polymers are not always transferrable to the same extent to fiber composite systems [8-9].

Recently, it has become an established procedure to develop polymer nanocomposites by commixing a polymeric phase with one or more reinforcing nano-scale materials, hence

generating remarkable physical properties in the developed material. As of now, nanotechnology in the context of filament-wound pressure piping and vessels has received only limited attention [10-11]. Since leakage failure is the consequence of matrix cracking in a polymeric composite pipe, incorporating a nano-scale phase may be an effective means for enhancing matrix toughness to resist transverse cracking. The notion underlying such efforts is to improve matrix toughness and thus effectively reduce fluid leakage in filament-wound pressure bearing structures. With this intention in mind, two different types of nanoparticles were investigated in this study, i.e. inorganic clay I.30E [11-14] and organic triblock-copolymer M52N [11, 15-19].

The study presented in this chapter investigated the proposition that incorporation of nanoparticles into a material system (polymer resin) can be an effective means to inhibit and/or impede transverse matrix cracking. As a consequence leakage failure of filament-wound composite pipe is expected to be suspended or delayed based on the postulation of increased crack resistance by the nanoparticle filled epoxy matrix. In this study several epoxy-nanoparticle formulations were developed, and filament-wound hybrid fiber-reinforced nanocomposites with various concentrations of nanoparticles were fabricated. Mechanical and fracture studies of bulk epoxy nanocomposites were performed, and hybrid filament-wound epoxy composite tubes were subjected to biaxial stress testing. Thus, this research provided considerable insight into the micro-failure mechanism of filament-wound fiber-reinforced tubulars in the presence of nano-inclusions.

8.2 RESULTS AND DISCUSSION

8.2.1 TOM Microscopy Study of Bulk Epoxy Nanocomposites

Transmission optical microscopy (TOM) allowed visualization of polymer deformation by identifying the birefringence and voided zone underneath the fracture surface. Assuming that a propagating crack would leave behind traces of a subsurface damage zone, TOM was employed to confirm the presence of a plastic zone for the pre-crack geometries shown in Figure 3.15. Figure 8.1 shows the existence of matrix deformation or shear banding that occurred under plane-strain fracture. The birefringent region for a sharp crack is mainly confined in the process zone near the starter crack (see Figure 8.1(b)), whereas for a blunt

crack the birefringent region shown in Figure 8.1(c) traverses the whole cross-section due to crack-tip plasticity. Dean et al. [15-16] and Hydro and Pearson [17] reported similar subsurface localized matrix deformation for block-copolymer (i.e. PEO-PEP, PMMA-PBuA-PMMA) modified epoxy. TOM images taken under bright field and cross-polarized light conditions represent a toughened epoxy containing 1 wt% M52N. The size of the crack-tip plastic zone can be estimated theoretically according to the Irwin equation [20]. In a plane-strain condition, the Irwin equation, i.e. Equation (7.1) yields the radii of the plastic zone 7.52 μm and 80.04 μm for the sharp and blunt crack geometries, respectively. In terms of the linear elastic fracture mechanics, the stress situation at the crack-tip can adequately explain the damage behavior as observed by TOM microscopy. Under plane-strain condition, a triaxial state of stress caused an intense stress field at the sharp crack-tip, thereby imposing restrictions on the plastic zone size. For the blunt crack-tip the stress is distributed over a wider section (mimicking a state of plane-stress) that contributed to the formation of a relatively larger plastic zone. In the later sections it will be shown that these differences in the stress field have a considerable effect on the toughening mechanism of the modified epoxy.

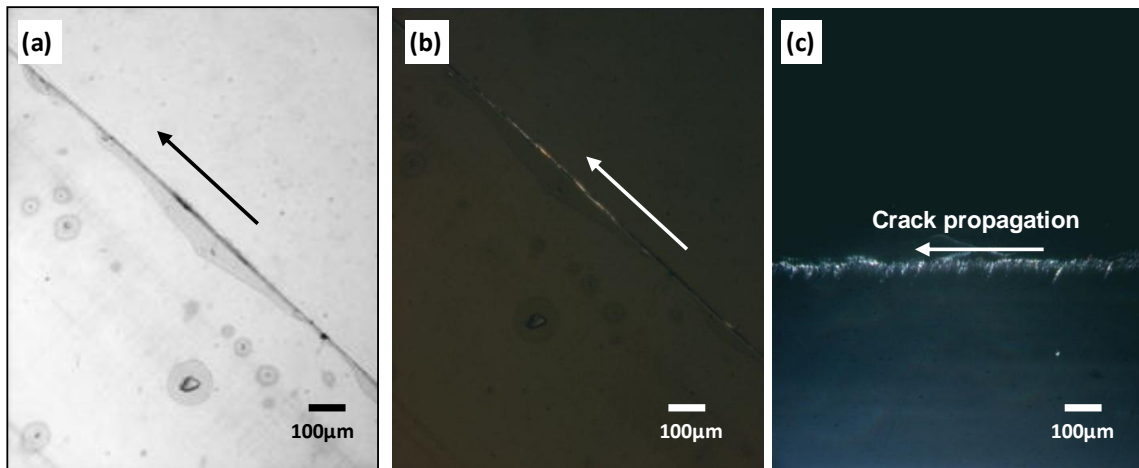


Figure 8.1 TOM images of cured block-copolymer/epoxy blend: sharp pre-cracked fracture surface examined under (a) bright field, (b) cross-polarized light and (c) blunt pre-cracked surface under cross-polarized light.

8.2.2 Fracture Properties of Bulk Epoxy Nanocomposites

As mentioned earlier, fracture toughness of the neat epoxy was estimated to be $0.78 \text{ MPa m}^{0.5}$. In Figures 8.2 and 8.3 average stress intensity factors of neat epoxy and its nanocomposites (i.e. incorporating I.30E nanoclay and M52N block-copolymer respectively) are compared for the sharp and blunt pre-crack geometries. Note that in the following, error bars shown in graphs represent plus and minus one standard deviation for tests performed in triplicate or greater; lines represent first or second degree polynomial trend lines. Only marginal or no improvement in fracture toughness was achieved for nanocomposites with a sharp crack, and for a sample containing 2 wt% I.30E with a blunt crack a moderated drop in fracture energy of up to 10% was observed (see Figure 8.2). According to Zilg et al. [12] and Zerda and Lesser [13], a mostly intercalated structure rather than an exfoliated nanocomposite improves toughness by exposing additional surface area during the propagation of a sharp crack. However, clay nanocomposites prepared in this study behaved differently, primarily due to partial exfoliation of the nanoclay, and secondly, because of the relatively smaller size of the intercalated nanoclay. It has been shown in Chapter 4 (in Figure 4.18) that most of the particles are very small on the micron level, indicating a rather uniform distribution of submicron-size particles. The ultrasonic mixing process is considered to be the cause for the breakdown of clay agglomerates into the submicron-size. In Chapter 4, micromechanisms of the fracture process were explored and discussed in light of the insignificant toughening effect of nanoclay in epoxy matrix. Presented in Section 4.2.4, the fracture surface morphology of the nanoclay filled epoxy evidenced repeated perturbation of the crack front from its original propagation path due to the presence of submicron intercalated clay. This resulted from the bifurcation and/or deflection of the primary crack into multiple secondary cracks which are not necessarily coplanar [21].

As presented in Figure 8.3 the behavior of block-copolymer filled epoxy was rather different. It is shown that a sharp pre-cracked nanocomposite containing 5 wt% M52N yields an almost twofold improvement in toughness, which reveals a direct contribution of block-copolymer loading on fracture toughness. Pearson and Yee [22-23] observed cavitation induced plastic deformation for rubber toughened epoxy, and Wu et al. [19] described a similar crack resistance phenomenon for nanostructured (micelle) block-copolymer modified epoxy. The author also observed similar phenomena during the fracture process. It is documented in

Section 5.2.4 that cavitation of the spherical micelles occurred during the fracture process. This is substantiated by the presence of minute spherical cavities with approximately ~20 nm size that are randomly dispersed in the polymer matrix. Hydrostatic tension ahead of the sharp crack-tip caused cavitation of the rubbery core of the block-copolymer resulting in localized shear deformation of the epoxy matrix; both are energy absorption mechanisms. In the case of blunt cracks only a minor enhancement in critical stress intensity became obvious, which is assumed to be the effect of crack-tip plasticity evidenced by a large deformation zone shown in TOM microscopy in Figure 8.1(c). Thus, without any discernible distinction in fracture energy between the block-copolymer modified epoxy and the neat epoxy the behavior with a blunt crack practically resembles tensile fracture. Subramaniyan and Sun [14] documented an equivalent effect of crack-tip zone plasticity in their study of organoclay and core-shell rubber toughened epoxy. As discussed by Subramaniyan and Sun [14] it appears that fracture behavior associated with propagation of blunt cracks is dominated by a stress concentration factor and not a stress intensity factor at failure.

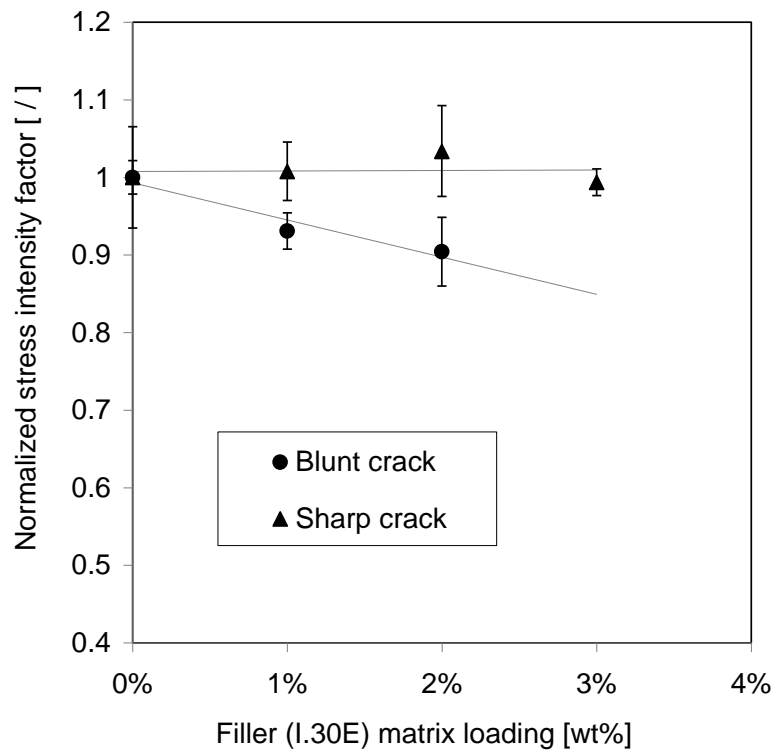


Figure 8.2 Critical stress intensity factors of nanocomposites relative to I.30E nanoclay concentration.

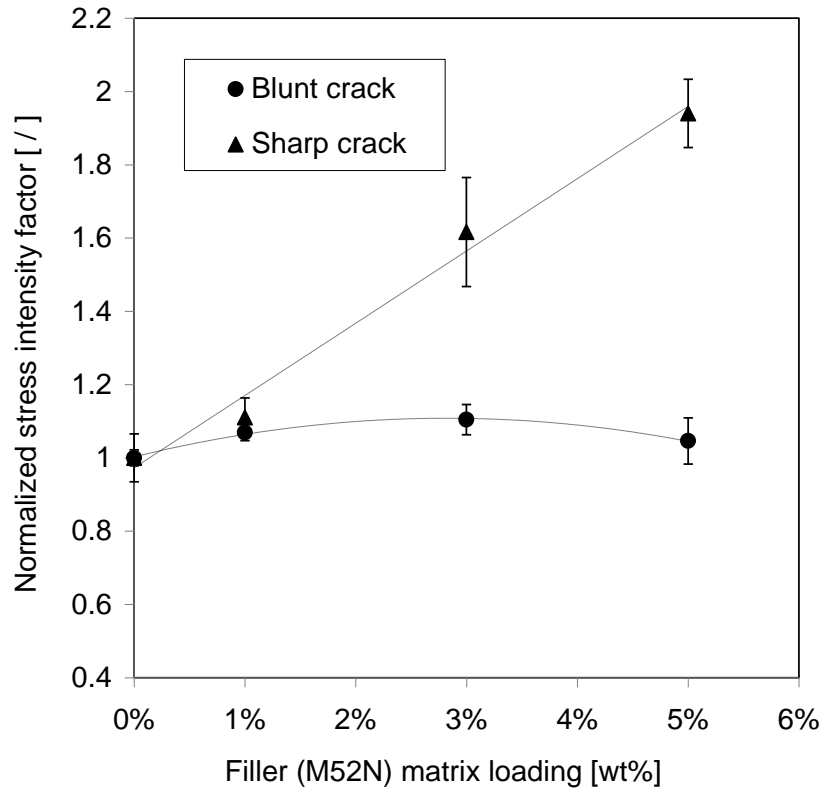


Figure 8.3 Critical stress intensity factors of nanocomposites relative to M52N block-copolymer concentration.

8.2.3 Mechanical Properties of Hybrid Nanocomposite Tubes

The fabrication method and mechanical testing of the hybrid fiber-reinforced nanocomposite tubes are presented in Sections 2.2.6 and 3.12, respectively. Prior to mechanical testing of the hybrid fiber-reinforced nanocomposite tubes, fiber volume fractions were determined by resin burn-out testing, and nominal wall thicknesses were also calculated. Corresponding data are summarized in Table 8-1. Tube samples made with I.30E and M52N exhibited, for the most part, decreasing fiber volume fraction with increasing nanofiller content. Accordingly, the reverse trend resulted for the wall thicknesses, which increased with rising nanofiller content. An increase in resin viscosity with nanofiller loading is assumed to have caused this behavior.

Table 8-1 Fiber volume fraction and nominal wall thickness for fiber-reinforced nanocomposite tubes.

Particle-matrix loading	Fiber volume fraction (%)	Nominal wall thickness (mm)
0 wt% (Neat)	66.8	1.306
1 wt% I.30E	59.9	1.472
2 wt% I.30E	59.9	1.472
3 wt% I.30E	58.8	1.499
1 wt% M52N	66.0	1.333
3 wt% M52N	65.9	1.341
5 wt% M52N	65.2	1.355

8.2.3.1 Qualitative Analysis of Functional and Structural Failure

In the present test case two obvious failure events were observed in the filament-wound composite tubes under the applied loading condition. For the pressure vessel type loading investigated here functional failure always preceded structural failure of the tubes. Functional failure was manifested by weepage, which is a passive fluid leakage mechanism through the tube wall. Weepage ultimately affects the capacity of fluid containment by a pressurized tubular terminating its useful service life. Leakage is the consequence of micro-damage within the polymer matrix phase and does not primarily affect the load-bearing capacity and structural integrity of the specimen. Noticeable changes in leakage rate can be a valuable indicator of the damaged state in the pipe structure as it depends on such parameters as crack density, size and interconnectivity. In composite pipes, micro-cracks develop parallel to the fiber direction due to resultant transverse loading acting perpendicular to the fiber [3] (see Figure 8.4 (a)). Fine striations formed by transverse cracking are mainly confined in the specific lamina where they initiated. It should be noted here that transverse matrix cracking phenomenon is only possible by having an opening mode of positive displacement acting transverse to the fiber direction [6]. Microscopy inspection of the cracking mechanism by Jones and Hull [1] identified that both transverse matrix cracking and inter-ply delamination processes were operative at the time of fracture in filament-wound pipes. The tubes manufactured

in this study appeared to be opaque due to differences in the refractive indices of the basalt fibers and epoxy resin. As such, the investigation of micro-crack initiation and progression by visualization was not possible during pressure testing.

It is presumed that with increasing load more cracks would accumulate and coalesce; hence, small oil-wet zones were apparent on the outer surface of the pipe. This phenomenon of fluid penetration originating from internal matrix cracks ultimately wets the whole tube perimeter forming droplets to pour down. Intuitively, it can be inferred from the droplet formation that an extensive network of cracks had developed through the matrix to cause fluid loss. Post failure inspection of functionally failed fiber-reinforced composite tubes revealed multiple aligned, nearly homogenously distributed cracks, which form numerous interconnected fluid pathways from the inner to the outer pipe surface. The majority of these cracks are oriented parallel to the fiber direction with crossover undulation points indicating delamination of the laminates [3].

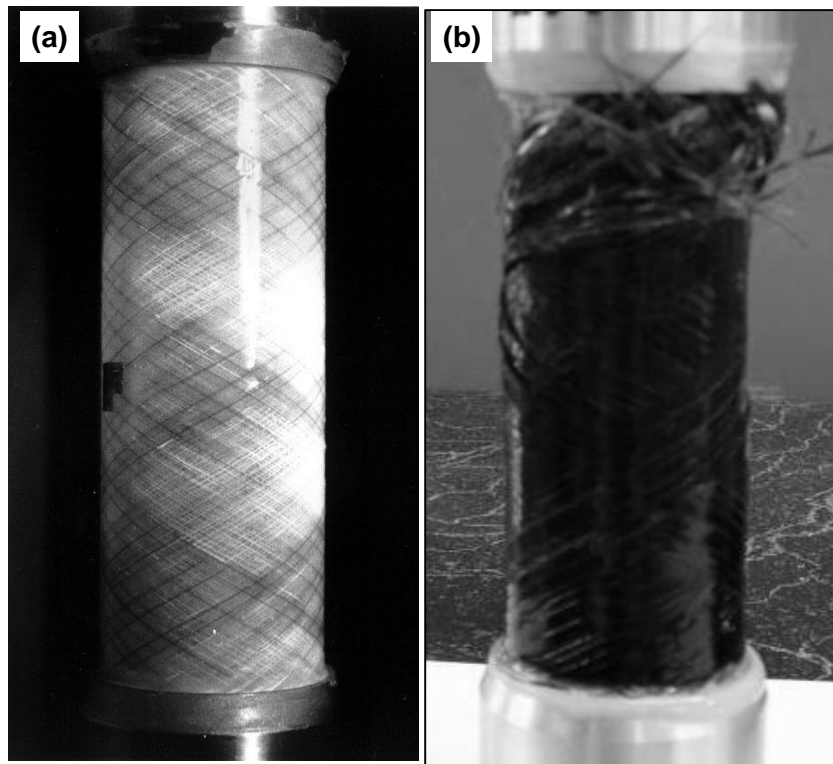


Figure 8.4 Photographs of specimen failure mode: (a) functional failure (epoxy/glass fiber tube) and (b) structural failure (epoxy/basalt fiber tube).

The tests were continued surpassing the leakage failure point until the intensifier fluid was exhausted by a catastrophic rupture of the specimen. The breakdown was sudden producing a localized perforation of the pipe that frequently occurred near one of the end connections. Structural failure in composite tubulars was therefore recognized as the loss of ultimate structural integrity. Transverse matrix cracking resulted in considerable damage to the polymer, facilitating the realignment of fibers in the direction of maximum principal stress, i.e. the 55° direction [24]. Being constrained at the specimen end connections, the fibers experienced localized fiber bending. These stress concentrations at the end caps are considered to be the cause for failure to occur remotely close to the tube ends. At failure opening, broken and frayed fiber strands could be seen, which is typically the characteristic of a predominately fiber dominated failure (see Figure 8.4 (b)). Clearly, functional failure did not coincide with the structural failure event. While the former is dominated by a micro structural progressive damage mechanism, the latter is controlled by a macro damage mode.

8.2.3.2 Biaxial Stress-strain Response

Figures 8.5 and 8.6 illustrate the biaxial stress versus strain plots of the composite tubes made with 3 wt% filler concentration. Stress and strain values were computed in the principal direction of the applied loading. An almost linear stress-strain response can be observed in hoop direction (Figure 8.5) before functional failure, whereas for the axial direction non-linear behavior was present long before the functional failure point (Figure 8.6). Considering the studied fiber configuration of $\pm 60^\circ$, the axial deformation is largely influenced by the response of the polymer, and this deformation was greater for the block-copolymer modified resin system. As load increases, a steady shift from linearity to non-linear behavior is indicative of beginning of matrix cracking and damage propagation, which manifested itself in a decrease in stiffness. The stress-strain behavior substantiates the idea that a matrix dominated progressive damage mode is operative over the loading range. In the composite tubes with M52N and I.30E modified epoxy, functional failure occurred at axial strains of 1.07% and 0.6% and circumferential strains of 0.25% and 0.2%, respectively.

Table 8-2 summarizes failure stresses (i.e. functional and structural failure strengths) of the tested nanocomposite tubes. Failure stresses were calculated by following the method outlined in Section 3.12. The hoop and axial leakage failure stresses of the neat epoxy

tube were found to be 175.40 MPa and 91.26 MPa, respectively. Following leakage failure a more complex deformation process associated with significant non-linear behavior was observed upon further stressing of the composite tube. It was noticed that the hoop stress-strain behavior changed from a rising trend toward decreasing strain, and that axial strain increased significantly after the functional failure. This has been observed before in other studies [4], and was related to a decreasing transverse stiffness of the composite pipe. As a result of substantial matrix cracking, the fibers tend to realign themselves along the direction of the resulting force. The fiber realignment process thus causes changes in the specimen geometry, affecting circumferential and axial directional strains in the gage section of the specimen. Burst failure stresses of 476.92 MPa and 246.9 MPa were recorded in hoop and axial direction for neat epoxy pipe. The sample therefore endured an approximately 2.7 times higher structural failure load than for functional failure. This clearly demonstrates the susceptibility of these tubular pressure vessels to leakage damage under the given loading condition and specimen lay-up configuration.

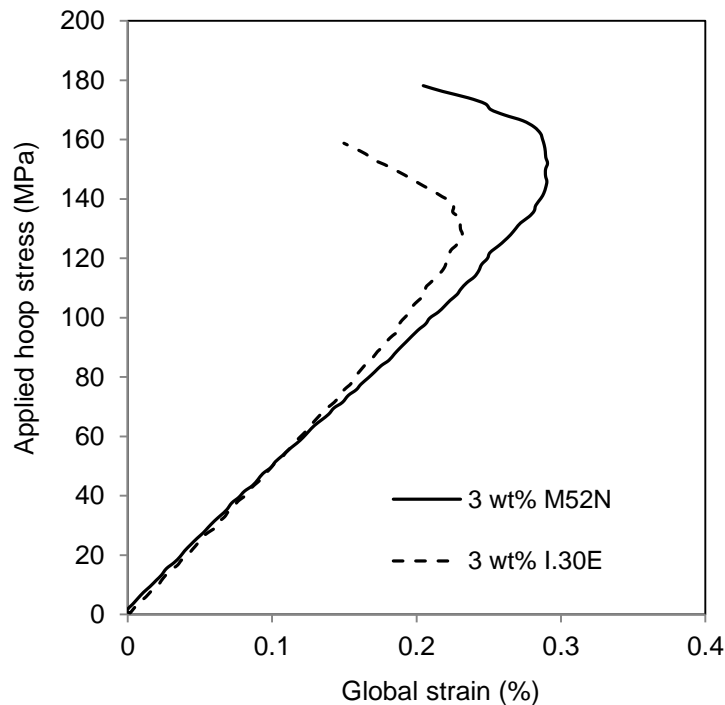
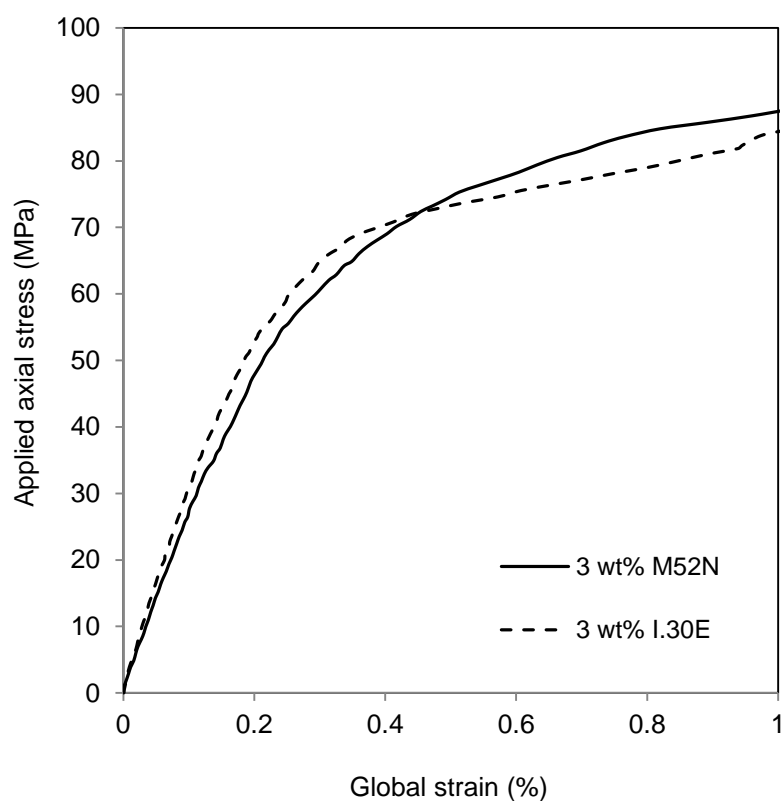


Figure 8.5 Hoop stress-strain response for [2H:1A] loading of $[\pm 60_3]_T$ wound tubes containing 3 wt% filler-matrix content.

Table 8-2 Experimental failure stresses of hybrid fiber-reinforced nanocomposite tubes.

Particle-matrix loading	Functional failure stress		Structural failure stress	
	Hoop (MPa)	Axial (MPa)	Hoop (MPa)	Axial (MPa)
0 wt% (Neat)	175.40	91.26	476.92	246.90
1 wt% I.30E	151.94	78.48	372.76	191.96
2 wt% I.30E	132.99	69.02	346.29	178.57
3 wt% I.30E	147.86	76.18	349.86	179.96
1 wt% M52N	181.68	94.10	452.78	233.99
3 wt% M52N	173.85	90.17	445.30	230.10
5 wt% M52N	161.72	83.77	446.21	230.34

**Figure 8.6** Axial stress-strain response for [2H:1A] loading of $[\pm 60_3]_T$ wound tubes containing 3 wt% filler-matrix content.

8.2.3.3 Fracture Analysis of Hybrid Nanocomposite Tubes

It is a common inference that transverse matrix cracking initiates near or at the fiber-matrix interface and then transmits through the resin matrix. Matrix cracks usually initiate at very low global strain levels due to high strain concentrations near the fiber resulting from the elastic discontinuity at the interface [1, 25]. Figure 8.7 depicts the influence of nanofiller loadings on maximum hoop strain, which usually is congruent with the leakage point at this loading ratio. Maximum hoop strain of the unmodified epoxy tubes was measured to occur at a mechanical strain of approximately 2400 $\mu\epsilon$. Note that in the published literature it was reported that functional failure occurred at about ~0.3% transverse-to-the-fiber strain for specimens having fiber arrangement and loading condition comparable to this study [6]. For a M52N loading of 5 wt% an increase in leakage failure strain of about 30% was observed. Hence, M52N significantly enhanced the leakage failure strain and at the same time, somewhat reduced stress-strain non-linearity. These results correspond to those reported by Garrett and Bailey [26] and Sjogren and Berglund [27-28], who demonstrated a significant increase in transverse cracking strains as a direct consequence of modifier concentration. Conversely, for nanoclay modified tubes the leakage failure strain remained practically unaffected, and a maximum of 10% increase in strain was observed for 3 wt% nanoclay in the matrix.

Functional and structural hoop failure stresses are presented with corresponding nanofiller loadings in Figures 8.8 and 8.9. The graph for M52N block-copolymer modified epoxy reveals that the hoop stress at leakage increased by only 4% with the addition of 1 wt% M52N (see Figure 8.8). For the remainder of block-copolymer concentrations a less pronounced effect on leakage strength was noticed, and a simultaneous decrease in leakage and burst strength was observed for 5 wt% M52N. Test data for tubes made with I.30E filled polymer showed that the nanoclay imparted significant reductions in both the leakage and burst failure strengths (see Figure 8.9). In summary, failure strength reductions were strongly correlated with I.30E loading, whereas strength values remained relatively stable when the polymer matrix was reinforced with M52N block-copolymer.

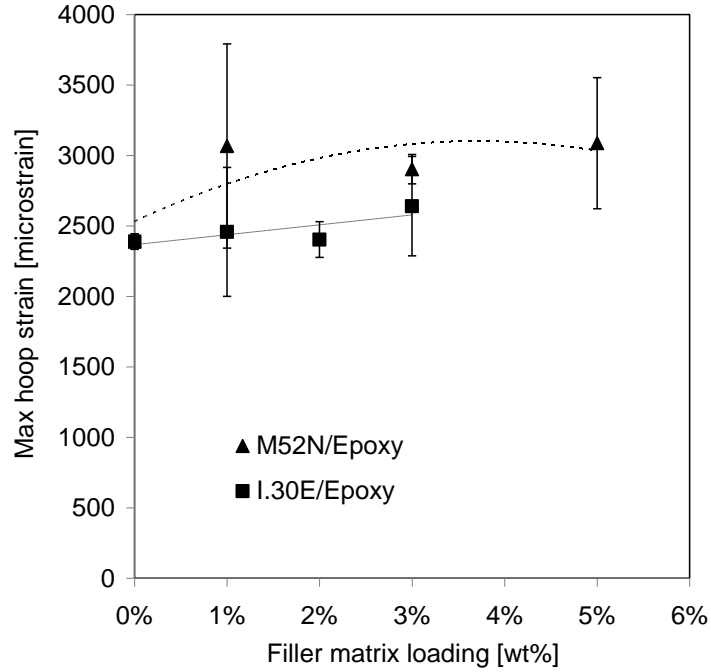


Figure 8.7 Maximum hoop strain corresponding to functional failure of hybrid nanocomposite tubes as a function of nanofiller loading.

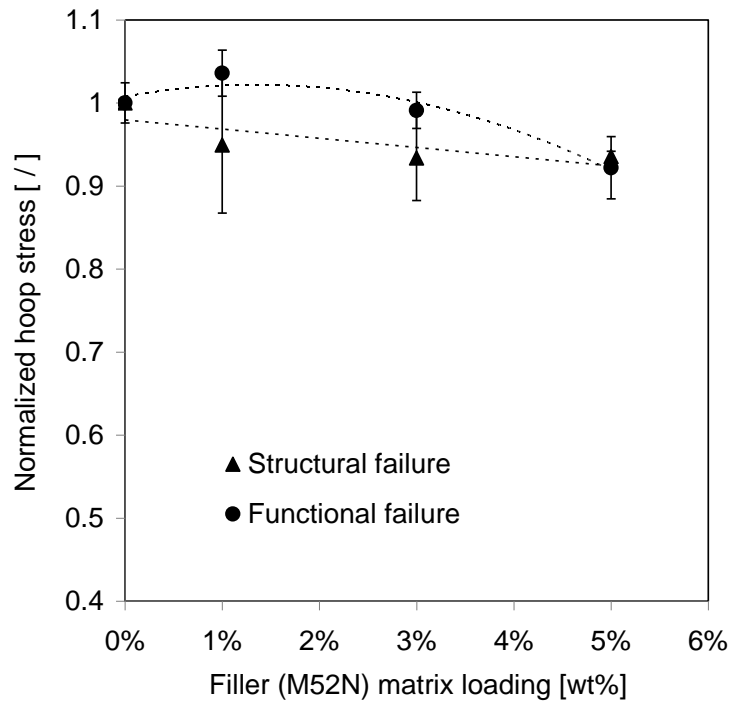


Figure 8.8 Hoop failure stress of hybrid nanocomposite tubes as a function of M52N block-copolymer loading.

In other studies with tubes made with pure epoxy it was observed that transverse cracks initiated at low global strain in zones of high fiber packing followed by sudden unstable crack growth. Crack initiation likely occurred by adhesive debonding at the fiber-matrix interface where local strain concentrations are high. Transverse cracking associated with interfacial debonding was observed by various researchers [27-28], and others have described the instantaneous crack propagation phenomenon [29-30]. In the case of block-copolymer modified epoxy, the enhanced matrix ductility caused a build-up of strain energy until the sudden release of this energy resulted in initiation and subsequent crack propagation. It appears that matrix toughness significantly affected crack initiation and/or debonding processes due to improved polymer ductility. Delayed debonding may also be the outcome of better interfacial adhesion between the fiber and the matrix [28], possibly due to a sizing effect of the P[(MMA-*co*-DMA)-*b*-BuA-*b*-(MMA-*co*-DMA)] block-copolymer on the basalt fiber material [31]. As a consequence, increased strains at leakage failure were observed. However, the influence of M52N block-copolymer addition on the amount and/or extent of cracking seems to have been insignificant as evidenced by only minor improvements in leakage failure stresses. It is assumed that restrictions imposed by adjacent fibers on the crack-tip plastic zone affected the propagation of transverse cracks, and also restricted the ability of nano-features associated with M52N block-copolymer addition, i.e. spherical micelles to cavitate and cause matrix shear yielding. It has been reported that in a fiber-polymer composite, fibers appear to constrain the crack-tip deformation zone [8]. This effect is more pronounced in a toughened polymer than in a brittle matrix. As a result, the development of matrix crack networks and associated fluid leakage was not diminished to an extent that one may have expected based on fracture toughness improvements in block-copolymer modified epoxy resin. The above statements are also confirmed by the study conducted on interlaminar fracture behavior of nanoparticle modified epoxy/basalt fiber-reinforced laminates presented in Chapter 7. Influenced by congruent trends between composite pipe leakage strengths and fracture energies ascertained for nanocomposite samples with a blunt crack, it was hypothesized that transverse matrix cracking in filament-wound tubes, which includes both the initiation and propagation of micro-cracks, resembles tensile fracture behavior in a brittle matrix material.

For the nanoclay modified epoxy material it was concluded that the presence of few flocculated clay particles provided an uneven distribution of stress concentration points throughout the epoxy matrix, which supposedly acted as initiation sites for transverse matrix cracks. Due to enhanced stress fields resulting from the interaction of clay aggregates and the applied loading, leakage strength of the composite tubes was degraded. The cause for reduced structural strength is believed to also lay with the aforementioned distribution of stress concentration points. Substantial matrix cracking further caused reduced structural strength. In the presence of a weakened fiber-matrix load-sharing mechanism, fibers failed at their weakest points at reduced global load levels. The degraded matrix also allowed fibers to realign along the direction of the resulting force (55° to the axial direction), thus imposing additional loading upon the fibers.

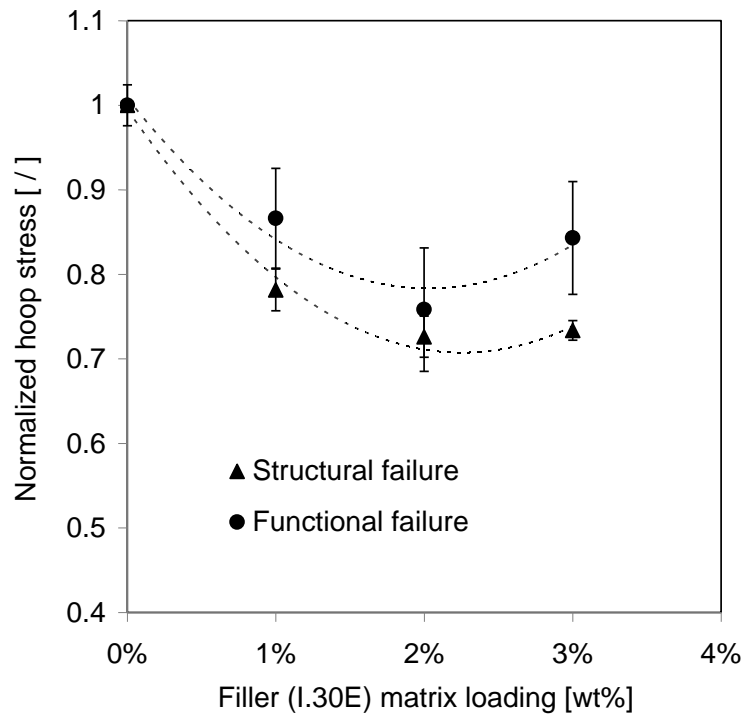


Figure 8.9 Hoop failure stress of hybrid nanocomposite tubes as a function of I.30E nanoclay loading.

8.3 CONCLUSIONS

The common intuition about transverse matrix cracking is that it is the consequence of stress acting transverse to the fiber direction. Based on these observations the idea was to reinforce the relatively brittle epoxy matrix with a nano-particulate phase with the intent to mitigate the progression of micro-cracks. Yet, the intended reinforcement effect could not be realized, despite a considerable improvement in fracture toughness for one type of the tested nanocomposite system, i.e. the M52N triblock-copolymer modified epoxy.

In the bulk nanocomposite system modification of epoxy with M52N rendered significant improvements of epoxy toughness by a process of particle cavitation and localized shear deformation of the matrix. In contrast, I.30E clay exhibited an almost negligible influence on epoxy toughness, where the fracture properties of the nanocomposites are dictated by the exfoliated and intercalated morphology of the clay.

It was hypothesized that the transverse cracking process for fiber composite tubes made with M52N block-copolymer toughened epoxy begins with prolonged straining followed by fiber-matrix interfacial debonding and immediate crack propagation. Crack progression was also influenced by alteration of the crack-tip stress field by adjacent fibers. In case of the I.30E nanoclay modified epoxy pipes, transverse matrix cracking was further accelerated in the presence of micron size clay aggregates which acted as stress concentrators. Even though leakage failure strain improved moderately for some of the hybrid nanocomposite tubes, these enhancements proved insignificant for the leakage failure strength, and the damage mechanism was found to practically resemble that of the neat epoxy composite tubes.

REFERENCES

1. JONES, M.L.C. and HULL, D., 1979. Microscopy of failure mechanisms in filament-wound pipe. *Journal of Materials Science*, **14**(1), pp. 165-174.
2. ELLYIN, F., CARROLL, M., KUJAWSKI, D. and CHIU, A.S., 1997. Behavior of multidirectional filament wound fibreglass/epoxy tubulars under biaxial loading. *Composites Part A: Applied Science and Manufacturing*, 28(9-10), pp. 781-790.
3. MARTENS, M. and ELLYIN, F., 2000. Biaxial monotonic behavior of a multidirectional glass fiber epoxy pipe. *Composites Part A: Applied Science and Manufacturing*, **31**(9), pp. 1001-1014.

4. MEIJER, G. and ELLYIN, F., 2008. A failure envelope for 60 filament wound glass fibre reinforced epoxy tubulars. *Composites Part A: Applied Science and Manufacturing*, **39**(3), pp. 555-564.
5. MERTINY, P., ELLYIN, F. and HOTHAN, A., 2004. An experimental investigation on the effect of multi-angle filament winding on the strength of tubular composite structures. *Composites Science and Technology*, **64**(1), pp. 1-9.
6. MERTINY, P. and ELLYIN, F., 2002. Influence of the filament winding tension on physical and mechanical properties of reinforced composites. *Composites Part A: Applied Science and Manufacturing*, **33**(12), pp. 1615-1622.
7. GARG, A.C. and MAI, Y.-W., 1988. Failure mechanisms in toughened epoxy resins- A review. *Composites Science and Technology*, **31**(3), pp. 179-223.
8. HUNSTON, D.L., 1984. Composite interlaminar fracture: effect of matrix fracture energy. *Composites technology review*, **6**(4), pp. 176-180.
9. BRADLEY, W.L., 1989. Understanding the translation of neat resin toughness into delamination toughness in composites. *Mechanical and corrosion properties. Series A, Key engineering materials*, **37**, pp. 161-198.
10. MILLER, S.G. and MEADOR, M.A., 2007. POLYMER- LAYERED SILICATE NANOCOMPOSITES FOR CRYOTANK APPLICATIONS, *Collection of Technical Papers - AIAA/ASME/ASCE/AHS/ASC Structures, Structural Dynamics and Materials Conference 2007*, pp. 7530-7538.
11. BASHAR, M.T., SUNDARARAJ, U. and MERTINY, P., 2011. Study of Matrix Micro-cracking in Nanoclay and Acrylic Tri-block-copolymer Modified Epoxy/basalt Fiber-reinforced Pressure-retaining Structures. *Express polymer letters*, **5**, pp. 882-896.
12. ZILG, C., MÜLHAUPT, R. and FINTER, J., 1999. Morphology and toughness/stiffness balance of nanocomposites based upon anhydride-cured epoxy resins and layered silicates. *Macromolecular Chemistry and Physics*, **200**(3), pp. 661-670.
13. ZERDA, A.S. and LESSER, A.J., 2001. Intercalated clay nanocomposites: Morphology, mechanics, and fracture behavior. *Journal of Polymer Science, Part B: Polymer Physics*, **39**(11), pp. 1137-1146.

14. SUBRAMANIYAN, A.K. and SUN, C.T., 2007. Toughening polymeric composites using nanoclay: Crack tip scale effects on fracture toughness. *Composites Part A: Applied Science and Manufacturing*, **38**(1), pp. 34-43.
15. DEAN, J.M., LIPIC, P.M., GRUBBS, R.B., COOK, R.F. and BATES, F.S., 2001. Micellar structure and mechanical properties of block copolymer-modified epoxies. *Journal of Polymer Science, Part B: Polymer Physics*, **39**(23), pp. 2996-3010.
16. DEAN, J.M., GRUBBS, R.B., SAAD, W., COOK, R.F. and BATES, F.S., 2003. Mechanical properties of block copolymer vesicle and micelle modified epoxies. *Journal of Polymer Science, Part B: Polymer Physics*, **41**(20), pp. 2444-2456.
17. HYDRO, R.M. and PEARSON, R.A., 2007. Epoxies toughened with triblock copolymers. *Journal of Polymer Science, Part B: Polymer Physics*, **45**(12), pp. 1470-1481.
18. GERARD, P., BOUPAT, N.P., FINE, T., GERVAT, L. and PASCAULT, J.-P., 2007. Toughness properties of lightly crosslinked epoxies using block copolymers. *Macromolecular Symposia*, **256**, pp. 55-64.
19. WU, J., THIO, Y.S. and BATES, F.S., 2005. Structure and properties of PBO-PEO diblock copolymer modified epoxy. *Journal of Polymer Science, Part B: Polymer Physics*, **43**(15), pp. 1950-1965.
20. HSIEH, T.H., KINLOCH, A.J., MASANIA, K., SOHN LEE, J., TAYLOR, A.C. and SPRENGER, S., 2010. The toughness of epoxy polymers and fibre composites modified with rubber microparticles and silica nanoparticles. *Journal of Materials Science*, **45**(5), pp. 1193-1210.
21. LEE, J. and YEE, A.F., 2000. Role of inherent matrix toughness on fracture of glass bead filled epoxies. *Polymer*, **41**(23), pp. 8375-8385.
22. PEARSON, R.A. and YEE, A.F., 1986. Toughening Mechanisms in Elastomer-modified Epoxies. Part 2: Microscopy Studies. *Journal of Materials Science*, **21**(7), pp. 2475-2488.
23. YEE, A.F. and PEARSON, R.A., 1986. Toughening mechanisms in elastomer-modified epoxies - Part 1 Mechanical studies. *Journal of Materials Science*, **21**(7), pp. 2462-2474.

24. MERTINY, P. and GOLD, A., 2007. Quantification of leakage damage in high-pressure fibre-reinforced polymer composite tubular vessels. *Polymer Testing*, **26**(2), pp. 172-179.
25. ASP, L.E., BERGLUND, L.A. and TALREJA, R., 1996. Prediction of matrix-initiated transverse failure in polymer composites. *Composites Science and Technology*, **56**(9), pp. 1089-1097.
26. GARRETT, K.W. and BAILEY, J.E., 1977. Effect of Resin Failure Strain on the Tensile Properties of Glass Fiber-reinforced Polyester Cross-ply Laminates. *Journal of Materials Science*, **12**(11), pp. 2189-2194.
27. SJOGREN, B.A. and BERGLUND, L.A., 1999. Toughening mechanisms in rubber-modified glass fiber/unsaturated polyester composites. *Polymer Composites*, **20**(5), pp. 705-712.
28. SJOGREN, B.A. and BERGLUND, L.A., 2000. Effects of matrix and interface on damage in GRP cross-ply laminates. *Composites Science and Technology*, **60**(1), pp. 9-21.
29. WANG, A.S.D., 1984. Fracture Mechanics of Sublaminar Cracks in Composite Materials. *Composites technology review*, **6**(2), pp. 45-62.
30. PARVIZI, A., GARRETT, K. and BAILEY, J., 1978. Constrained Cracking in Glass Fiber-Reinforced Epoxy Cross-Ply Laminates. *Journal of Materials Science*, **13**(1), pp. 195-201.
31. LI, Y., LIN, Q., CHEN, L. and ZHOU, X., 2009. Assembly of triblock copolymer brush at glass fiber/polystyrene interface and its effect on interfacial shear strength. *Composites Science and Technology*, **69**(11-12), pp. 1919-1924.

Chapter 9

Conclusions

9.1 SUMMARY OF RESEARCH FINDINGS AND CONTRIBUTIONS

In this study, the effect of nano-reinforcements on matrix micro-cracking of filament-wound composite structures was explored. The motivation for the current research arose from the hypothesis that homogeneously dispersed nano-inclusions in a polymer matrix would prevent or mitigate transverse-to-the-fibers crack initiation and subsequent propagation. The present study investigated morphology, physical, chemical, thermal, mechanical and fracture properties of bulk epoxy nanocomposites and hybrid fiber-reinforced epoxy nanocomposite structures. The nanocomposites with an epoxy matrix were prepared with various concentrations of two types of commercially available nanofillers i.e. organoclay and acrylic triblock-copolymer. Flat specimens for interlaminar fracture testing and tubular samples for pressure testing were filament-wound for this investigation.

The present study demonstrated that variations in the nanoclay dispersion method and the type of organic modifier can significantly affect the resulting nanocomposite morphology, and hence, the enhancement or even reduction of mechanical properties of epoxy-clay nanocomposites. For the acrylic triblock-copolymer modified epoxy, improved toughness without major reductions of important thermo-mechanical properties was ascertained. It was observed that the final properties were greatly influenced by the concentrations and constituents of the block-copolymers, their self-assemble morphology and the induced deformation mechanics in the matrix under applied loading. A particularly notable finding of this study is that tailorable and thus application-optimal mechanical property enhancements in an epoxy can be achieved through the formation of a ternary nanocomposite system where both intercalated nanoclay and nanostructured block-copolymer coexist.

The study of filament-wound fiber-reinforced laminates revealed that delamination crack initiation was not influenced by the presence of nanoparticles in the matrix, whereas a decreasing fiber volume fraction significantly improved interlaminar fracture energy. This investigation showed that for strain energy values exceeding about 700 J/m^2 an increase in resin toughness does not adequately transfer into interlaminar fracture toughness of fiber composites if the fiber volume fraction remained constant. The second specimen type studied herein, i.e. composite pipes modified with either the organic and inorganic nanoparticles, exhibited moderate improvements in leakage failure strain; however, reductions in functional failure (weepage) and structural failure (burst) strength were observed.

This thesis research makes valuable contributions to science and engineering as this project provided considerable insight into the micro-failure mechanism of filament-wound fiber-reinforced tubulars in the presence of nano-inclusions. Prior to this thesis work and resulting publications, the subject matter had received inadequate attention in the technical literature. The presented results illustrate the promise and potential of nanofiller modification for composite structures, especially for pressure-bearing filament-wound vessels and piping used for the storage and transport of fluids in the energy industry.

9.2 TOPICS OF FUTURE STUDY

The significant complexity associated with matrix micro-cracking in filament-wound composite structures makes it difficult to reasonably model leakage failure events with existing analytical and numerical methods. Due to the presence of multiple cracks and their interaction and coalescence during the matrix cracking process, it was recognized that fracture mechanics modeling must be prohibitively complex. As such, the characterization and standardization of composite pressure-retaining structures are presently done primarily by rigorous experimental investigations. To alleviate the requirement for time consuming and extensive testing, the following approaches are recommended which will involve both the experimental and theoretical study of the weepage failure phenomena.

9.2.1 Permeability Based Leakage Modeling to Detect Functional Failure in Composite Pipe

This proposed research intends to develop a mechanistic material damage model that will effectively be applicable to predict functional failure events in various pressurized composite vessels. In this scheme, an empirical permeability criterion will establish a relationship between local leakage failure strain and fluid permeability in individual plies. Previously, Mertiny and Gold [1-2] investigated a permeability based leakage assessment method similar to that proposed by Wolodko [3] for composite pipes. The noted leak detection method was based on Darcy's law with the assumption of uniformly distributed and interconnected fluid pathways through the damaged composite structure [4]. This method cannot adequately quantify the extent of damage state in individual plies, as damage is predominantly inhomogeneous and discontinuous. This procedure is also dependent on other weepage failure quantification techniques (e.g. a specific fluid volume loss technique) to determine an intrinsic permeability parameter. For the proposed methodology, permeability is considered to depend on the damage condition specific to the individual ply relative to the matrix crack initiation and progression in a representative composite pressure vessel. The global permeability of the composite will then be established on the basis of a series combination of this local permeability value in each lamina [5-6]. An adequate description for fluid transmission across interfaces between laminae may have to be defined as well. Therefore, it is hypothesized that the damage state in terms of permeability of the respective lamina can be characterized through the local strain in a lamina. An empirical permeability-strain relationship may thus be developed, which would then allow the prediction of functional failure from the stress-strain response of any composite vessel. Thus, the proposed model will establish a standard failure criterion for various cylindrical specimens having different geometries and fiber layup configurations.

9.2.2 Micromechanical Modeling of Damage in Nanoparticle Filled Composite Pipe

As a continuation of the work completed thus far, it is proposed to investigate the effect of a nanoparticle modified matrix phase on the damage in fiber-reinforced composite pipes through micro-mechanical modeling. The proposed numerical modeling assumes the filament-wound composite to be an orthotropic continuum having a fiber architecture that resembles a periodic array. Figure 9.1 illustrates how a two-cell model of the filament-wound tube can be implemented for the intended fiber orientation. This meso/micro-mechanical model is similar to the rhombohedral repeated unit cell model employed by Xia et al. [7] for angle ply $[\pm\theta]$ laminates. The laminate is considered to be a periodic array of the two-cell repeating units in the in-plane direction, with each cell consisting of a single fiber in $+\theta$ or $-\theta$ direction. The model neglects undulations and crossovers of the filaments, and each successive layer is thought to be made of a single continuous lamina having a specific fiber orientation. Assuming a uniform fiber distribution throughout, the fiber diameter in the unit cell is estimated from the fiber volume fraction of the tested filament-wound pipes.

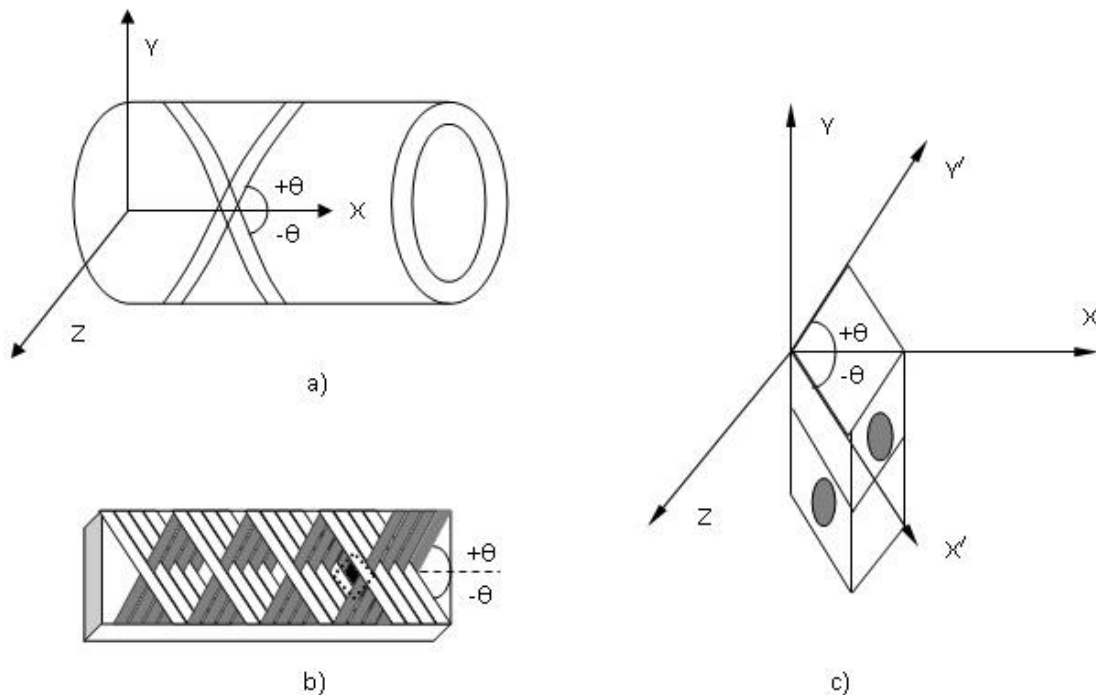


Figure 9.1 Unit-cell model for filament-wound composite pipe.

Unified periodic boundary conditions will be adopted for the two-cell model as illustrated by Xia et al. [7] for a unidirectional laminate with off-axis loading. To develop the constitutive model for a fiber/polymer/nano-phase (e.g. basalt/EPON826/M52N) composite system, the polymer/nano-phase material will be assumed as a single homogenous continuum having linear elastic properties. The elastic constants that will be used for polymer/nano-phase are taken from the experiments done on different bulk nanocomposite samples. If needed, even a non-linear viscoelastic constitutive model can be implemented taking into consideration time-dependent properties of the matrix material [8]. In the proposed model, the fiber reinforcement should be specified as linear elastic.

In the proposed approach it should be explored to model matrix crack initiation and propagation by a smeared crack approach as presented by Rots [9], and which may be correlated with a suitable matrix damage criteria (e.g. maximum strain criteria, maximum stress criteria, equivalent stress criteria). Xia et al. [10] in their study used a maximum principal strain criterion, i.e. $\varepsilon_I \geq \varepsilon_f$ indicating that the matrix will crack if the maximum principal strain ε_I exceeds the matrix failure strain ε_f . The maximum failure strain can be conveniently estimated from the experimental data of epoxy and its nanocomposites as shown in Figure 3.12. Once cracks are generated they cause a reduced composite stiffness as the matrix is unable to transfer tensile and shear loads across the crack plane. Therefore, a post-damaged constitutive model may be employed. It may be adequate to consider perfect bonding between the fiber and the matrix discounting interfacial debonding. If interfacial failure is the dominating failure mechanism then a cohesive interface damage model may effectively be implemented. Figure 9.2(a) shows the global stress-strain response derived from biaxial testing of a filament-wound tube. A similar response is expected from the micro-mechanical modeling, which will be compared against the experimental results. From Figure 9.2(a) two separate moduli can be specified by drawing two tangents to the curve, and their knee point refer to accelerated matrix cracking which usually is congruent with the leakage point. In Figure 9.2(b) bi-axial straining of the filament-wound pipe in axial and hoop direction is shown, where the beginning of the negative slope is an indication of the onset of leakage. It is therefore

expected that the proposed micro-mechanical model would allow for the identification of leakage events as well as the corresponding failure stress and strain values.

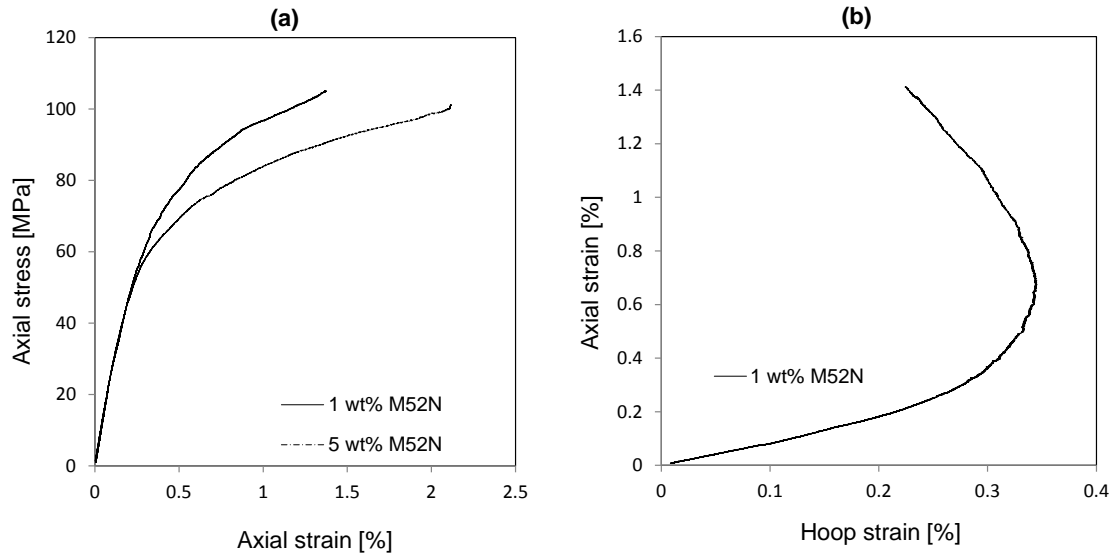


Figure 9.2 (a) Axial stress-strain response and (b) bi-axial straining of the filament-wound pipe.

9.2.3 Final Considerations

In Chapter 7 of this thesis, an extensive investigation substantiated that interlaminar fracture toughness is increased by decreasing fiber volume fraction because more energy is being expended when the crack-tip plastic zone has less interference from adjacent fibers [11]. Also, the findings in Chapter 8 for filament-wound tubes highlighted the fact that increasing fiber spacing would ease restrictions imposed by fibers on the crack-tip deformation zone, thereby lessening the probability of transverse crack initiation and subsequent propagation [12]. Both of the above propositions imply the objective of facilitating less constrained matrix deformation in the course of the applied loading of a composite structure. It has been conjectured in this study that due to the constraining influence of the fibers, matrix fracture is dominated by a brittle failure process rather than matrix deformation processes [13]. Conversely, the advantage of having higher resin content may result in reduced structural strength properties of a composite tubular, in

which case a balance has to be found between the leakage improvement and associated degradation in burst strength.

This study disputes the notion put forward previously by some researchers [14-16] that improving transverse cracking strain would enhance leakage resistance or leakage failure strength of the composite piping. Even though it was possible to improve cracking strain by increasing matrix ductility via incorporation of a second rubbery phase, it did not inhibit or mitigate weepage failure of composite pipes. In the same manner, it can be conceptualized that modifying the epoxy resin chemistry, e.g. by flexibilizing the epoxy backbone, increasing epoxide equivalent weight or lowering cross-link density, would have a rather insignificant effect on transverse cracking strength as well. In fact, this thesis research suggests that the transverse cracking phenomenon is to some extent analogous to tensile failure in bulk epoxy. Consequently, the notion of enhancing polymer toughness appears not to be an effective means for resolving the issue of transverse matrix cracking in filament-wound composites. Intuitively, it is plausible that raising polymer toughness brings about disadvantage of lowering other physical properties, such as strength and glass-transition temperature, which was observed herein for rigid (i.e. clay) and flexible (i.e. nanostructured block-copolymer) dispersed particulate systems. Alternative to the above methods, one could shift to a completely different resin system that should provide considerably higher ultimate strength and elongation than the present epoxy resin. Certainly, a possible route for improving leakage failure behavior, besides employing a lined piping structure, would be to optimize the fiber architecture (stacking sequence, fiber angle, lamina thickness etc.) of the filament-wound structures.

REFERENCES

1. MERTINY, P. and GOLD, A., 2007. Quantification of leakage damage in high-pressure fibre-reinforced polymer composite tubular vessels. *Polymer Testing*, **26**(2), pp. 172-179.
2. Mertiny, P., and Gold, A. Investigation of leakage failure and permeability properties of high-pressure fiber-composite pipes and vessels. CSME forum 2006. Calgary, Canada, May 2006.

3. Wolodko, Y., Biaxial fatigue and leakage characteristics of fiber reinforce composite tubes. *PhD Thesis*, University of Alberta, Edmonton, Alberta, 1999.
4. KUMAZAWA, H., AOKI, T. and SUSUKI, I., 2003. Analysis and Experiment of Gas Leakage Through Composite Laminates for Propellant Tanks. *AIAA Journal*, **41**(10), pp. 2037-2044.
5. ROY, S. and BENJAMIN, M., 2004. Modeling of permeation and damage in graphite/epoxy laminates for cryogenic fuel storage. *Composites Science and Technology*, **64**(13-14), pp. 2051-2065.
6. PEDDIRAJU, P., NOH, J., WHITCOMB, J. and LAGOUDAS, D.C., 2007. Prediction of cryogen leak rate through damaged composite laminates. *Journal of Composite Materials*, **41**(1), pp. 41-71.
7. XIA, Z., ZHANG, Y. and ELLYIN, F., 2003. A unified periodical boundary conditions for representative volume elements of composites and applications. *International Journal of Solids and Structures*, **40**(8), pp. 1907-1921.
8. ZHANG, Y., XIA, Z. and ELLYIN, F., 2005. Nonlinear viscoelastic micromechanical analysis of fibre-reinforced polymer laminates with damage evolution, *Micromechanics of Materials 2005*, Elsevier Ltd, pp. 591-604.
9. ROTS, J.G., 1991. Smearred and discrete representations of localized fracture. *International Journal of Fracture*, **51**(1), pp. 45-59.
10. XIA, Z., CHEN, Y. and ELLYIN, F., 2000. A meso/micro-mechanical model for damage progression in glass-fiber/epoxy cross-ply laminates by finite-element analysis. *Composites Science and Technology*, **60**(8), pp. 1171-1179.
11. BASHAR, M.T., SUNDARARAJ, U. and MERTINY, P., 2013. Mode-I Interlaminar Fracture Behavior of Nanoparticle Modified Epoxy/Basalt Fibre-Reinforced Laminates. *Polymer testing*, **32**, pp. 402-412.
12. BASHAR, M.T., SUNDARARAJ, U. and MERTINY, P., 2011. Study of Matrix Micro-cracking in Nanoclay and Acrylic Tri-block-copolymer Modified Epoxy/basalt Fiber-reinforced Pressure-retaining Structures. *Express polymer letters*, **5**, pp. 882-896.
13. ASP, L.E., BERGLUND, L.A. and TALREJA, R., 1996. A Criterion for Crack Initiation in Glassy Polymers Subjected to a Composite-like Stress State. *Composites Science and Technology*, **56**, pp. 1291-1301.

14. JONES, M.L.C. and HULL, D., 1979. Microscopy of failure mechanisms in filament-wound pipe. *Journal of Materials Science*, **14**(1), pp. 165-174.
15. SJOGREN, B.A. and BERGLUND, L.A., 1999. Toughening mechanisms in rubber-modified glass fiber/unsaturated polyester composites. *Polymer Composites*, **20**(5), pp. 705-712.
16. SJOGREN, B.A. and BERGLUND, L.A., 2000. Effects of matrix and interface on damage in GRP cross-ply laminates. *Composites Science and Technology*, **60**(1), pp. 9-21.

Appendix A

EXPERIMENTALLY GENERATED GRAPHS

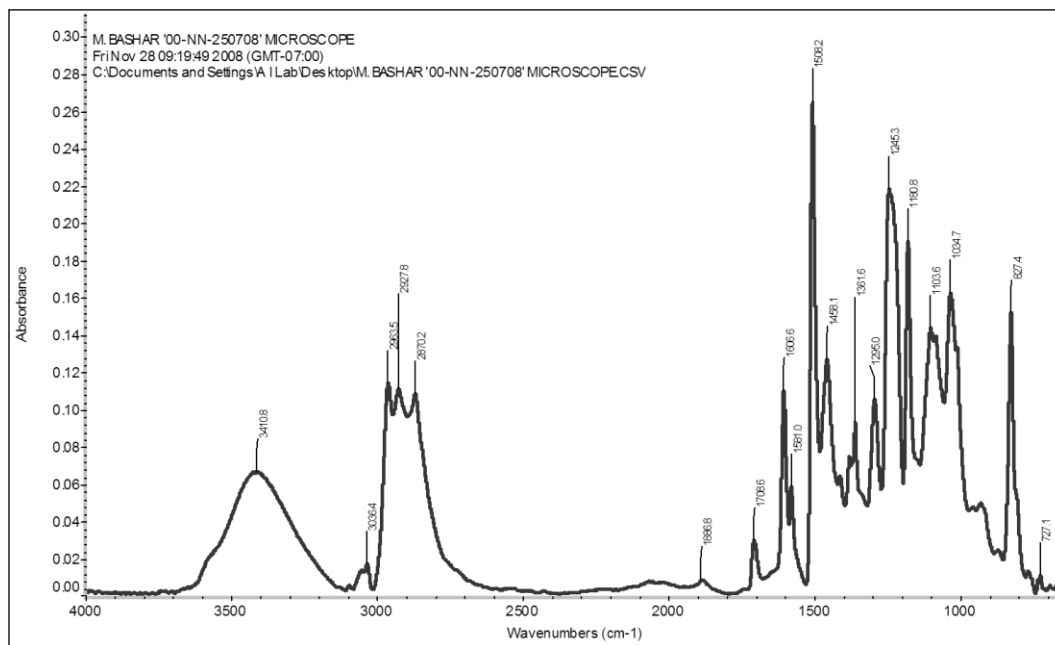


Figure A.1 FTIR spectrum of neat epoxy.

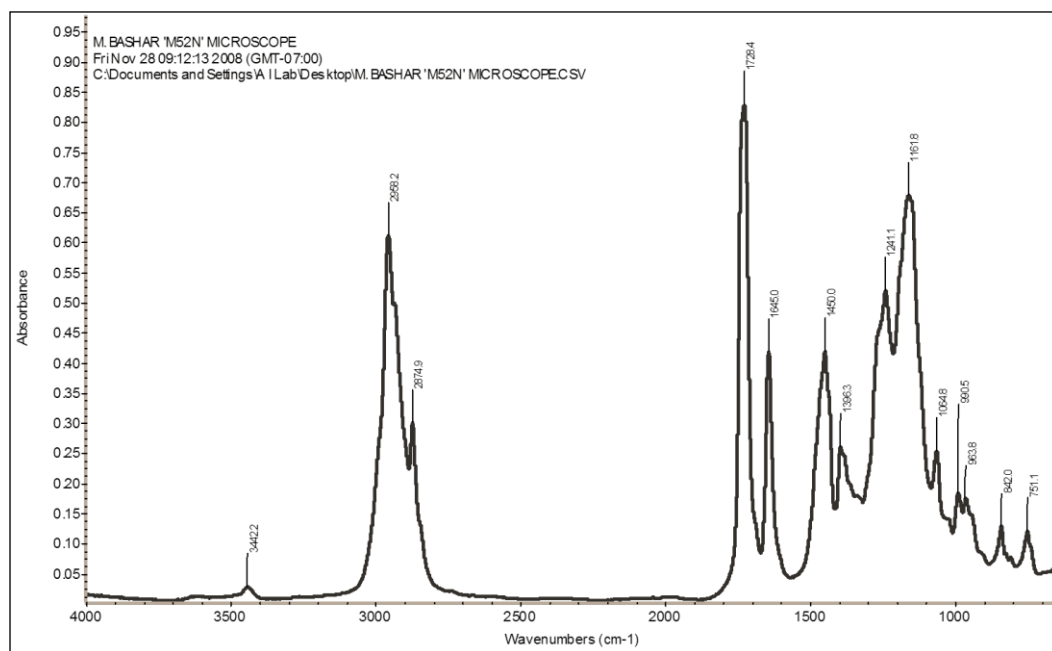


Figure A.2 FTIR spectrum of pure M52N block-copolymer.

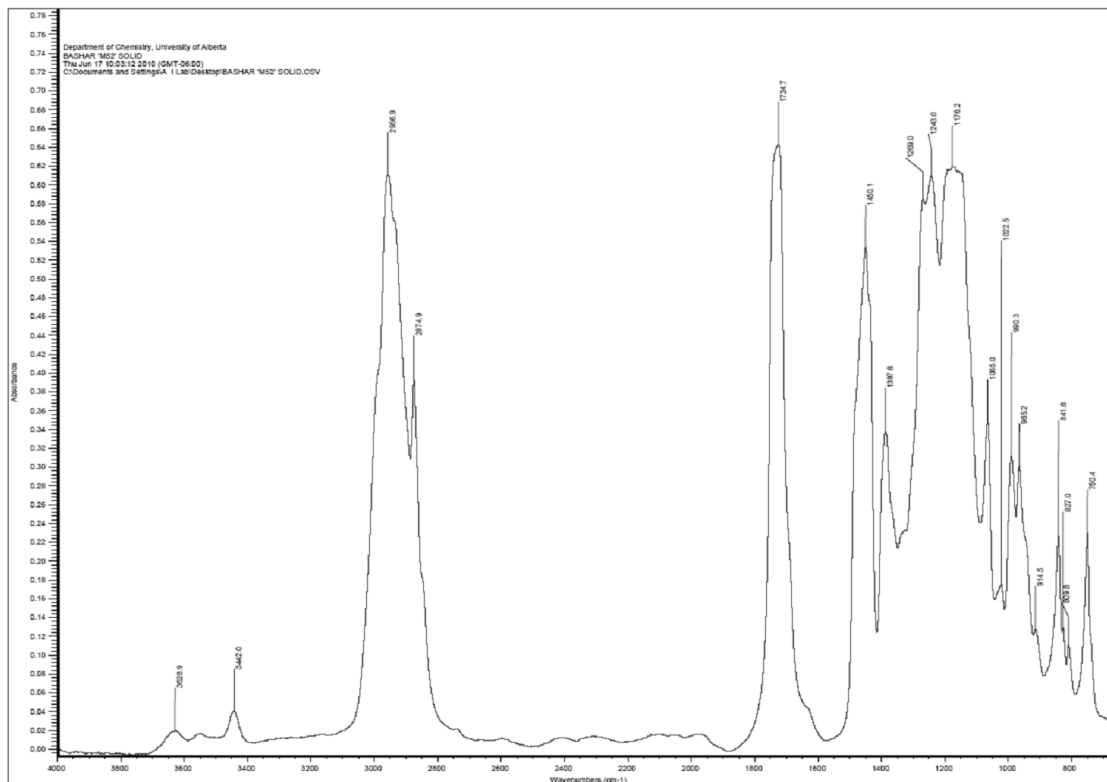


Figure A.3 FTIR spectrum of pure M52 block-copolymer.

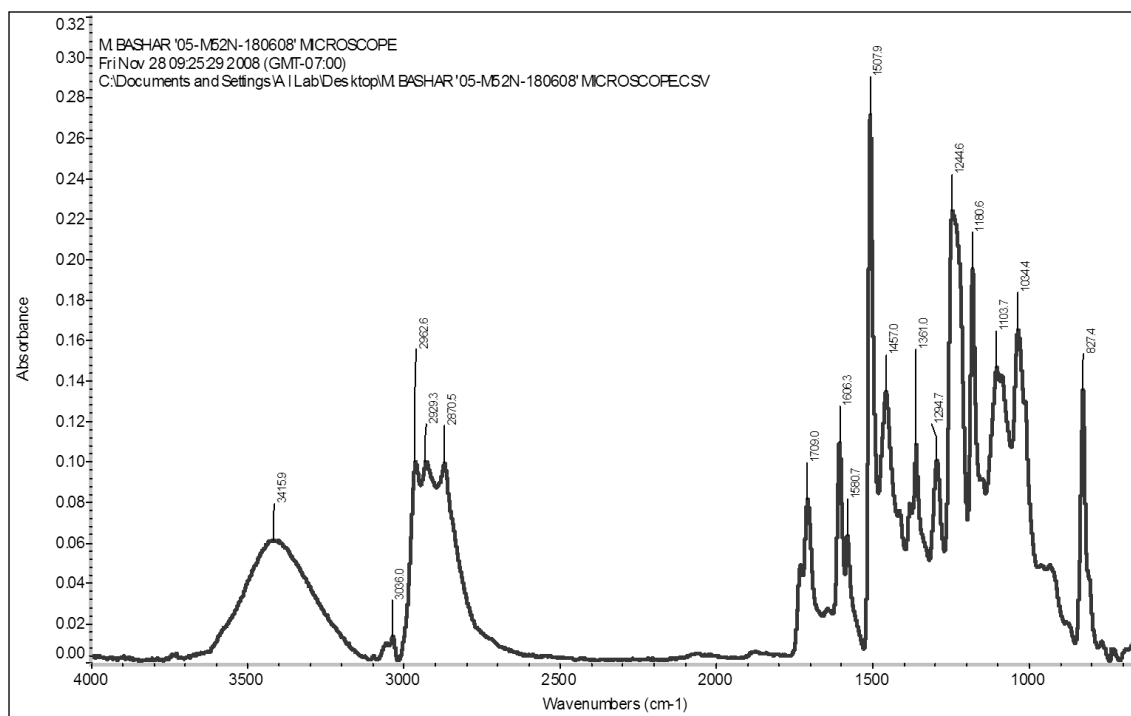


Figure A.4 FTIR spectrum of 5 wt% M52N block-copolymer modified epoxy.

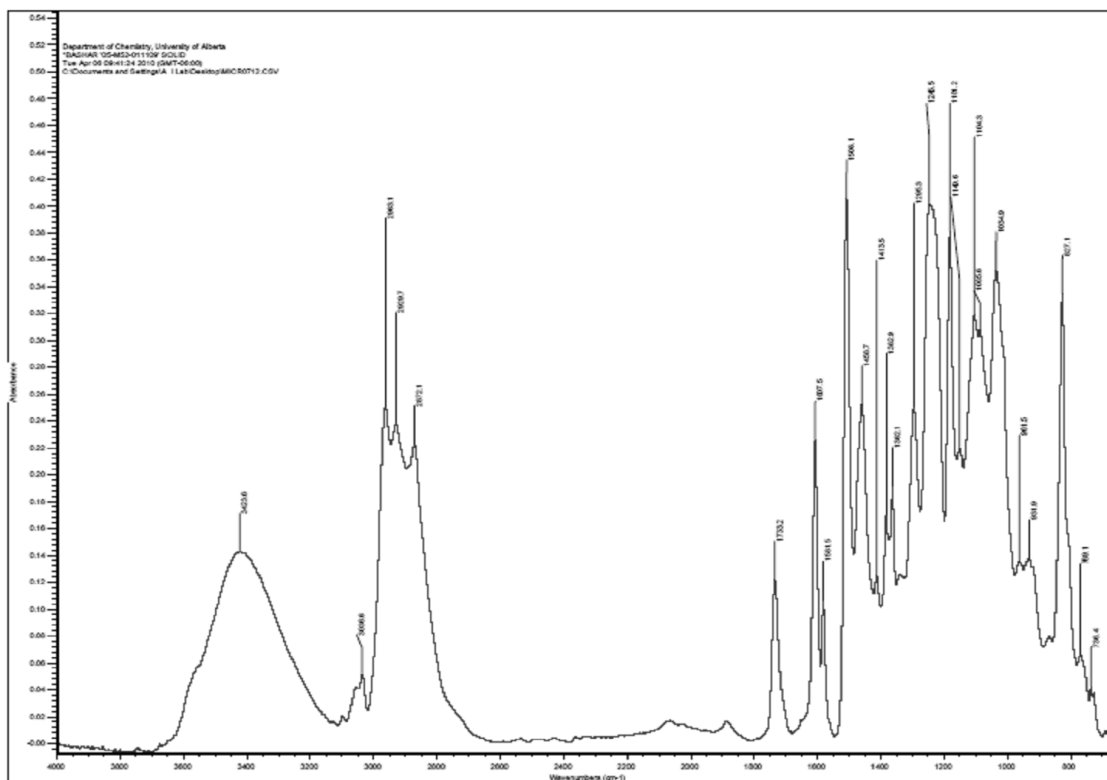


Figure A.5 FTIR spectrum of 5 wt% M52 block-copolymer modified epoxy.

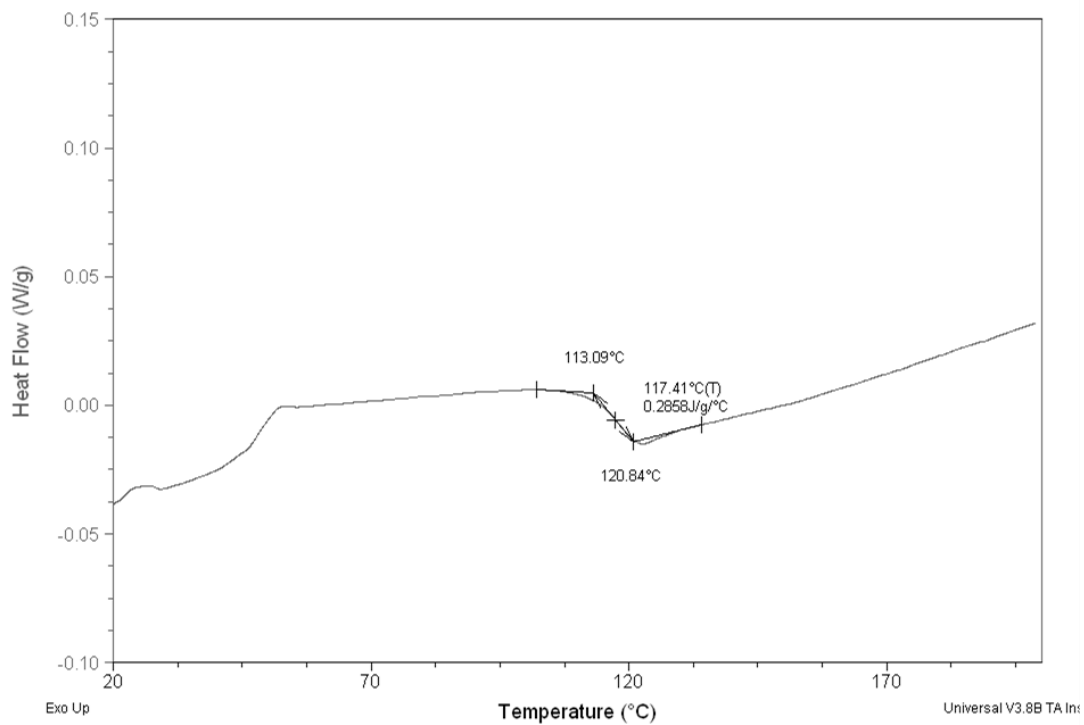


Figure A.6 DSC test result of neat epoxy.

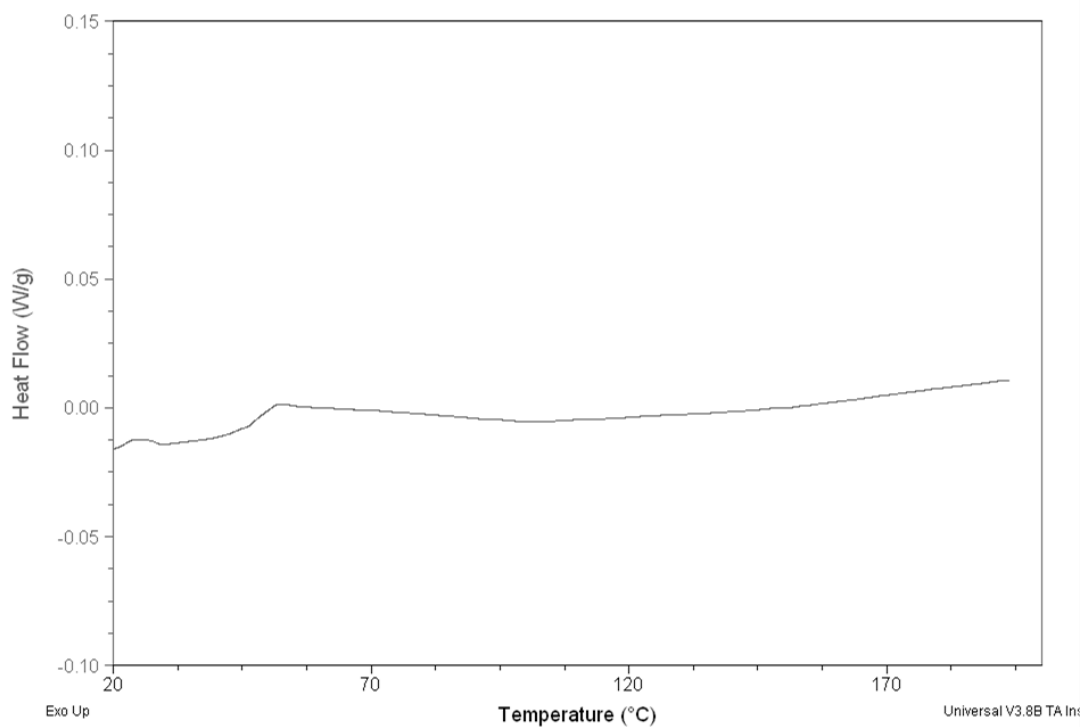


Figure A.7 DSC thermogram of pure M52N block-copolymer.

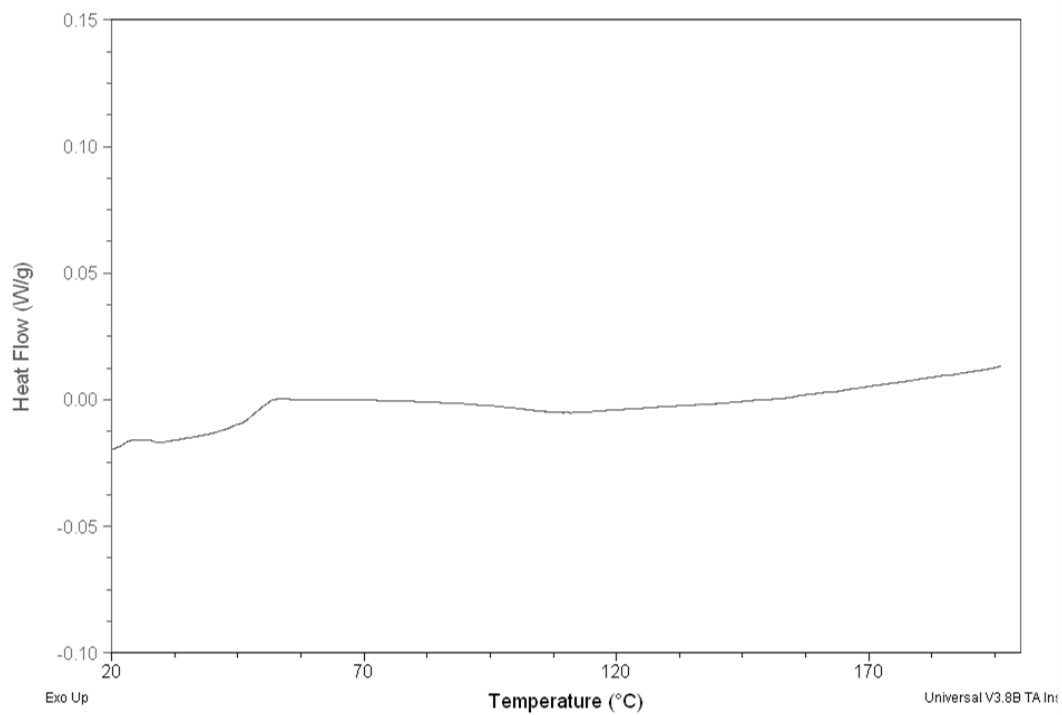


Figure A.8 DSC thermogram of pure M52 block-copolymer.

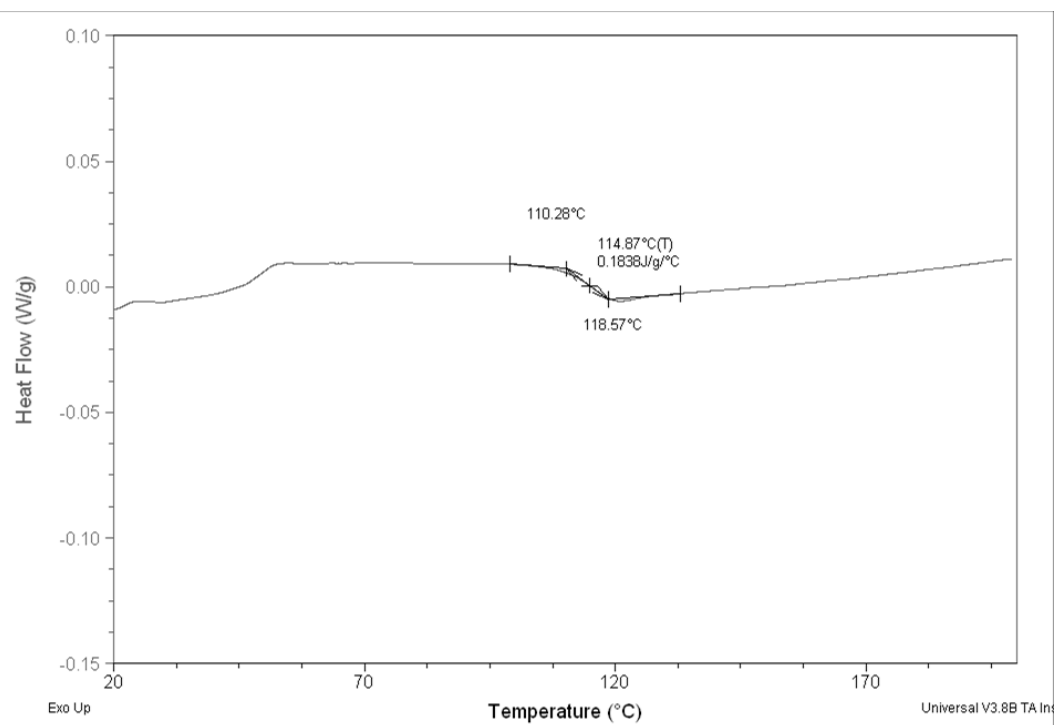


Figure A.9 DSC thermogram of 1 wt% I.30E filled epoxy nanocomposite. (Ultrasonic mixing) (01-I.30-041109)

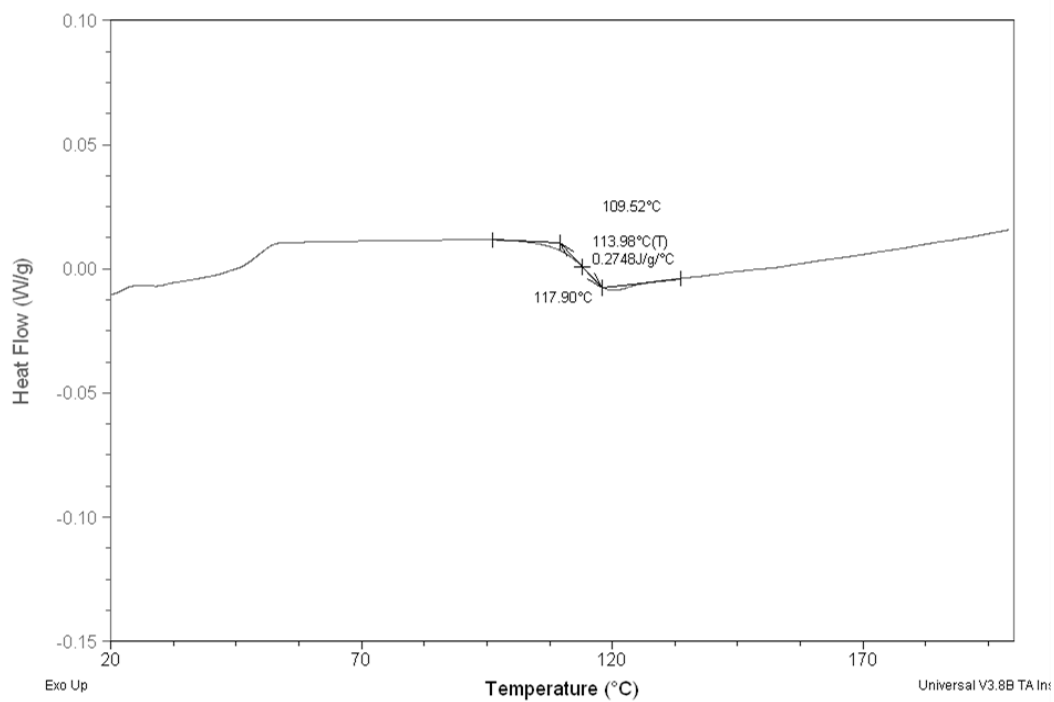


Figure A.10 DSC thermogram of 2 wt% I.30E filled epoxy nanocomposite. (Ultrasonic mixing)
(02-I.30-071109)

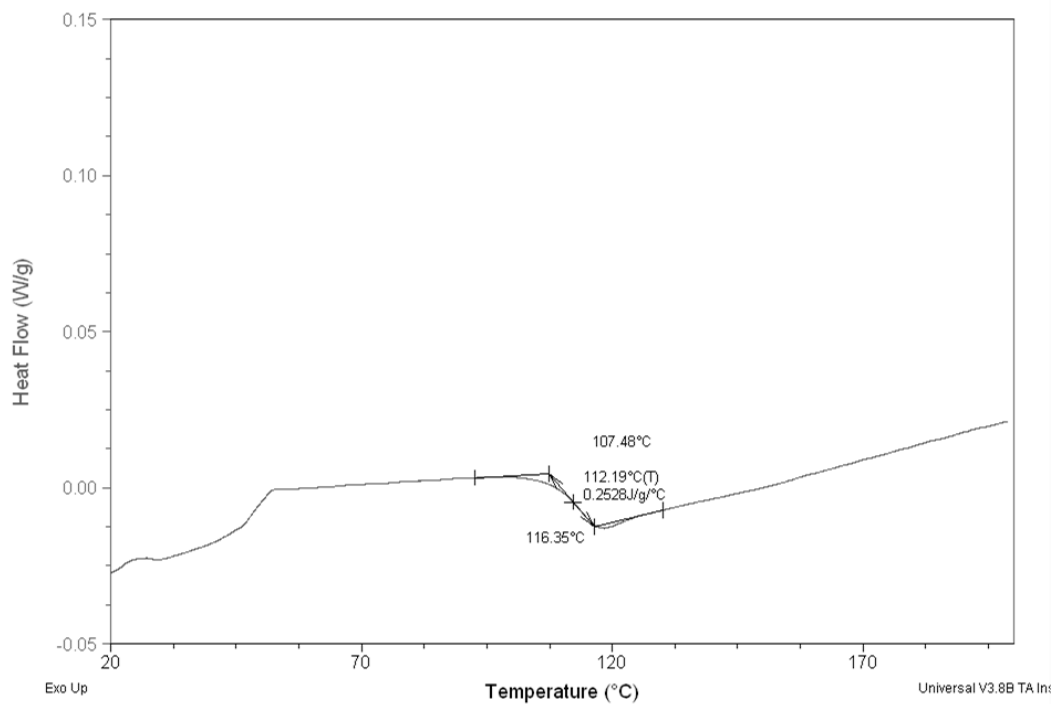


Figure A.11 DSC thermogram of 3 wt% I.30E filled epoxy nanocomposite. (Ultrasonic mixing)
(03-I.30-111109)

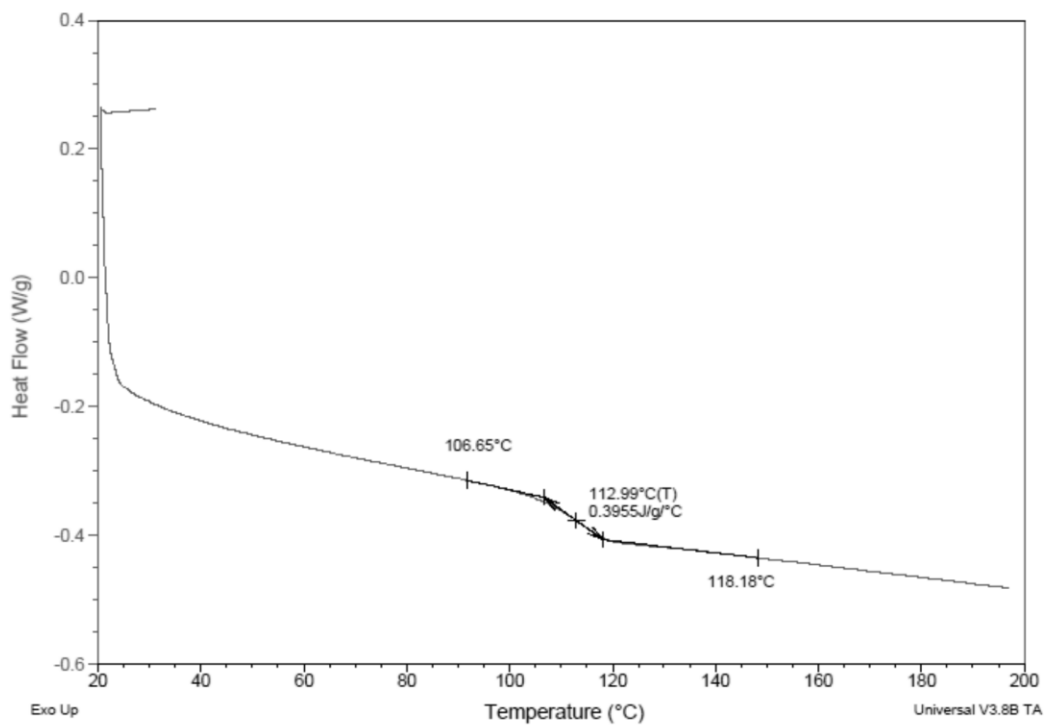


Figure A.12 DSC thermogram of 1 wt% I.30E filled epoxy nanocomposite. (Mechanical mixing)
(01-I.30-210610)

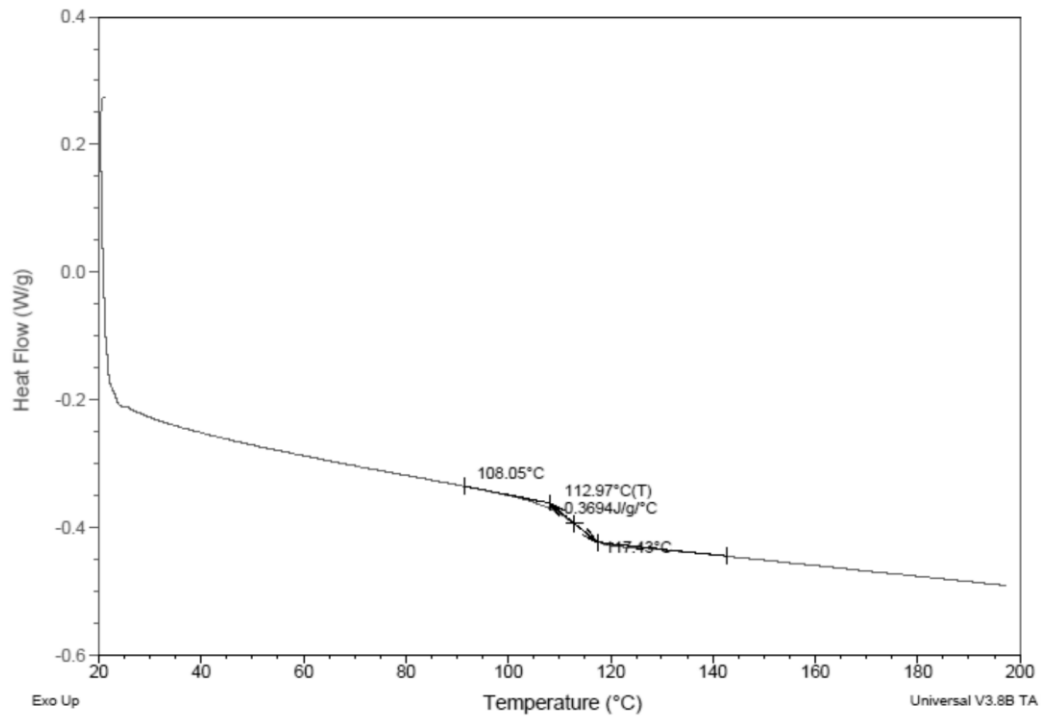


Figure A.13 DSC thermogram of 2 wt% I.30E filled epoxy nanocomposite. (Mechanical mixing)
(02-I.30-220610)

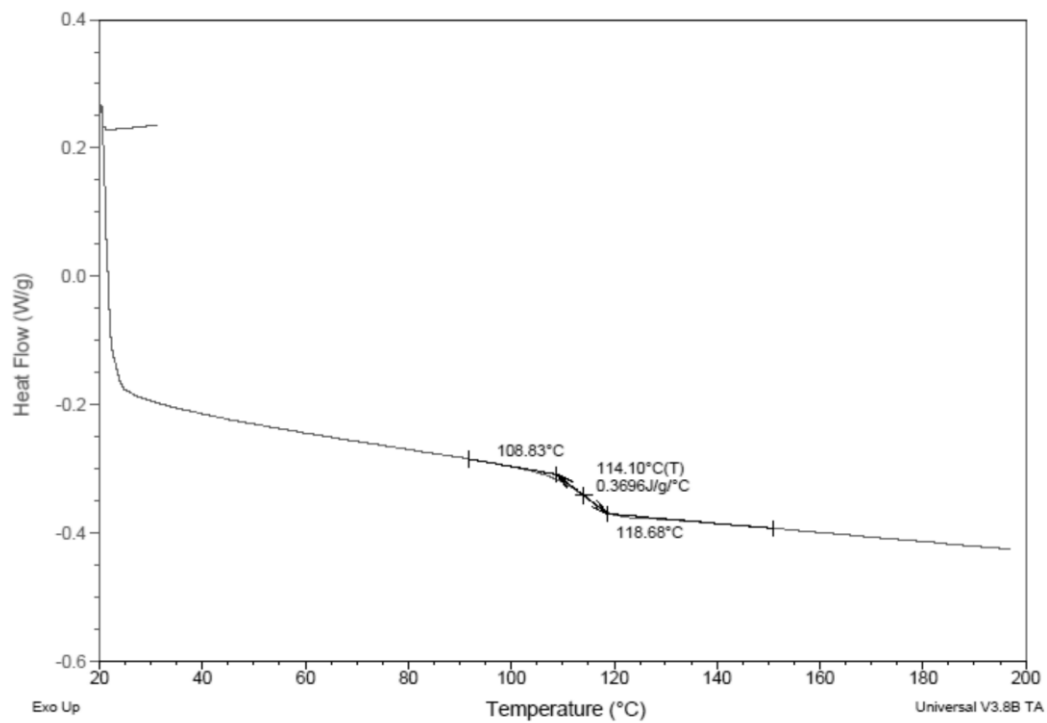


Figure A.14 DSC thermogram of 3 wt% I.30E filled epoxy nanocomposite. (Mechanical mixing)
(02-I.30-230610)

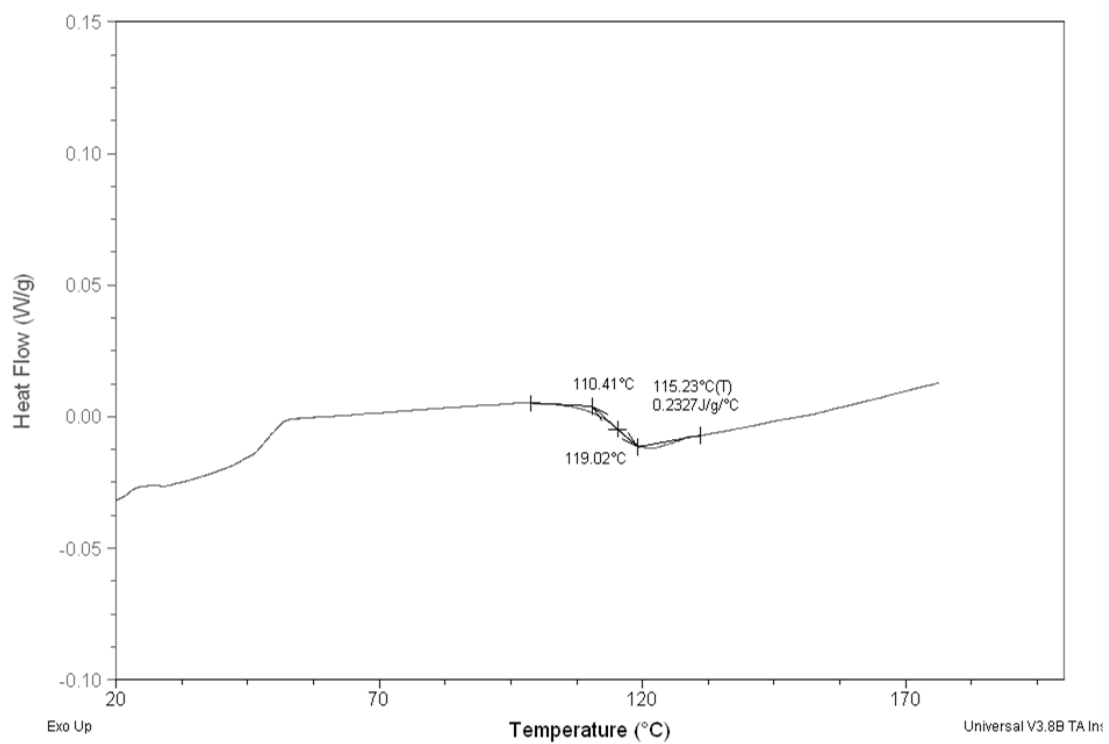


Figure A.15 DSC thermogram of 1 wt% M52N modified epoxy. (01-M52N-261009)

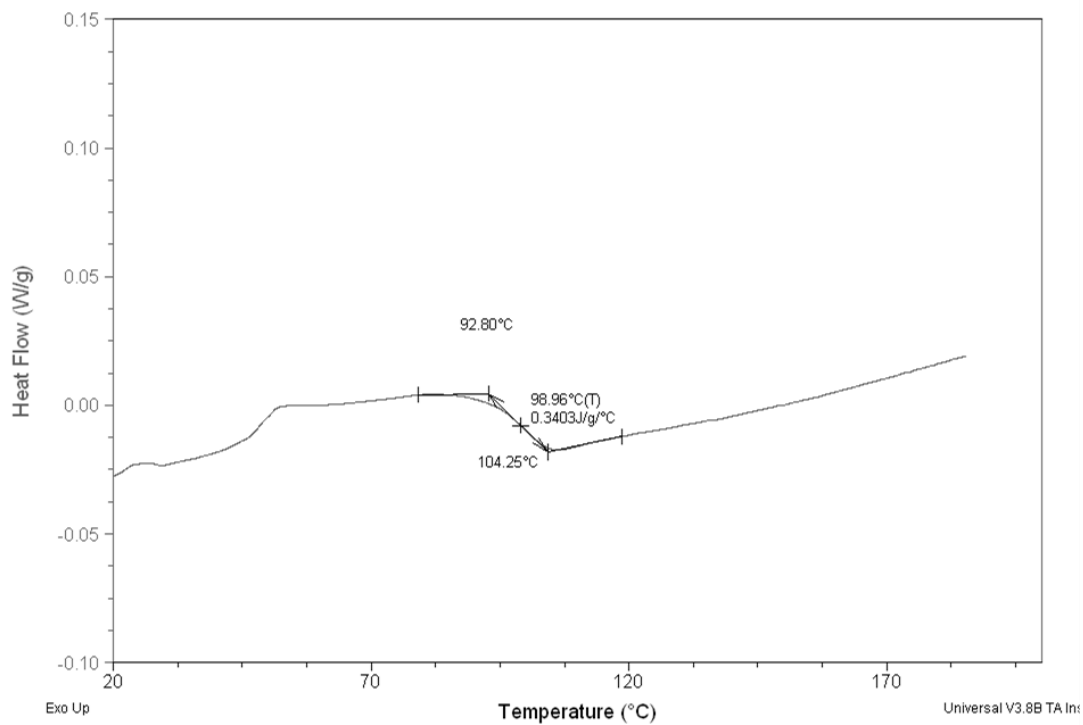


Figure A.16 DSC thermogram of 3 wt% M52N modified epoxy. (03-M52N-281009)

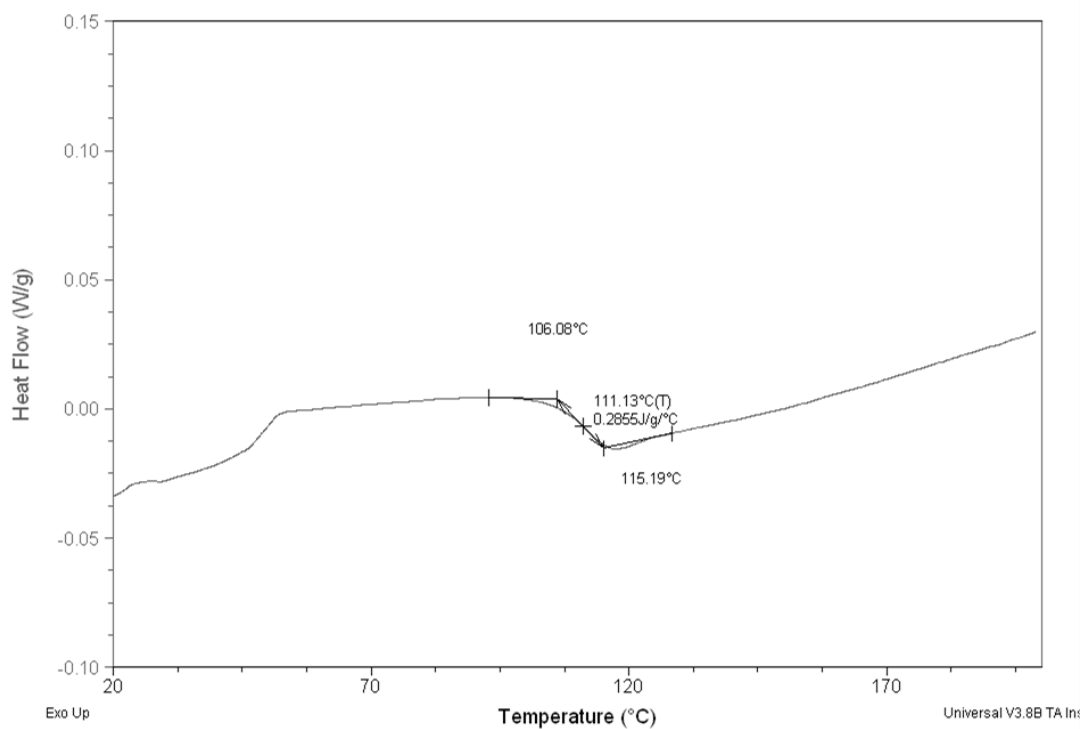


Figure A.17 DSC thermogram of 5 wt% M52N modified epoxy. (05-M52N-311009)

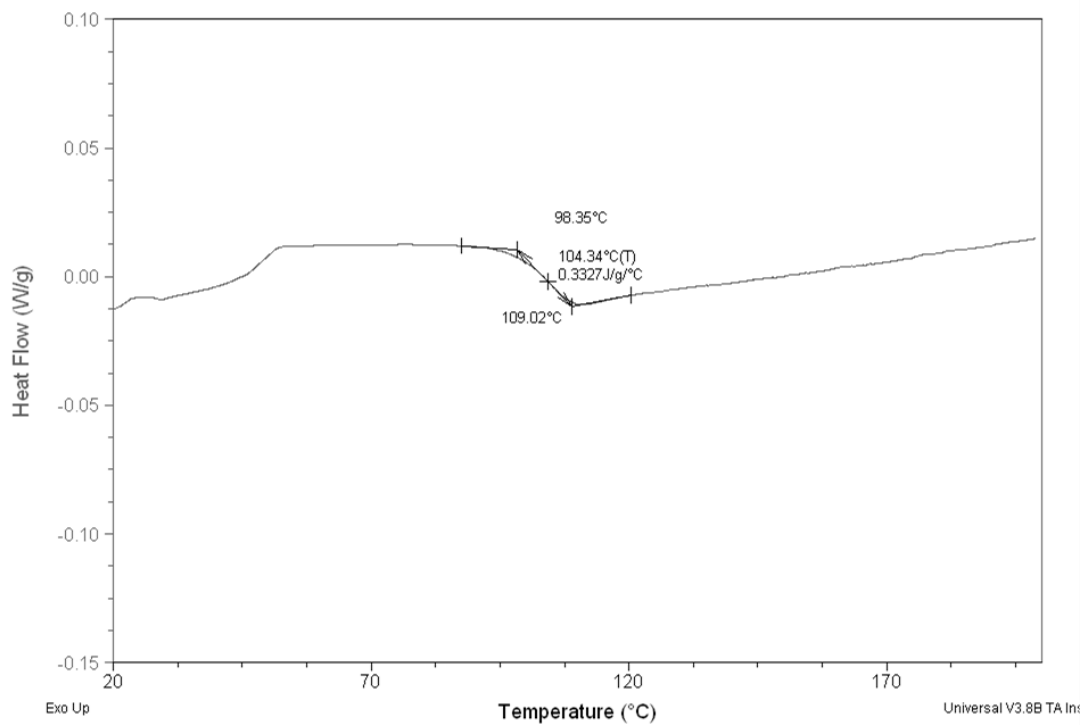


Figure A.18 DSC thermogram of 1 wt% M52 modified epoxy. (01-M52-291009)

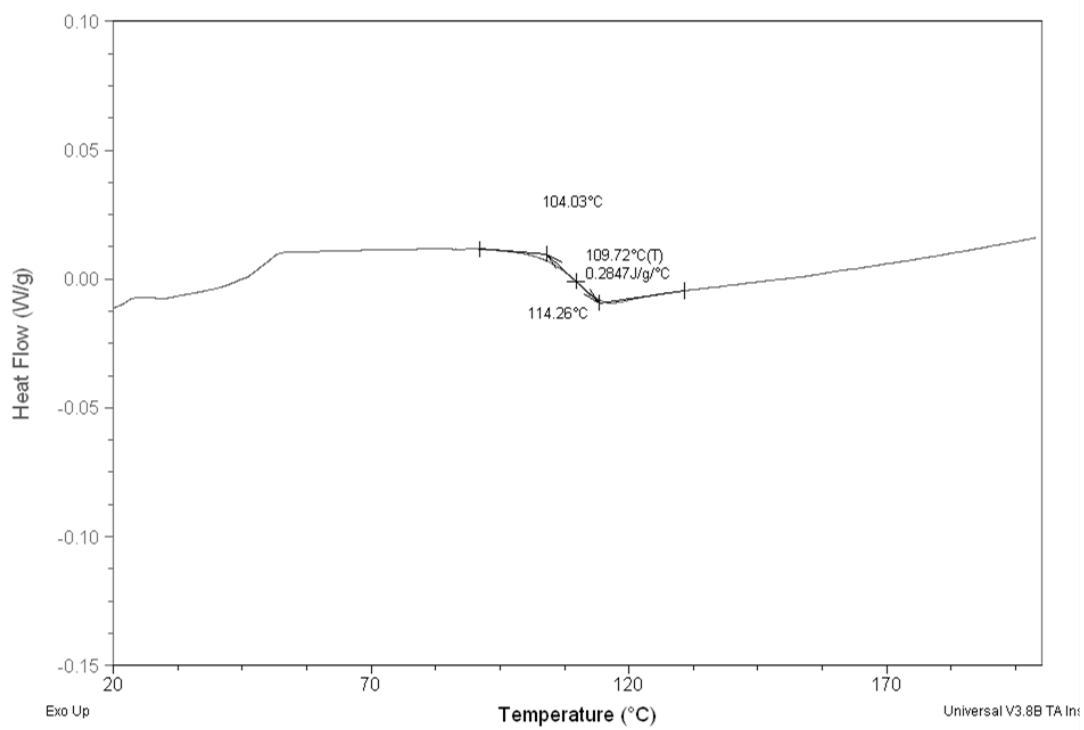


Figure A.19 DSC thermogram of 3 wt% M52 modified epoxy. (03-M52-301009)

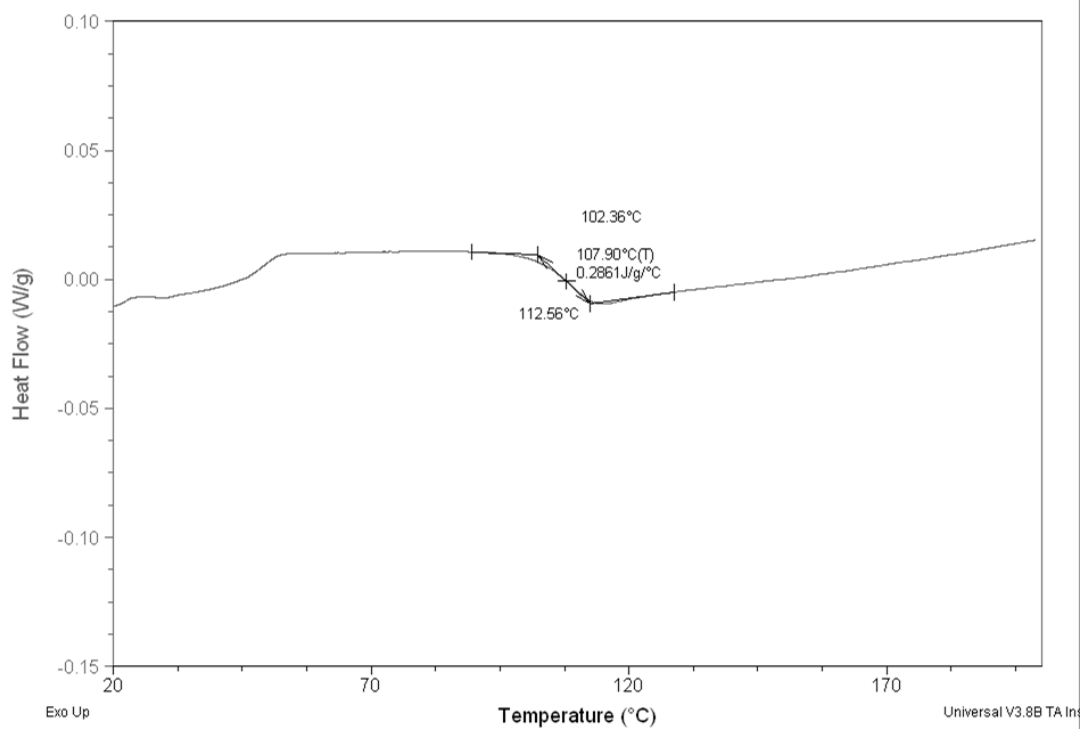


Figure A.20 DSC thermogram of 5 wt% M52 modified epoxy. (05-M52-011109)

Appendix B

EXPERIMENTAL DATA

Table B-1 Tensile properties of the epoxy nanocomposites. (Load control test)

Sample name	Sample no	Filler-matrix loading (wt%)	Tensile modulus (GPa)	Tensile strength (MPa)	% Tensile strain (%)
00-NN-250708	1	(Neat epoxy)	2.94	83.68	8.59
	2		2.77	80.02	8.29
	3		2.77	82.33	8.66
	4		2.80	82.82	8.59
Epoxy-clay nanocomposites prepared by ultrasonic dispersion method					
01-I.30-050209-2	1	1 wt% I.30E	3.21	82.46	5.51
	2		3.29	86.77	6.89
	3		3.26	84.3	6.09
	4		3.28	84.62	5.92
	5		3.23	85.19	6.19
02-I.30-060209	1	2 wt% I.30E	3.18	79.89	5.23
	2		3.24	81.32	5.73
	3		3.24	77.32	4.39
	4		3.27	83.99	6.70
03-I.30-100209-2	1	3 wt% I.30E	3.35	71.69	3.33
	2		3.40	79.31	4.52
	3		3.32	78.93	4.49
	4		3.36	76.91	4.00
01-I.28-190610	1	1 wt% I.28E	2.78	63.55	3.97
	2		2.83	64.21	4.11
	3		2.80	63.83	4.04
	4		2.76	59.92	3.74
01-PGW-180610	1	1 wt% PGW	2.89	72.46	5.08
	2		2.86	64.74	3.66
	3		2.80	73.64	5.60
	4		2.83	74.44	5.72
Epoxy-clay nanocomposites prepared by mechanical mixing technique					
01-I.30-060211	1	1 wt% I.30E	2.86	68.23	3.86
	2		2.82	72.17	4.65
	3		2.87	74.41	5.04
	4		2.82	76.40	5.65
02-I.30-020211	1	2 wt% I.30E	2.92	69.89	3.89

Table B-1 (continued)

Sample name	Sample no	Filler-matrix loading (wt%)	Tensile modulus (GPa)	Tensile strength (MPa)	% Tensile strain (%)
02-I.30-020211	2	2 wt% I.30E	2.89	69.36	3.96
	3		2.94	69.63	3.93
	4		2.93	70.35	4.06
03-I.30-010211	1	3 wt% I.30E	2.97	70.40	3.97
	2		2.96	68.05	3.63
	3		2.99	68.93	3.74
Acrylic triblock-copolymer modified epoxy					
01-M52N-110708	1	1 wt% M52N	2.65	79.17	8.66
	2		2.74	79.17	9.37
	3		2.73	77.91	8.84
	4		2.72	78.93	8.55
02-M52N-070608	1	2 wt% M52N	2.49	78.68	9.37
	2		2.63	77.32	9.01
	3		2.53	78.9	9.29
03-M52N-180810	1	3 wt% M52N	2.68	72.04	9.15
	3		2.69	76.13	9.62
05-M52N-180608	1	5 wt% M52N	2.66	78.12	10.50
	2		2.66	77.56	9.92
	3		2.67	77.24	9.89
	4		2.57	77.85	8.72
01-M52-050708	1	1 wt% M52	2.74	79.43	7.89
	2		2.71	79.68	7.33
	3		2.83	78.4	6.82
	4		2.96	81	6.38
02-M52-050608	1	2 wt% M52	2.74	74.83	6.01
	2		2.75	73.05	5.79
	3		2.92	78.36	7.25
	4		2.65	77.66	7.36
03-M52-170708	1	3 wt% M52	2.71	74.85	6.18
	2		2.72	74.69	6.55
	3		2.72	79.59	7.52
	4		2.77	77.61	8.02
05-M52-210708	1	5 wt% M52	2.75	75.12	7.12
	2		2.82	75.98	6.43
	3		2.80	75.44	6.48
	4		2.76	75.89	8.73

Table B-2 Tensile properties of epoxy nanocomposites. (Stroke control test)

Sample name	Sample no	Filler-matrix loading (wt%)	Tensile modulus (GPa)	Tensile strength (MPa)	% Tensile strain (%)
00-NN-300607	2	(Neat epoxy)	2.92	73.07	8.37
	3		2.86	74.24	8.94
	4		2.86	72.46	8.20
Epoxy-clay nanocomposites prepared by ultrasonic dispersion method					
01-I.30-050209-1	1	1 wt% I.30E (1C)	3.15	77.77	6.69
	2		3.24	79.31	8.12
	3		3.20	79.06	7.71
	4		3.03	77.72	6.87
	5		3.12	78.67	6.68
03-I.30-100209-1	2	3 wt% I.30E (3C)	3.32	80.06	4.25
	3		3.36	77.9	3.73
	4		3.28	74.65	3.44
	5		3.36	76.3	3.65
Acrylic triblock-copolymer modified epoxy					
01-M52N-160608	1	1 wt% M52N (1B)	2.68	72.6	9.31
	2		2.68	72.89	9.64
	4		2.66	72.79	9.28
03-M52N-230708	2	3 wt% M52N (3B)	2.63	69.49	7.98
	3		2.69	69.45	9.46
03-M52N-300708	1		2.58	69.62	10.49
	2		2.60	69.53	10.63
05-M52N-140708	1		5 wt% M52N	2.64	68
	2	2.61		67.41	9.54
	3	2.58		67.37	11.04
Epoxy hybrid nanocomposites					
01I.30-01M52N-270209	1	1B&1C	3.11	78.16	7.59
	2		3.09	76.97	8.56
	3		2.99	77.56	8.91
	5		3.07	77.77	8.29
03I.30-01M52N-240510	1	1B&3C	3.24	73.69	4.16
	2		3.34	78.92	5.10
	3		3.34	75.44	4.14
	4		3.31	77.67	5.61
01I.30-03M52N-250510	1	3B&1C	3.01	82.64	8.17
	2		2.96	81.58	8.59
	3		2.84	78.99	7.51
	4		2.97	80.54	8.41
	5		3.04	82.37	9.07

Table B-3 Dynamic mechanical analysis test results.

Sample name	Sample no	Filler-matrix loading (wt%)	Storage modulus (GPa)
00-NN-100211	Epoxy_Tem	(Neat epoxy)	2.69
	1		2.50
	2		2.61
	3		2.67
01-M52N-170810	1	1 wt% M52N	2.68
	2		2.52
	3		2.62
	4		2.64
	5		2.54
03-M52N-180810	1	3 wt% M52N	2.49
	2		2.38
	3		2.62
	4		2.73
	5		2.66
05-M52N-190810	1	5 wt% M52N	2.44
	2		2.56
	3		2.56
	4		2.47
	5		2.53
01-M52-090810	1	1 wt% M52	2.70
	2		2.62
	3		2.71
	4		2.89
03-M52-120810	1	3 wt% M52	2.56
	2		2.70
	3		2.54
	4		2.50
05-M52-130810	1	5 wt% M52	2.62
	2		2.61
	3		2.78
	4		2.60
	8		2.57
	10		2.39

Table B-4 Nanocomposite fracture test results. (Sharp crack system)

Sample name	Sample no	Filler-matrix loading (wt%)	Crack length (mm)	Fracture toughness (MPa.m ⁵)	Strain energy (J/m ²)
00-NN-151209	2	(Neat epoxy)	9.52	0.87	283
	3		9.85	0.73	204
	4		10.36	0.80	243
	5		10.15	0.74	213
	7		9.90	0.76	227
	8		10.19	0.78	243
Epoxy-clay nanocomposite fabricated by ultrasonic mixing method					
01-I.30-041109	30	1 wt% I.30E	9.60	0.77	218
	31		9.52	0.76	208
	32		9.60	0.78	232
	36		9.52	0.83	234
	37		9.56	0.80	232
02-I.30-071109	41	2 wt% I.30E	9.52	0.75	235
	42		9.77	0.80	234
	43		10.02	0.88	258
	44		10.07	0.83	249
	45		9.60	0.77	232
	46		9.52	0.80	256
03-I.30-111109	47	3 wt% I.30E	9.52	0.79	239
	48		9.69	0.78	220
	49		9.77	0.77	232
	50		9.73	0.76	220
01-I.28-091109	51	1 wt% I.28E	9.69	1.05	347
	52		9.52	1.02	386
	53		9.69	0.84	374
01-PGW-091109	54	1 wt% PGW	9.81	0.76	308
	56		9.56	0.75	206
Epoxy-clay nanocomposite prepared by mechanical mixing method					
01-I.30-210610	2	1 wt% I.30E	10.45	0.77	220
	3		11.04	0.74	215
	5		10.83	0.77	248
	7		10.74	0.84	271
02-I.30-220610	1	2 wt% I.30E	10.74	0.88	297
	3		10.70	0.79	245
	5		11.12	0.82	231
	7		11.04	0.85	280

Table B-4 (continued)

Sample name	Sample no	Filler-matrix loading (wt%)	Crack length (mm)	Fracture toughness (MPa.m ⁵)	Strain energy (J/m ²)
03-I.30-230610	3	3 wt% I.30E	10.11	0.95	329
	4		10.96	0.84	312
	5		9.69	0.93	304
	6		10.96	1.02	366
	7		9.85	0.92	281
Acrylic triblock-copolymer modified epoxy					
01-M52N-261009	11	1 wt% M52N	9.56	0.91	308
	12		9.52	0.89	298
	13		9.52	0.86	298
	14		9.56	0.81	228
03-M52N-281009	15	3 wt% M52N	9.64	1.38	604
	16		10.02	1.34	491
	17		9.94	1.17	465
	18		9.85	1.16	421
05-M52N-311009	20	5 wt% M52N	9.81	1.53	825
	21		9.90	1.49	805
	22		10.24	1.47	727
	23		9.98	1.45	701
01-M52-291009	9	1 wt% M52	10.28	1.00	361
	10		9.85	1.06	423
	57		9.81	0.99	343
	58		10.19	0.98	332
	59		10.07	0.90	300
03-M52-301009	69	3 wt% M52	10.62	1.29	586
	70		10.70	1.38	670
03-M52-100810	3		10.96	1.20	570
	5		9.85	1.24	601
05-M52-011109	72		5 wt% M52	10.32	1.59
	75	10.02		1.54	839
05-M52-110810	4	9.60		1.54	963
	5	9.85		1.42	796
	6	10.15		1.51	872
	8	9.81	1.45	860	
Epoxy hybrid nanocomposites					
01I.30-01M52N-081109	33	1B&1C	9.52	0.88	292
	34		9.52	0.90	302
	35		9.60	0.85	246
	38		9.69	0.86	303

Table B-4 (continued)

Sample name	Sample no	Filler-matrix loading (wt%)	Crack length (mm)	Fracture toughness (MPa.m ⁵)	Strain energy (J/m ²)
01I.30-01M52N-081109	39	1B&1C	9.85	0.80	249
	40		9.60	0.82	257
03I.30-01M52N-210810	1	1B&3C	10.28	0.75	235
	2		9.77	0.84	245
	3		9.85	0.85	261
	4		10.24	0.74	207
01I.30-03M52N-200810	1	3B&1C	10.02	1.22	555
	2		9.77	1.25	557
	3		9.77	1.21	527
	4		9.85	1.27	607

Table B-5 Nanocomposite fracture test results. (Blunt crack system)

Sample name	Sample no	Filler-matrix loading (wt%)	Crack length (mm)	Fracture toughness (MPa.m ⁵)	Strain energy (J/m ²)
00-NN-220908	1	(Neat epoxy)	10.5	2.70	2549
	2		10.5	2.65	2577
00-NN-071108	1		10.5	2.58	2525
Epoxy-clay nanocomposites fabricated by ultrasonic mixing method					
01-I.30-180109	1	1 wt% I.30E	10.5	2.46	2127
	2		10.5	2.52	2315
	3		10.5	2.40	2014
02-I.30-210109	1	2 wt% I.30E	10.5	2.27	1693
	2		10.5	2.39	1655
	3		10.5	2.51	1961
Acrylic triblock-copolymer modified epoxy					
01-M52N-120908	1	1 wt% M52N	10.5	2.89	2891
	2		10.5	2.82	2747
01-M52N-190908	1		10.5	2.77	3031
03-M52N-180908	1	3 wt% M52N	10.5	3.03	3078
	2		10.5	2.92	3086
03-M52N-131108	1		10.5	2.81	2922
05-M52N-170908	1	5 wt% M52N	10.5	2.68	2319
	2		10.5	2.96	2966
05-M52N-101108	1		10.5	2.66	2604
01-M52-100908	1	1 wt% M52	10.5	2.68	2522
	2		10.5	2.77	2686
	3		10.5	2.65	2553
03-M52-110908	1	3 wt% M52	10.5	2.74	2553
	2		10.5	2.76	2511
	3		10.5	2.69	2506
05-M52-160908	1	5 wt% M52	10.5	2.57	2436
	2		10.5	2.68	2620
	3		10.5	2.57	2521

Table B-6 Mode-I interlaminar fracture toughness test data of the flat laminates.

Sample name	Sample no	Particle-matrix loading (wt%)	Fiber volume fraction	Interlaminar fracture energy (J/m ²)		
				Initiation		Propagation
				NL	VIS	
Neat	2	(Neat epoxy)	0.64	109	208	630
	3			126	287	581
	5			117	244	624
	7			126	229	563
Neat_vol	1	(Neat epoxy)	0.55	242	487	876
	2			241	449	775
	3			238	428	901
	4			206	360	745
	5			213	336	683
01-I.30	2	1 wt% I.30E	0.58	149	277	530
	3			133	231	566
	5			172	292	458
	7			185	332	474
	8			141	314	433
03-I.30	1	3 wt% I.30E	0.50	192	376	733
	2			201	352	713
	3			183	381	533
	5			194	329	729
	6			193	379	528
01-M52N	1	1 wt% M52N	0.59	135	334	683
	2			186	418	567
	5			166	382	532
	6			214	351	593
03-M52N	1	3 wt% M52N	0.63	161	336	699
	4			148	359	620
	5			125	358	639
	6			156	318	514
	7			172	401	581
03-M52N_vol	2	3 wt% M52N	0.53	403	846	1203
	3			423	675	1396
	4			413	744	1149
	5			410	685	1050
05-M52N	1	5 wt% M52N	0.56	222	495	750
	3			252	519	807
	4			240	561	852
	5			298	570	736

Table B-7 Mode-I interlaminar fracture energy of the flat laminates calculated by different data reduction methods.

Load point displacement (mm)	Applied load (N)	Delamination length a, (mm)	Interlaminar fracture energy (J/m ²)		
			MBT method	CC method	MCC method
Specimen name: Neat-02					
4.14	29.46	50	109	122	124
6.67	35.35	51	208	231	217
7.08	36.69	52	226	250	238
8.12	39.03	53	272	299	283
8.96	40.67	54	308	338	319
10.42	45.66	55	396	433	411
12.92	45.26	60	456	487	469
15.21	44.86	65	499	525	517
18.33	44.96	70	568	589	587
21.04	43.06	75	591	604	608
23.75	42.01	80	617	624	637
26.46	39.38	85	613	613	628
28.96	39.22	90	637	631	664
32.29	36.47	95	631	620	648
35.41	35.30	100	641	625	660
Specimen name: Neat-03					
5.21	29.08	50	126	141	140
8.96	38.94	51	287	318	296
10.16	41.82	52	345	380	354
11.21	44.41	53	398	436	410
12.25	43.67	54	422	460	425
13.08	42.92	55	437	474	434
14.75	41.90	60	452	478	455
17.25	41.00	65	488	505	491
19.75	39.87	70	514	523	518
22.25	39.19	75	539	540	548
25.37	36.99	80	552	545	553
27.87	36.67	85	573	559	583
30.58	35.53	90	582	561	594
33.50	33.84	95	581	554	592
36.59	32.72	100	589	556	600
Specimen name: Neat-05					
5.13	26.27	50	117	127	125
8.26	34.49	51	244	263	246
9.30	37.61	52	296	317	299
10.34	39.46	53	340	363	342

Table B-7 (continued)

Load point displacement (mm)	Applied load (N)	Delamination length a, (mm)	Interlaminar fracture energy (J/m^2)		
			MBT method	CC method	MCC method
11.38	39.90	55	368	389	370
13.41	42.54	60	433	448	450
15.91	43.07	65	490	497	513
18.42	39.62	70	492	491	506
21.75	40.55	75	563	554	583
24.67	38.63	80	577	561	594
27.58	35.66	85	567	545	575
31.54	33.31	90	578	550	574
36.12	34.65	95	659	621	663
39.67	34.63	100	693	647	705
Specimen name: Neat-07					
4.75	30.47	50	126	139	134
7.04	37.96	51	229	251	234
8.08	40.96	52	280	305	284
8.71	44.06	53	320	347	329
9.33	45.53	54	349	378	360
9.75	46.22	55	365	393	378
11.38	47.67	60	412	434	437
14.71	47.26	65	497	513	513
17.00	45.87	70	526	535	543
19.71	42.17	75	530	532	535
22.42	43.04	80	585	579	599
24.92	39.91	85	574	562	581
26.79	37.55	90	554	537	563
29.08	35.88	95	549	527	559
32.00	35.73	100	577	549	593
Specimen name: Neat_vol-01					
5.62	51.02	50	242	269	252
8.33	70.08	51	487	536	501
9.58	77.09	52	607	665	624
10.21	79.80	53	660	719	681
11.04	79.45	54	702	760	714
11.46	80.98	55	732	789	751
13.14	77.88	60	758	798	781
15.43	78.23	65	842	869	874
16.89	66.60	70	742	752	749

Table B-7 (continued)

Load point displacement (mm)	Applied load (N)	Delamination length a, (mm)	Interlaminar fracture energy (J/m ²)		
			MBT method	CC method	MCC method
21.47	66.64	80	850	837	880
23.56	60.65	85	809	787	825
26.26	60.04	90	852	820	876
30.22	57.84	95	904	861	915
33.56	56.50	100	940	887	951
Specimen name: Neat_vol-02					
5.62	51.35	50	241	265	257
8.33	65.58	51	449	491	463
10.00	70.84	52	574	625	580
10.42	72.00	53	600	649	609
10.83	73.82	54	631	679	646
11.46	73.25	55	654	700	663
12.27	73.56	60	660	690	699
13.94	70.96	65	682	698	725
15.40	66.08	70	663	666	704
17.69	60.29	75	660	652	684
20.19	55.17	80	655	638	663
23.10	58.80	85	762	733	790
25.60	55.34	90	759	722	780
29.15	52.74	95	788	742	798
31.65	50.72	100	789	736	800
Specimen name: Neat_vol-03					
5.62	52.14	50	238	259	245
8.13	65.79	51	428	462	427
8.54	68.11	52	459	493	462
9.58	72.29	53	540	576	540
10.42	75.26	54	603	640	602
11.04	75.68	55	635	670	631
12.38	78.52	60	694	714	715
14.88	77.57	65	778	783	796
16.76	76.64	70	820	809	847
19.05	71.20	75	822	797	837
21.34	67.79	80	835	797	845
23.42	63.77	85	822	775	829
27.80	63.96	90	936	871	933
29.88	63.03	95	950	874	960

Table B-7 (continued)

Load point displacement (mm)	Applied load (N)	Delamination length a, (mm)	Interlaminar fracture energy (J/m^2)		
			MBT method	CC method	MCC method
Specimen name: Neat_vol-04					
6.04	46.51	50	206	242	225
8.33	59.73	51	360	421	389
9.58	62.95	52	431	500	458
10.21	65.05	53	469	540	499
11.04	68.20	54	525	601	560
11.66	68.53	55	551	626	584
13.83	69.13	60	624	687	662
15.50	68.04	65	652	700	699
17.17	66.13	70	668	699	721
19.46	60.31	75	658	675	693
21.75	59.51	80	694	698	733
24.25	58.13	85	723	715	764
26.75	55.16	90	726	707	761
29.46	52.27	95	728	699	755
33.21	53.16	100	803	761	837
Specimen name: Neat_vol-05					
4.96	56.51	50	213	232	214
6.62	67.64	51	336	364	330
7.25	72.17	52	388	416	381
7.67	74.57	53	418	447	414
8.08	76.14	54	445	472	441
8.50	76.58	55	465	490	459
8.71	74.51	60	437	448	450
11.00	75.82	65	532	531	538
12.46	74.31	70	561	548	569
14.12	72.34	75	589	564	597
16.63	72.44	80	663	623	667
18.92	69.23	85	689	638	684
20.58	68.10	90	707	645	708
22.25	62.53	95	673	606	666
23.71	60.22	100	664	591	660
Specimen name: 01-I.30-02					
4.41	37.84	50	149	160	157
6.49	48.29	51	277	294	282
7.53	50.83	52	333	352	333

Table B-7 (continued)

Load point displacement (mm)	Applied load (N)	Delamination length a, (mm)	Interlaminar fracture energy (J/m^2)		
			MBT method	CC method	MCC method
8.99	50.86	54	386	405	375
9.62	52.09	55	417	436	405
10.88	53.41	60	453	463	455
12.96	47.02	65	446	448	431
14.63	48.40	70	488	484	486
16.09	44.37	75	465	455	461
17.96	42.26	80	470	454	465
19.84	41.56	85	485	464	486
22.33	40.71	90	510	483	512
25.67	41.27	95	567	533	572
28.58	37.97	100	557	519	550
Specimen name: 01-I.30-03					
4.74	33.18	50	133	146	142
6.82	40.72	51	231	253	238
7.65	41.49	52	261	283	263
8.90	44.45	53	321	346	319
9.53	45.57	54	347	373	345
9.64	43.99	55	335	358	332
11.54	47.22	60	404	421	412
14.04	44.01	65	431	441	427
16.12	45.80	70	487	489	494
18.83	41.90	75	493	488	486
21.33	42.33	80	536	524	536
24.04	41.24	85	561	541	560
26.54	38.78	90	556	531	552
28.20	38.27	95	558	527	564
30.70	38.59	100	588	550	604
Specimen name: 01-I.30-05					
4.78	38.33	50	172	189	185
6.66	47.51	51	292	319	306
7.28	48.05	52	318	346	330
7.70	48.13	53	332	360	343
8.54	51.27	54	386	417	400
8.72	51.70	55	392	422	410
10.17	50.77	60	419	443	444
11.84	43.26	65	389	406	397

Table B-7 (continued)

Load point displacement (mm)	Applied load (N)	Delamination length a, (mm)	Interlaminar fracture energy (J/m^2)		
			MBT method	CC method	MCC method
15.80	41.18	75	438	446	450
17.88	39.46	80	450	454	462
19.55	36.96	85	438	438	449
22.46	35.26	90	457	453	463
24.13	36.17	95	480	473	502
26.63	32.70	100	458	448	469
Specimen name: 01-I.30-07					
4.70	41.27	50	185	201	198
6.78	52.30	51	332	360	347
7.20	51.92	52	345	372	357
7.82	54.49	53	387	417	403
8.45	54.62	54	413	443	425
8.86	56.26	55	440	470	457
10.66	54.40	60	477	501	494
13.16	52.12	65	528	547	537
14.83	51.69	70	554	568	575
16.50	46.19	75	520	527	531
17.75	44.02	80	504	506	523
19.83	37.71	85	458	456	458
21.50	36.55	90	458	453	464
24.00	36.20	95	483	474	493
26.08	36.01	100	499	487	517
Specimen name: 01-I.30-08					
4.34	36.81	50	141	161	160
7.26	49.66	51	314	356	336
7.68	51.24	52	337	381	363
8.30	53.32	53	374	421	404
8.93	53.22	54	396	443	423
9.13	52.83	55	397	442	425
10.96	51.49	60	434	474	464
12.84	49.41	65	459	491	487
14.51	42.82	70	423	447	437
15.96	39.53	75	407	424	419
17.84	38.61	80	422	433	437
19.50	38.55	85	438	445	463
21.59	34.92	90	419	422	434

Table B-7 (continued)

Load point displacement (mm)	Applied load (N)	Delamination length a, (mm)	Interlaminar fracture energy (J/m ²)		
			MBT method	CC method	MCC method
25.75	34.03	100	446	441	472
Specimen name: 03-I.30-01					
4.81	45.09	50	192	211	206
7.31	59.18	51	376	412	391
8.15	61.65	52	431	469	444
8.56	62.60	53	453	491	468
9.40	64.24	54	503	542	516
8.96	60.62	55	446	479	462
10.98	64.08	60	541	569	570
13.06	65.94	65	623	643	665
15.15	59.67	70	616	626	642
17.65	57.99	75	660	662	684
20.15	54.04	80	667	660	681
21.81	51.50	85	654	641	673
25.15	52.57	90	734	712	760
28.27	51.63	95	775	745	803
32.02	47.06	100	766	731	771
Specimen name: 03-I.30-02					
4.46	47.40	50	201	217	215
6.54	57.43	51	352	378	359
6.96	59.73	52	384	410	395
7.38	60.80	53	408	434	420
8.21	62.98	54	463	491	473
8.45	64.04	55	478	505	493
10.82	66.01	60	587	611	605
12.49	64.48	65	619	635	645
14.57	61.95	70	653	662	678
16.66	60.93	75	692	694	725
19.57	56.35	80	712	707	727
22.70	52.63	85	731	721	733
24.36	49.96	90	709	694	717
26.45	46.90	95	689	670	696
28.74	47.56	100	726	701	749
Specimen name: 03-I.30-03					
4.81	44.35	50	183	201	197
7.52	59.92	51	381	416	396

Table B-7 (continued)

Load point displacement (mm)	Applied load (N)	Delamination length a, (mm)	Interlaminar fracture energy (J/m ²)		
			MBT method	CC method	MCC method
9.40	62.81	53	485	524	489
9.82	63.42	54	505	542	510
10.23	61.85	55	506	541	507
11.48	60.27	60	519	542	529
13.56	61.24	65	586	601	604
15.44	55.61	70	572	577	579
17.31	54.08	75	591	587	602
18.98	51.95	80	592	579	607
20.64	47.42	85	559	542	568
21.89	45.34	90	542	519	557
23.98	40.75	95	510	484	513
26.48	39.46	100	522	491	525
Specimen name: 03-I.30-05					
3.99	59.21	50	194	214	207
5.66	71.74	51	329	360	337
6.07	72.89	52	354	386	361
6.91	75.76	53	413	447	414
7.74	76.77	54	463	498	455
7.66	74.06	55	436	467	430
8.40	73.82	60	448	468	456
10.07	73.91	65	507	518	515
12.15	72.39	70	567	569	568
13.40	70.74	75	580	572	588
15.69	70.71	80	646	628	653
17.57	68.34	85	667	640	672
19.86	68.23	90	719	682	728
22.15	66.27	95	746	700	753
24.86	64.65	100	784	728	787
Specimen name: 03-I.30-06					
4.01	52.24	50	193	216	219
6.30	66.23	51	379	422	407
6.93	67.83	52	421	466	448
7.55	68.19	53	454	501	478
7.97	69.77	54	483	531	510
8.38	68.51	55	492	539	515
10.12	66.42	60	538	578	561

Table B-7 (continued)

Load point displacement (mm)	Applied load (N)	Delamination length a, (mm)	Interlaminar fracture energy (J/m^2)		
			MBT method	CC method	MCC method
14.29	61.73	70	623	650	640
15.75	55.34	75	581	600	590
16.79	55.03	80	584	596	611
18.46	45.02	85	499	504	498
19.71	45.78	90	515	517	532
21.37	46.83	95	546	544	579
23.87	44.34	100	552	546	580
Specimen name: 01-M52N-01					
4.79	35.23	50	135	149	143
8.33	50.74	51	334	365	335
9.17	52.20	52	373	405	371
9.58	52.50	53	387	418	385
10.00	54.14	54	411	442	413
10.83	56.31	55	457	489	459
12.28	56.67	60	491	511	503
15.61	57.40	65	597	607	601
18.53	57.86	70	677	675	681
21.03	57.36	75	724	709	732
22.69	51.63	80	669	645	669
24.36	49.64	85	660	627	666
27.07	46.71	90	660	619	659
30.40	47.06	95	715	664	719
32.69	44.43	100	697	640	699
Specimen name: 01-M52N-02					
5.00	44.70	50	186	197	199
8.12	62.66	51	418	441	432
8.75	63.96	52	454	475	467
9.58	66.26	53	508	529	520
10.21	64.82	54	522	541	526
11.46	63.20	55	564	581	550
12.19	61.19	60	546	549	549
14.90	58.16	65	598	589	586
16.36	56.06	70	598	579	594
17.61	53.28	75	580	552	583
19.28	49.11	80	557	523	556
20.73	47.61	85	554	513	560

Table B-7 (continued)

Load point displacement (mm)	Applied load (N)	Delamination length a, (mm)	Interlaminar fracture energy (J/m ²)		
			MBT method	CC method	MCC method
25.32	44.21	95	574	520	579
26.98	43.86	100	582	523	598
Specimen name: 01-M52N-05					
5.21	41.32	50	166	183	174
8.75	57.44	51	382	418	380
9.37	59.62	52	419	456	419
10.21	62.36	53	472	510	471
10.63	62.96	54	490	526	489
11.17	62.44	55	504	538	500
12.23	62.50	60	521	541	532
14.52	58.77	65	551	557	550
16.60	61.42	70	624	618	638
18.06	54.47	75	573	557	575
19.31	52.12	80	559	534	567
20.77	48.31	85	533	501	537
22.44	44.84	90	511	475	512
25.15	44.10	95	541	496	541
27.44	42.20	100	543	492	540
Specimen name: 01-M52N-06					
5.23	49.87	50	214	234	223
7.31	59.12	51	351	380	350
7.73	60.30	52	373	402	373
8.14	60.70	53	390	418	390
8.77	63.35	54	433	461	434
9.40	62.19	55	449	476	443
9.98	61.54	60	444	459	455
12.07	62.01	65	510	516	521
14.36	60.37	70	559	555	565
16.44	59.93	75	603	589	612
18.11	55.22	80	583	560	585
20.19	53.03	85	595	564	596
21.86	49.88	90	579	543	579
23.94	47.52	95	579	537	577
26.65	47.58	100	619	568	621
Specimen name: 03-M52N-01					
5.21	38.67	50	161	179	175

Table B-7 (continued)

Load point displacement (mm)	Applied load (N)	Delamination length a, (mm)	Interlaminar fracture energy (J/m^2)		
			MBT method	CC method	MCC method
10.00	53.34	52	416	456	415
10.42	56.00	53	449	489	455
11.04	56.01	54	470	509	473
11.67	56.13	55	491	529	492
13.78	60.87	60	592	622	613
16.49	56.93	65	626	642	632
18.57	54.81	70	643	647	650
20.65	53.10	75	658	650	669
23.15	50.63	80	670	651	678
25.24	48.12	85	662	635	671
28.57	45.96	90	685	649	685
31.49	44.54	95	701	656	701
33.99	45.77	100	747	692	765
Specimen name: 03-M52N-04					
5.62	31.50	50	148	161	153
9.58	45.61	51	359	389	359
10.42	47.34	52	400	430	398
11.25	49.90	53	449	480	450
11.67	48.26	54	444	473	441
12.29	50.34	55	482	510	483
13.53	47.94	60	475	490	482
16.45	45.54	65	517	523	513
18.95	44.66	70	552	548	549
21.24	43.76	75	575	562	577
23.53	42.69	80	591	570	598
26.03	40.36	85	589	561	593
29.57	39.78	90	630	593	633
32.28	36.26	95	600	559	594
36.03	37.18	100	659	608	660
Specimen name: 03-M52N-05					
4.79	30.86	50	125	137	135
9.17	46.86	51	358	391	364
10.42	49.11	52	420	456	422
11.25	50.77	53	463	500	465
11.67	52.82	54	493	529	502

Table B-7 (continued)

Load point displacement (mm)	Applied load (N)	Delamination length a, (mm)	Interlaminar fracture energy (J/m ²)		
			MBT method	CC method	MCC method
13.84	52.24	60	536	559	554
16.34	46.91	65	535	547	537
18.63	48.33	70	594	597	609
21.34	46.49	75	620	614	633
24.05	43.79	80	626	611	633
26.55	41.81	85	628	606	636
29.05	39.28	90	617	588	621
31.97	39.56	95	654	618	669
35.92	36.97	100	659	616	660
Specimen name: 03-M52N-06					
4.72	38.48	50	156	168	163
7.43	50.61	51	318	341	319
7.85	51.75	52	338	361	340
8.26	51.81	53	352	373	353
8.68	52.79	54	372	392	374
9.42	53.84	55	406	426	405
11.15	54.19	60	453	465	457
13.02	55.76	65	512	516	527
15.10	52.68	70	530	525	539
15.93	50.84	75	512	499	533
18.02	45.95	80	497	478	506
20.52	42.98	85	504	479	504
22.60	40.06	90	494	465	490
25.10	41.31	95	541	504	547
27.18	38.09	100	518	478	518
Specimen name: 03-M52N-07					
4.83	39.80	50	172	184	179
8.16	55.69	51	401	428	398
8.79	58.57	52	448	475	448
9.20	59.88	53	472	499	476
9.62	59.69	54	485	510	488
10.24	58.55	55	500	523	496
10.52	56.46	60	463	475	481
13.23	53.89	65	522	526	526
15.31	51.59	70	545	542	548
16.98	48.80	75	540	530	545

Table B-7 (continued)

Load point displacement (mm)	Applied load (N)	Delamination length a, (mm)	Interlaminar fracture energy (J/m ²)		
			MBT method	CC method	MCC method
22.19	43.96	85	574	551	566
24.06	42.84	90	578	550	578
26.36	41.81	95	590	557	594
28.44	39.98	100	583	546	589
Specimen name: 03-M52N_vol-02					
6.88	75.30	50	403	449	427
10.83	101.46	51	846	934	861
12.50	107.66	52	1022	1122	1025
13.12	109.24	53	1075	1172	1080
13.54	109.10	54	1094	1186	1100
13.77	109.08	55	1099	1184	1113
16.12	112.67	60	1253	1312	1290
19.25	106.21	65	1333	1363	1342
21.75	100.59	70	1353	1355	1354
22.79	98.18	75	1316	1293	1353
25.50	87.47	80	1251	1208	1250
26.96	85.40	85	1233	1174	1256
29.25	79.91	90	1199	1126	1214
31.75	75.35	95	1177	1091	1186
35.08	72.55	100	1203	1103	1205
Specimen name: 03-M52N_vol-03					
6.46	76.37	50	423	473	445
8.54	93.51	51	675	752	703
9.58	100.74	52	804	891	838
10.62	106.04	53	926	1020	961
11.46	109.87	54	1021	1119	1060
12.29	113.70	55	1118	1219	1162
14.55	113.57	60	1239	1322	1299
17.05	108.94	65	1311	1371	1365
20.17	102.42	70	1377	1417	1407
22.25	95.51	75	1342	1360	1369
25.17	86.72	80	1310	1310	1306
27.88	85.95	85	1369	1353	1382
29.96	84.57	90	1382	1351	1419
32.67	81.90	95	1396	1352	1440
35.38	81.17	100	1436	1378	1501

Table B-7 (continued)

Load point displacement (mm)	Applied load (N)	Delamination length a, (mm)	Interlaminar fracture energy (J/m ²)		
			MBT method	CC method	MCC method
6.88	77.00	50	413	457	433
10.00	96.77	51	744	820	754
11.46	102.04	52	888	971	886
12.08	104.17	53	944	1026	943
12.50	105.96	54	981	1060	987
12.92	105.84	55	1000	1074	1007
15.31	105.35	60	1112	1161	1121
16.97	105.49	65	1168	1190	1203
18.64	101.68	70	1172	1170	1219
22.39	89.69	75	1181	1157	1166
24.89	85.45	80	1193	1148	1172
26.35	82.24	85	1161	1101	1157
27.18	80.58	90	1123	1051	1150
30.72	77.94	95	1178	1089	1194
32.81	73.27	100	1136	1038	1148
Specimen name: 03-M52N_vol-05					
5.65	83.58	50	410	440	422
7.94	100.64	51	685	730	679
8.35	102.53	52	724	768	720
8.77	104.72	53	765	808	765
9.40	106.96	54	826	867	824
10.02	105.99	55	861	900	850
11.26	101.93	60	872	892	872
12.93	99.30	65	917	921	923
14.60	88.71	70	873	862	861
16.47	85.68	75	901	877	891
18.35	82.33	80	915	880	908
20.43	81.74	85	963	916	966
22.93	81.06	90	1023	962	1032
26.26	78.23	95	1081	1008	1077
29.60	75.85	100	1132	1046	1120
Specimen name: 05-M52N-01					
6.04	46.46	50	222	245	237
10.00	63.56	51	495	544	504
11.46	65.76	52	580	632	577
12.08	65.61	53	602	653	596

Table B-7 (continued)

Load point displacement (mm)	Applied load (N)	Delamination length a, (mm)	Interlaminar fracture energy (J/m ²)		
			MBT method	CC method	MCC method
13.75	66.79	55	680	729	666
14.43	67.55	60	680	709	698
17.76	64.39	65	754	768	752
20.47	63.62	70	814	812	814
22.35	58.17	75	772	756	765
24.02	55.35	80	752	725	752
25.68	52.43	85	728	691	731
28.18	49.15	90	716	672	714
31.10	49.46	95	763	707	769
34.43	48.43	100	794	728	800
Specimen name: 05-M52N-03					
6.04	53.58	50	252	282	274
9.58	70.40	51	519	577	536
10.83	74.39	52	612	675	626
11.67	73.78	53	646	708	651
12.08	73.45	54	657	716	662
12.62	71.10	55	657	711	653
13.79	72.88	60	693	730	716
16.08	67.30	65	706	726	713
17.75	62.29	70	684	688	687
19.41	60.98	75	696	688	709
21.29	59.60	80	711	691	731
24.21	61.41	85	796	762	829
27.29	58.53	90	819	773	842
30.25	54.93	95	817	762	829
33.16	50.82	100	796	735	795
Specimen name: 05-M52N-04					
6.04	46.97	50	240	258	253
10.42	64.61	51	561	600	557
11.04	66.90	52	607	646	606
11.67	68.08	53	644	682	644
12.29	68.62	54	675	710	674
12.92	70.61	55	720	754	723
14.50	69.71	60	749	766	768
17.00	69.14	65	820	822	845
19.09	64.09	70	806	795	825

Table B-7 (continued)

Load point displacement (mm)	Applied load (N)	Delamination length a, (mm)	Interlaminar fracture energy (J/m ²)		
			MBT method	CC method	MCC method
23.88	58.11	80	824	789	840
27.01	56.96	85	871	823	888
30.34	53.20	90	872	816	876
33.25	50.90	95	876	810	878
35.13	45.22	100	788	722	778
Specimen name: 05-M52N-05					
6.02	53.59	50	298	328	337
9.56	65.62	51	570	625	601
10.18	64.82	52	591	645	617
10.60	65.37	53	611	665	641
11.22	65.75	54	642	695	671
11.61	67.21	55	669	721	707
13.84	68.14	60	754	799	809
15.92	66.27	65	791	825	856
18.01	61.82	70	786	809	847
20.51	57.34	75	784	797	836
22.59	52.81	80	754	758	799
25.30	47.98	85	728	726	758
28.42	43.28	90	703	695	714
31.34	43.82	95	749	735	775
34.47	42.56	100	765	746	794

Table B-8 Fiber volume fraction data for the flat laminate samples. (Mode-I interlaminar fracture test samples)

Sample name	Filler-matrix loading	Tow tension (N)	Lamina layers	Sample mass (g)	Fiber mass (g)	Fiber volume fraction
Neat	(Neat epoxy)	26.7	8	7.42	6.05	0.66
		26.7	8	6.74	5.38	0.63
Neat_vol		0.0	8	7.39	5.56	0.57
		0.0	8	6.81	4.98	0.54
01-I.30	1 wt% I.30E	26.7	8	4.14	3.13	0.57
		26.7	8	2.80	2.13	0.58
03-I.30	3 wt% I.30E	26.7	8	5.26	3.68	0.50
		26.7	8	5.30	3.67	0.50
01-M52N	1 wt% M52N	26.7	8	7.70	5.93	0.59
		26.7	8	7.58	5.67	0.56
		26.7	8	5.24	4.04	0.59
		26.7	8	5.81	4.60	0.62
03-M52N	3 wt% M52N	26.7	8	8.10	6.43	0.62
		26.7	8	3.40	2.74	0.64
		26.7	8	8.54	6.71	0.61
03-M52N_vol		0.0	8	6.52	4.81	0.55
		0.0	8	7.31	5.15	0.51
05-M52N	5 wt% M52N	26.7	8	8.66	6.56	0.57
		26.7	8	8.07	5.91	0.54

Table B-9 Experimentally determined functional failure (leakage) stresses of filament-wound composite pipes for 2-to-1 hoop-to-axial loading ratio.

Filler-matrix loading (wt%)	Sample name	FVF	Failure pressure (kPa)	Axial failure load (N)	Hoop stress (MPa)	Axial stress (MPa)
Neat epoxy	T007	0.68	12124	965.2	175.29	90.66
	T008	0.66	12139	1144.4	175.51	91.87
1 wt% M52N	T003	0.66	12976	1071.1	183.91	95.28
	T004	0.66	13054	1111.8	185.03	96.07
	T022		12429	977.4	176.09	90.94
3 wt% M52N	T005	0.65	12652	1014.0	178.21	92.13
	T006	0.67	12235	953.0	172.29	88.90
	T023		12147	1152.5	171.04	89.50
5 wt% M52N	T001	0.65	11087	863.4	154.37	79.62
	T002	0.66	11756	912.2	163.77	84.45
	T024		11987	1115.9	167.02	87.23
1 wt% I.30E	T012	0.59	12715	1075.1	163.16	84.37
	T013	0.61	11141	924.5	142.79	73.74
	T014		11688	957.0	149.87	77.32
2 wt% I.30E	T015		10864	920.4	139.20	71.99
	T016	0.60	11040	1010.0	141.48	73.58
	T017		9247.6	843.0	118.28	61.50
3 wt% I.30E	T018	0.61	10931	863.4	137.55	70.75
	T019	0.57	11554	928.5	145.46	74.91
	T020		12743	1062.9	160.57	82.90

Table B-10 Experimentally determined structural failure (burst) stresses of filament-wound composite pipes for 2-to-1 hoop-to-axial loading ratio.

Filler-matrix loading (wt%)	Sample name	FVF	Failure pressure (kPa)	Axial failure load (N)	Hoop stress (MPa)	Axial stress (MPa)
Neat epoxy	T007	0.68	32243	2524.9	468.75	242.17
	T008	0.66	33363	2777.4	485.09	251.63
1 wt% M52N	T003	0.66	32355	2553.4	460.86	238.05
	T004	0.66	28818	2366.1	410.31	212.50
	T022		34196	2663.4	487.17	251.43
3 wt% M52N	T005	0.65	33373	2598.2	472.57	243.84
	T006	0.67	30055	2317.2	425.44	219.38
	T023		30933	2598.2	437.91	227.09
5 wt% M52N	T001	0.65	31612	2431.3	442.93	228.28
	T002	0.66	31905	2451.6	447.05	230.39
	T024		32020	2647.1	448.66	232.34
1 wt% I.30E	T012	0.59	27869	2243.9	359.27	185.17
	T013	0.61	29306	2309.1	377.87	194.47
	T014		29559	2345.7	381.15	196.25
2 wt% I.30E	T015		27821	2191	358.65	184.58
	T016	0.60	26731	2191	344.55	177.79
	T017		26045	2162.5	335.67	173.36
3 wt% I.30E	T018	0.61	27141	2101.4	343.55	176.49
	T019	0.57	27947	2227.6	353.79	182.09
	T020		27825	2219.5	352.24	181.30